REPORT TITLE:

ACTIVE CATHODES FOR SUPER-HIGH POWER DENSITY SOLID OXIDE FUEL CELLS THROUGH SPACE CHARGE EFFECTS

Reporting Period Start Date: October 1, 2002
Reporting Period End Date: September 30, 2005
Principal Author: Professor Anil V. Virkar
Date Report Was Issued: April 10, 2006
DOE Award Number: DE-FC26-02NT41602
Name and Address of Submitting Organization:

Department of Materials Science & Engineering
122 S. Central Campus Drive
University of Utah
Salt Lake City, UT 84112

ABSTRACT

This report briefly summarizes the work done over the duration of the project, beginning October 1, 2003 and ending September 30, 2005. This project was on understanding cathode mechanisms in intermediate temperature solid oxide fuel cells (SOFC) and developing superior cathodes. A particular emphasis was on the role of defect chemistry and the role of space charge effects. It was hypothesized that the space charge should have a major effect on cathode activation polarization. If the space charge increases oxygen vacancy concentration, it should be beneficial. On the other hand, if space charge suppresses oxygen vacancy concentration, it may adversely affect the cathodic reaction. It was determined that a combined effect of porous body microstructure/defect chemistry can be significant on transport and polarization. Also explored extensively was the role of interfaces, where electrode reactions occur, on transport through oxygen ion conducting materials. In particular, fundamental aspects of transport were theoretically examined. The analysis has significant implications on the very measurement of overpotential using the so-called three electrode system. In the area of cathode polarization, an important property concerns the chemical surface exchange coefficient, k_{chem}. An experimental technique was developed which allows for the measurement k_{chem} using porous bodies. Some of the work conducted under this project has been published in the open literature. Copies of the papers are included here in lieu of a detailed report. Much of it has been reported in text form in the quarterly reports submitted. Also included in this report are the manuscripts yet to be submitted for publication.

LIST OF PAPERS PUBLISHED

1) "Theoretical Analysis of the Role of Interfaces in Transport through Oxygen Ion and Electron Conducting Membranes", A. V. Virkar, *J. Power Sources*, **147** 8-31 (2005).
2) "Estimation of Charge-Transfer Resistivity of Pt Cathode on YSZ Electrolyte using Patterned Electrodes", R. Radhakrishnan and S. C. Singhal, *J. Electrochem. Soc.*, **152** (5) A927-A936 (2005).
3) "Investigation of Electrolyte Stability using Amperometric Sensors: Implications Concerning Electrode Polarization Measurements", in SOFC-IX, edited by S. C. Singhal and J. Mizusaki, p. 1057-1067, Electrochemical Society Proceedings Volume 2005-7, (2005).
4) "Measurement of Transport Properties of Perovskite Cathodes", R. Ganeshanathan and A. V. Virkar, in SOFC-IX, edited by S. C. Singhal and J. Mizusaki, p. 1487-1498, Electrochemical Society Proceedings Volume 2005-7, (2005).
5) "Effect of Microstructure and Space Charge on Cathode Polarization", F. Zhao and A. V. Virkar, in SOFC-IX, edited by S. C. Singhal and J. Mizusaki, p. 1521-1531, Electrochemical Society Proceedings Volume 2005-7, (2005).

PREPRINTS

1) "Effect of Morphology and Space Charge on Conduction through Porous Bodies", F. Zhao and A. V. Virkar.

BRIEF SUMMARY OF THE WORK PERFORMED

In what follows, brief summary of the work done is given. This is given as summaries of each of the papers (and the preprint) described here. Copies of the papers are attached as part of this final report.

Paper 1: "Theoretical Analysis of the Role of Interfaces in Transport through Oxygen Ion and Electron Conducting Membranes", A. V. Virkar, *J. Power Sources*, **147** 8-31 (2005).

Summary

This manuscript examines transport through oxygen ion and electronic conducting membranes including electrode/membrane interfaces by explicitly incorporating both ionic and electronic transport through the membranes and across interfaces. Spatial variation of electrochemical potential of oxygen ions, $\tilde{\mu}_{O^{-2}}$, electrochemical potential of electrons, $\tilde{\mu}_e$ (or reduced negative electrochemical potential of electrons, $\varphi = -\tilde{\mu}_e / e$, where e is the electronic charge), and chemical potential of molecular oxygen, μ_{O_2}, through membrane and across interfaces are examined as functions of transport properties of membranes and interfacial regions. The analysis shows that description of transport across electrode/membrane interfaces requires two transport parameters – one for ions, and another for electrons. The transport equations are applied to fuel cells, pressure-driven oxygen separation through mixed ionic-electronic conducting (MIEC) membranes, and voltage-driven oxygen separation through predominantly oxygen ion conducting membranes. In fuel cells and MIEC oxygen separation membranes, the μ_{O_2} varies monotonically between the two end values corresponding to those at the two electrodes. Thus, in fuel cells and MIEC oxygen separation membranes, the stability of the membrane is assured as long as the oxygen partial pressure, p_{O_2}, on the fuel side or the permeate side is above the decomposition oxygen partial pressure of the membrane. By contrast, in voltage-driven oxygen separation membranes, μ_{O_2} in the membrane can lie outside of the end values. Thus, in the case of oxygen separation under an applied voltage, the transport properties of the material and the interfaces determine membrane stability. Implications of the analysis concerning the applicability of the so-called the three-electrode system under an applied voltage to investigate electrode polarization are presented. It is shown that the use of the three-electrode system for the estimation of electrode kinetics can lead to significant errors at high applied voltages, and may result in overestimation of electrocatalytic activity of the electrode. This manuscript also defines electrode overpotential in terms of the rate of potential useful work degraded as an irreversible process at an electrode and the net current measured in the external circuit. The as-defined overpotential may not be experimentally measurable.

Key Words: Mixed ion-electronic conductors; oxygen ion conductors; fuel cells; oxygen separation; transport across interfaces.

Paper 2: "Estimation of Charge-Transfer Resistivity of Pt Cathode on YSZ Electrolyte using Patterned Electrodes", R. Radhakrishnan and S. C. Singhal, *J. Electrochem. Soc.*, **152** (5) A927-A936. (2005)

Summary

Yttria-Stabilized Zirconia (YSZ) electrolyte discs with patterned platinum (Pt) electrodes having different three phase boundary (TPB) lengths (l_{TPB}), but the same electrode-electrolyte interface area, were deposited on one of the two faces using photomicrolithography. Platinum counter electrode was applied on the other face, and a platinum wire reference electrode was positioned along the cylindrical surface. Impedance spectra under zero applied bias were obtained in oxygen partial pressures, (p_{O_2}), ranging between 10^{-3} and 1 atm and over a range of temperatures between 650 and 800°C. Area specific charge transfer resistance, R_{ct}, was found to vary inversely with l_{TPB}. The value of charge transfer resistivity, ρ_{ct}, corresponding to the charge transfer reaction occurring at TPB, was estimated at various temperatures and p_{O_2}. The R_{ct} and ρ_{ct} decrease with increasing p_{O_2} and with increasing temperature. The activation energy for the overall charge transfer reaction was found to vary between 0.75 eV at a p_{O_2} of 0.001 atm and 1.63 eV for a p_{O_2} of 1 atm.

Key words: Patterned electrode, Charge transfer resistance, Three-phase boundary, Impedance spectroscopy, Oxygen reduction reaction

Paper 3: "Investigation of Electrolyte Stability using Amperometric Sensors: Implications Concerning Electrode Polarization Measurements", in SOFC-IX, edited by S. C. Singhal and J. Mizusaki, p. 1057-1067, Electrochemical Society Proceedings Volume 2005-7, (2005)

Summary

Amperometric sensors with yttria-stabilized zirconia (YSZ) discs and YSZ cylinders were made with platinum electrodes applied on the YSZ disc, which served as working (inside) and counter (outside) electrodes, and a platinum wire electrode positioned along the circumference of the disc. Two sets of platinum electrodes were applied on the YSZ cylinder, one inside and the other outside. The YSZ cylinder was attached to the YSZ disc using a sealing glass. A YSZ disc with a tiny diffusion hole was glass-sealed on the other end of the YSZ cylinder. The amperometric sensor was tested at 800°C in air over an applied DC voltage range from zero to 2.5 V. The measured current over a voltage range from ~0.4 to ~1.6 V exhibited a plateau. For applied voltage ≥ 1.7 V, the measured current increased, with a rapid increase for applied voltage ≥ 1.9 V. This rapid rise is consistent with the development of nonstoichiometry or the occurrence of YSZ electrolyte decomposition. The voltage between the reference and the working electrodes was measured. Based on this information, the cathodic activity of the platinum working

electrode was estimated. Implications concerning the use of the three electrode system for the study of electrode polarization are discussed.

Paper 4: "Measurement of Transport Properties of Perovskite Cathodes", R. Ganeshanathan and A. V. Virkar, in SOFC-IX, edited by S. C. Singhal and J. Mizusaki, p. 1487-1498, Electrochemical Society Proceedings Volume 2005-7, (2005)

Summary

Conductivity relaxation experiments were conducted on porous $La_{0.5}Sr_{0.5}CoO_{(3-\delta)}$ (LSC50) samples over a temperature range from 350 to 750°C, and over an oxygen partial pressure, p_{O_2}, switch between 0.04 and 0.06 atm in order to determine the surface exchange coefficient, k_{chem}. The normalized conductivity data could be fitted to a first order kinetic equation. The time constant decreased with decreasing temperature between ~750 and ~450°C, but sharply increased with decreasing temperature between 450 and 350°C. The corresponding k_{chem} was estimated using three models: (a) A porous body model wherein it is assumed that the kinetics of surface exchange is the slowest. (b) Solution to the diffusion equation assuming the particles can be approximated as spheres. (c) Solution to the diffusion equation assuming the particles can be approximated as cylinders. The values of k_{chem} obtained from the three models were in good agreement. In all cases, it was observed that k_{chem} increases with decreasing temperature between 750 and 450°C, but below 450°C, it sharply decreases with further decrease in temperature.

Paper 5: "Effect of Microstructure and Space Charge on Cathode Polarization", F. Zhao and A. V. Virkar, in SOFC-IX, edited by S. C. Singhal and J. Mizusaki, p. 1521-1531, Electrochemical Society Proceedings Volume 2005-7, (2005)

Summary

Bar-shaped samples of porous samaria-doped ceria (SDC) with large neck sizes were fabricated using a three-step method. In the first step, two phase samples containing NiO + SDC were fabricated by sintering powder compacts. In the second step, NiO was reduced to Ni at 800°C in a hydrogen-containing atmosphere. In the third step, Ni was removed by acid leaching, leading to the formation of porous SDC samples with wide inter-particle necks. The conductivity of bar samples was measured using a DC 4-probe technique between 650 and 800°C. The samples were then annealed at 1200 and 1400°C. The conductivity of the samples was again measured between 650 and 800°C. It was observed that the lower the annealing temperature, the lower was the conductivity. Anode-supported cells were fabricated with cathode made of Sr-doped $LaCoO_3$ (LSC) and SDC, wherein the SDC layer was formed by the three-step method. Cell performance was measured at 800°C with the cells subjected to thermal treatments at 1200 and 1400°C prior to infiltration of LSC using aqueous salt solutions. It was observed that the lower the annealing temperature, the lower was the cell performance. The observed behavior is attributed in part to space charge effects. Thermal treatments, however, may also lead to precipitation of insulating phases at grain boundaries thereby increasing resistance and lowering cell performance.

Preprint 1: "Effect of Morphology and Space Charge on Conduction through Porous Bodies", F. Zhao and A. V. Virkar.

Summary

An analytical model on the role of connectivity on electrical conductivity of porous bodies, including the roles of grain boundaries and space charge, was developed. Porous samaria-doped ceria (SDC) samples were fabricated using two methods: (1) conventional sintering of powder compacts and (2) a method comprising the fabrication of sintered NiO + SDC two phase samples, followed by reduction of NiO to Ni, and the removal of Ni by acid leaching. The latter method can fabricate porous sample with preferred high porosity and larger inter-particle neck. Electrical conductivities of as-fabricated bar samples were measured using DC 4-probe technique. The electrical conductivity of some of porous SDC samples fabricated using leaching process, as a function of temperature and oxygen partial pressure, is measured with DC 4-probe method. It was observed that the neck size has significant effect on the effective conductivity of porous body. The increase of electrical conductivity with reducing oxygen partial pressure can be explained well by the space charge model. Finally the model was applied to composite electrode. The effect of morphology of porous ionic conductor framework in composite cathode on electrode polarization was discussed.

Available online at www.sciencedirect.com

SCIENCE DIRECT®

Journal of Power Sources xxx (2005) xxx–xxx

JOURNAL OF POWER SOURCES

www.elsevier.com/locate/jpowsour

Theoretical analysis of the role of interfaces in transport through oxygen ion and electron conducting membranes

Anil V. Virkar*

Department of Materials Science and Engineering, 122 South Central Campus Drive, University of Utah, Salt Lake City, UT 84112, USA

Received 22 December 2004; accepted 17 January 2005

Abstract

This manuscript examines transport through oxygen ion and electronic conducting membranes including electrode/membrane interfaces by explicitly incorporating both ionic and electronic transport through the membranes and across interfaces. Spatial variation of electrochemical potential of oxygen ions, $\tilde{\mu}_{O^{2-}}$, electrochemical potential of electrons, $\tilde{\mu}_e$ (or reduced negative electrochemical potential of electrons, $\varphi = -\tilde{\mu}_e/e$, where e is the electronic charge), and chemical potential of molecular oxygen, μ_{O_2}, through membrane and across interfaces are examined as functions of transport properties of membranes and interfacial regions. The analysis shows that description of transport across electrode/membrane interfaces requires two transport parameters—one for ions, and the other for electrons. The transport equations are applied to fuel cells, pressure-driven oxygen separation through mixed ionic–electronic conducting (MIEC) membranes, and voltage-driven oxygen separation through predominantly oxygen ion conducting membranes. In fuel cells and MIEC oxygen separation membranes, the μ_{O_2} varies monotonically between the two end values corresponding to those at the two electrodes. Thus, in fuel cells and MIEC oxygen separation membranes, the stability of the membrane is assured as long as the oxygen partial pressure, p_{O_2}, on the fuel side or the permeate side is above the decomposition oxygen partial pressure of the membrane. By contrast, in voltage-driven oxygen separation membranes, μ_{O_2} in the membrane can lie outside of the end values. Thus, in the case of oxygen separation under an applied voltage, the transport properties of the material and the interfaces determine membrane stability. Implications of the analysis concerning the applicability of the so-called the three-electrode system under an applied voltage to investigate electrode polarization are presented. It is shown that the use of the three-electrode system for the estimation of electrode kinetics can lead to significant errors at high applied voltages, and may result in overestimation of electrocatalytic activity of the electrode. This manuscript also defines electrode overpotential in terms of the rate of potential useful work degraded as an irreversible process at an electrode and the net current measured in the external circuit. The as-defined overpotential may not be experimentally measurable.

Keywords: Mixed ion–electronic conductors; Oxygen ion conductors; Fuel cells; Oxygen separation; Transport across interfaces

1. Introduction

Many oxides transport both ionic (cationic and/or anionic) and electronic species. Of particular interest for applications such as fuel cells, water electrolysis, potentiometric oxygen sensors, oxygen separation under an applied voltage, etc. are materials, which can predominantly transport oxygen ions. For oxygen separation from air under an applied pressure gradient, materials, which exhibit significant transport of both oxygen ions and electronic defects, are of interest. Such materials are known as mixed ionic–electronic conductors (MIEC). Transport in oxygen ion conductors or in MIEC materials can be described by phenomenological equations, which have been well established for over 50 years [1–5]. Several published works have applied these transport equations for investigating ionic and electronic transport through membranes [6–11]. In most of these studies, the focus was on transport through membranes with emphasis on the role of defect chemistry, but rarely on the role of interfaces. In those

---

* Tel.: +1 801 581 5396; fax: +1 801 581 4816.
E-mail address: anil.virkar@m.cc.utah.edu.

0378-7753/$ – see front matter © 2005 Elsevier B.V. All rights reserved.
doi:10.1016/j.jpowsour.2005.01.038

Nomenclature

B_i	mobility of species i
C_i	concentration of species i
e	electronic charge
E, E_0	Nernst voltage
E_A	applied voltage
E_M	measured voltage
F	Faraday constant
g_e	electronic specific conductance
g_i	ionic specific conductance
j_i	flux of species i
I_e	electronic current density
I_i	current density due to species i (also ionic current density)
I_L	load current (density)
k_B	Boltzmann constant
ℓ	membrane thickness
n_{O_2}	number of moles of O_2 gas
p_{O_2}	partial pressure of molecular oxygen
r_e	electronic area specific resistance
r_i	ionic area specific resistance
R	ideal gas constant
R_e	electronic area specific resistance of the membrane including interfaces
R_i	ionic area specific resistance of the membrane including interfaces
R_L	load
t	time
t_i	ionic transference number
T	temperature
V_pore	volume of pore
z_i	valence of species i

Greek letters

δ	interface thickness
η	overpotential
μ_i	chemical potential of species i
$\tilde{\mu}_e$	electrochemical potential of electrons
$\tilde{\mu}_i$	electrochemical potential of species i
μ_{O_2}	chemical potential of oxygen gas
$\tilde{\mu}_{\mathrm{O}^{2-}}$	electrochemical potential of oxygen ions
$\mu_{\mathrm{O}_2}^{\mathrm{decomp}}$	decomposition oxygen chemical potential of the membrane
$\mu_{\mathrm{O}_2}^{\mathrm{membrane}}$	chemical potential of oxygen in the membrane
$\mu_{\mathrm{O}_2}^{\mathrm{I}}$	chemical potential of oxygen in the gas phase close to the electrode I/membrane interface
$\mu_{\mathrm{O}_2}^{\mathrm{II}}$	chemical potential of oxygen in the gas phase close to the electrode II/membrane interface
ρ_e	electronic resistivity
ρ_i	ionic resistivity
σ_e	electronic conductivity
σ_i	conductivity due to species i (also ionic conductivity)
φ	reduced (negative) electrochemical potential of electrons
φ^{I}	reduced (negative) electrochemical potential of electrons outside the membrane close to the electrode I/membrane interface
φ^{II}	reduced (negative) electrochemical potential of electrons outside the membrane close to the electrode II/membrane interface
Φ	electrostatic potential (Galvani)

studies which have examined transport through membranes taking into account interfaces, the focus has been on either ion transport across interfaces or electron transport across interfaces, but usually not both. Phenomenological transport equations for the flux of a charged species are usually written in terms of the gradient in electrochemical potential of the species involved and the relevant transport parameters. A fundamental assumption made, albeit often tacitly, is that of the existence of local equilibrium, which leads to relations between electrochemical potentials of charged species and chemical potentials of neutral species [2,3]. For example, for the case of oxygen ions and neutral oxygen molecules (or atoms), local equilibrium may be described in terms of oxygen molecules (or atoms), electrons and oxygen ions as the species participating in the reaction.

The above general framework is assumed regardless of the prevailing point defects, vacancies or interstitials or both. Additional equations can be written in terms of the concentrations and transport properties of point defects. This, however, often requires one to make simplifying assumptions concerning the thermodynamics of defects. The assumption of local equilibrium is universally made, either explicitly or implicitly [12]. The assumption of local equilibrium in a system also implies the existence of equilibrium at any position in the system, wherein the system may be single phase or may consist of multiple phases—including the gas phase. Transport of a species occurs from one position to another (adjacent) position in response to difference (gradient) in the relevant thermodynamic potential. In MIEC materials, the transport of both ions and electronic defects is taken into account, as the conductivities of the two species are nonzero finite, and often comparable. However, when dealing with materials that are predominantly ionic conductors with negligible electronic conductivity, often it has been the practice to ignore the electronic transport altogether [13]. This may be satisfactory if the interest is only in the net current flowing through the material. The neglect of electronic current, however, amounts to an inconsistency insofar as the assumption of local equilibrium is concerned. That is, the assumption of local equilibrium and the simultaneous neglect of electronic conduction are contradictory assumptions. If local equilibrium is assumed, which is almost always necessary for writing down relevant transport equations, the electronic conductivity cannot be assumed to be identically equal to zero. In many cases, this inconsistency often does not lead to significant problems. However, as will be discussed in this manuscript, and has been discussed to some extent in earlier manuscripts, there are many situations in which the neglect of electronic current, however small, leads to substantial difficulties in analysis—and thus also in the interpretation of experimental results [14–16].

In devices such as fuel cells and MIEC oxygen separation membranes, no external voltage is applied. Whatever voltage is developed across the membrane is the result of differences in chemical potentials of neutral species imposed and the transport properties of the membrane. However, when dealing with devices such as oxygen separation membranes under an externally applied voltage, the system then has an additional (experimental) degree of freedom, which has important consequences concerning the design of experiments and the interpretation of data, especially concerning studies on electrode kinetics or in oxygen separation under an applied voltage or water electrolysis. In devices such as solid oxide fuel cells, it is generally not possible to obtain an accurate measurement of electrode overpotential, since it is necessary to place a reference electrode on the surface—unlike in aqueous electrochemistry wherein it can be immersed in the liquid electrolyte. In order to circumvent this problem, often the so-called three-electrode system is used, wherein the electrolyte is in the form of a thick pellet. The working electrode, the counter electrode, and the reference electrode are placed in an axisymmetric arrangement. Then, to investigate electrode kinetics at the working electrode, which may be a prospective cathode for a fuel cell, an external voltage is applied across the counter and the working electrodes. An assumption is made that the externally applied voltage is essentially equivalent to that generated by the application of an external chemical potential difference, and all that is required is to measure the current (density) as a function of overpotential, the latter measured with respect to the reference electrode—and corrected for ohmic losses. This approach is assumed to represent the situation at a real cathode in a fuel cell. As will be demonstrated in this manuscript, the three-electrode system is fundamentally and physically different from a fuel cell and its use under an externally applied voltage to investigate electrode kinetics can lead to substantial error—where the magnitude of the error depends upon a number of parameters, including the magnitude of the applied voltage.

This manuscript first develops transport equations using the standard phenomenological approach. The difference compared to much of the prior work, however, is the inclusion of the electronic current in a predominantly ionic conductor—and especially its role in the estimation of the local chemical potential of oxygen, μ_{O_2}, which determines the stability of the material, and also the net current flowing through the system. This also implies the inclusion of both ionic and electronic currents through the membrane and across the electrode/membrane interfaces. Three cases of practical interest are examined: (1) oxygen separation using an MIEC membrane, (2) a fuel cell, and (3) oxygen separation under the application of an external voltage. The implications of the latter are examined for the often-used three-electrode system under an applied voltage for the investigation of electrode kinetics. All equations are developed for the case where the transport properties of a given region are constant, independent of position and μ_{O_2}. Although in many materials the transport properties are μ_{O_2}-dependent—and thus are functions of position—such a simplifying assumption is deemed necessary to allow for the development of simple analytical equations. This approach also allows for description in terms of simple equivalent circuits. If quantitative relations between transport parameters and μ_{O_2} are known, which is rarely the case for most materials (and interfacial regions), it would be a straightforward matter to numerically solve the relevant transport equations.

2. Theoretical analysis

In what follows, transport only under isothermal conditions is addressed. It is also assumed that gas transport through the porous electrodes to the electrode/membrane interfaces is sufficiently fast such that concentration polarization is negligible.[1] General transport equation for a one-dimensional flux is given by [2]:

$$j_i = -C_i B_i \nabla \tilde{\mu}_i = -C_i B_i \frac{\mathrm{d}\tilde{\mu}_i}{\mathrm{d}x} \tag{1}$$

(assuming the flux of a charged species occurs down its electrochemical potential gradient) in # (cm^{-2} s^{-1}), where C_i and B_i are, respectively, concentration and mobility of species i, and the electrochemical potential of species i is given by

$$\tilde{\mu}_i = \mu_i + z_i e \Phi \tag{2}$$

where μ_i is the chemical potential of species i (J or ergs), z_i the valence of species i, e the electronic charge (C), and Φ the local electrostatic potential or Galvani potential (V).

The current density due to species i for a one-dimensional case is given by

$$I_i = z_i e j_i = -\frac{\sigma_i}{z_i e} \nabla \tilde{\mu}_i = -\frac{\sigma_i}{z_i e} \frac{\mathrm{d}\tilde{\mu}_i}{\mathrm{d}x} \tag{3}$$

in A cm^{-2}, where $\sigma_i = z_i^2 e^2 C_i B_i$ is the conductivity due to species i (S cm^{-1}) = $1/\rho_i$, where ρ_i is the resistivity (Ω cm). In the above, μ_i and $\tilde{\mu}_i$ are defined on a per species (per ion, per electron, per atom, or per molecule) basis. If defined on

---

[1] In practice, this assumption often may not be valid. For example, this assumption may not be valid when using the three-electrode system under an externally applied voltage, the implications of which are discussed later. Also, this assumption is almost certainly not valid in devices such as solid oxide fuel cells, which use porous electrodes several microns in thickness.

a per mole basis, e is replaced by the Faraday constant, F ($\mathrm{C\,mol^{-1}}$).

Local equilibrium is assumed to prevail everywhere in the system [12]. The cation sublattice is assumed to be rigid in what follows. For an oxygen ion conductor, the equilibrium of interest is the following, namely:

$$\tfrac{1}{2}\mathrm{O_2} + 2\mathrm{e}' \rightarrow \mathrm{O^{2-}} \tag{4}$$

Thus, at (local—at any position in the system) equilibrium [2,12]

$$\tfrac{1}{2}\mu_{\mathrm{O_2}} + 2\tilde{\mu}_e = \tilde{\mu}_{\mathrm{O^{2-}}} \tag{5}$$

where

$$\tilde{\mu}_{\mathrm{O^{2-}}} = \mu_{\mathrm{O^{2-}}} - 2e\Phi \tag{6a}$$

and

$$\tilde{\mu}_e = \mu_e - e\Phi \tag{6b}$$

Local equilibrium also implies that any changes made in chemical or electrochemical potentials (at any given position) must satisfy the following relation:

$$\tfrac{1}{2}\delta\mu_{\mathrm{O_2}} + 2\delta\tilde{\mu}_e = \delta\tilde{\mu}_{\mathrm{O^{2-}}} \tag{7}$$

where δX denotes a small deviation in the thermodynamic potential X from the equilibrium state. The above implies that the material in question must be able to transport at least two of the species (at least two of $\mathrm{O_2}$ (O), $\mathrm{O^{2-}}$ and e), in and out, in order to maintain local equilibrium. This also implies that when potential gradients exist, one can never have the flux of any of the species (participating in the equilibrium reaction) in the above, identically equal to zero. That is, even for a predominantly ionic conductor, we must always have $I_e \neq 0$, even though it may be small. This has important implications concerning the chemical potential of oxygen and thus the very stability of the material, which will be discussed in this manuscript.

Ionic and electronic current densities are given respectively by[2]

$$I_i = I_{\mathrm{O^{2-}}} = \frac{\sigma_{\mathrm{O^{2-}}}}{2e}\nabla\tilde{\mu}_{\mathrm{O^{2-}}} = \frac{\sigma_i}{2e}\nabla\tilde{\mu}_i = \frac{\sigma_i}{2e}\frac{\mathrm{d}\tilde{\mu}_i}{\mathrm{d}x} \tag{8}$$

where i is written for $\mathrm{O^{2-}}$, and

$$I_\mathrm{e} = \frac{\sigma_e}{e}\nabla\tilde{\mu}_e = \frac{\sigma_e}{e}\frac{\mathrm{d}\tilde{\mu}_e}{\mathrm{d}x} \tag{9}$$

Let us write

$$\varphi = -\frac{\tilde{\mu}_e}{e} = -\frac{\mu_e}{e} + \Phi \tag{10}$$

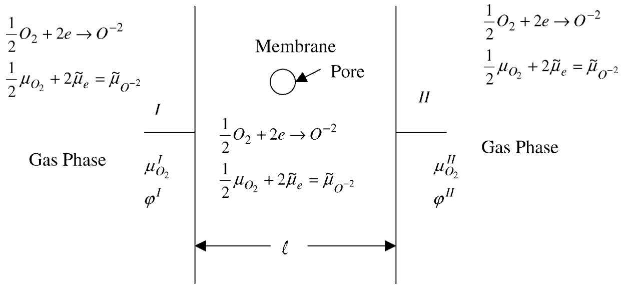

Fig. 1. A schematic illustration of a membrane of thickness ℓ, which can transport $\mathrm{O^{2-}}$, e, and thus O, across which exists a difference in chemical potentials of oxygen, $(\mu^{\mathrm{I}}_{\mathrm{O_2}} - \mu^{\mathrm{II}}_{\mathrm{O_2}})$, and a difference in reduced (negative) electrochemical potentials of electrons $(\varphi^{\mathrm{I}} - \varphi^{\mathrm{II}})$. Local equilibrium in the system implies that the reaction $\frac{1}{2}\mathrm{O_2} + 2\mathrm{e}' \rightarrow \mathrm{O^{2-}}$ is in equilibrium everywhere in the system. This means if a pore of volume V_{pore} exists at some position in the membrane, the oxygen partial pressure in the pore will be that corresponding to the local chemical potential of oxygen $\mu_{\mathrm{O_2}} = \mu^0_{\mathrm{O_2}} + RT\ln p_{\mathrm{O_2}}$, where $\mu^0_{\mathrm{O_2}}$ is the standard state chemical potential and the ideal gas law is assumed. Thus, the number of moles of $\mathrm{O_2}$ in the pore is given by $n_{\mathrm{O_2}} = p_{\mathrm{O_2}}V_{\mathrm{pore}}/RT$. If now $V_{\mathrm{pore}} \rightarrow 0$, then $n_{\mathrm{O_2}} \rightarrow 0$. Yet, the local $p_{\mathrm{O_2}}$ (and $\mu_{\mathrm{O_2}}$) is well defined.

which is the Hebb notation [1]. Here φ is the (negative) reduced electrochemical potential of electrons (V). Using this notation:

$$I_e = -\sigma_e\frac{\mathrm{d}\varphi}{\mathrm{d}x} \tag{11}$$

and

$$I_i = \frac{\sigma_i}{4e}\frac{\mathrm{d}\mu_{\mathrm{O_2}}}{\mathrm{d}x} - \sigma_i\frac{\mathrm{d}\varphi}{\mathrm{d}x} \tag{12}$$

Fig. 1 shows a schematic illustration of a membrane, which can transport $\mathrm{O^{2-}}$, e, and thus O (and thus also $\mathrm{O_2}$), at the two electrodes of which, different chemical potentials of oxygen and different electrochemical potentials of electrons may exist. It is assumed that local equilibrium prevails at all positions in the system, including the gas phase just outside the membrane. Fig. 1 also shows the significance of local equilibrium in a fully dense material, via an example of a pore whose volume approaches zero. If a small pore exists at any position within the membrane, the local $\mu_{\mathrm{O_2}}$ is related to the local oxygen partial pressure, $p_{\mathrm{O_2}}$, by $\mu_{\mathrm{O_2}} = \mu^0_{\mathrm{O_2}} + k_{\mathrm{B}}T\ln p_{\mathrm{O_2}}$, with the number of moles of $\mathrm{O_2}$ in the pore, $n_{\mathrm{O_2}}$, related to $p_{\mathrm{O_2}}$, the pore volume and temperature by the ideal gas law.[3] If the pore volume approaches zero, the number of moles of oxygen in the pore, $n_{\mathrm{O_2}}$, approaches zero. However, the $\mu_{\mathrm{O_2}}$ and the $p_{\mathrm{O_2}}$ continue to exist.Transport of ions and electrons also occurs across the two-electrode/electrolyte interfaces. The interface thicknesses are generally not known—and not well defined either. This is because interfacial regions can often be diffuse—due to compositional gradients and space charge effects. It will, nevertheless, be assumed here that the

---

[2] Even though in most oxygen ion conductors, transport of oxygen ions occurs by a vacancy mechanism, all transport equations are given here in a generic form—that is, without reference to a specific defect type.

[3] Or another appropriate gas law, depending upon the pressure and temperature. In this manuscript, it is assumed that the ideal gas law is applicable over the entire $p_{\mathrm{O_2}}$ range.

'interfacial' regions are of certain thicknesses and describe transport properties through the two interfaces in terms of the transport properties of interfacial regions of certain properties and thicknesses:

σ_i' and δ'—ionic conductivity and thickness of electrode I/membrane interface;
σ_e' and δ'—electronic conductivity and thickness of electrode I/membrane interface;
σ_i'' and δ''—ionic conductivity and thickness of electrode II/membrane interface;
σ_e'' and δ''—electronic conductivity and thickness of electrode II/membrane interface.

Thus, specific ionic conductance of interface I, namely g_i', is

$$g_i' = \frac{\sigma_i'}{\delta'} = \frac{1}{r_i'} \tag{13a}$$

in $\Omega^{-1}\,\mathrm{cm}^{-2}$ or $\mathrm{S\,cm}^{-2}$, and r_i' is the specific ionic resistance of interface I in $\Omega\,\mathrm{cm}^2$, and specific electronic conductance of interface I, namely g_e', is

$$g_e' = \frac{\sigma_e'}{\delta'} = \frac{1}{r_e'} \tag{13b}$$

in $\Omega^{-1}\,\mathrm{cm}^{-2}$ or $\mathrm{S\,cm}^{-2}$, and r_e' is the specific electronic resistance of interface I in $\Omega\,\mathrm{cm}^2$. Similarly, specific ionic and electronic conductances of interface II are given by

$$g_i'' = \frac{\sigma_i''}{\delta''} = \frac{1}{r_i''} \tag{13c}$$

and

$$g_e'' = \frac{\sigma_e''}{\delta''} = \frac{1}{r_e''} \tag{13d}$$

respectively. The preceding assumes, for simplicity, that the transport properties over the interface thickness are constant. This of course need not be the case, and general equations can be written as follows:

$$g_i' = \frac{1}{\int_0^{\delta'} \frac{\mathrm{d}x}{\sigma_i'(x)}} = \frac{1}{r_i'} \tag{14}$$

and similarly for the other specific conductances or resistances. The spatial dependence of transport properties implied in Eq. (14) is through their dependence on μ_{O_2}. In what follows, transport properties of the interfacial regions are assumed to be constant over the thickness and independent of p_{O_2}.[4] It will also be assumed that the interface thicknesses are much smaller than the membrane thickness, that is, δ', $\delta'' \ll \ell$. It is to be noted that while it is generally not possible to separately determine conductivities and thicknesses of interface regions, the specific interface conductances (g_i', g_i'', g_e' and g_e'') or the specific interface resistances (r_i', r_i'', r_e' and r_e'') can in principle be measured experimentally.

Using the above terminology, ionic and electronic current densities across the interfaces are given by[5]

$$\begin{aligned} I_i' &= -\frac{g_i'}{4e}\{\mu_{O_2}^{\mathrm{I}} - \mu_{O_2}'\} + g_i'\{\varphi^{\mathrm{I}} - \varphi'\} \\ &= -\frac{1}{4e}\frac{\mu_{O_2}^{\mathrm{I}} - \mu_{O_2}'}{r_i'} + \frac{\varphi^{\mathrm{I}} - \varphi'}{r_i'} \end{aligned} \tag{15}$$

and

$$\begin{aligned} I_i'' &= -\frac{g_i''}{4e}\{\mu_{O_2}'' - \mu_{O_2}^{\mathrm{II}}\} + g_i''\{\varphi'' - \varphi^{\mathrm{II}}\} \\ &= -\frac{1}{4e}\frac{\mu_{O_2}'' - \mu_{O_2}^{\mathrm{II}}}{r_i''} + \frac{\varphi'' - \varphi^{\mathrm{II}}}{r_i''} \end{aligned} \tag{16}$$

as the ionic current densities across the two interfaces, and

$$I_e' = g_e'\{\varphi^{\mathrm{I}} - \varphi'\} = \frac{\varphi^{\mathrm{I}} - \varphi'}{r_e'} \tag{17}$$

and

$$I_e'' = g_e''\{\varphi'' - \varphi^{\mathrm{II}}\} = \frac{\varphi'' - \varphi^{\mathrm{II}}}{r_e''} \tag{18}$$

as the electronic current densities across the two interfaces. In the preceding equations, μ_{O_2}' and φ' are, respectively, chemical potential of oxygen and reduced (negative) electrochemical potential of electrons in the membrane, just inside electrode I/membrane interface; μ_{O_2}'' and φ'' the corresponding quantities in the membrane just inside interface II. In steady state:[6]

$$I_i' = I_i'' = I_i \tag{19}$$

and

$$I_e' = I_e'' = I_e \tag{20}$$

where I_i and I_e are, respectively, ionic and electronic current densities through the bulk of the membrane. In general, transport properties of most electrolyte or MIEC materials depend upon the local oxygen partial pressure, p_{O_2}, or chemical potential, μ_{O_2}. Thus, the relevant equations are (11) and (12), where the transport properties are μ_{O_2}-dependent, and thus position dependent. Integration of Eq. (12) gives [3]

$$\int_0^{\ell} I_i\,\mathrm{d}x = I_i\ell = \frac{1}{4e}\int_{'}^{''} \sigma_i\,\mathrm{d}\mu_{O_2} - \int_{'}^{''} \sigma_i\,\mathrm{d}\varphi \tag{21}$$

---

[4] In general, the transport parameters of interfacial regions are functions of p_{O_2}. For example, a simple analysis based on adsorption shows that usually $r_i' \propto p_{O_2}^{-1/n'}$, where n' is a positive number typically an integer. This aspect is ignored here since the objective is to provide analytical equations to describe general features. For any given material, if the dependence is known, it is a trivial matter to incorporate it and solve equations numerically.

[5] If the transport properties vary across the interfaces, then the relevant transport equations are of the form $I_i = \frac{1}{\delta'}\left\{\frac{1}{4e}\int_0^{\delta'} \sigma_i'\,\mathrm{d}\mu_{O_2} - \int_0^{\delta'} \sigma_i'\,\mathrm{d}\varphi\right\}$.

[6] In three dimensions, the criterion for steady state is given by $\nabla\cdot I_i = 0$ and $\nabla\cdot I_e = 0$, where I_i and I_{e} are vectors.

and integration of Eq. (11) gives

$$\int_0^{\ell} I_e\,\mathrm{d}x = I_e\ell = -\int_{'}^{''} \sigma_e\,\mathrm{d}\varphi \tag{22}$$

where the integration is between the two (just inside) electrode/membrane interfaces. In what follows, ionic and electronic conductivities of the membrane will be assumed to be constant, independent of position. This allows explicit determination of fluxes in terms of transport properties, and more importantly the estimation of μ'_{O_2} and μ''_{O_2}, and φ' and φ'' in terms of measurable parameters. Also, this makes it possible to analyze a number of cases of interest analytically. The preceding equations then become

$$I_i = -\frac{\sigma_i}{4e\ell}\{\mu'_{O_2} - \mu''_{O_2}\} + \frac{\sigma_i}{\ell}\{\varphi' - \varphi''\} \tag{23}$$

and

$$I_e = \frac{\sigma_e}{\ell}\{\varphi' - \varphi''\} \tag{24}$$

The parameters, which are known (or which can in principle be determined experimentally) are the following: $\sigma_i, \sigma_e, g'_i = (1/r'_i)$, $g'_e = (1/r'_e)$, $g''_i = (1/r''_i)$, $g''_e = (1/r''_e)$, ℓ, $\mu^{\mathrm{I}}_{O_2}$, $\mu^{\mathrm{II}}_{O_2}$, φ^{I}, φ^{II}, I_i, and I_e. The unknowns are: μ'_{O_2}, μ''_{O_2}, φ', and φ''.

From the transport of electrons across interface I:

$$\varphi' = \varphi^{\mathrm{I}} - \frac{I_e}{g'_e} = \varphi^{\mathrm{I}} - r'_e I_e \tag{25}$$

From the transport of electrons across interface II:

$$\varphi'' = \varphi^{\mathrm{II}} + \frac{I_e}{g''_e} = \varphi^{\mathrm{II}} + r''_e I_e \tag{26}$$

From the transport of oxygen ions across interface I:

$$\mu'_{O_2} = \mu^{\mathrm{I}}_{O_2} + 4e\left(\frac{g'_e I_i - g'_i I_e}{g'_e g'_i}\right) = \mu^{\mathrm{I}}_{O_2} + 4e(r'_i I_i - r'_e I_e) \tag{27}$$

From the transport of oxygen ions across interface II:

$$\mu''_{O_2} = \mu^{\mathrm{II}}_{O_2} - 4e\left(\frac{g''_e I_i - g''_i I_e}{g''_e g''_i}\right) = \mu^{\mathrm{II}}_{O_2} - 4e(r''_i I_i - r''_e I_e) \tag{28}$$

Eqs. (25)–(28) describe the unknown potentials, namely, μ'_{O_2}, μ''_{O_2}, φ', and φ'', in terms of transport properties of interfaces and the net ionic and electronic current densities, namely I_i and I_e. An important point to note from Eqs. (27) and (28) is that even for a predominantly oxygen ion conducting membrane, one cannot a priori assume either r'_e or r''_e to be infinite, which makes I_e zero and the μ_{O_2} in the membrane indeterminate (product of ∞ and 0) and violates the criterion of local equilibrium.[7]. Thus, r'_e and r''_e can be very large, but not infinite. Eqs. (27) and (28) also show that usually $\mu'_{O_2} \neq \mu^{\mathrm{I}}_{O_2}$ and $\mu''_{O_2} \neq \mu^{\mathrm{II}}_{O_2}$, as this would require terms in parentheses to be identically zero—which would a very rare and a special case, and not a general case. As evident from Eqs. (27) and (28), the chemical potentials of O_2 just inside the interfaces (in the membrane) depend upon the values of r'_i, r'_e, r''_i, r''_e, I_i, and I_e.

In terms of the reduced electrochemical potentials of electrons at the two electrodes, the net electronic current density is given by

$$I_e = \frac{\varphi^{\mathrm{I}} - \varphi^{\mathrm{II}}}{\ell\rho_e + r'_e + r''_e} \tag{29}$$

and in terms of the chemical potentials of oxygen and the reduced electrochemical potentials of electrons at the two electrodes, the net ionic current density is given by

$$I_i = -\frac{1}{4e}\frac{\mu^{\mathrm{I}}_{O_2} - \mu^{\mathrm{II}}_{O_2}}{\ell\rho_i + r'_i + r''_i} + \frac{\varphi^{\mathrm{I}} - \varphi^{\mathrm{II}}}{\ell\rho_i + r'_i + r''_i} \tag{30}$$

Eqs. (29) and (30) for the electronic and ionic current densities, respectively, are given in terms of parameters which, in principle, are measurable. In what follows, the above equations are used to examine the various cases outlined earlier.

2.1. The generalized form of chemical potential of oxygen as a function of position in a membrane without the incorporation of interfaces

In what follows, let us first examine the chemical potential of oxygen as a function of position in a membrane, without the incorporation of the effect of interfaces. This approach leads to simple analytical expressions. Let us consider a membrane of thickness ℓ. The chemical potentials of oxygen at the two sides are $\mu^{\mathrm{I}}_{O_2}$ at $x = 0$ and $\mu^{\mathrm{II}}_{O_2}$ at $x = \ell$. The net electronic and ionic current densities through the membrane are given by Eqs. (11) and (12). In general, the conductivities are functions of position (which actually are functions of position-dependent chemical potential). Summing the two current densities, rearranging the terms and integrating gives:

$$\mu_{O_2}(x) = \mu^{\mathrm{I}}_{O_2} + 4e(I_i + I_e)\int_0^x \frac{\mathrm{d}x}{\sigma_i(x)} + 4e\int_{\varphi^{\mathrm{I}}}^{\varphi(x)}\left(\frac{\sigma_i(x) + \sigma_e(x)}{\sigma_i(x)}\right)\mathrm{d}\varphi(x) \tag{31}$$

The preceding shows that the chemical potential of oxygen within the membrane can be completely described by Eq. (31) provided the net current flowing through the membrane, namely $I_i + I_e$ is known, and transport properties are known as functions of position. Eq. (31) is applicable for both steady and transient states. In the transient state, all dependent variables are also time dependent, that is $\sigma_i(x, t)$, $\sigma_e(x, t)$, $\mu_{O_2}(x, t)$, $\varphi(x, t)$, $I_i(x, t)$ and $I_e(x, t)$. Yet, Kirchoff's laws are assumed applicable, which gives $I_i(x, t) + I_e(x, t) = I_{\mathrm{total}}(t)$. That is, the net current density, $I_{\mathrm{total}}(t)$, is a function of time alone. In what follows, we will only consider the steady state. In the preceding it is assumed that the chemical potentials of

---

[7] Obviously, r_e cannot be infinite either, as discussed in [14].

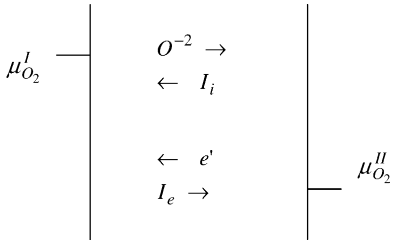

Fig. 2. A schematic illustration of an MIEC membrane under an applied difference of chemical potential of oxygen, with no applied voltage difference. Electronic and ionic currents are of equal magnitude but are in the opposite directions.

oxygen just inside the two interfaces are the same as in the local atmospheres. The exact details of the variation of $\mu_{O_2}(x)$ with position depends upon the magnitudes and spatial dependencies of the transport properties of the membrane, the end values of the chemical potentials, namely $\mu^{I}_{O_2}$ and $\mu^{II}_{O_2}$, and the end values of the reduced electrochemical potentials of electrons, namely φ^{I} and φ^{II}. If analytical relations are known between transport properties and position, Eq. (31) can be readily used to determine $\mu_{O_2}(x)$ as a function of position.[8] This is a special case wherein an assumption is made that $\mu'_{O_2} = \mu^{I}_{O_2}$ and $\mu''_{O_2} = \mu^{II}_{O_2}$. However, there is no justification for this assumption in a general case, as already stated previously. That is, in a general case, $\mu'_{O_2} \neq \mu^{I}_{O_2}$ and $\mu''_{O_2} \neq \mu^{II}_{O_2}$. Under such conditions, it is not possible to obtain a simple analytical equation (such as the one given in Eq. (31)) with transport properties dependent upon position. The objective of this work is to explore the role of interfaces and obtain explicit expressions for μ'_{O_2} and μ''_{O_2}. Hence, a simplifying assumption is made here that transport parameters are spatially invariant in the membrane. In order to account for the interfaces, as stated earlier, properties of the interfaces are separately included.

2.2. An MIEC oxygen separation membrane

In what follows, the transport properties are assumed to be independent of position within the membrane. In this case of an MIEC oxygen separation membrane, no voltage is applied across the membrane. However, a chemical potential difference of oxygen is imposed across the membrane. As there is a chemical potential difference across the membrane, a corresponding difference in electrochemical potential of electrons is created. Fig. 2 shows a schematic illustration of a MIEC membrane across which there is a gradient in the chemical potential of oxygen. Let $\mu^{I}_{O_2} > \mu^{II}_{O_2}$. Since neither an external voltage is applied, nor the membrane is externally shorted, the net current is zero. That is, $I_i + I_e = 0$ or $I_e = -I_i$.

For $\mu^{I}_{O_2} > \mu^{II}_{O_2}$, oxygen ion transport occurs from I to II (from left to right in Fig. 2). That is $I_i < 0$, and therefore, $I_e > 0$.

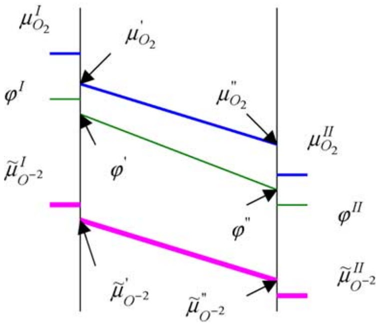

Fig. 3. Schematic variations of μ_{O_2}, $\tilde{\mu}_{O^{2-}}$ and φ for the case depicted in Fig. 2. Abrupt changes in μ_{O_2}, φ, and $\tilde{\mu}_{O^{2-}}$ are shown across interfaces since $\delta', \delta'' \ll \ell$.

The chemical potential of oxygen just below the interface at I given by Eq. (27) becomes

$$\mu'_{O_2} = \mu^{I}_{O_2} + 4e\left(\frac{g'_e + g'_i}{g'_e g'_i}\right) I_i = \mu^{I}_{O_2} - 4e\left(\frac{g'_e + g'_i}{g'_e g'_i}\right) |I_i|$$
$$= \mu^{I}_{O_2} - 4e(r'_i + r'_e)|I_i| \quad (32)$$

That is, $\mu'_{O_2} < \mu^{I}_{O_2}$.

Similarly, the reduced (negative) electrochemical potential of electrons just inside interface I is given by

$$\varphi' = \varphi^{I} - \frac{I_e}{g'_e} = \varphi^{I} + \frac{I_i}{g'_e} = \varphi^{I} - \frac{|I_i|}{g'_e} = \varphi^{I} - r'_e|I_i| \quad (33)$$

That is, $\varphi' < \varphi^{I}$.

Similar equations can be written for μ_{O_2} and φ just inside interface at II, namely μ''_{O_2} and φ''. For example note that

$$\mu''_{O_2} = \mu^{II}_{O_2} - 4e\left(\frac{g''_e + g''_i}{g''_e g''_i}\right) I_i = \mu^{II}_{O_2} + 4e\left(\frac{g''_e + g''_i}{g''_e g''_i}\right) |I_i|$$
$$= \mu^{II}_{O_2} + 4e(r''_i + r''_e)|I_i| \quad (34)$$

That is, $\mu''_{O_2} > \mu^{II}_{O_2}$.

The reduced (negative) electrochemical potential of electrons just inside interface II is similarly given by

$$\varphi'' = \varphi^{II} + \frac{|I_i|}{g''_e} = \varphi^{II} + r''_e|I_i| \quad (35)$$

That is, $\varphi'' > \varphi^{II}$.

Note also that $I_e = \frac{\sigma_e}{\ell}\{\varphi' - \varphi''\} > 0$ or $\varphi' > \varphi''$. Rearrangement of Eq. (23) gives

$$\{\mu'_{O_2} - \mu''_{O_2}\} = -\frac{4e\ell}{\sigma_i} I_i + 4e\{\varphi' - \varphi''\} \quad (36)$$

Since $I_i < 0$ and $\varphi' > \varphi''$, it is clear that $\mu'_{O_2} > \mu''_{O_2}$.

Thus, for an MIEC membrane, for the experimentally selected conditions corresponding to $\mu^{I}_{O_2} > \mu^{II}_{O_2}$, it is seen that $\mu^{I}_{O_2} > \mu'_{O_2} > \mu''_{O_2} > \mu^{II}_{O_2}$ and $\varphi^{I} > \varphi' > \varphi'' > \varphi^{II}$, regardless of the absolute values of transport parameters of the bulk membrane and interfaces. Fig. 3 shows the schematic variations of μ_{O_2} and φ for this case, where it is tacitly assumed that

---

[8] An important point to note is that the transport properties are functions of μ_{O_2}, and their dependence on position is through the dependence of the chemical potential on position.

$r'_e \sim r''_e \sim r_e$. Finally, as the transport of oxygen ions occurs from left to right, note that $\tilde{\mu}^{\mathrm{I}}_{\mathrm{O}^{2-}} > \tilde{\mu}'_{\mathrm{O}^{2-}} > \tilde{\mu}''_{\mathrm{O}^{2-}} > \tilde{\mu}^{\mathrm{II}}_{\mathrm{O}^{2-}}$. The spatial variation of $\tilde{\mu}_{\mathrm{O}^{2-}}$ is also shown in Fig. 3.

Since $\mu^{\mathrm{I}}_{\mathrm{O}_2} > \mu'_{\mathrm{O}_2} > \mu''_{\mathrm{O}_2} > \mu^{\mathrm{II}}_{\mathrm{O}_2}$, as long as $\mu^{\mathrm{II}}_{\mathrm{O}_2} > \mu^{\mathrm{decomp}}_{\mathrm{O}_2}$, where $\mu^{\mathrm{decomp}}_{\mathrm{O}_2}$ is the chemical potential of oxygen below which membrane decomposition can occur, the stability of the membrane is assured. An important point to note, however, is that the membrane may continue to be stable even if $\mu^{\mathrm{II}}_{\mathrm{O}_2} < \mu^{\mathrm{decomp}}_{\mathrm{O}_2}$, provided $\mu''_{\mathrm{O}_2} > \mu^{\mathrm{decomp}}_{\mathrm{O}_2}$. That is, interface properties are expected to have a profound effect in dictating membrane stability. The interface properties may also depend upon the atmosphere. For example, for a given $\mu^{\mathrm{II}}_{\mathrm{O}_2}$ (and thus for a given $p^{\mathrm{II}}_{\mathrm{O}_2}$), the μ''_{O_2} may be different in $\mathrm{H}_2/\mathrm{H}_2\mathrm{O}$ and $\mathrm{CO}/\mathrm{CO}_2$ atmospheres. Thus, it is possible that a given MIEC may be stable (permeate side) in one gas mixture but not in the other, even though the p_{O_2} in the two atmospheres is identical.

Substitution for μ'_{O_2}, μ''_{O_2}, φ', and φ'' in terms of respective current densities and transport properties of the two interfaces into Eq. (23) gives

$$\begin{aligned}\varphi^{\mathrm{I}} - \varphi^{\mathrm{II}} &= \frac{1}{4e}\{\mu^{\mathrm{I}}_{\mathrm{O}_2} - \mu^{\mathrm{II}}_{\mathrm{O}_2}\} + I_i\left[\frac{\ell}{\sigma_i} + \frac{g'_i + g''_i}{g'_i g''_i}\right]\\ &= \frac{1}{4e}\{\mu^{\mathrm{I}}_{\mathrm{O}_2} - \mu^{\mathrm{II}}_{\mathrm{O}_2}\} + I_i[\ell\rho_i + r'_i + r''_i] \qquad (37)\end{aligned}$$

Also, from the equations for I_i and I_e, and noting that $I_i + I_e = 0$, using Eqs. (29) and (30) it is easy to see that

$$\varphi^{\mathrm{I}} - \varphi^{\mathrm{II}} = \frac{\ell\rho_e + r'_e + r''_e}{[\ell\rho_e + r'_e + r''_e] + [\ell\rho_i + r'_i + r''_i]}\,\frac{\mu^{\mathrm{I}}_{\mathrm{O}_2} - \mu^{\mathrm{II}}_{\mathrm{O}_2}}{4e} \qquad (38)$$

Thus, in general

$$\varphi^{\mathrm{I}} - \varphi^{\mathrm{II}} < \frac{\mu^{\mathrm{I}}_{\mathrm{O}_2} - \mu^{\mathrm{II}}_{\mathrm{O}_2}}{4e}$$

If $[\ell\rho_e + r'_e + r''_e] \gg [\ell\rho_i + r'_i + r''_i]$, then

$$\varphi^{\mathrm{I}} - \varphi^{\mathrm{II}} \approx \frac{\mu^{\mathrm{I}}_{\mathrm{O}_2} - \mu^{\mathrm{II}}_{\mathrm{O}_2}}{4e} = E_0 \qquad (39)$$

where E_0 is the Nernst potential.

Equivalent circuit. It is customary to represent an equivalent circuit for a bulk MIEC in terms of a Nernst voltage, generated by the imposed chemical potential difference, and ionic and electronic resistances [17]. However, for interfaces, the common practice has often been to use a capacitor in combination with a resistor [18]. The charged capacitor then models the voltage difference created by the chemical potential difference, and in fact a so-called chemical capacitance can be defined, which is meant to embody the relevant thermodynamics. The concept of chemical capacitance has also been used by some to model a bulk MIEC membrane. In such a case, a (chemical) capacitor is introduced between two sets of parallel ionic and electronic resistor segments. Fig. 4(a) shows a schematic illustration. In steady state, no current flows through the capacitor, while the ionic current is uniform in the ionic segments, and the electronic current is uniform in the electronic segments. In a transient state, the ionic currents in the two ionic segments are different and so are the electronic currents in the two electronic segments. However, Kirchoff's laws continue to hold, that is, $\nabla\cdot(I_i + I_e) = 0$, which for a one-dimensional case reduces to $I_i + I_e = \text{constant}$. Also, in the transient state, there is a net current flowing through the capacitor.

In this manuscript, however, internal EMF sources will be used to model bulk as well as interfacial regions. Since the chemical potential varies spatially (including across interfaces), representation of interfacial regions in terms of Nernst voltages is a natural extension of the usual practice of representing bulk regions in terms of Nernst voltages. That is, there is no particular requirement, which states that one must use capacitors to describe the interfacial regions, if an EMF source is used to describe the bulk regions.

In what follows, rationale for the choice of internal EMFs to describe both bulk and interfacial regions of an MIEC under an applied chemical potential is first described. Consider the application of a net chemical potential difference across a membrane such that the position-dependent chemical potential of oxygen given by $\mu_{\mathrm{O}_2}(x)$, is a continuous function of position, x. Thus, the chemical potential at $x + \mathrm{d}x$ is given by $\mu_{\mathrm{O}_2}(x + \mathrm{d}x) = \mu_{\mathrm{O}_2}(x) + \mathrm{d}\mu_{\mathrm{O}_2}(x)$. The corresponding Nernst voltage across the slice $\mathrm{d}x$ is given by $\mathrm{d}E(x) = \frac{\mathrm{d}\mu_{\mathrm{O}_2}(x)}{4e}$. The local ionic and electronic area specific resistances for the slice are $\mathrm{d}r_i(x) = \rho_i(x)\,\mathrm{d}x$ and $\mathrm{d}r_e(x) = \rho_e(x)\,\mathrm{d}x$. The corresponding equivalent circuit for the slice is shown in Fig. 4(b). Note that the electronic and the ionic segments are joined at the ends (nodes). The significance is that the existence of local equilibrium corresponding to the reaction $\frac{1}{2}\mathrm{O}_2 + 2e' \rightarrow \mathrm{O}^{2-}$ requires the transport of ionic and electronic currents to any position, which corresponds to joining of the electronic and the ionic segments at the nodes. The equivalent circuit for the entire membrane (by discretizing it in slices of thickness $\mathrm{d}x$) is shown in Fig. 4(c). Now, no charge accumulation can occur at any node. In such a case, Kirchoff's equations must be applicable, which means

$$\begin{aligned}I_i(x, t) + I_e(x, t) &= I_i(x + \mathrm{d}x, t) + I_e(x + \mathrm{d}x, t) = \cdots\\ &= I_i(x + n\,\mathrm{d}x, t) + I_e(x + n\,\mathrm{d}x, t) \qquad (40)\end{aligned}$$

where t denotes time and n the number of differential segments. Eq. (40) is applicable both under transient and steady state conditions. For this reason, the time dependence is explicitly included. Under transient conditions, ionic current entering a node may be different from that leaving the node, and similarly for the electronic current, yet consistent with the above identity.[9] In such a case, all dependent variables,

---

[9] The same situation exists if one uses a capacitor (Fig. 4(a)) to describe transport. In this case, the magnitude of the difference in ionic currents entering and exiting the capacitor is the same as the magnitude of the electronic currents entering and exiting the capacitor.

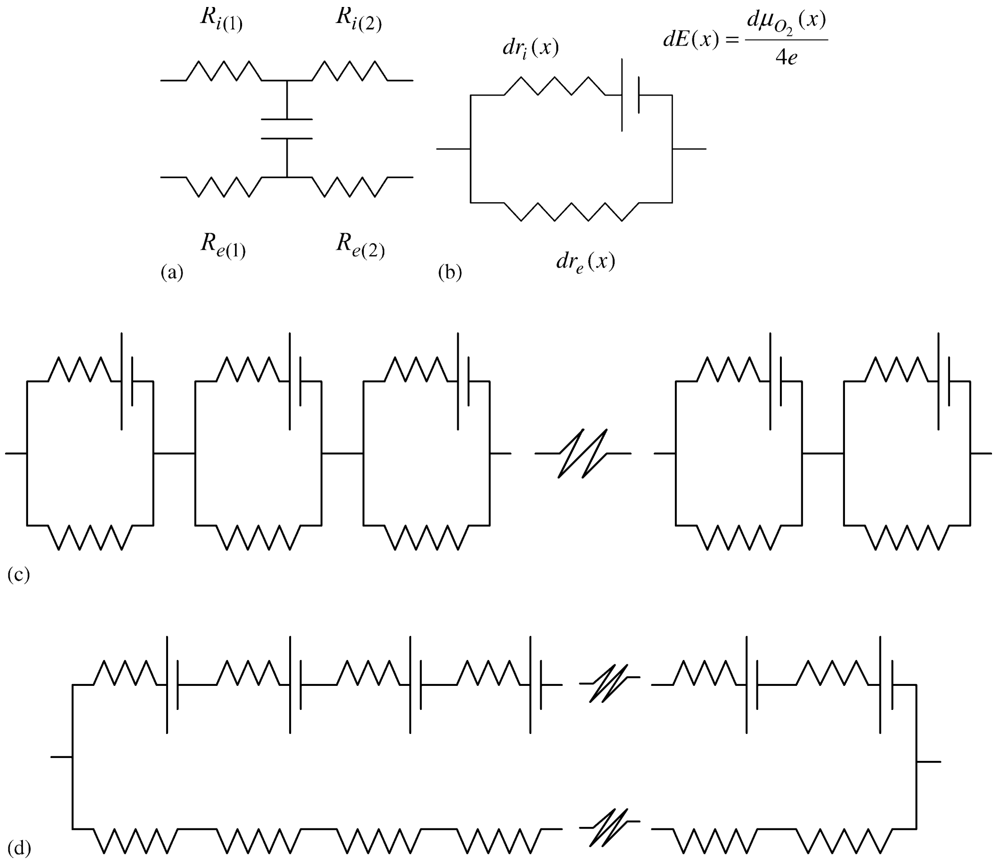

Fig. 4. (a) An equivalent circuit describing spatial variation of transport parameters through an MIEC using a chemical capacitance. (b) An equivalent circuit describing spatial variation of transport parameters through a slice dx of an MIEC using an internal EMF source, which is related to local variation in chemical potential of oxygen, d$\mu_{O_2}(x)$. (c) An equivalent circuit describing spatial variation of transport parameters through an MIEC. The equivalent circuit is applicable for both transient and steady states. For the transient state, the ionic and electronic currents are functions of position and time. However, Kirchoff's laws continue to be valid. In steady state, the ionic and electronic currents are independent of time and position (for a one-dimensional problem). (d) An equivalent circuit describing spatial variation of transport parameters through an MIEC. The equivalent circuit is applicable only for steady state.

including $\mu_{O_2}(x)$, are time dependent. Thus, in a transient state, $I_i(x, t) + I_e(x, t) = I_i(x + dx, t) + I_e(x + dx, t)$, however $I_i(x, t) \neq I_i(x + dx, t)$ and $I_e(x, t) \neq I_e(x + dx, t)$. The corresponding equivalent circuit is shown in Fig. 4(c). In such a case, the electronic and the ionic segments must be joined at the nodes. Also, in such a case, the ionic and the electronic current densities are in general time dependent.

In steady state, in addition, the divergence of ionic and electronic currents must be individually zero, that is, $\nabla \cdot I_i = 0$ and $\nabla \cdot I_e = 0$, and obviously current densities are not time dependent. For a one-dimensional case, this implies that $I_i(x) = I_i(x + dx) = I_i(x + 2\,dx) = \cdots = I_i(x + n\,dx) = \cdots$ and $I_e(x) = I_e(x + dx) = I_e(x + 2\,dx) = \cdots = I_e(x + n\,dx) = \cdots$. Under such conditions, the equivalent circuit may also be described by that in Fig. 4(d). Nevertheless, it is to be recognized that the general equivalent circuit applicable for both the transient and steady states is that given in Fig. 4(c). If this equivalent circuit is used for steady state, then it should be further specified that both the ionic and electronic currents satisfy the conditions $\nabla \cdot I_i = 0$ and $\nabla \cdot I_e = 0$. For a one-dimensional case, this is equivalent to ionic and electronic currents being spatially invariant. If one uses a capacitor instead, then the equivalent circuit given in Fig. 4(a) is applicable in both transient and steady states. For the steady state, no current flows through the capacitor.

The choice of μ_{O_2}-independent and position-independent properties for any given region allows for a simple equivalent circuit representation of the MIEC membrane just described. The corresponding equivalent circuit is given in Fig. 5. Note again the representation in terms of internal EMF sources rather than charged capacitors—which is consistent with the spatial variation in μ_{O_2}. The internal EMFs are given by

$$E' = \frac{\mu^{\mathrm{I}}_{O_2} - \mu'_{O_2}}{4e} = \frac{RT}{4F} \ln\left(\frac{p^{\mathrm{I}}_{O_2}}{p'_{O_2}}\right) = \frac{k_B T}{4e} \ln\left(\frac{p^{\mathrm{I}}_{O_2}}{p'_{O_2}}\right) \tag{41}$$

$$E_i = \frac{\mu'_{O_2} - \mu''_{O_2}}{4e} = \frac{RT}{4F} \ln\left(\frac{p'_{O_2}}{p''_{O_2}}\right) = \frac{k_B T}{4e} \ln\left(\frac{p'_{O_2}}{p''_{O_2}}\right) \tag{42}$$

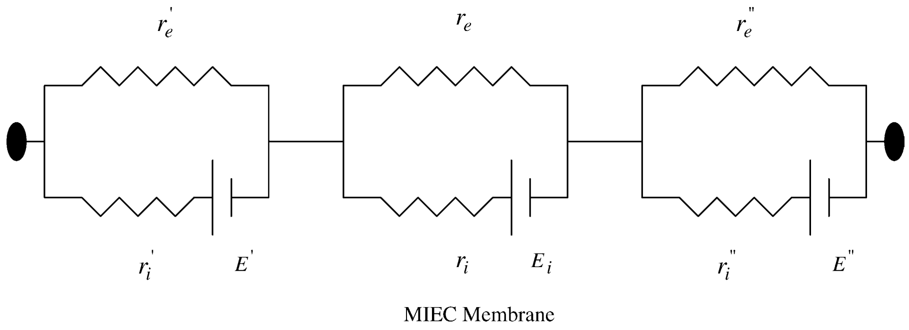

Fig. 5. An equivalent circuit for the MIEC membrane. The circuit elements between the two filled elliptical symbols are not physically separable; they collectively represent the equivalent circuit. All E's (E', E_i, E'') are of the same sign.

$$E'' = \frac{\mu''_{O_2} - \mu^{II}_{O_2}}{4e} = \frac{RT}{4F} \ln\left(\frac{p''_{O_2}}{p^{II}_{O_2}}\right) = \frac{k_B T}{4e} \ln\left(\frac{p''_{O_2}}{p^{II}_{O_2}}\right) \tag{43}$$

and their sum is given by

$$E = E' + E_i + E'' = \frac{\mu^{I}_{O_2} - \mu^{II}_{O_2}}{4e} = \frac{RT}{4F} \ln\left(\frac{p^{I}_{O_2}}{p^{II}_{O_2}}\right)$$
$$= \frac{k_B T}{4e} \ln\left(\frac{p^{I}_{O_2}}{p^{II}_{O_2}}\right) \tag{44}$$

The equivalent circuit can be readily used to solve for the currents flowing through the membrane, subject to the condition that in steady state $I_i' = I_i'' = I_i$ and $I_e' = I_e'' = I_e$.[10] And, also in this case of an MIEC membrane, $I_i + I_e = 0$. Let us write

$$R_i = r_i' + \ell\rho_i + r_i'' = r_i' + r_i + r_i'' \tag{45}$$

and

$$R_e = r_e' + \ell\rho_e + r_e'' = r_e' + r_e + r_e'' \tag{46}$$

where $r_i = \ell\rho_i = \ell/\sigma_i$ and $r_e = \ell\rho_e = \ell/\sigma_e$. It is easy to see that

$$I_i = -I_e = -\frac{E}{R_i + R_e} \tag{47}$$

The measured voltage across the MIEC membrane is

$$E_M = \varphi^{I} - \varphi^{II} = I_e R_e = \frac{E R_e}{R_i + R_e} \tag{48}$$

Thus, the effective ionic transference number of the membrane, including interfacial effects, is given by

$$t_i = \frac{E_M}{E} = \frac{R_e}{R_i + R_e} = \frac{r_e' + r_e + r_e''}{r_i' + r_i + r_i'' + r_e' + r_e + r_e''} \tag{49}$$

Often, the measurement of open circuit voltage across an MIEC is used to estimate the transference number of the membrane material, the latter given by

$$t_i^m = \frac{r_e}{r_i + r_e} \tag{50}$$

It is clear that only in a special case when $r_e \gg r_e' + r_e''$ and $r_i + r_e \gg r_i' + r_i'' + r_e' + r_e''$, will the measurement of open circuit voltage (OCV) give the material ionic transference number, t_i^m. That is, in general, the measurement of OCV cannot be used to determine the ionic or the electronic transference numbers of the material. This conclusion is similar to the one arrived at by Liu and Hu, who evaluated the effect of interfacial polarization on the apparent transference numbers of MIEC materials [19]. The effect of interfacial resistance on the apparent transference numbers in MIEC materials has also been examined by Kharton and Marques [20].

2.3. A solid oxide fuel cell

In a solid oxide fuel cell, one electrode is exposed to fuel (anode) and the other electrode is exposed to oxidant (cathode). The membrane is of a predominantly ion conducting material, usually an oxygen ion conductor. During operation, an external load is connected such that a net, finite, nonzero current flows through the membrane (and of course through the external circuit). Thus, the net current is not zero, that is $I_i + I_e \neq 0$. In what follows, electrode I is the cathode, and electrode II is the anode. During cell operation, oxygen ions transport from I to II through the membrane. It is also clear that $\mu^{I}_{O_2} > \mu^{II}_{O_2}$. Note also that $\varphi^{I} > \varphi^{II}$. Since the membrane is predominantly an ionic conductor, that is, $r_e + r_e' + r_e'' \gg r_i + r_i' + r_i''$, it is clear that $|I_i| \gg |I_e|$. It is to be emphasized that, for the reasons already discussed, there must be a finite, nonzero I_e, to ensure that local equilibrium is established. Fig. 6 shows a schematic illustration.

In this case also, Eq. (37), which gives the difference between the reduced electrochemical potentials of electrons at the two electrodes in terms of the difference in chemical potentials of oxygen at the two electrodes, the ionic current density, and the net ionic resistance, is applicable. Note that there are no terms containing I_e in Eq. (37). However, it is important to note that I_e is not zero, although usually $|I_e| \ll |I_i|$ in the present case of fuel cells. Thus, the net measured current

---

[10] The equivalent circuit, as stated above, can also be used for analysis of the transient problem wherein $\nabla \cdot I_i \neq 0$ and $\nabla \cdot I_e \neq 0$, although $\nabla \cdot (I_i + I_e) = 0$, as discussed for one-dimensional cases in [15,16].

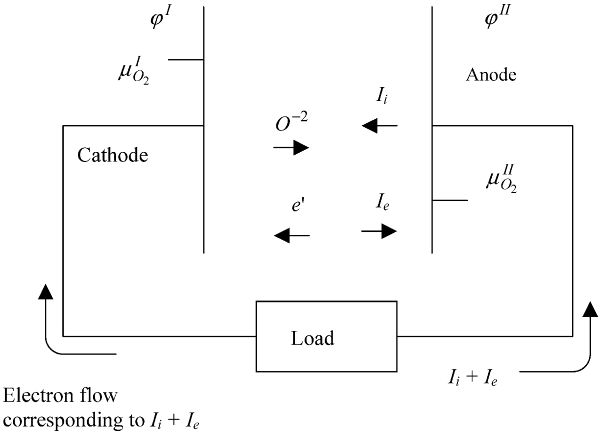

Fig. 6. A schematic illustration of a fuel cell showing the directions of oxygen ion and electron transport through the membrane. Electronic and ionic currents are in the opposite directions.

is essentially the ionic current. Also, note that $I_i < 0$. Thus, writing I as the magnitude of the measured current, note that $I_i \approx -I$. Then Eq. (37) becomes

$$\varphi^{\mathrm{I}} - \varphi^{\mathrm{II}} \approx \frac{1}{4e}\{\mu^{\mathrm{I}}_{\mathrm{O}_2} - \mu^{\mathrm{II}}_{\mathrm{O}_2}\} - I\left\{\frac{\ell}{\sigma_i} + \frac{g'_i + g''_i}{g'_i g''_i}\right\}$$
$$= \frac{1}{4e}\{\mu^{\mathrm{I}}_{\mathrm{O}_2} - \mu^{\mathrm{II}}_{\mathrm{O}_2}\} - I\{\ell\rho_i + r'_i + r''_i\} \qquad (51)$$

When the fuel cell is at open circuit, the net current flowing through the external circuit, $I = 0$, which corresponds to the Nernst voltage, E_0, given by Eq. (39). This is equivalent to the establishment of (near) global equilibrium for the electrochemical potential of oxygen ions, $\tilde{\mu}_{\mathrm{O}^{2-}}$, that is $\nabla\tilde{\mu}_{\mathrm{O}^{2-}} \approx 0$. Note of course that $\nabla\tilde{\mu}_{\mathrm{O}^{2-}}$ is not identically zero, and therefore, the ionic current is not identically zero either. This situation is now equivalent to an MIEC, albeit with a very low electronic transference number, and thus $I_e = -I_i$, but with a very small magnitude. Now, consider the following seven cases corresponding to the open circuit condition: Case I: $r_e \gg r'_e, r''_e$, Case II: $r'_e \gg r_e, r''_e$, Case III: $r''_e \gg r_e, r'_e$, Case IV: $r'_e, r''_e \gg r_e$, Case V: $r_e, r''_e \gg r'_e$, Case VI: $r_e, r'_e \gg r''_e$, and Case VII: $r'_e \sim r_e \sim r''_e$. The variations of $\tilde{\mu}_{\mathrm{O}^{2-}}$, φ and μ_{O_2} for the seven cases are shown in Fig. 7. All seven cases correspond to the open circuit condition, with $[\ell\rho_e + r'_e + r''_e] \gg [\ell\rho_i + r'_i + r''_i]$, and therefore $\nabla\tilde{\mu}_{\mathrm{O}^{2-}} \approx 0$. The corresponding difference between φ^{I} and φ^{II} for all seven cases is nearly equal to the Nernst voltage, given by Eq. (39). Note, however, that the details of the variations of μ_{O_2} and φ through the interfaces and membrane depend upon the relative values of electronic resistances of the interfaces and the membrane. From the standpoint of membrane stability in a low p_{O_2} atmosphere (stability against reduction), the most preferred case is that depicted in case III, which shows that if $r''_e \gg r_e, r'_e$, the μ_{O_2} just inside the anode/electrolyte interface (that is μ''_{O_2}) will be close to the cathode side chemical potential of oxygen, namely $\mu^{\mathrm{I}}_{\mathrm{O}_2}$. This means, under such conditions, in principle, it may be possible to use an otherwise unstable electrolyte in fuel atmosphere, such as rare earth-oxide doped bismuth oxide for example, for a fuel cell application.[11] All cases considered correspond to the open circuit condition, such that $I_i + I_e = 0$. Thus, this is exactly the same as an MIEC membrane, and thus μ_{O_2} varies monotonically from the value at one electrode to the other.

When the fuel cell is shorted:

$$\varphi^{\mathrm{I}} - \varphi^{\mathrm{II}} = 0 \quad \text{or} \quad \varphi^{\mathrm{I}} = \varphi^{\mathrm{II}}$$

Thus, in this case, the electronic current density is zero, i.e., $I_e = 0$. The corresponding short circuit current density, which is exclusively due to ionic transport through the membrane, is given by

$$I_s = \frac{\mu^{\mathrm{II}}_{\mathrm{O}_2} - \mu^{\mathrm{I}}_{\mathrm{O}_2}}{4e\left\{\frac{\ell}{\sigma_i} + \frac{g'_i + g''_i}{g'_i g''_i}\right\}} = \frac{\mu^{\mathrm{II}}_{\mathrm{O}_2} - \mu^{\mathrm{I}}_{\mathrm{O}_2}}{4e\{\ell\rho_i + r'_i + r''_i\}} \qquad (52)$$

Since $I_i < 0$, it is clear from Eqs. (27) and (28) that in this case also the μ_{O_2} varies monotonically. The corresponding variations of $\tilde{\mu}_{\mathrm{O}^{2-}}$, φ and μ_{O_2} for the case corresponding to $r'_e \sim r''_e \sim r_e$ are shown in Fig. 8. Various cases can be readily examined for different relative values of electronic specific resistances, similar to Fig. 7. It can be readily shown that for a given overall performance (voltage versus current density), the spatial variations of μ_{O_2} and φ can vary over a wide range, depending upon the relative values of electronic resistances.

Now let us examine the spatial variations of μ_{O_2} and φ across a fuel cell membrane when the fuel cell is under load. The chemical potentials of oxygen just inside the interfaces are given earlier. Note that $I_i < 0$ but $I_e > 0$. Thus, the term $(r'_i I_i - r'_e I_e)$ can be replaced by $-(r'_i|I_i| + r'_e|I_e|)$. An important point is that even when $|I_e| \ll |I_i|$, it is possible for $r'_i|I_i|$ and $r'_e|I_e|$ to be of comparable magnitudes, provided $r'_e \gg r'_i$. That is, the contribution of I_e for the estimation of μ_{O_2} cannot be a priori ignored. Thus, the chemical potentials of oxygen just under the interfaces are given by

$$\mu'_{\mathrm{O}_2} = \mu^{\mathrm{I}}_{\mathrm{O}_2} - 4e\left(\frac{g'_e|I_i| + g'_i|I_e|}{g'_e g'_i}\right)$$
$$= \mu^{\mathrm{I}}_{\mathrm{O}_2} - 4e(r'_i|I_i| + r'_e|I_e|) < \mu^{\mathrm{I}}_{\mathrm{O}_2} \qquad (53)$$

and

$$\mu''_{\mathrm{O}_2} = \mu^{\mathrm{II}}_{\mathrm{O}_2} + 4e\left(\frac{g''_e|I_i| + g''_i|I_e|}{g''_e g''_i}\right)$$
$$= \mu^{\mathrm{II}}_{\mathrm{O}_2} + 4e(r''_i|I_i| + r''_e|I_e|) > \mu^{\mathrm{II}}_{\mathrm{O}_2} \qquad (54)$$

and that the contribution of I_e to the chemical potential of oxygen cannot be a priori ignored. Thus, it is clear that $\mu^{\mathrm{I}}_{\mathrm{O}_2} > \mu'_{\mathrm{O}_2} > \mu''_{\mathrm{O}_2} > \mu^{\mathrm{II}}_{\mathrm{O}_2}$. That is, for all cases (open circuit, short circuit, and under load) of a fuel cell, the μ_{O_2} varies monotonically between the two end values. Also, therefore, as long as $\mu^{\mathrm{II}}_{\mathrm{O}_2}$ (or more accurately μ''_{O_2}) is greater than the decomposition chemical potential of the solid electrolyte,

---

[11] There are several difficulties, however, which may make this impractical.

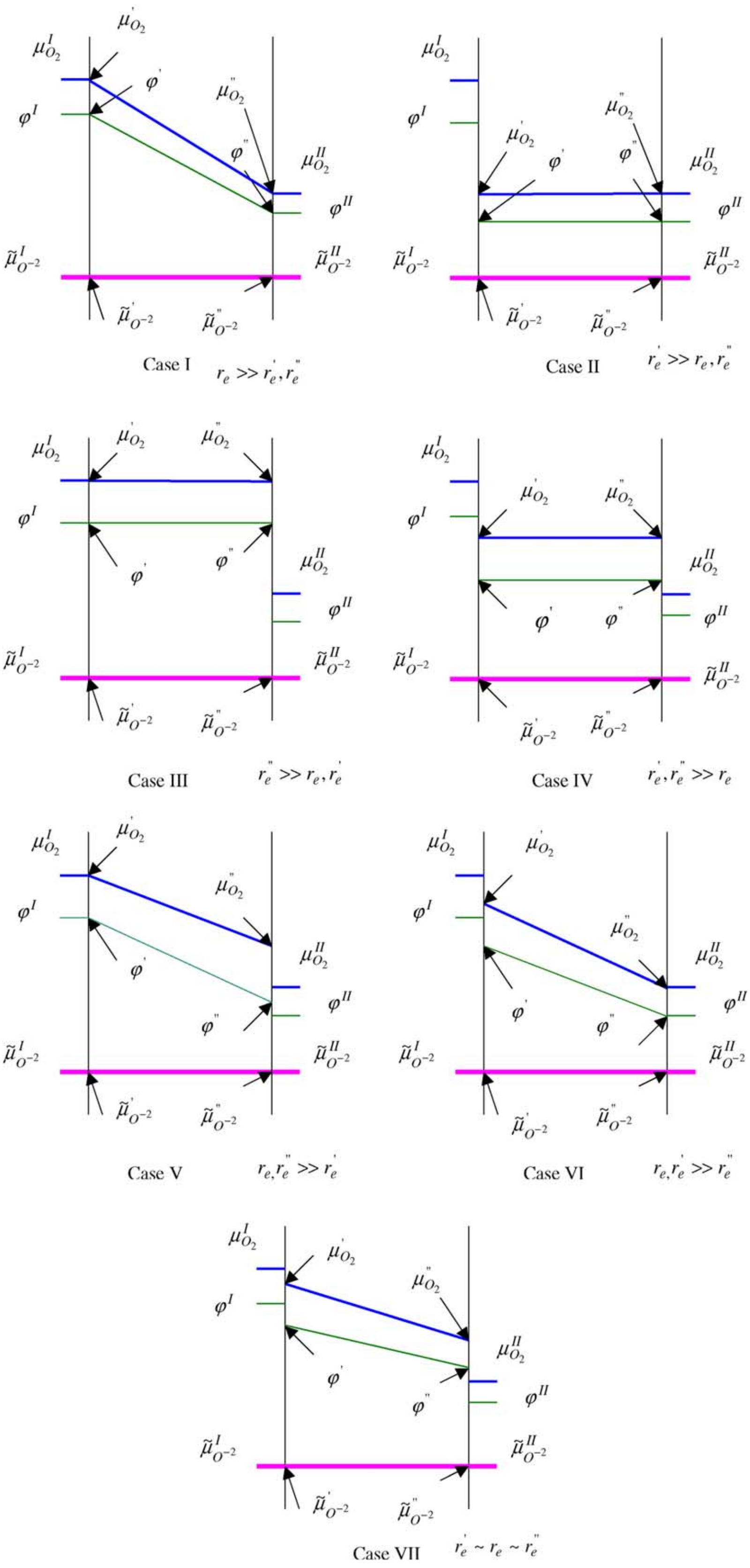

Fig. 7. Schematic variations of $\tilde{\mu}_{O^{2-}}$, φ and μ_{O_2} for different values of electronic specific resistances at open circuit through a fuel cell. Case I: $r_e \gg r'_e, r''_e$, Case II: $r'_e \gg r_e, r''_e$, Case III: $r''_e \gg r_e, r'_e$, Case IV: $r'_e, r''_e \gg r_e$, Case V: $r_e, r''_e \gg r'_e$, Case VI: $r_e, r'_e \gg r''_e$, and Case VII: $r'_e \sim r_e \sim r''_e$. For all seven cases shown above, $R_e >> R_i$, and $\Delta\mu_{O_2} = \mu^{I}_{O_2} - \mu^{II}_{O_2} =$ fixed, which leads to $\Delta\varphi = \varphi^{I} - \varphi^{II} \approx$ fixed, and $\nabla\tilde{\mu}_{O^{2-}} \approx 0$ (near global equilibrium for O^{2-}).

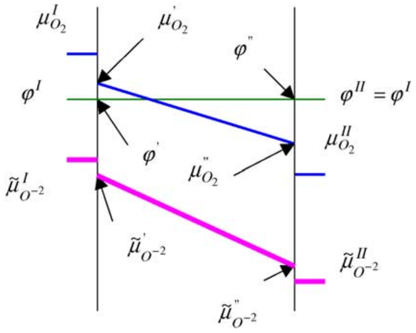

Fig. 8. Schematic variations of $\tilde{\mu}_{O^{2-}}$, φ and μ_{O_2} for a shorted cell. Note that for a shorted cell, $\Delta\varphi=\varphi^{I}-\varphi^{II}=0$, and the electronic current through the cell is zero.

$\mu_{O_2}^{\text{decomp}}$, decomposition of the electrolyte cannot occur. It is also clear that $\varphi^{I}>\varphi'>\varphi''>\varphi^{II}$. Schematic variations of the chemical potential of oxygen, the reduced electrochemical potential of electrons, and the electrochemical potential of oxygen ions for a fuel cell under load are shown in Fig. 9 for the case corresponding to $r_e'\sim r_e''\sim r_e$. Note that this is qualitatively similar to that for the case of MIEC oxygen separation membrane shown in Fig. 3. Similar cases can be considered for other values of electronic area specific resistances.

Similar to the discussion on MIEC oxygen separation membranes, the corresponding equivalent circuit for a fuel cell is given in Fig. 10, with once again the provision that in steady state one must have $I_i=I_i'=I_i''$ and $I_e=I_e'=I_e''$. The equivalent circuit is similar to that for the MIEC membrane, with the exception that there is now an external load, whose resistance is given by R_L (in $\Omega\,\text{cm}^2$). The internal EMFs, and their relation to the net oxygen chemical potential difference are the same as for the MIEC membrane. However, the currents are different, by virtue of the presence of an external load. It is easy to show that

$$I_i=-\frac{E(R_e+R_L)}{R_LR_e+R_i(R_e+R_L)} \tag{55}$$

$$I_e=\frac{ER_L}{R_LR_e+R_i(R_e+R_L)} \tag{56}$$

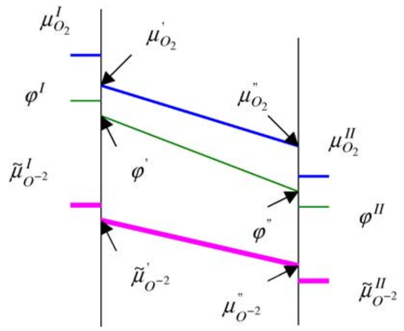

Fig. 9. Schematic variations of $\tilde{\mu}_{O^{2-}}$, φ and μ_{O_2} across a fuel cell under load.

and

$$I_L=-\frac{ER_e}{R_LR_e+R_i(R_e+R_L)} \tag{57}$$

In the above, the units of I_i, I_e and I_L are in A cm^{-2}. Note that as $R_L\to\infty$, I_i and I_e are identical in magnitude (but opposite in sign, of course), and given by Eq. (47), which is the same as for an MIEC membrane. The load current, I_L, is given by

$$I_L=I_i+I_e \tag{58}$$

The overpotentials. For a fuel cell operating with a finite, nonzero current flowing through the external circuit, there are losses associated with electrodes as well as the ohmic loss through the cell. When no load is connected, some loss continues to occur due to internal electronic leakage.[12] The rate of external work done or power is given by $I_L^2R_L=VI_L$ where V is the voltage across the load. The rates of losses through the electrodes and through the electrolyte can be similarly calculated.

For example, for electrode I (cathode), the rate of loss (degradation of potential work into heat—an irreversible process) is given by

$$I_i^2r_i'+I_e^2r_e' \tag{59}$$

If r_i' and r_e' are not constant, but depend upon the local chemical potential of oxygen, then this aspect will have to be included in the analysis. For the purposes of the present discussion, r_i' and r_e' are assumed to be constant. The usual approach is to define overpotential at an electrode as a measure of the loss of useful voltage into irreversible processes. The implication is clearly that the product of the *measured* overpotential and the *measured* current (which naturally is through the external circuit) is the rate of loss of potential work into an irreversible process (heat generation). Since the measurement of current, namely I_L, is a straight forward matter, we will define overpotential at electrode I by η' such that

$$\eta'I_L=I_i^2r_i'+I_e^2r_e' \tag{60}$$

Thus:

$$\eta'=\frac{I_i^2r_i'+I_e^2r_e'}{I_L}=\frac{I_i^2r_i'+I_e^2r_e'}{I_i+I_e} \tag{61}$$

In the above, the overpotential at electrode I, η', is *defined* (not necessarily measurable) in terms of the rate of loss of potential useful work and the *measured* current in the external circuit, I_L. Since the rate of loss of potential work must be equal to or greater than zero (a measure of the degree of irreversibility), the product $\eta'I_L$ must be positive. In terms of the measurable parameters, the ionic and the electronic

---

[12] In a typical fuel cell with negligible electronic leakage, this loss is negligible, yet cannot be identically zero. However, if the electrolyte is based on ceria, internal electronic leakage can be significant.

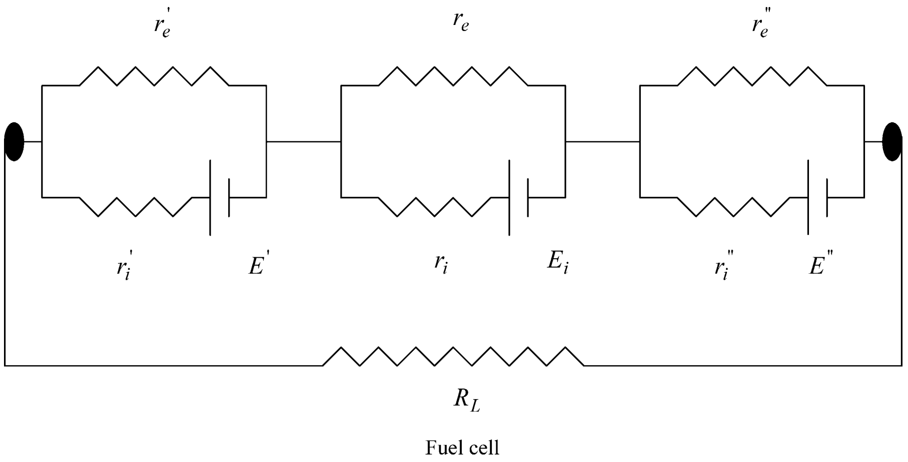

Fig. 10. An equivalent circuit for a fuel cell under an external load. The circuit elements between the two filled elliptical symbols are not physically separable; they collectively represent the equivalent circuit. All E's (E', E_i, E'') are of the same sign.

currents are given, respectively, by

$$I_i = -\frac{E}{R_i + R_e} + \frac{I_L R_e}{R_i + R_e} \tag{62}$$

and

$$I_e = \frac{E}{R_i + R_e} + \frac{I_L R_i}{R_i + R_e} \tag{63}$$

Note that as $I_L \to 0$ (open circuit), $I_e = -I_i$. Substitution for I_i and I_e, respectively, from (62) and (63) into (61) and rearrangement gives

$$\eta' = \frac{(R_e^2 r_i' + R_i^2 r_e') I_L}{(R_i + R_e)^2} + \frac{2E(R_i r_e' - R_e r_i')}{(R_i + R_e)^2} + \frac{E^2 (r_i' + r_e')}{I_L (R_i + R_e)^2} \tag{64}$$

As-defined, the parameters, which can be measured, at least in principle, are the ionic and the electronic area specific resistances of the electrolyte and interfacial regions, and the current flowing through the external circuit, I_L, while η' is calculated using Eq. (64). Interesting conclusions emerge from Eq. (64). Consider first the short circuit limit. For this case, $I_e = 0$[13] and $I_i = -\frac{E}{R_i}$. Substitution into Eq. (60) or (64) and simplification gives $\eta'(\text{short circuit}) = -\frac{E}{R_i} r_i'$. This is simply the net current flowing through the external circuit multiplied by the ionic charge transfer resistance of electrode I.

Now consider the open circuit case. Under open circuit condition, no net current flows through the external circuit, that is $I_L = 0$. As no current flows through the external circuit, the obvious expectation is that the overpotential is zero. However, as discussed in what follows, this conclusion is erroneous. This is because, as long as the electronic conductivity is not identically zero, it means, $I_e = -I_i \neq 0$. Thus, at open circuit condition, according to the definition of η' given in Eqs. (60), (61) and (64), $\eta' \to -\infty$ or $|\eta'| \to \infty$. This looks like a strange conclusion. An important point to note, however, is that the relevant physical quantity is *not* the overpotential, η'. The relevant physical quantity is $\eta' I_L$; which is the rate of loss of potential useful work as heat (an irreversible process) through electrode I (cathode). Note that while $\eta' \to -\infty$ or $|\eta'| \to \infty$ as $I_L \to 0$, the product $\eta' I_L \to \frac{E^2(r_i'+r_e')}{(R_e+R_i)^2}$—is a finite positive limit—as $I_L \to 0$. But this is simply the rate of loss of potential work as heat through electrode I due to internal leakage. This is the significance of overpotential at open circuit.

An examination of Eq. (64) shows that the dependence of η' on I_L is nonlinear. This is despite the fact that all processes are assumed to be describable by various resistances.[14] The limit of Eq. (64) as $R_e \to \infty$ gives[15]

$$\eta' = I_L r_i' \tag{65}$$

which is the usual result. But this is valid only if the electronic resistance is infinite (very large compared to the ionic resistance). Also, only in this case the η' is the same as the experimentally measured overpotential.

The preceding suggests that a plot of I_L versus η'[16] should strictly not go through (0, 0) coordinates. Eq. (64) shows that there should be a minimum in $|\eta'|$. This minimum occurs at

---

[13] That is, the electronic current is identically equal zero. This, however, does not imply that local equilibrium is violated. The reason the electronic current is zero in this case is because the electrodes are shorted. In such a case, even though I_e through the membrane is zero, that through the combined system comprising the membrane and the external short is not zero. Also, the preceding is only for steady state. If the steady state has not been established, the position and time-dependent electronic current, $I_e(x, t)$, through the membrane need not be zero, even when externally shorted.

[14] Note, however, that the relationship between voltage across the cell and the measured current is still linear and is given by $V = \frac{ER_e}{(R_i+R_e)} - \left(\frac{R_i R_e}{R_i+R_e}\right)|I_L|$. If $R_e \to \infty$, this reduces to the usual equation $V = E - R_i|I_L|$.

[15] Once again, to emphasize, R_e strictly cannot go to infinity since this violates the assumption of local equilibrium. The above simply implies that R_e is very large.

[16] To reemphasize, the as-defined η' is calculated, not measured.

a current density given by

$$|I_L(\min)| = E\sqrt{\frac{r_i' + r_e'}{R_e^2 r_i' + R_i^2 r_e'}} \tag{66}$$

Note that when $R_e \to \infty$, $|I_L(\min)| \to 0$. Note also that although $|\eta'|$ exhibits a minimum, the product $I_L\eta'$ monotonically increases with increasing $|I_L|$, from its lowest value at OCV to its highest value at short circuit. This means, the rate of loss of potential useful work due to irreversibility of the process associated with overpotential, monotonically increases with load current.

For electrode II (anode) and the bulk membrane, similar equations can be written. They are as follows:

For electrode II (anode):

$$\eta'' = \frac{(R_e^2 r_i'' + R_i^2 r_e'')I_L}{(R_i + R_e)^2} + \frac{2E(R_i r_e'' - R_e r_i'')}{(R_i + R_e)^2} + \frac{E^2(r_i'' + r_e'')}{I_L(R_i + R_e)^2} \tag{67}$$

In the short circuit limit

$$\eta''(\text{short circuit}) = -\frac{E}{R_i} r_i'' \tag{68}$$

and under open circuit conditions

$$\eta'' I_L \to \frac{E^2(r_i'' + r_e'')}{(R_e + R_i)^2} \quad \text{as} \quad I_L \to 0$$

The limit of Eq. (67) as $R_e \to \infty$ gives $\eta'' = I_L r_i''$.
For the bulk membrane:

$$\eta_i = \frac{(R_e^2 r_i + R_i^2 r_e)I_L}{(R_i + R_e)^2} + \frac{2E(R_i r_e - R_e r_i)}{(R_i + R_e)^2} + \frac{E^2(r_i + r_e)}{I_L(R_i + R_e)^2} \tag{69}$$

In the short circuit limit

$$\eta_i(\text{short circuit}) = -\frac{E}{R_i} r_i \tag{70}$$

and under open circuit conditions

$$\eta_i I_L \to \frac{E^2(r_i + r_e)}{(R_e + R_i)^2} \quad \text{as} \quad I_L \to 0$$

The limit of Eq. (69) as $R_e \to \infty$ gives $\eta = I_L r_i$.

The total polarization loss is the sum of the three, namely

$$\eta = \eta' + \eta_i + \eta'' \tag{71}$$

which is also given by

$$\eta = \frac{R_e R_i}{R_i + R_e} I_L + \frac{E^2}{I_L(R_i + R_e)} \tag{72}$$

Note that when $R_e \to \infty$, $\eta \to I_L R_i$. From Eq. (72), the rate of loss of potential work into heat (irreversible process) in all parts of the cell is given by

$$\eta I_L = \frac{R_e R_i}{R_i + R_e} I_L^2 + \frac{E^2}{R_i + R_e} \tag{73}$$

which for $R_e \to \infty$ reduces to $I_L^2 R_i$.

Overpotentials in terms of thermodynamic potentials. The overpotential can be expressed in terms of chemical potential of O_2, μ_{O_2}, and reduced (negative) electrochemical potential of electrons, φ, by substituting for I_i and I_e into Eq. (60), and using Eqs. (29) and (30). In general, rather complicated equations result. In what follows, only the limiting case wherein the electronic resistance is much greater than the ionic resistance will be examined, that is, the case corresponding to $R_e \to \infty$. For this case, it can be readily shown that overpotential at electrode I is given by

$$\eta' = \frac{\tilde{\mu}^{\mathrm{II}}_{O^{2-}} - \tilde{\mu}^{\mathrm{I}}_{O^{2-}}}{2e} \frac{r_i'}{R_i'} \tag{74}$$

given in terms of the net drop in electrochemical potential of oxygen ions across the cell, the ionic resistance of the interface at I, and the net ionic resistance, or

$$\eta' = \frac{\tilde{\mu}'_{O^{2-}} - \tilde{\mu}^{\mathrm{I}}_{O^{2-}}}{2e} \tag{75}$$

given in terms of the drop in electrochemical potential of oxygen across electrode I. As defined, the η' is negative, and the net current, I_L, is also negative. Similar equations can be written for η'' and η_i in terms of electrochemical potentials of oxygen ions. Note, however, that Eqs. (74) and (75) are valid only if the net electronic resistance is much larger than the net ionic resistance. Also, only in such a case the measured overpotential is the same as η' defined here.

2.4. Oxygen separation under the application of an external voltage

Such would be the case with yttria-stabilized zirconia (YSZ) or rare earth oxide-doped ceria as the electrolyte, with suitable electrodes applied on the two surfaces. In the first two cases considered, namely an MIEC membrane and a fuel cell, the $\Delta\mu_{O_2}$ and $\Delta\varphi$ are related to each other. Specifically, upon the application of $\Delta\mu_{O_2}$ across the membrane, a corresponding $\Delta\varphi$ appears across the membrane. In the present case, an external voltage is applied across the two electrodes, which effectively fixes the $\Delta\varphi$ across the membrane. This provides an additional experimental degree of freedom. Fig. 11 shows a schematic illustration.

In the present situation, note that oxygen is being pumped through the membrane from left to right. Thus, $I_i < 0$. Similarly, electrons are also being pumped through the membrane from left to right. Thus, $I_e < 0$. That means, both I_i and I_e are of the same sign, unlike the previous two cases. In this case, both $\Delta\mu_{O_2}$ and $\Delta\varphi$ are experimental parameters, which can

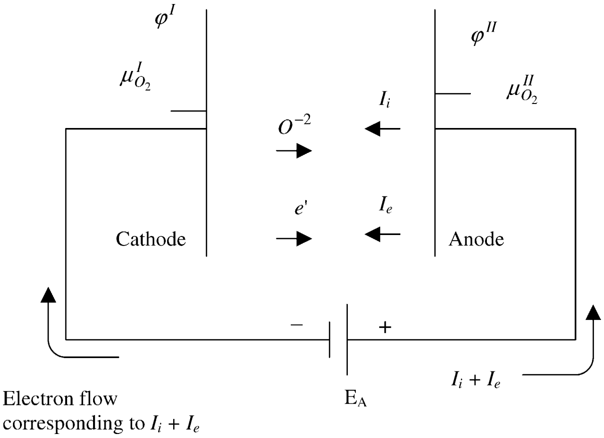

Fig. 11. A schematic illustration of an oxygen separation membrane under an externally applied voltage. Electronic and ionic currents are in the same direction.

be arbitrarily selected. The general transport equations are the same as before, and the net electronic and ionic current densities are given by Eqs. (29) and (30), respectively.

The oxygen ion current, as before, is given by Eq. (23), and the chemical potentials of oxygen just under the two interfaces are given, as before, by Eqs. (27) and (28). Since now both $I_i < 0$ and $I_e < 0$, Eqs. (27) and (28) can be written as follows:

$$\mu'_{O_2} = \mu^{I}_{O_2} + 4e\left(\frac{-g'_e|I_i| + g'_i|I_e|}{g'_e g'_i}\right) = \mu^{I}_{O_2} - 4e(r'_i|I_i| - r'_e|I_e|) \tag{76}$$

and

$$\mu''_{O_2} = \mu^{II}_{O_2} - 4e\left(\frac{-g''_e|I_i| + g''_i|I_e|}{g''_e g''_i}\right) = \mu^{II}_{O_2} + 4e(r''_i|I_i| - r''_e|I_e|) \tag{77}$$

Note the negative sign in parentheses. Thus, if $r'_i|I_i| > r'_e|I_e|$, note that $\mu'_{O_2} < \mu^{I}_{O_2}$, and if $r'_i|I_i| < r'_e|I_e|$, note that $\mu'_{O_2} > \mu^{I}_{O_2}$. Similarly, if $r''_i|I_i| > r''_e|I_e|$, note that $\mu''_{O_2} > \mu^{II}_{O_2}$, and if $r''_i|I_i| < r''_e|I_e|$, note that $\mu''_{O_2} < \mu^{II}_{O_2}$.

In the following discussion, it will first be assumed that $r'_i|I_i| \gg r'_e|I_e|$ and $r''_i|I_i| \gg r''_e|I_e|$. Thus, note that $\mu'_{O_2} < \mu^{I}_{O_2}$ and $\mu''_{O_2} > \mu^{II}_{O_2}$. Substitution of Eq. (30) into Eq. (76) gives

$$\mu'_{O_2} = \mu^{I}_{O_2} - \frac{\{\mu^{I}_{O_2} - \mu^{II}_{O_2}\}r'_i}{\ell\rho_i + r'_i + r''_i} + \frac{4e\{\varphi^{I} - \varphi^{II}\}r'_i}{\ell\rho_i + r'_i + r''_i} \tag{78}$$

Suppose the chemical potential of oxygen is the same at both electrodes, that is $\mu^{I}_{O_2} = \mu^{II}_{O_2}$. Then:

$$\mu'_{O_2} = \mu^{I}_{O_2} + \frac{4e\{\varphi^{I} - \varphi^{II}\}r'_i}{\ell\rho_i + r'_i + r''_i} = \mu^{I}_{O_2} - \frac{4e\{\varphi^{II} - \varphi^{I}\}r'_i}{\ell\rho_i + r'_i + r''_i} \tag{79}$$

Since $\varphi^{II} > \varphi^{I}$, note that $\mu'_{O_2} < \mu^{I}_{O_2}$. The absolute value of μ'_{O_2} in relation to $\mu^{I}_{O_2}$ depends upon the various transport parameters, especially r'_i, and the net voltage difference, namely, $\Delta\varphi = \varphi^{II} - \varphi^{I}$. The higher are the r'_i and $\Delta\varphi = \varphi^{II} - \varphi^{I}$, the lower is μ'_{O_2}. If μ'_{O_2} is lower than the decomposition potential of the electrolyte, decomposition can occur, effectively increasing the magnitude of the ionic current density, beyond that given by Eq. (23). In the case of zirconia, for example, the decomposition reaction may involve the following steps. When the $\mu'_{O_2} < \mu^{\mathrm{decomp}}_{O_2}$, reaction:

$$ZrO_2 \rightarrow Zr^{4+} + 2O^{2-}$$

occurs just under electrode I. The oxygen ions released transport through the membrane to electrode II where the following reaction occurs:

$$2O^{2-} \rightarrow O_2(g) + 4e'$$

The electrons released transport in the external circuit to electrode I where the following reaction occurs:

$$Zr^{4+} + 4e \rightarrow Zr(\text{metal})$$

The net reaction is

$$ZrO_2 \rightarrow Zr(\text{metal, formed at negative electrode}) + O_2(\text{g, released at positive electrode})$$

The corresponding current appears in the external circuit, in addition to the current due to oxygen pumping from left to right. An important point is that the corresponding electron transport occurs in the external circuit.

Also an important point to note is that only in a very special case would one have $\mu'_{O_2} = \mu^{I}_{O_2}$.[17] In almost all practical situations, such as the one assumed here, one would almost always have $\mu'_{O_2} < \mu^{I}_{O_2}$ (for the assumed case of $r'_i|I_i| \gg r'_e|I_e|$).

Similar analysis can be carried out for the interface at II. For the case of $\mu^{I}_{O_2} = \mu^{II}_{O_2}$, it is seen that

$$\mu''_{O_2} = \mu^{I}_{O_2} + \frac{4e\{\varphi^{II} - \varphi^{I}\}r''_i}{\ell\rho_i + r'_i + r''_i} \tag{80}$$

for the assumed case of $r''_i|I_i| \gg r''_e|I_e|$. That is, one would have

$$\mu''_{O_2} > \mu^{II}_{O_2} = \mu^{I}_{O_2}$$

Schematic variations of μ_{O_2} and φ for this special case are shown in Fig. 12. Also shown in the figure is a schematic variation of $\tilde{\mu}_{O^{2-}}$.

If, on the other hand, $r'_i|I_i| < r'_e|I_e|$ and $r''_i|I_i| < r''_e|I_e|$, we would have had $\mu'_{O_2} > \mu^{I}_{O_2}$ and $\mu''_{O_2} < \mu^{II}_{O_2}$. In such a case, the variation of μ_{O_2} and φ would be as shown schematically in Fig. 13. In such a case, the decomposition of the electrolyte can occur at the positive electrode instead. Once again the

---

[17] For the general case (Eq. (76)), for μ'_{O_2} to be equal to $\mu^{I}_{O_2}$, it is necessary that $r'_i|I_i| - r'_e|I_e| = 0$. Clearly, this is a very rare case, and unlikely to be realized in practice.

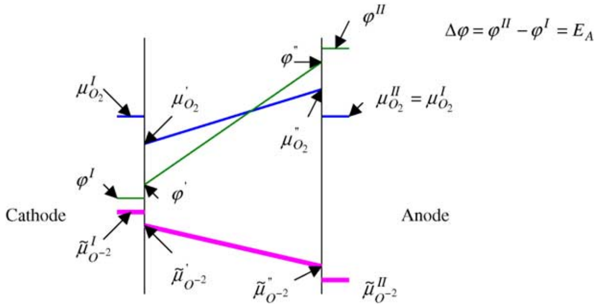

Fig. 12. Schematic variations of μ_{O_2}, φ, and $\tilde{\mu}_{O^{2-}}$ across an oxygen separation membrane under an externally applied voltage. It is assumed here that $r'_i|I_i| > r'_e|I_e|$ and $r''_i|I_i| > r''_e|I_e|$. Note that the $\tilde{\mu}_{O^{2-}}$ decreases from left to right, consistent with net oxygen transport from left to right.

reaction steps are as follows. When the $\mu''_{O_2} < \mu^{\mathrm{decomp}}_{O_2}$, reaction

$$ZrO_2 \rightarrow Zr^{4+} + 2O^{2-}$$

occurs just under electrode II. Also at electrode II

$$2O^{2-} \rightarrow O_2(g) + 4e'$$

Electrons released transport through the external circuit to electrode I, and then through the membrane towards electrode II, where the following reaction occurs:

$$Zr^{4+} + 4e' \rightarrow Zr(\mathrm{metal})$$

The net reaction is

$$ZrO_2 \rightarrow Zr(\mathrm{metal,\ formed\ at\ positive\ electrode}) + O_2(\mathrm{g,\ released\ at\ positive\ electrode})$$

In this case, however, it is necessary for the corresponding electron transport to occur through the membrane. Since the membrane is predominantly an ionic conductor, electronic conduction is expected to be negligible. The implication is that although the analysis shows that decomposition can occur at the positive electrode, the associated transport kinetics may be very sluggish. Thus, in practice, this case may not be observed.

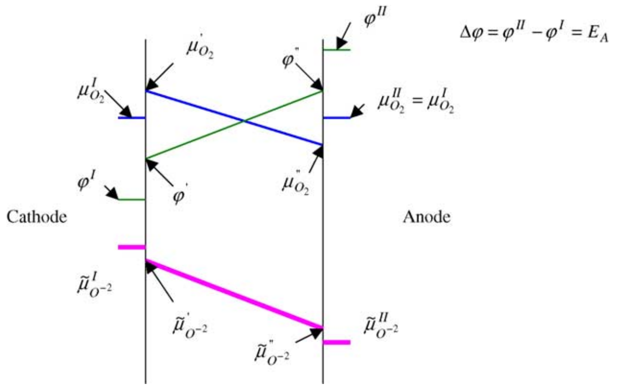

Fig. 13. Schematic variations of μ_{O_2}, φ, and $\tilde{\mu}_{O^{2-}}$ across an oxygen separation membrane under an externally applied voltage. It is assumed here that $r'_i|I_i| < r'_e|I_e|$ and $r''_i|I_i| < r''_e|I_e|$. Note that the $\tilde{\mu}_{O^{2-}}$ decreases from left to right, consistent with net oxygen transport from left to right.

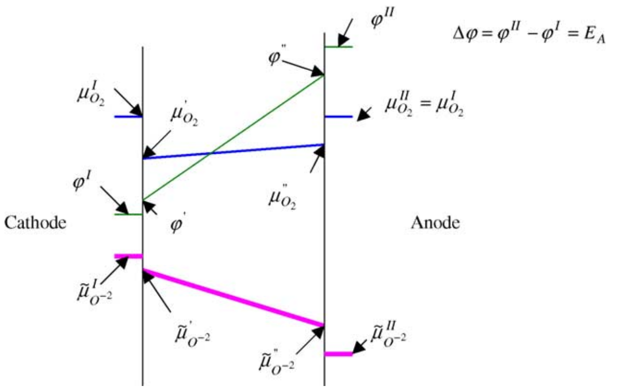

Fig. 14. Schematic variations of μ_{O_2}, φ, and $\tilde{\mu}_{O^{2-}}$ across an oxygen separation membrane under an externally applied voltage. It is assumed here that $r'_i|I_i| > r'_e|I_e|$ and $r''_i|I_i| < r''_e|I_e|$. In this case, the μ_{O_2} in the membrane everywhere is lower than that in the gas phase. Whether the μ_{O_2} increases or decreases from left to right depends upon relative magnitudes of transport parameters. Note that the $\tilde{\mu}_{O^{2-}}$ decreases from left to right, consistent with net oxygen transport from left to right.

Additional cases can be similarly considered. They are as follows:

Suppose $r'_i|I_i| < r'_e|I_e|$, so that $\mu'_{O_2} > \mu^{\mathrm{I}}_{O_2}$, and $r''_i|I_i| < r''_e|I_e|$, so that $\mu''_{O_2} < \mu^{\mathrm{II}}_{O_2}$. Fig. 14 shows the expected variation of the chemical potential of oxygen through the membrane for $\mu^{\mathrm{II}}_{O_2} = \mu^{\mathrm{I}}_{O_2}$. Note that in this case, the μ_{O_2} in the membrane is lower than that in the gas phase.

Suppose now $r'_i|I_i| > r'_e|I_e|$, so that $\mu'_{O_2} < \mu^{\mathrm{I}}_{O_2}$, and $r''_i|I_i| > r''_e|I_e|$, so that $\mu''_{O_2} > \mu^{\mathrm{II}}_{O_2}$. Fig. 15 shows the expected variation of the chemical potential of oxygen through the membrane. In this case, the μ_{O_2} in the membrane is higher than that in the gas phase. The preceding shows the importance of incorporating the electronic current through

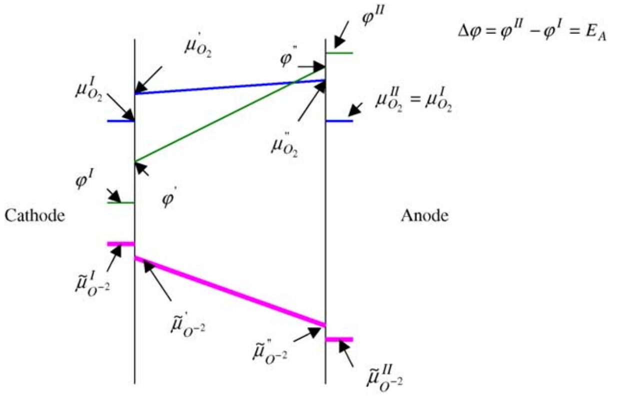

Fig. 15. Schematic variations of μ_{O_2}, φ, and $\tilde{\mu}_{O^{2-}}$ across an oxygen separation membrane under an externally applied voltage. It is assumed here that $r'_i|I_i| < r'_e|I_e|$ and $r''_i|I_i| > r''_e|I_e|$. In this case, the μ_{O_2} in the membrane everywhere is higher than that in the gas phase. Whether the μ_{O_2} increases or decreases from left to right depends upon relative magnitudes of transport parameters. Note that the $\tilde{\mu}_{O^{2-}}$ decreases from left to right, consistent with net oxygen transport from left to right.

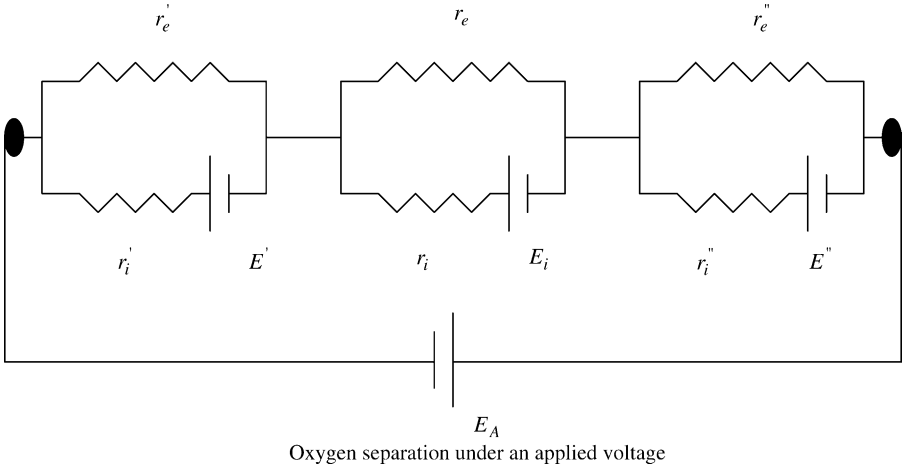

Fig. 16. An equivalent circuit for an oxygen separation membrane under an applied DC voltage. The circuit elements between the two filled elliptical symbols are not physically separable; they collectively represent the equivalent circuit. The E's (E', E_i, E'') can be of different signs, and depend upon the applied voltage, E_A, and the logarithm of the ratio of oxygen partial pressures at the two electrodes. Their sum, however, is independent E_A, but depends only on the logarithm of the ratio of oxygen pressures at the two electrodes.

bulk and also across interfaces, however small, into the transport equations, even when dealing with membranes made of predominantly oxygen ion conductors.

The equivalent circuit for an oxygen separation membrane under an externally applied voltage is given in Fig. 16 with the provision that in steady state $I_i = I_i' = I_i''$ and $I_e = I_e' = I_e''$. The same equivalent circuit is applicable for the transient case, in which the ionic and electronic currents are functions of position and time, but Kirchoff's equations continue to hold.[18] In what follows, only the steady state is considered. In this case, as before:

$$E = E' + E_i + E'' = \frac{RT}{4F}\ln\left(\frac{p'_{O_2}}{p^{I}_{O_2}}\right) + \frac{RT}{4F}\ln\left(\frac{p''_{O_2}}{p'_{O_2}}\right) + \frac{RT}{4F}\ln\left(\frac{p^{II}_{O_2}}{p''_{O_2}}\right) = \frac{RT}{4F}\ln\left(\frac{p^{II}_{O_2}}{p^{I}_{O_2}}\right) = \frac{k_B T}{4e}\ln\left(\frac{p^{II}_{O_2}}{p^{I}_{O_2}}\right) \qquad (81)$$

In the previous two examples, that is an MIEC membrane and a fuel cell, all three internal EMFs were of the same sign—consistent with a monotonic variation of μ_{O_2} from one side to the other. In the present example of voltage-driven oxygen separation, however, this is not the case. Thus, the signs of the three EMFs in general are different as discussed earlier. An important point to note is that the net E in the above equation, however, is still independent of the externally applied voltage, and is only a function of $\Delta\mu_{O_2}$ existing across the membrane. However, the individual internal EMFs, namely, E', E_i, and E'' are functions of the applied voltage, E_A, and thus do determine the stability of the membrane. For the case where $\mu^{I}_{O_2} = \mu^{II}_{O_2}$, the $E = 0$. The corresponding internal EMFs at steady state are given by

$$E' = E_A\left(\frac{r_e'}{R_e} - \frac{r_i'}{R_i}\right), \qquad E_i = E_A\left(\frac{r_e}{R_e} - \frac{r_i}{R_i}\right) \quad \text{and}$$
$$E'' = E_A\left(\frac{r_e''}{R_e} - \frac{r_i''}{R_i}\right) \qquad (82)$$

Note that the terms in parentheses determine the signs of the individual EMFs, yet the sum of the three EMFs is zero.

If $\mu^{I}_{O_2} \neq \mu^{II}_{O_2}$, then $E \neq 0$. Then, it can be readily shown that the various EMFs are given by

$$E' = E_A\left(\frac{r_e'}{R_e} - \frac{r_i'}{R_i}\right) + E\frac{r_i'}{R_i},$$
$$E_i = E_A\left(\frac{r_e}{R_e} - \frac{r_i}{R_i}\right) + E\frac{r_i}{R_i} \quad \text{and}$$
$$E'' = E_A\left(\frac{r_e''}{R_e} - \frac{r_i''}{R_i}\right) + E\frac{r_i''}{R_i} \qquad (83)$$

and the sum of the three EMFs equals that given by Eq. (81).

The overpotentials. In the case of oxygen pumping under an applied voltage, an external agency does work on the system. Under isothermal conditions, with oxygen gas assumed to behave as an ideal gas, the internal energy is a function of temperature only. Thus, no change in the internal energy occurs upon isothermal pumping. We will first consider here the case wherein the oxygen partial pressures at the two electrodes are identical so that $\mu^{I}_{O_2} = \mu^{II}_{O_2}$ and the net E given by Eq. (81) is zero. This means all work done on the system is degraded as heat (an irreversible process). The net ionic and electronic current densities are given by $I_i = -\frac{E_A}{R_i}$ and $I_e = -\frac{E_A}{R_e}$. Then, the rate of loss of input work into heat at electrode I is given by

$$I_i^2 r_i' + I_e^2 r_e' = E_A^2\left(\frac{r_i'}{R_i^2} + \frac{r_e'}{R_e^2}\right) \qquad (84)$$

---

[18] For membranes with spatially dependent transport properties (but without the incorporation of interfacial effects), the transient case was previously examined in [15,16].

Once again, the overpotential η' is *defined* in terms of the current measured in the external circuit, I, by

$$\eta' I = I_i^2 r_i' + I_e^2 r_e' = E_A^2 \left(\frac{r_i'}{R_i^2} + \frac{r_e'}{R_e^2} \right) \tag{85}$$

where $I = -E_A \left(\frac{1}{R_i} + \frac{1}{R_e} \right)$ and the overpotential is given by

$$\eta' = -E_A \frac{r_i' R_e^2 + r_e' R_i^2}{R_i R_e (R_i + R_e)} \tag{86}$$

In this case, as I_i and I_e are of the same sign, the η' is the same as the measured overpotential. If the electronic resistance is much larger than the ionic resistance, that is in the limit $R_e \to \infty$, the above reduces to

$$\eta' = -\frac{E_A}{R_i} r_i' = I r_i' \tag{87}$$

In terms of electrochemical potential of oxygen ions, the overpotential can be given as before by

$$\eta' = \frac{\tilde{\mu}'_{O^{2-}} - \tilde{\mu}^{I}_{O^{2-}}}{2e} \tag{88}$$

In the above, as-defined, both I and η' are negative. Similar equations can be given for η and η'', which are, respectively, overpotential losses across the bulk membrane and electrode II. It is readily shown that the net rate of degradation of input work into heat is given by $(\eta' + \eta + \eta'')I = E_A^2 \left(\frac{1}{R_i} + \frac{1}{R_e} \right)$, which for $R_e \to \infty$ reduces to $\frac{E_A^2}{R_i}$.

Suppose we now consider the case wherein $\mu^{I}_{O_2} \neq \mu^{II}_{O_2}$, such that $E = \frac{\mu^{II}_{O_2} - \mu^{I}_{O_2}}{4F} \neq 0$. In such a case, it can readily shown that the ionic and electronic currents are given by

$$I_i = -\frac{E_A - E}{R_i} \quad \text{and} \quad I_e = -\frac{E_A}{R_e} \tag{89}$$

When 1 mol of oxygen gas is pumped from $p^{I}_{O_2}$ to $p^{II}_{O_2}$, the amount of potential work degraded as heat is

$$Q = 4F(E_A - E) + \frac{4FEE_A}{E_A - E} \frac{R_i}{R_e} \tag{90}$$

and the net work of compressing 1 mol of gas from $\mu^{I}_{O_2}$ ($p^{I}_{O_2}$) to $\mu^{II}_{O_2}$ ($p^{II}_{O_2}$) is given by $w = 4FE = RT \ln \left(\frac{p^{II}_{O_2}}{p^{I}_{O_2}} \right)$. Note that if $R_e \gg R_i$ (or $R_e \to \infty$), the above reduces to $Q \approx 4F(E_A - E)$. If, however, $R_e \neq \infty$, but if $E_A = E$, then the $Q \to \infty$. Note that in this case, $I_i = 0$. Thus, it will take infinite time to transport 1 mol of oxygen. However, $I_e \neq 0$. As a result, infinite electronic charge will have to be transported in the time required to transport 1 mol of oxygen gas, which leads to $Q \to \infty$. Finally, the overpotentials can be easily determined in terms of I_i, I_e and the various area specific resistances, using the approach described earlier.

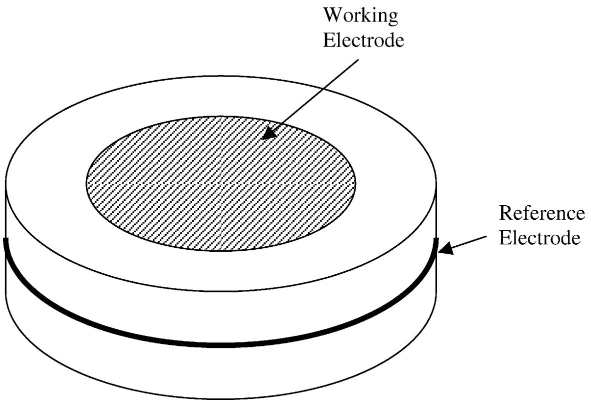

Fig. 17. A schematic illustration of the three-electrode system. A DC voltage is applied across the working electrode and the counter electrode (on the opposite face). Both current and voltage between the working and the reference electrodes are measured as a function of the applied voltage. Usually, the testing is conducted in air, although can be conducted in other environments.

2.5. *The analysis of three-electrode system*

Often, the placement of a reference electrode in devices such as solid oxide fuel cells (SOFC) raises questions concerning the validity of the measurement, because the reference electrode location is on the surface. In thin, electrolyte film, electrode-supported SOFC, this leads to substantial errors. In an attempt to circumvent these uncertainties, several investigators have used the three-electrode system. It consists of a thick electrolyte disc, upon which working and counter electrodes are placed on the opposite sides of the disc in a symmetric arrangement, and a reference electrode is placed in a symmetric arrangement with respect to the two electrodes. Fig. 17 shows a typical arrangement. Then, in order to investigate electrode kinetics at the working electrode, which may be a prospective cathode for SOFC, a DC voltage is applied across the working and the counter electrodes.[19] Both current through the cell and voltage across the working and reference electrodes are measured as functions of the applied voltage. Corrected for the ohmic loss, the measured voltage between the working and the reference electrodes gives a measure of the electrode overpotential at the working electrode. In what follows, implications of such measurements are described using the analysis presented so far.

The membrane or the disc is predominantly an oxygen ion conductor. Thus, note that $|I_e| \ll |I_i|$. In the following illustration, it is assumed that $r_i'|I_i| \gg r_e'|I_e|$ and $r_i''|I_i| \gg r_e''|I_e|$.[20]

---

[19] In many experimental procedures, the instrument is operated in such a mode so as to only track the voltage between the working and the reference electrodes, and little attention is paid to the actual voltage between the working and the counter electrodes. It is to be emphasized that from the standpoint of electrolyte stability and the present discussion, it is important to know the actual applied voltage, which is between the working and the counter electrodes. That is, the measurement of voltage between the working and reference electrodes is not sufficient to describe the problem completely.

[20] Since $|I_i| \gg |I_e|$, this also implies that $R_e \gg R_i$.

The chemical potential of oxygen just under interface I is given by Eq. (78). The testing is typically done in air. Thus, the chemical potential of oxygen at the two electrodes (just outside the electrodes) is the same. If concentration polarization is negligible, the chemical potentials of oxygen at the two electrode/electrolyte interfaces, namely $\mu_{O_2}^{I}$ and $\mu_{O_2}^{II}$ are identical, that is $\mu_{O_2}^{I} = \mu_{O_2}^{II}$. Let us consider this case first. Eq. (78) then becomes

$$\mu'_{O_2} = \mu_{O_2}^{II} - \frac{4e\{\varphi^{II} - \varphi^{I}\}r'_i}{\ell\rho_i + r'_i + r''_i} \tag{91}$$

If μ'_{O_2} decreases below the decomposition chemical potential, $\mu_{O_2}^{decomp}$, the decomposition can occur just under electrode I, which manifests as excess current. It is also possible that a nonstoichiometry (oxygen deficiency) may develop at a lower applied voltage, which can also lead to excess current (beyond that due to the cathodic reaction, namely $\frac{1}{2}O_2 + 2e' \rightarrow O^{2-}$). Since the experimenter has no way of determining how much of the current is due to decomposition (or nonstoichiometry development) and how much is actually attributable to the cathodic reaction occurring at electrode I, the entire current is inadvertently assigned to the cathodic reaction leading to an overestimation of cathodic activity, and thus an incorrect result. The $\mu_{O_2}^{decomp}$ can in principle be estimated from the known thermodynamic data. The usual assumption made during such tests is that all that needs to be done is to correct for the ohmic drop, in order to ensure that the applied voltage is less than some critical value to ensure that the chemical potential in the electrolyte is greater than $\mu_{O_2}^{decomp}$ [21]. For the condition $\mu'_{O_2} \approx \mu_{O_2}^{decomp}$, Eq. (91) can be rearranged as

$$\varphi^{II} - \varphi^{I} \approx \left(\frac{\mu_{O_2}^{II} - \mu_{O_2}^{decomp}}{4e}\right)\left(\frac{\ell\rho_i + r'_i + r''_i}{r'_i}\right) \tag{92}$$

Eq. (92) shows that if the applied voltage exceeds the above value, decomposition of the electrolyte will occur at electrode I. The equation, however, shows that there is no way to correct for the ohmic loss as usually both r'_i and r''_i are unknowns. In the extreme case in which $r'_i \gg r''_i$ and $r'_i \gg \ell\rho_i$, Eq. (92) reduces to

$$\varphi^{II} - \varphi^{I} \approx \left(\frac{\mu_{O_2}^{II} - \mu_{O_2}^{decomp}}{4e}\right) \tag{93}$$

Eq. (93) gives the minimum applied voltage necessary to cause decomposition of the electrolyte for the relative values of transport parameters assumed here. Beyond this voltage, the measured current will have two components; current due to the cathodic reaction and current due to decomposition. In many cases, nonstoichiometry may appear at applied voltages lower than given by Eq. (92) or (93), and this also will contribute to excess current. In either case, the measured current will be greater than that corresponding to the cathodic reaction, leading to an overestimation of the electrode activity. That is, one may erroneously conclude that the electrocatalytic activity of the prospective cathode is far better than it really is. Fig. 18 shows a schematic illustration of the experimentally measured current (or current density) plotted versus experimentally measured overpotential in a typical three-electrode system under an applied DC bias. In the schematic illustration shown in Fig. 18, both the current and overpotential are plotted on linear scales. Hence the curvature is concave up. If the overpotential is plotted on a linear scale but the current is plotted on a logarithmic scale, the curvature will be convex up.

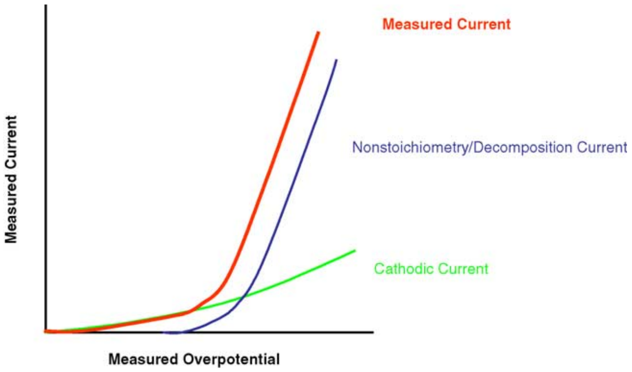

Fig. 18. A schematic illustration of the measured current (or current density) (—) vs. measured overpotential (corrected for the ohmic drop) using a three-electrode system under an applied DC voltage. It contains two parts: (a) the cathodic current (—), namely due to the reaction $\frac{1}{2}O_2 + 2e' \rightarrow O^{2-}$, and (b) the current due to the development of nonstoichiometry or decomposition (—). In practice, it is quite possible that the nonstoichiometry/decomposition current may be much greater than the cathodic current. Under such conditions, the three-electrode system can grossly overestimate the cathodic activity. The schematic shows both current and overpotential plotted on linear scales. If the current is plotted on a logarithmic scale, the curves will be convex up.

In the preceding discussion, it was assumed that concentration polarization is negligible. In practice, if the electrode thickness is large and/or electrode porosity is low, such an assumption may not be justifiable. A review of literature shows that rarely is any attention paid to this aspect (thickness and porosity) of the working electrode when making such measurements. Suppose, for example, that concentration polarization is not small at the working electrode, cathode (electrode I). In such a case under an applied voltage, the variation of oxygen partial pressure through electrode I will schematically appear as shown in Fig. 19.[21] In such a case, $\mu_{O_2}^{I} < \mu_{O_2}^{II}$ where, as before, $\mu_{O_2}^{I}$ is the chemical potential of oxygen just outside the interface between electrode I and the electrolyte. In the extreme case, if the porosity is low and/or the electrode thickness is large, the net cathodic current is gas phase diffusion-limited or concentration polarization-limited (through the porous electrode). In such a case, the $p_{O_2}^{I}$ reaches some low value, such that beyond some applied

---

[21] Although in Fig. 19 the variation in p_{O_2} is shown linear, this need not be the case. If there is a gradation in porosity, the variation in p_{O_2} will be nonlinear.

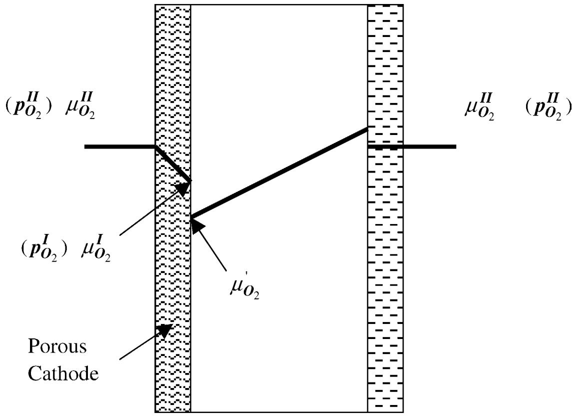

Fig. 19. A schematic variation of oxygen chemical potential, μ_{O_2} (or oxygen partial pressure, p_{O_2}) across a membrane under an applied DC voltage. It is assumed here that concentration polarization is negligible at electrode II. However, at electrode I, it is significant. As a result, there is a variation of μ_{O_2} (and p_{O_2}) through the porous cathode. The variation in p_{O_2} is expected to be approximately linear. In such a case, if $p^{\mathrm{I}}_{O_2} \ll p^{\mathrm{II}}_{O_2}$, the net flux arriving at the electrode I/electrolyte interface is essentially fixed (concentration polarization limit), and is proportional to $(p^{\mathrm{II}}_{O_2} - p^{\mathrm{I}}_{O_2}) \approx p^{\mathrm{II}}_{O_2}$, beyond some threshold applied voltage. In such a case, the current due to the cathodic reaction, namely $\frac{1}{2}O_2 + 2e' \to O^{2-}$, is constant, independent of the applied voltage. However, the μ'_{O_2} continues to decrease with increasing applied voltage. If μ'_{O_2} decreases below $\mu^{\mathrm{decomp}}_{O_2}$, the electrolyte decomposes resulting in additional (excess) current. If the material exhibits nonstoichiometry, current due to the development of nonstoichiometry can appear before decomposition. Either way, the measured current includes both the cathodic current and that due to decomposition/nonstoichiometry.

voltage, $p^{\mathrm{I}}_{O_2} \ll p^{\mathrm{II}}_{O_2}$. In such a case, the cathodic current (due to the cathodic reaction) is fixed. However, if decomposition or nonstoichiometry develops, the measured current will continue to increase with the applied voltage. In such a case, the measured current density, I, versus the measured overpotential, η_m, would have little to do with the actual cathodic reaction. Fig. 20 shows a schematic illustration of the cathodic current, the current due to decomposition/nonstoichiometry, and the measured current as a function of the measured overpotential. From Eq. (78), the minimum applied voltage necessary to effect decomposition is given by

$$\varphi^{\mathrm{II}} - \varphi^{\mathrm{I}} \approx \left(\frac{\mu^{\mathrm{I}}_{O_2} - \mu^{\mathrm{decomp}}_{O_2}}{4e}\right)\left(\frac{\ell\rho_i + r'_i + r''_i}{r'_i}\right) + \left(\frac{\mu^{\mathrm{II}}_{O_2} - \mu^{\mathrm{I}}_{O_2}}{4e}\right) \tag{94}$$

Since

$$\left(\frac{\ell\rho_i + r'_i + r''_i}{r'_i}\right) > 1$$

it is clear that $\Delta\varphi = \varphi^{\mathrm{II}} - \varphi^{\mathrm{I}}$, the applied voltage necessary to cause decomposition given by Eq. (94), is lower than that given by Eq. (92). That is, if significant concentration polarization exists at the working electrode, the decomposition (or the development of nonstoichiometry) will occur at a lower voltage. If, however, $r'_i \gg r''_i$ and $r'_i \gg \ell\rho_i$, then Eq. (94) reduces to Eq. (93). Several cases can be examined corresponding to various relative values of transport parameters, and the details will albeit vary. However, the important conclusion is the same, namely that in the three-electrode system under an applied DC voltage, current due either to the development of nonstoichiometry in the electrolyte or due to electrolyte decomposition can occur, in addition to the current due to the cathodic reaction. The intended purpose of the three-electrode system is to investigate electrode kinetics, i.e., to investigate relationship between cathodic overpotential and the current due to the cathodic reaction, namely $\frac{1}{2}O_2 + 2e' \to O^{2-}$. The net measured current, however, will most likely include two contributions: current due to the cathodic reaction and current due to the occurrence of decomposition/nonstoichiometry. It is possible that under certain conditions the current due to decomposition/nonstoichiometry may completely overwhelm the cathodic current. In such cases, the three-electrode system will result in significant overestimation of cathodic electrocatalytic activity, and may not be a reliable technique, especially at high, applied voltages, and when the material readily develops nonstoichiometry—such as ceria. It can be shown experimentally that current due to nonstoichiometry/electrolyte decomposition can be several times that due to the cathodic reaction under relatively modest applied voltages [22].

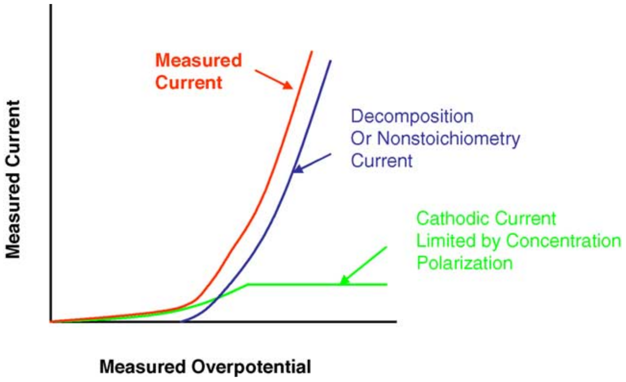

Fig. 20. A schematic illustration of the measured current (—) vs. the measured overpotential using the three-electrode system with significant concentration polarization present. The measured current consists of two contributions: (a) the cathodic current (—), namely, $\frac{1}{2}O_2 + 2e' \to O^{2-}$, which becomes concentration polarization limited beyond some applied voltage. (b) The decomposition of nonstoichiometry current (—), which begins beyond some applied voltage. The schematic shows both current and overpotential plotted on linear scales. If the current is plotted on a logarithmic scale, the curves will be convex up.

3. Discussion

The main objective of this manuscript was to develop transport equations through mixed oxygen ion and electronic conducting membranes, and through predominantly oxygen ion conducting membranes, by incorporating transport across interfaces. The analysis assumes the usual criteria of local equilibrium and electroneutrality. As emphasized, the assumption of local equilibrium implies that electronic current cannot be assumed to be identically zero,[22] even in a predominantly oxygen ion conductor, such as zirconia. This has important implications concerning the chemical potential of oxygen in the membrane, and thus the very stability of the membrane. It is well known that many factors dictate transport through membranes and across interfaces, and the assumption of transport parameters as constants (independent of oxygen partial pressure) is an oversimplification. At the same time, however, such a simplification is deemed necessary in order to elucidate the fundamental phenomena in a simple analytical framework, which is not possible if one incorporates the dependence of transport parameters on defect chemistry and on local p_{O_2}.[23] If the exact dependencies of transport parameters on p_{O_2} (or μ_{O_2}) are known for a given material and interfacial regions, which is rarely the case, numerical solutions to transport equations can be readily developed. Such an approach was not chosen here, as the purpose was to focus on fundamental aspects of transport, with emphasis on interfaces, and not on any specific material with any particular defect structure. In this framework, three cases were examined: (1) MIEC oxygen separation, (2) fuel cells, and (3) voltage-driven oxygen separation.

For the case of MIEC oxygen separation, it was shown that the μ_{O_2} always varies through the membrane monotonically between the two end values (corresponding to the two atmospheres), regardless of the nature and the details of interfacial processes. This has important implications concerning the thermodynamic stability of the membrane. The analysis shows that to ensure membrane stability, it is necessary that $\mu''_{O_2} > \mu_{O_2}^{\text{decomp}}$, a condition which could be achieved even if $\mu_{O_2}^{\text{II}} < \mu_{O_2}^{\text{decomp}}$. Thus, the implication is that if a membrane is used for the production of syngas, for example, it is necessary to ensure that $\mu''_{O_2} > \mu_{O_2}^{\text{decomp}}$. That is, the transport properties, especially across interfaces, must be so adjusted to ensure that $\mu''_{O_2} > \mu_{O_2}^{\text{decomp}}$. The exact variation of μ_{O_2} through the membrane depends upon the various transport parameters, including those of interfaces. This implies that one may need to deposit a thin (a few nanometers) layer of some material of appropriate transport properties on the permeate side to ensure stability of an otherwise unstable membrane in the imposed atmosphere. The same general conclusions apply to fuel cells. That is, depending upon electrode effects, an otherwise unstable electrolyte may exhibit stability in fuel. It is known, for example, that a fuel cell made with phase-stabilized cubic or rhombohedral Bi_2O_3 readily decomposes to metallic bismuth in hydrogen as fuel. However, it has been observed that the same fuel cell remains stable when operated in lightly humidified (∼3% H_2O) methane, even when the μ_{O_2} in the fuel is lower than $\mu_{O_2}^{\text{decomp}}$ [23]. This suggests that electrode characteristics must be such that with methane as a fuel, μ''_{O_2} must be greater than $\mu_{O_2}^{\text{decomp}}$, that is $\mu''_{O_2} > \mu_{O_2}^{\text{decomp}}$, even when $\mu_{O_2}^{\text{II}} < \mu_{O_2}^{\text{decomp}}$. A possible approach to preventing decomposition of bismuth oxide based electrolyte is the deposition of a more stable material such as YSZ or rare earth oxide-doped ceria, such as samaria-doped ceria (SDC), on the side exposed to fuel. By suitably tailoring the properties and thicknesses of the two regions, analysis based on bulk transport suggests that it may be possible to prevent electrolyte decomposition by ensuring that the μ_{O_2} in bismuth oxide never goes below the corresponding $\mu_{O_2}^{\text{decomp}}$ [14]. However, the required thickness of YSZ or SDC to prevent decomposition is often comparable to or may even be much greater than that of bismuth oxide, which defeats the very purpose of using a high conductivity bismuth oxide based electrolyte [14,24]. The present work suggests that a more profitable approach may involve modification of the anode/electrolyte interface. This, for example, could be the case III from Fig. 7, where $r''_e \gg r_e, r'_e$. Thus, the present work suggests a possible approach for using Bi_2O_3-based electrolytes by suitably modifying the anode/electrolyte interface.

For fuel cells, equations for electrode overpotentials in terms of ionic and electronic current densities, and interfacial transport parameters were developed. The usual definition of overpotential is as a measure of the loss of useful voltage in irreversible processes. From the standpoint of thermodynamics, however, the overpotential loss should strictly be described in terms of the rate of loss of potential work (which can be derived as decrease in free energy) into heat. The usual approach is to describe the overpotential as a measurable voltage loss, as a function of current (measured in the external circuit). The inclusion of internal electronic leakage, when the overpotential loss is given as a measure of the potential work degraded as heat, leads to the conclusion that at OCV, the overpotential, defined as the rate of loss of potential work at an electrode divided by the measured current, is actually infinite. This is because even when no current is flowing in the external circuit, part of the potential work is continually being degraded as heat due to internal electronic leakage. As stated earlier, the electronic current can never be zero when potential gradients exist, with the result that at OCV, the as-defined overpotential is singular—or infinite. Also, the overpotential as-defined may not be measurable. At the same time, however, the relevant physical parameter is the product of the as-defined overpotential and current, which is always finite, and is a measure of the rate of degradation of potential work into heat (an irreversible process). In a typical practical

---

[22] Unless shorted externally.

[23] There are many published reports, which have incorporated the defect chemistry details into the analysis. However, this necessitated making simplifying assumptions regarding the thermodynamics of defects. Also, in so doing, the important features of electron transport across interfaces were generally overlooked. This not only leads to incomplete description of transport, but also does not permit the estimation of μ_{O_2} inside the membrane, unless further simplifying assumptions are made about μ_{O_2} variation across interfaces. For example, Eq. (31) can explicitly give $\mu_{O_2}(x)$ when it is assumed that $\mu'_{O_2} = \mu_{O_2}^{\text{I}}$ and $\mu'_{O_2} = \mu_{O_2}^{\text{II}}$, an assumption which is rarely justified.

case wherein the electronic leakage is usually negligible, and a finite current flows through the external circuit (such that $|I_L| \approx |I_i| \gg |I_e|$), the overpotential defined here is essentially the same as the usual one, and measured experimentally.

In both MIEC oxygen separation membranes and fuel cells, the μ_{O_2} and φ are interrelated. In voltage-driven oxygen separation systems, however, both μ_{O_2} and φ can be independently varied, which implies an additional (experimental) degree of freedom. In such a case, the μ_{O_2} in the membrane can lie outside of the end values. That is, $\mu_{O_2}^{\text{membrane}}$, can be greater or lower than $\mu_{O_2}^{\text{I}}$ and/or $\mu_{O_2}^{\text{II}}$. Transport parameters of the membrane and across interfaces, and the applied voltage determine the actual variation of μ_{O_2} in the membrane. Figs. 12–15 show the various possibilities. An important point to note is that by virtue of the fact that $\mu_{O_2}^{\text{membrane}}$ can lie outside of the end values implies that it is possible for $\mu_{O_2}^{\text{membrane}}$ to be lower than $\mu_{O_2}^{\text{decomp}}$. Under such conditions, localized membrane decomposition or nonstoichiometry can occur. This has important implications concerning the use of the so-called three-electrode system under an applied DC voltage for the measurement of electrode polarization behavior. The analysis shows that in the three-electrode system, a significant contribution to the net measured current can occur from membrane decomposition (or the development of nonstoichiometry), leading to an inadvertent overestimation of electrode electrocatalytic activity. The present work thus shows that caution should be exercised in using the three-electrode system under an applied DC bias for the investigation of electrocatalytic activity of an electrode. It is also possible that the μ_{O_2} in the membrane may be much greater than both $\mu_{O_2}^{\text{I}}$ and $\mu_{O_2}^{\text{II}}$ under an applied DC voltage. In such a case, cracking of the membrane can occur under an applied DC voltage, as has been previously shown theoretically and experimentally [15,16].

All transport equations are given under the simplifying assumption that transport properties are independent of μ_{O_2}, which allows one to obtain simple analytical equations. At the same time, the fact that the chemical potential of oxygen is a function of position, $\mu_{O_2}(x)$, implies that small changes in composition are presumed to occur until steady state is established. The net integrated oxygen flux arriving or leaving an elemental region dx is directly related to the interrelationship between composition (stoichiometry) and μ_{O_2}. If for a given change in μ_{O_2}, namely $\Delta\mu_{O_2}$, the change in composition is small (narrow stoichiometry range), this means the capacity of the internal EMF will also be small. If chemical capacitors are used to describe the equivalent circuit, then it will imply that the magnitude of the chemical capacitance is small. This may likely be the case with zirconia. Alternatively, if for a given change in μ_{O_2}, namely $\Delta\mu_{O_2}$, the change in composition is large (wide stoichiometry range), this means the capacity of the internal EMF will also be large. If chemical capacitors are used, then it will imply that the magnitude of the chemical capacitance is large. This may likely be the case with ceria. Regardless of whether internal EMF or chemical capacitors are used, it is clear that a complete description of transport will require relationship between composition (stoichiometry) and μ_{O_2}, which will most likely have to be determined experimentally. Unfortunately, this is rarely known for any material with any degree of certainty.

4. Summary

In the present manuscript equations were developed to describe transport of oxygen ions and electrons through membranes by explicitly taking into account interface properties. The fundamental assumptions made are the same as in virtually all of the earlier studies, namely, the existence of electroneutrality and local equilibrium. The assumption of local equilibrium is shown to imply that electronic current cannot be entirely neglected, however small, to ensure that local chemical potential of oxygen, μ_{O_2}, is uniquely defined. That is, even in a predominantly oxygen ion conductor, electronic transport must be taken into account. Transport of oxygen ions and electrons through the membrane as well as across electrode/membrane interfaces was taken into account in the present work. These equations were then applied to fuel cells, MIEC oxygen separation membranes under an applied pressure gradient, voltage-driven oxygen separation, and the three-electrode system which is often used for the study of electrode kinetics. It was shown that in fuel cells or MIEC oxygen separation membranes, as long as the chemical potential of oxygen on the reducing side (anode in the case of fuel cells; permeate side for MIEC oxygen separation or fuel side for the synthesis of syngas using MIEC membranes) is greater than the chemical potential of oxygen corresponding to membrane thermodynamic stability, membrane decomposition should not occur. Membrane may continue to be stable even if the chemical potential of oxygen in the anode gas (fuel cells) or permeate side (MIEC membranes) is lower than the decomposition chemical potential, provided the interface transport properties are suitably tailored such that the chemical potential of oxygen just inside the interface is greater than the decomposition chemical potential, that is $\mu_{O_2}'' > \mu_{O_2}^{\text{decomp}}$. However, in the case of oxygen separation under the action of an applied voltage, depending upon the magnitude of the applied voltage and the relative transport parameters of the membrane and interfacial regions, the chemical potential of oxygen in the membrane inside the interfaces can go below the decomposition chemical potential. In such a case, membrane decomposition can occur, or a nonstoichiometry may develop. This has significant implications concerning the use of the so-called three-electrode system for the study of electrode kinetics, for example for the study of a prospective cathode for SOFC. The significance is that measurements made using the three-electrode system under high applied voltages may yield erroneous conclusions concerning cathode activity, since the net current generated will consist of two terms: (a) that due to the actual cathodic reaction, namely $\frac{1}{2}O_2 + 2e' \rightarrow O^{2-}$, and (b) that due to the occurrence of decomposition and/or the development of nonstoichiometry (oxygen deficiency). In a typical experiment, the measured current is invariably attributed to the cathodic reaction, thereby overestimating the cathodic activity of the prospective cathode, since the experimenter has no way of separating the two. In many cases, the current due to nonstoichiometry/decomposition may be much larger than the cathodic current, leading to large errors in the estimation of cathodic activity. The analysis also shows that the decomposition (or the development of oxygen deficiency) may occur just under the positive electrode or just under the negative electrode, depending upon the relative magnitudes of ionic and electronic transport parameters of the bulk and the interfaces. In practice, however, the occurrence of decomposition (or the development of oxygen deficiency) under the positive electrode is deemed unlikely. This is because in such a case, the electrons required for the neutralization of the cation (Zr^{4+} to Zr) transport through the membrane, which may be kinetically hindered if the electronic conductivity is low. Decomposition (or the development of oxygen deficiency) under the positive electrode, however, is likely in the case of ceria-based membranes under appropriate conditions since electronic conductivity of ceria is typically much higher, especially at low p_{O_2}.

All transport equations are given in a general form, without invoking any particular defect structure. The rationale is that fundamental stability issues are not dependent on the types and nature of defects. All transport equations are given assuming transport parameters to be independent of μ_{O_2}. Because of this assumption, the spatial variations of μ_{O_2}, φ, and $\tilde{\mu}_{O^{2-}}$ through the membrane are shown to be linear. This assumption also allows the use of simple equivalent circuits. Bulk regions were modeled using a combination of ionic and electronic area specific resistances for the bulk and an internal EMF source. Interfacial regions were also modeled using internal EMF sources, instead of capacitors, in combination with ionic and electronic area specific resistances. This is entirely consistent with the definition of Nernst voltage in terms of the net $\Delta\mu_{O_2}$ across an interface. As such, its modeling as an EMF source is equally appropriate, and in fact, is more consistent with the general thermodynamic framework. Usually the transport parameters are μ_{O_2}-dependent. In such cases, the variation of μ_{O_2}, φ, and $\tilde{\mu}_{O^{2-}}$ will not be spatially linear. If the dependencies for a given material and interfacial regions are precisely known, which is rarely the case, the spatial variations of μ_{O_2}, φ, and $\tilde{\mu}_{O^{2-}}$ can be easily evaluated numerically—if not analytically. Such an approach was not selected here. The simplification made may only alter the details, but not the broader, general conclusions.

Acknowledgements

This work was supported by the U.S. Department of Energy under contract no. DE-FC26-02NT41602.

References

[1] M.H. Hebb, J. Chem. Phys. 20 (1952) 185.
[2] L. Heyne, Mass Transport in Oxides, NBS Special Publication 296, 1968, pp. 149–164.
[3] C. Wagner, Prog. Solid-State Chem. 10 (1) (1975) 3–16.
[4] H. Rickert, Electrochemistry of Solids: An Introduction, Springer-Verlag, Berlin, 1982.
[5] H. Schmalzried, Chemical Kinetics of Solids, VCH Publication, Weinheim, 1995.
[6] N.S. Choudhury, J.W. Patterson, J. Electrochem. Soc. 118 (9) (1971) 1398–1403.
[7] D.S. Tannhauser, J. Electrochem. Soc. 125 (8) (1978) 1277–1282.
[8] I. Riess, J. Electrochem. Soc. 128 (10) (1981) 2077–2081.
[9] S. Yuan, U.B. Pal, J. Electrochem. Soc. 143 (10) (1996) 3214–3222.
[10] H. Nafe, J. Electrochem. Soc. 144 (11) (1997) 3922–3929.
[11] R. Singh, K.T. Jacob, J. Appl. Electrochem. 33 (2003) 571–576.
[12] D. Kondepudi, I. Prigogine, Modern Thermodynamics, Wiley, New York, 1998.
[13] R.D. Armstrong, M. Todd, in: P.G. Bruce (Ed.), Solid State Chemistry, Cambridge University Press, Cambridge, UK, 1995.
[14] A.V. Virkar, J. Electrochem. Soc. 138 (5) (1991) 1481–1487.
[15] A.V. Virkar, J. Mater. Sci. 20 (1985) 552–562.
[16] A.V. Virkar, J. Nachlas, A.V. Joshi, J. Diamond, J. Am. Ceram. Soc. 73 (11) (1990) 3382–3390.
[17] P. Kofstad, High-temperature Oxidation of Metals, Wiley, New York, 1966.
[18] J.R. Macdonald, Impedance Spectroscopy, A Wiley-Interscience Publication, Wiley, New York, 1987.
[19] M. Liu, H. Hu, J. Electrochem. Soc. 143 (6) (1996) L109.
[20] V.V. Kharton, F.M.B. Marques, Solid State Ion. 140 (2001) 381–394.
[21] H. Matsumoto, S. Hamajima, T. Yajima, H. Iwahara, J. Electrochem. Soc. 148 (10) (2001) D121–D124.
[22] A.V. Virkar, Y. Jiang, Submitted to Proceedings of the SOFC-IX, Electrochemical Society, 2005.
[23] W. Lawless, Private communication, 2003.
[24] J.-Y. Park, E.D. Wachsman, in: S.C. Singhal, M. Dokiya (Eds.), Proceedings of the Eighth International Symposium SOFC VIII, Electrochemical Society, Pennington, NJ, 2003, pp. 289–298.

Journal of The Electrochemical Society, **152** (5) A927-A936 (2005)
0013-4651/2005/152(5)/A927/10/$7.00 © The Electrochemical Society, Inc.

Estimation of Charge-Transfer Resistivity of Pt Cathode on YSZ Electrolyte Using Patterned Electrodes

Rajesh Radhakrishnan,[a] Anil V. Virkar,[a,*,z] and S. C. Singhal[b,]**

[a]*Department of Materials Science and Engineering, University of Utah, Salt Lake City, Utah 84112, USA*
[b]*Pacific Northwest National Laboratory, Richland, Washington 99352, USA*

Yttria-stabilized zirconia (YSZ) electrolyte disks with patterned platinum (Pt) electrodes having different three phase boundary (TPB) lengths (l_{TPB}), but the same electrode-electrolyte interface area, were deposited on one of the two faces using photomicrolithography. Platinum counter electrode was applied on the other face, and a platinum wire reference electrode was positioned along the cylindrical surface. Impedance spectra under zero applied bias were obtained in oxygen partial pressures, (p_{O_2}), ranging between 10^{-3} and 1 atm and over a range of temperatures between 650 and 800°C. Area-specific charge-transfer resistance, R_{ct}, was found to vary inversely with l_{TPB}. The value of charge-transfer resistivity, ρ_{ct}, corresponding to the charge-transfer reaction occurring at TPB, was estimated at various temperatures and p_{O_2}. The R_{ct} and ρ_{ct} decrease with increasing p_{O_2} and with increasing temperature. The activation energy for the overall charge-transfer reaction was found to vary between 0.75 eV at a p_{O_2} of 0.001 atm and 1.63 eV for a p_{O_2} of 1 atm.

Manuscript received December 5, 2004. Available electronically March 30, 2005.

Platinum is one of the most investigated catalysts for electrochemical reduction of oxygen.[1,2] The reaction of oxygen reduction occurring at the cathode of a solid oxide fuel cell (SOFC) can be given by

$$\mathrm{O_2(g) + 4e' = 2\ O^{-2}} \qquad [1]$$

Many studies have been conducted on the investigation of the cathode reaction mechanism and to assess the performance of electrodes.[3,4] The reaction given in Eq. 1 consists of many sub-steps, the details of which are not well understood. It is generally assumed that the reaction steps include adsorption of oxygen, dissociation of molecular species into atomic species, migration of molecular or atomic species on the surface of the electrode or electrolyte, the occurrence of electron-transfer reaction, and the transfer of ions into the solid electrolyte.[3] Cathodic activation polarization is the total voltage loss occurring in all of the above-mentioned steps. It is important to reduce the cathodic activation polarization to as low a value as possible to increase the efficiency of the SOFC and also to lower the operating temperature.

The reduction of oxygen molecules to oxygen ions and their transfer into the electrolyte can occur via two different pathways depending on the ionic and electronic transport properties of the cathode material.[4] First is a three phase boundary (TPB) path, which includes oxygen gas diffusion, adsorption of oxygen on the electrode surface, diffusion of (possibly dissociated) oxygen species along the surface toward the TPB where the electrolyte, electrode, and gas phase meet, followed by ionization (electron transfer) and ionic transfer into electrolyte. The second path involves the two phase boundary (2PB) between the cathode material and the gas phase and consists of oxygen gas diffusion, adsorption on the cathode surface, dissociation, electron transfer on the surface of the cathode, oxygen ionization, incorporation into the cathode at the 2PB between the cathode and the gas phase, oxygen ion transport through the cathode, and the transfer of ions into the electrolyte.

It is generally assumed that with a predominantly electronic-conducting cathode (such as platinum) and predominantly oxygen-ion-conducting electrolyte [such as Yttria-stabilized zirconia (YSZ)], the electrochemical reaction of oxygen reduction and ion transfer given by Eq. 1 occurs at the TPB between the cathode, the electrolyte, and the gas phase (the first path). The corresponding geometric parameter, which governs the overall reaction kinetics, is the length of the TPB per unit area of the cathode-electrolyte macroscopic interface, given by l_{TPB} in units of cm^{-1}.

Several studies have been reported wherein attempts were made to elucidate the exact relation between the length of TPB and the charge-transfer resistance.[5-8] In real electrodes which may consist of porous composite mixtures of lanthanum strontium manganese oxide (LSM) and YSZ, or other materials for example, the length of TPB cannot be directly determined, albeit it can be estimated using techniques in quantitative stereology. This, in fact, has been done in a limited number of studies.[9-11] From an experimental standpoint, however, a direct approach would be to deposit the electrode material, *e.g.*, LSM, in a specific geometric pattern over an electrolyte disk, *e.g.*, YSZ, and measure the polarization resistance using techniques such as impedance spectroscopy. Such an approach has been recently used to study the overall charge-transfer reaction at both the anode and the cathode. For example, Mizusakai *et al.* and Bieberle *et al.* have investigated the reaction mechanism at nickel (Ni) anode-YSZ electrolyte–gas phase TPB.[12,13] Similarly, Horita *et al.* used electrolyte disks with patterned LSM electrodes, conducting secondary ion mass spectroscopy (SIMS) analysis of oxygen isotope diffusion under the influence of an externally applied voltage to image the charge-transfer regions, and concluded that the most active site for the charge-transfer reaction is the TPB region.[14,15] Brichzin *et al.*, who used circular microelectrodes of LSM of different areas to study the dependence of cathodic polarization on the geometry, observed that the polarization resistance varies with the inverse of the square of the microelectrode diameter under zero applied bias and concluded that the oxygen reduction reaction occurs at the surface of LSM.[16] Investigation by the authors of this paper[17] shows a linear relation between $1/R_{\mathrm{ct}}$ and l_{TPB} for patterned LSM electrodes on YSZ, consistent with the occurrence of charge transfer predominantly at TPB, in agreement with the results of Horita *et al.*[14,15] It appeared that while the charge-transfer resistance is inversely proportional to l_{TPB}, consistent with the charge-transfer reaction occurring mainly at the TPB, at 800°C some transport also occurs through LSM.[17] However, it was found that even though oxygen reduction reaction at the surface of LSM and subsequent transport of oxygen ions through LSM is possible at 800°C, its contribution to the overall charge-transfer reaction is much lower compared to that occurring at a TPB.

The objective of the present work was to investigate the cathode reaction mechanism at a platinum electrode using patterned electrodes. Many studies have been reported on the oxygen reduction kinetics at platinum electrodes, but there appear to be no reported studies using platinum electrodes of well-defined geometry as used in this study.[18-25] In addition, there is no unanimity on the exact details of the cathodic reaction process, though it is generally believed that the reaction steps include adsorption of oxygen, dissociation of molecular species into atomic species, migration of mo-

[*] Electrochemical Society Active Member.
[**] Electrochemical Society Fellow.
[z] E-mail: anil.virkar@m.cc.utah.edu

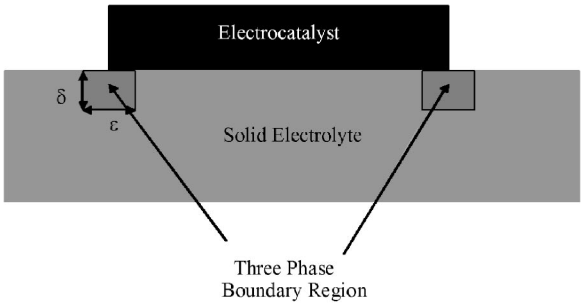

Figure 1. Model for charge transfer at a TPB. In this figure the dimensions are not to scale. While the electrode thickness, width, and electrolyte dimension are on the order of micrometers, the region through which the actual charge transfer occurs (ε and δ) are on the order of angstroms.

lecular or atomic species to the TPB region, the occurrence of electron-transfer reaction, and the transfer of ions across the TPB region into the solid electrolyte. Often for simplicity it is assumed that one of these is the rate-limiting step with the rest of the steps being close to equilibrium, although this is often an oversimplification. Several rate-limiting steps in the charge-transfer mechanism have been reported and the variation of the polarization resistance on p_{O_2} has been reported to follow either $p_{O_2}^{-1/2}$ or $p_{O_2}^{-1}$ dependence.[18-27] The reported literature thus shows that while the p_{O_2} dependence of the charge-transfer resistance is reasonable, the details of the overall reaction mechanisms are not well understood.

The present work was undertaken to investigate charge-transfer characteristics at the Pt/YSZ/gas-phase TPB using patterned electrodes and compare the results with those obtained on the LSM/YSZ/gas-phase system.[17] Patterned platinum electrodes of well-defined TPBs were sputter-deposited on sintered YSZ disks and impedance spectroscopy under zero applied bias was used to obtain the polarization resistance over a range of temperatures between 650 and 800°C and a p_{O_2} range between 10^{-3} and 1 atm.

Theory

Dependence of R_{ct} on the TPB length (l_{TPB}).—In solid-state electrochemical devices, the charge-transfer reaction given by Eq. 1 occurs at the TPB between the electrocatalyst (electrode), the electrolyte, and the gas phase, provided the electrocatalyst is a predominantly electronic conductor. This is illustrated in Fig. 1. The relevant geometric parameter is the TPB line length, l_{TPB}, given in units of length per unit area of the electrode/electrolyte macroscopic interface. The TPB line where charge transfer occurs may be thought of as having a thickness, δ, and width, ε. In terms of the charge-transfer resistivity, ρ'_{ct}, width, ε, and thickness, δ, through which charge transfer occurs, and the TPB line length, l_{TPB}, the area-specific charge-transfer resistance corresponding to the overall charge-transfer reaction occurring at a TPB, R_{ct}^{TPB}, in units of Ω cm^2 is given by[28]

$$R_{ct}^{TPB} = \frac{\rho'_{ct}\delta}{\varepsilon l_{TPB}} \qquad [2]$$

The parameters δ and ε are expected to be on the order of a few angstroms, typical dimensions over which the actual charge transfer is expected to occur. The parameters ρ'_{ct}, δ, and ε are not amenable to independent measurements. Thus one can define an intrinsic charge-transfer resistivity, ρ_{ct}, by

$$\rho_{ct} = \frac{\rho'_{ct}\delta}{\varepsilon} \qquad [3]$$

and therefore the area-specific charge-transfer resistance is given by

$$R_{ct}^{TPB} = \frac{\rho_{ct}}{l_{TPB}} \qquad [4]$$

where, in principle, R_{ct}^{TPB} and l_{TPB} can be separately measured, thus facilitating the estimation of ρ_{ct}. Note that the R_{ct}^{TPB}, as-defined, may include the adsorption process, dissociation of molecular species into atomic species, migration of molecular or atomic species to the TPB region, the occurrence of electron-transfer reaction, and the transfer of ions across the TPB region. Hence, ρ_{ct} depends upon a number of parameters such as the oxygen partial pressure, temperature, electronic and ionic conductivities of the electrode and electrolyte, etc. However, it is microstructure-independent, and thus is a fundamental parameter that can be used to compare two electrode materials. For a given set of conditions of temperature and atmosphere, if the electrochemical reaction occurs at a TPB, it is expected that the dependence of R_{ct}^{TPB} on l_{TPB} is given by Eq. 4.

For the electrodes investigated in this study, the TPB length is attributed to three factors: (i) the TPB length of the particular geometric pattern prepared by photomicrolithography (l_{TPBp}), assuming smooth line edges; (ii) additional TPB length due to the possible waviness (α) of the edge at a microscopic level;[c] and (iii) the TPB that can occur in the electrode film due either to the inherent porosity of the substrate (electrolyte) and/or due to the defects, such as pits, that may occur during the preparation of the sputtered film and/or during heat-treatments (l_{TPB0}). Hence

$$l_{TPB} = l_{TPBp}(1 + \alpha) + l_{TPB0} \qquad [5]$$

The l_{TPBp} was varied over a wide range to study the effect of TPB length on area-specific charge-transfer resistance. The l_{TPB0} is expected to be more or less the same in all samples, because the electrode-electrolyte interface area was the same in all samples, and all samples were subjected to the same thermal treatments. The l_{TPB0} can be estimated using quantitative stereology.[29] When the electrode shows wavy edges at a microscopic level, α can be measured from high-magnification SEM images. Knowing l_{TPBp}, l_{TPB0}, and α, the l_{TPB} can be determined. Finally, if the solubility and diffusion of atomic oxygen in platinum is not negligible, some transport may well occur through the film. That is, platinum may exhibit some mixed ionic electronic conducting properties.[d] In such a case, the net area-specific charge-transfer resistance is given by R_{ct}, where

$$\frac{1}{R_{ct}} = \frac{1}{R_{ct}^{TPB}} + \frac{1}{R_{ct}^{MIEC}} = \frac{l_{TPB}}{\rho_{ct}} + \frac{A_A}{R_{ct}^{MIEC(A)}} \qquad [6]$$

in which R_{ct}^{MIEC} is the charge-transfer resistance associated with the permeation of atomic oxygen through platinum and ion transfer into the electrolyte, $R_{ct}^{MIEC(A)}$, is the area-specific charge-transfer resistance associated with the through transport of oxygen which scales with the area of the platinum electrode and A_A is the area fraction of the platinum electrode (microscopic electrode-electrolyte contact area). $R_{ct}^{MIEC(A)}$ is expected to be a function of the thickness of the platinum film. When the electrode is dense and if it can be assumed that $R_{ct}^{MIEC(A)}$ is rather large, negligible charge transfer is expected to occur through the bulk of the electrode. With this assumption, the total charge-transfer resistance R_{ct} is given by

$$R_{ct} = R_{ct}^{TPB} = \frac{\rho_{ct}}{l_{TPB}} \qquad [7]$$

The overall cathodic reaction.—The overall charge-transfer reaction is given by Eq. 1. In terms of oxygen vacancies as the predominant point defects in the electrolyte, $V_O^{\bullet\bullet}$, the reaction may be given by

---

[c] The waviness should also be there at the atomic level (or nanolevel). This waviness is assumed to be included in the ρ'_{ct} itself.

[d] Effectively, transport of atomic oxygen through platinum.

$$\frac{1}{2}\,O_2 + V_O^{\bullet\bullet} + 2e' \rightarrow O_O^{\times} \qquad [8]$$

where Kroger-Vink notation has been used. The overall reaction may consist of the following subreactions: Molecular adsorption

$$\frac{1}{2}\,O_2(g) \rightarrow \frac{1}{2}\,O_2(ads) \qquad [9]$$

Dissociation

$$\frac{1}{2}\,O_2(ads) \rightarrow O(ads) \qquad [10]$$

Charge transfer

$$O(ads) + V_O^{\bullet\bullet} + 2e' \rightarrow O_O^{\times} \qquad [11]$$

An alternative possibility includes charge transfer with the adsorbed species being molecular oxygen, namely

$$\frac{1}{2}\,O_2(ads) + V_O^{\bullet\bullet} + 2e' \rightarrow O_O^{\times} \qquad [12]$$

It is possible that none of the steps may be at equilibrium. In such a case, it is necessary to include the kinetics of each subreaction in the overall reaction scheme. For simplicity, we assume that the kinetics of adsorption is fast, and thus the adsorption reaction is at equilibrium. The overall charge-transfer kinetics is thus assumed to be dictated by the charge-transfer reaction.

Dependence of R_{ct} and ρ_{ct} on oxygen partial pressure (p_{O_2}).—The oxygen vacancy concentration in a typical electrolyte (*e.g.*, YSZ) is expected to be related to the dopant concentration and thus be constant over a wide range in p_{O_2} (and also temperature). The electron concentration in the electrocatalyst (platinum) is also expected to be independent of p_{O_2}. Thus, the possible p_{O_2} dependence of the charge-transfer reaction must be through the dependence of the surface oxygen coverage on p_{O_2}. The partial pressure dependence of the intrinsic charge-transfer resistivity at a TPB may then be given as

$$\rho_{ct} = \frac{\rho''_{ct}}{\theta} \qquad [13]$$

where θ is the surface coverage of oxygen[e] and ρ''_{ct} is the charge-transfer resistivity at $\theta = 1$. Substituting Eq. 13 into 7, R_{ct}^{TPB} may be given by

$$R_{ct} = R_{ct}^{TPB} = \frac{\rho''_{ct}}{\theta l_{TPB}} \qquad [14]$$

Because oxygen can adsorb as either molecular (associative) or atomic (dissociative) oxygen, it is important to consider both associative and dissociative adsorption. According to the Langmuir adsorption model, surface coverage for associative absorption, θ_{O_2}, is given by[30]

$$\theta_{O_2} = \frac{b' p_{O_2}}{1 + b' p_{O_2} + b'' p_{N_2}} \qquad [15]$$

where both oxygen and nitrogen are assumed to adsorb as molecular species, and b' and b'' are adsorption coefficients of molecular oxygen and nitrogen, respectively. Substituting Eq. 15 into 14 gives

$$R_{ct} = R_{ct}^{TPB} = \frac{\rho''_{ct}(1 + b' p_{O_2} + b'' p_{N_2})}{l_{TPB} b' p_{O_2}} \qquad [16]$$

The partial pressure of oxygen was varied in this study by using mixtures of oxygen and nitrogen, while keeping the total pressure at 1 atm., *i.e.*

$$p_{O_2} + p_{N_2} = 1 \qquad [17]$$

Thus, Eq. 16 can be written as

$$R_{ct} = R_{ct}^{TPB} = \frac{\rho''_{ct}\{(1 + b'') + (b' - b'')p_{O_2}\}}{l_{TPB} b' p_{O_2}} \qquad [18]$$

A plot of $1/R_{ct}$ *vs.* l_{TPB} should thus be a straight line passing through the origin with slope equal to $1/\rho_{ct}$, where ρ_{ct} is given by

$$\rho_{ct} = \frac{\rho''_{ct}(1 + b'')}{b' p_{O_2}} + \frac{\rho''_{ct}(b' - b'')}{b'} \qquad [19]$$

Note that a plot of ρ_{ct} *vs.* $1/p_{O_2}$ should be linear with slope $=\rho''_{ct}(1 + b'')/b'$ and intercept $=\rho''_{ct}(b' - b'')/b'$. Multiplying both sides of Eq. 19 by p_{O_2} gives

$$\rho_{ct} p_{O_2} = \frac{\rho''_{ct}(1 + b'')}{b'} + \frac{\rho''_{ct}(b' - b'')p_{O_2}}{b'} \qquad [20]$$

Thus, a plot of $\rho_{ct} p_{O_2}$ *vs.* p_{O_2} should be linear with slope $=\rho''_{ct}(b' - b'')/b'$ and intercept $=\rho''_{ct}(1 + b'')/b'$.

If the adsorption of nitrogen is negligible, then $b'' = 0$, and Eq. 19 becomes

$$\rho_{ct} = \frac{\rho''_{ct}}{b' p_{O_2}} + \rho''_{ct} \qquad [21]$$

and Eq. 20 becomes

$$\rho_{ct} p_{O_2} = \frac{\rho''_{ct}}{b'} + \rho''_{ct} p_{O_2} \qquad [22]$$

Thus, a plot of ρ_{ct} *vs.* $1/p_{O_2}$ should be linear with slope $=\rho''_{ct}/b'$ and intercept $=\rho''_{ct}$ and that of $\rho_{ct} p_{O_2}$ *vs.* p_{O_2} should be linear with slope $=\rho''_{ct}$ and intercept $=\rho''_{ct}/b'$. That is, ρ''_{ct} and b' can be estimated from either of these plots provided adsorption of nitrogen is negligible, and both should give the same values, if the p_{O_2} dependence of ρ_{ct} obeys the associative adsorption model.

If oxygen adsorbs as atomic oxygen, the surface coverage, θ_O is given by

$$\theta_O = \frac{b^* \sqrt{p_{O_2}}}{1 + b^* \sqrt{p_{O_2}} + b^{**} \sqrt{p_{N_2}}} \qquad [23]$$

where both oxygen and nitrogen adsorption are assumed to occur as atomic species, and b^* and b^{**} are the respective adsorption coefficients. Substituting Eq. 23 into 14 gives

$$R_{ct} = R_{ct}^{TPB} = \frac{\rho''_{ct}(1 + b^* \sqrt{p_{O_2}} + b^{**} \sqrt{p_{N_2}})}{l_{TPB} b^* \sqrt{p_{O_2}}} \qquad [24]$$

A further simplification of this equation can be obtained if the adsorption of nitrogen can be neglected, consistent with $b^{**} = 0$. Thus, setting $b^{**} = 0$ gives

$$R_{ct} = R_{ct}^{TPB} = \frac{\rho''_{ct}(1 + b^* \sqrt{p_{O_2}})}{l_{TPB} b^* \sqrt{p_{O_2}}} \qquad [25]$$

Again, 1/slope of the plot of $1/R_{ct}$ *vs.* l_{TPB} is the charge-transfer resistivity, ρ_{ct}, given by

$$\rho_{ct} = \frac{\rho''_{ct}}{b^* \sqrt{p_{O_2}}} + \rho''_{ct} \qquad [26]$$

A plot of ρ_{ct} *vs.* $1/\sqrt{p_{O_2}}$ should be linear with slope $=\rho''_{ct}/b^*$ and intercept $=\rho''_{ct}$. Multiplying both sides of Eq. 26 by $\sqrt{p_{O_2}}$ gives

$$\rho_{ct} \sqrt{p_{O_2}} = \frac{\rho''_{ct}}{b^*} + \rho''_{ct} \sqrt{p_{O_2}} \qquad [27]$$

---

[e] Which is strictly line coverage assuming charge transfer occurs at TPB.

A plot of $\rho_{ct}\sqrt{p_{O_2}}$ *vs.* $\sqrt{p_{O_2}}$ should also be linear with slope $=\rho''_{ct}$ and intercept $=\rho''_{ct}/b^*$. The two plots should give the same values of ρ''_{ct} and b^*, if the p_{O_2} dependence of ρ_{ct} obeys the dissociative adsorption model.

Experimental

Disks of YSZ (Tosoh Corp., Japan) were fabricated using conventional ceramic processing methods involving die-pressing of powder compacts followed by sintering in air. The powder was pressed in a circular die using a uniaxial press under a load of 4,500 kg. The disks obtained were then sintered at 1500°C for 5 h in air. The disks after sintering had dimensions of approximately 24 mm diam and 3.5 mm thickness. One surface of each disk was polished to a 1 μm finish. After polishing, a groove was machined along the cylindrical surface of the disk at a distance of nearly 1.5 mm from the polished surface. The disks were then cleaned in soap solution followed by rinsing in acetone, in deionized water, and dried at 500°C for 2 h.

Patterned (line patterns with electrode-electrolyte contact area fraction $A_A = 0.5$) platinum electrodes corresponding to a wide range of l_{TPBp} were fabricated on the polished surfaces in a circular area of 1 cm diam (area 0.785 cm^2) at the center of each disk using photomicrolithography and sputtering techniques. In order to obtain the line pattern of the electrode, the disk was initially coated with positive photoresist Shipley 1818 and was baked at 100°C for 5 min. The sample was then exposed to UV light for 20 s using previously prepared dark field masks with appropriate line patterns. The exposed samples were developed using MF 321 developer for nearly 30 s, rinsed in DI water, and dried. Samples with various patterns were prepared using different masks, each having the same A_A but different l_{TPBp}. The patterned samples were then loaded into a sputtering chamber. Platinum electrodes of nearly 1 μm thickness were sputter deposited using a platinum target by dc sputtering using argon plasma. The YSZ disks were held at a distance of ~15 cm from the target and were at room temperature during sputtering. The chamber pressure was kept at a low pressure (1 mTorr) to obtain a dense thin film of platinum. After sputtering the disks were washed in acetone to lift off the photoresist and the platinum film on top of the photoresist, giving rise to the desired platinum line pattern. The disks with platinum patterned electrodes were later annealed at 900°C for 2 h. The electrode morphology was examined before and after annealing, and after electrochemical testing using an optical profilometer and a scanning electron microscope (SEM).

A counter electrode of platinum was applied using platinum resinate, again in a circular area of 1 cm diam, at the center of the opposite face of the disk so that it is symmetric with respect to the patterned platinum working electrode. The disks were again annealed at 900°C for 2 h to remove organic components from platinum resinate and to obtain a well-bonded, porous platinum counter electrode. A platinum reference electrode in the form of a ring was positioned along the groove on the cylindrical surface of the disk.

Platinum mesh was used as contact on both working and counter electrodes. The sample was then assembled between two alumina rings with the help of two honeycomb alumina disks, two threaded rods, springs, and wing nuts. Care was taken to ensure that both the working and the counter electrodes were completely exposed to the external atmosphere, while firmly holding the platinum contact mesh onto the electrodes. Electrical connections were made to the platinum meshes by connecting platinum wires to them. The sample assembly was then placed inside an alumina tube such that the disk was near the closed end of the tube, with the working electrode always facing the closed end of the tube. The tube was tightly sealed using a rubber cork. Holes were drilled in the cork through which the platinum leads for electrical connection and the rods to hold the disk were inserted. Gas inlet and outlet tubes were also inserted through the rubber cork. The inlet tube was long enough to ensure the release of gas very close to the working electrode. The alumina tube containing the disk assembly was then placed in a horizontal tube furnace such that the disk was positioned near the center of the furnace. The tip of a thermocouple was placed very near the disk to measure the temperature. The inlet tube was connected to compressed gas cylinders containing premixed gases of desired compositions. A flow rate of nearly 200 ml/min was used to continuously circulate the desired premixed gas of a given oxygen partial pressure. The system was allowed to equilibrate at each condition of temperature and oxygen partial pressure before making measurements. Impedance spectra were obtained using a Solartron impedance/gain-phase analyzer (SI-1260) in combination with a Solartron electrochemical interface (SI-1287), over a range of temperatures between 650 and 800°C, and in gas mixtures with oxygen partial pressure ranging between 10^{-3} and 1 atm.

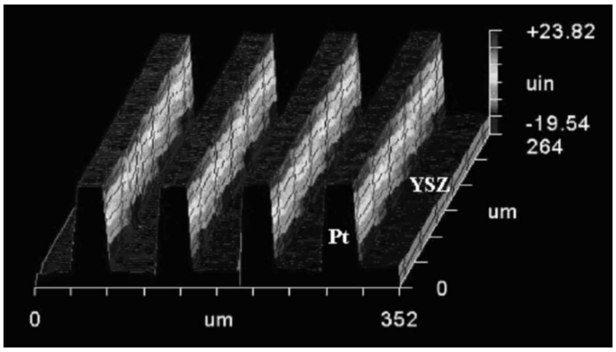

Figure 2. An optical profilometric trace of platinum-patterned electrode on YSZ with $l_{TPBp} = 250\ cm^{-1}$.

Results and Discussion

Morphology of the platinum electrode.—An optical profilometric trace of the as-sputtered platinum electrode is shown in Fig. 2 and an SEM image of the same is shown in Fig. 3a, both of which clearly show a well-defined line pattern. The l_{TPBp} of this sample was 250 cm^{-1}. The images show that the as-prepared electrode edges are smooth and continuous. This allows precise determination of the l_{TPBp}, which was varied from sample to sample by varying the width of the line and the space between the lines, while keeping the A_A constant. The l_{TPBp} for the various patterns, as-calculated from the geometry of the as-sputtered electrodes, were 500, 250, 100, and 50 cm^{-1} (corresponding to platinum line widths of 20, 40, 100, and 200 μm, respectively). An SEM image of the sample with $l_{TPBp} = 250\ cm^{-1}$ after testing is shown in Fig. 3b. After annealing and testing, the electrode morphology changed substantially. The edges of the electrode appeared wavy and the electrode developed pits. The waviness of the edges (α) increases the TPB length from l_{TPBp} to $l_{TPBp}(1 + \alpha)$. The pits inside the electrode area, which appear to form due to some de-wetting and coalescence, introduce additional TPB length, namely, l_{TPB_0}. Hence, the actual TPB length is given by Eq. 5. It was assumed that most of the morphological change occurred during annealing and the first few hours in the test setup, and thereafter the morphology did not change with time. Thus, for the calculations of charge-transfer resistance from a given sample, the final morphology was assumed for all measurements. The $l_{TPBp}(1 + \alpha)$ was estimated from SEM pictures by using a very thin thread. The thread was initially placed carefully along the jagged edges of the platinum electrode on high-magnification SEM images so that it follows the shape of the electrode edge as closely as possible. The thread was then straightened and its length was measured. The ratio of the thread length to the edge length gives $(1 + \alpha)$. The estimated value of α was found to be ~0.26. The l_{TPB_0} was estimated using techniques in quantitative stereology.[29] For this measurement, all tested samples were examined under SEM and several micrographs were obtained randomly on the patterned electrode area of each sample. Horizontal and vertical test lines were drawn on the images

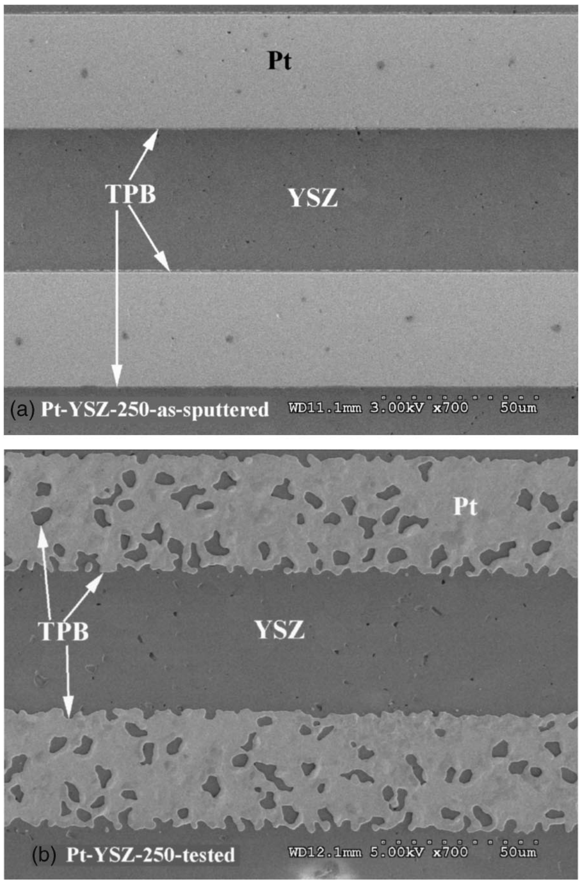

Figure 3. SEM images of a platinum patterned electrode on YSZ with $l_{\mathrm{TPBp}} = 250\ \mathrm{cm}^{-1}$ (a) as sputtered and (b) after testing.

of the platinum-covered surfaces and the point intersections per unit length (p_L), where the pits in the film intercept the test line, were measured. The length of the perimeter of the pores in the film per unit area (L_A) was estimated using the equation $L_A = (\pi/2)p_L$.[29] The average value of L_A was found to be $1588 \pm 28\ \mathrm{cm}^{-1}$. The area fraction of platinum in the patterned electrode, A_A, is 0.50. Therefore, we have $l_{\mathrm{TPB}_0} = A_A \times L_A = 0.50 \times 1588 = 794\ \mathrm{cm}^{-1}$. Using the estimated values of α and l_{TPB_0}, the total l_{TPB} values calculated for the four samples were ~1430, ~1110, ~920, and ~860 cm^{-1}, respectively, corresponding to l_{TPBp} of 500, 250, 100, and 50 cm^{-1}.

In the case of LSM-patterned electrodes examined in an earlier study, the electrode morphology did not change during annealing or testing.[17] The edges of LSM patterned electrodes appeared very smooth even under high-magnification SEM. Hence, in the case of LSM patterned electrodes, the α was taken to be zero in the analysis. Also l_{TPB_0} was mainly due to the defects (pores) in the substrate and no pits developed in the electrode area, unlike the case of platinum electrodes of this study. This could be due to possible better wetting between LSM and YSZ and/or slow transport (of cations) in LSM, which prevents shape changes at the low testing temperatures (<800°C).

Impedance analysis.—The impedance spectra obtained on patterned platinum electrodes deposited on YSZ with different l_{TPBp} in air at 800°C, and those obtained on a sample with $l_{\mathrm{TPBp}} = 250\ \mathrm{cm}^{-1}$ at various temperatures and in oxygen partial pressures, are given in Fig. 4-6. The impedance spectra typically consisted of suppressed semicircular arcs. The high-frequency intercept of the arc on the real axis (R_1) corresponds to the ohmic resistance, and the low-frequency intercept (R_2) corresponds to the total resistance of the half-cell (between the working and the reference electrodes). In Fig. 4 and 5, which correspond to measurements at 800°C, the ohmic part (R_1) is essentially the same. The R_1 for all samples with different l_{TPBp} in Fig. 4 is expected to be the same, because it is mainly due to the resistance of the YSZ disk between the working and the reference electrodes. R_1 does not change with change in p_{O_2} (Fig. 5), because over this p_{O_2} range, the ionic conductivity of YSZ is essentially independent of p_{O_2}. In addition, over the short duration of the experiment, the stoichiometry of the interior of the YSZ disk is not expected to change. In Fig. 6, in which measurements are given over a range of temperatures between 650 and 800°C, it can be seen that R_1 decreases with increasing temperature due to the temperature dependence of the ionic conductivity of YSZ. Polarization resistance of the electrode was obtained by subtracting R_1 from R_2. From the impedance spectra (Fig. 4-6) it is seen that the polarization resistance depends on l_{TPB}, the oxygen partial pressure, p_{O_2},

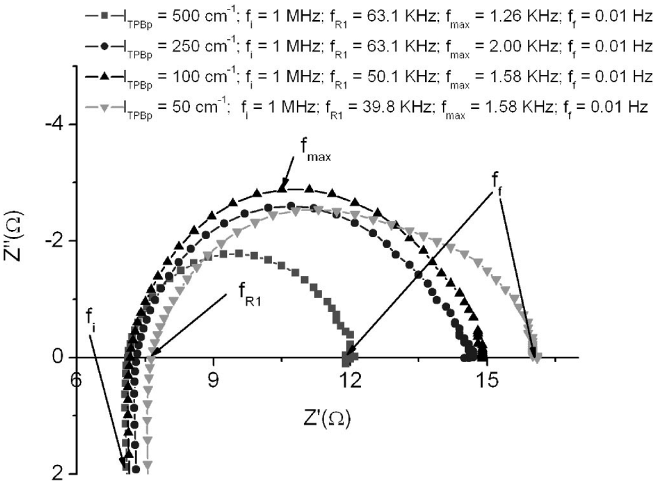

Figure 4. Impedance spectra obtained on YSZ disks with different l_{TPBp} in air at 800°C. The frequency ranges from $f_i = 1$ MHz to $f_f = 0.01$ Hz. The frequency at which each spectrum initially crosses the real axis of the impedance, f_{R_1}, and the frequency at which the imaginary part reaches its highest value (magnitude), $f_{\max}$, are marked on the spectra.

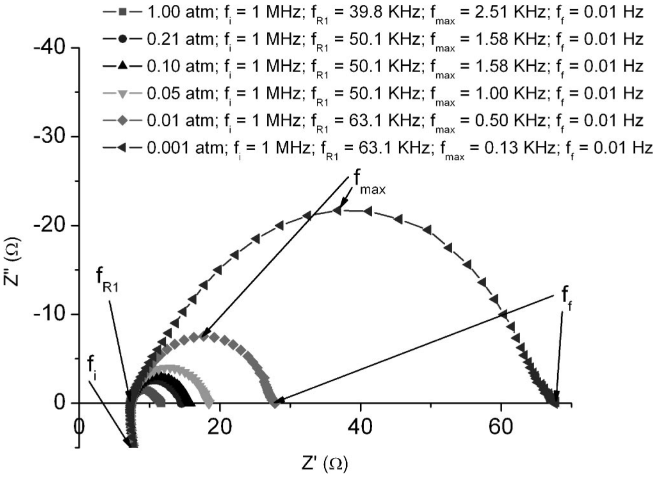

Figure 5. Impedance spectra obtained on a YSZ disk with $l_{\mathrm{TPBp}} = 250\ \mathrm{cm}^{-1}$ at 800°C at various p_{O_2}. The frequency ranges from $f_i = 1$ MHz to $f_f = 0.01$ Hz. The frequency at which each spectrum initially crosses the real axis of the impedance, f_{R1}, and the frequency at which the imaginary part reaches its highest value (magnitude), $f_{\max}$, are marked on the spectra.

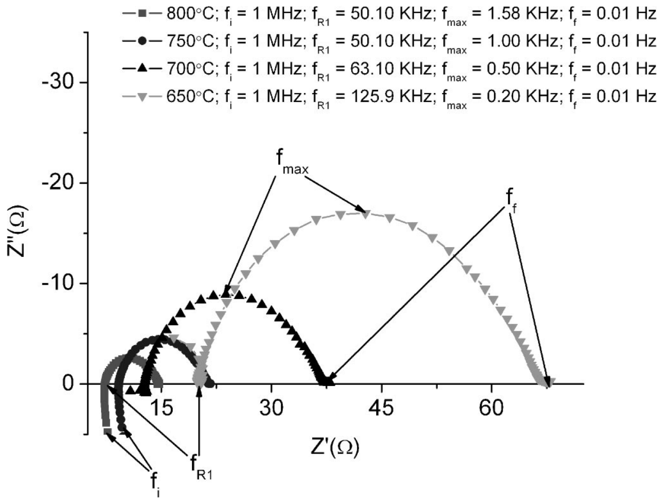

Figure 6. Impedance spectra obtained on a YSZ disk with l_{TPBp} = 250 cm^{-1} in air at various temperatures. The frequency ranges from f_i = 1 MHz to f_f = 0.01 Hz. The frequency at which each spectrum initially crosses the real axis of the impedance, f_{R1} and the frequency at which the imaginary part reaches its highest value (magnitude), f_{max}, are marked on the spectra.

and the temperature. R_{ct} was calculated by multiplying the polarization resistance with the total electrode area (0.785 cm^2).

Dependence of R_{ct} on the TPB length (l_{TPB}).—Figure 7a shows plots of $1/R_{ct}$ *vs.* l_{TPBp} at 800°C in atmospheres with different p_{O_2} and Fig. 8a shows similar plots in air at different temperatures. It is seen that $1/R_{ct}$ increases linearly with l_{TPBp}. The inverse of slope gives the charge-transfer resistivity divided by $(1 + \alpha)$, namely $\rho_{ct}/(1 + \alpha)$. It can be seen that a value of zero for l_{TPBp} gives a finite R_{ct} value, *i.e.*, a finite *y* intercept. This intercept is given by l_{TPB0}/ρ_{ct}. Similar nonzero intercepts for $1/R_{ct}$ have been reported for microfabricated Ni anodes and LSM cathodes.[12,13,17] The ratio of the *y* intercept to the slope of these plots (or the magnitude of the intercept on the negative *x* axis) gives $l_{TPB0}/(1 + \alpha)$. Figure 7b shows plots of $1/R_{ct}$ *vs.* $l_{TPB} = l_{TPBp}(1 + \alpha) + l_{TPB_0}$ at 800°C in atmospheres with different p_{O_2} and Fig. 8b shows similar plots in air at different temperatures. The inverse of slope of these plots gives the charge-transfer resistivity, ρ_{ct}, which is a function of temperature and p_{O_2}. It can also be seen that now the linear extrapolation essentially goes through the origin, which is consistent with the assumption that negligible oxygen transport occurs through platinum under the experimental conditions investigated, and virtually all of the charge transfer occurs at the TPBs. While varying the l_{TPBp} from 50 to 500 (ten fold), the actual l_{TPB} varied only from 860 to 1430 (1.67 fold), due to the significant contribution of l_{TPB0}. Hence, if the charge-transfer reaction were to take place only at the TPB, it is expected that R_{ct} should also vary by a factor of 1.67 for the range of l_{TPBp} studied. It was found that R_{ct} varied by nearly the same factor for the range of temperatures and pressures studied, indicating that the charge-transfer reaction predominantly occurs at the TPB. The values of ρ_{ct} at different temperatures and p_{O_2} were estimated from the plots of $1/R_{ct}$ *vs.* l_{TPB} and are summarized in Table I.

For LSM electrodes also, a linear relation between $1/R_{ct}$ and l_{TPBp} was observed, consistent with the occurrence of charge transfer reaction at TPB, but with a nonzero, finite value of $1/R_{ct}$ for zero l_{TPBp}.[17] The finite, nonzero value of $1/R_{ct}$ for zero l_{TPBp} in the case of LSM electrodes, however, could not be accounted for exclusively by l_{TPB_0}, especially at higher temperatures. The difference was attributed to the occurrence of some mixed conduction through LSM. The contribution of transport through LSM, however, was judged to be rather small at temperatures equal to or lower than 800°C. In the case of platinum electrodes, it appears that transport of oxygen through platinum is even smaller. Thus, it can be concluded that at temperatures lower than 800°C, the charge-transfer reaction in the case of platinum-YSZ system occurs almost exclusively at TPB.

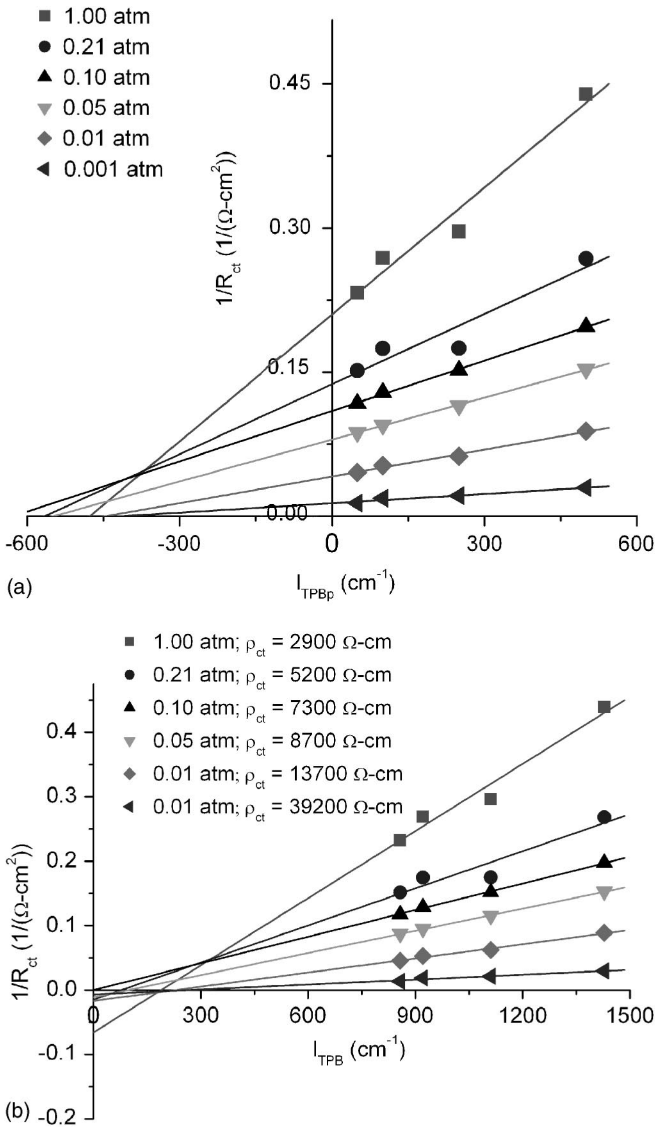

Figure 7. Plots of $1/R_{ct}$ *vs.* (a, top) l_{TPBp} and (b, bottom) l_{TPB} at 800°C at various p_{O_2}.

The estimated value of ρ_{ct} for platinum on YSZ at 800°C in air was nearly 20 times lower than that of LSM on YSZ, indicating that platinum is a better electrocatalyst for oxygen reduction on YSZ than LSM.

Dependence of R_{ct} and ρ_{ct} on oxygen partial pressure (p_{O_2}).—The measured R_{ct} was found to increase with decreasing p_{O_2}. Plots of ρ_{ct} *vs.* $1/p_{O_2}$ and $\rho_{ct}p_{O_2}$ *vs.* p_{O_2} (associative adsorption) and ρ_{ct} *vs.* $1/\sqrt{p_{O_2}}$ and $\rho_{ct}\sqrt{p_{O_2}}$ *vs.* $\sqrt{p_{O_2}}$ (dissociative adsorption) are given respectively in Fig. 9 and 10. It can be seen that in the two plots for associative adsorption (Fig. 9a and b) and those for dissociative adsorption (Fig. 10a and b) the slope in one plot (a) should be the intercept in the other (b) and vice-a-versa. The value of b' and b^* (Table II) and ρ''_{ct} (Table III) were estimated from the slopes and intercepts of the respective plots. These values estimated from Fig. 9a and b corresponding to the associative adsorption model do not agree very well with each other, but those estimated from Fig. 10a and b corresponding

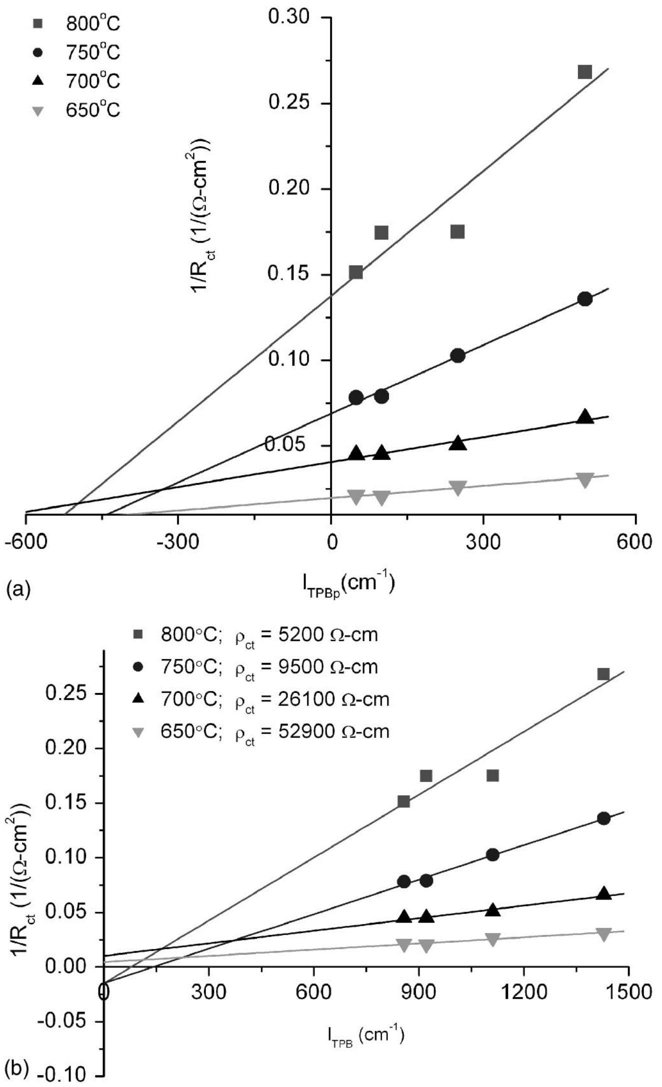

Figure 8. Plots of $1/R_{ct}$ *vs.* (a, top) l_{TPBp} and (b, bottom) l_{TPB} in air at various temperatures.

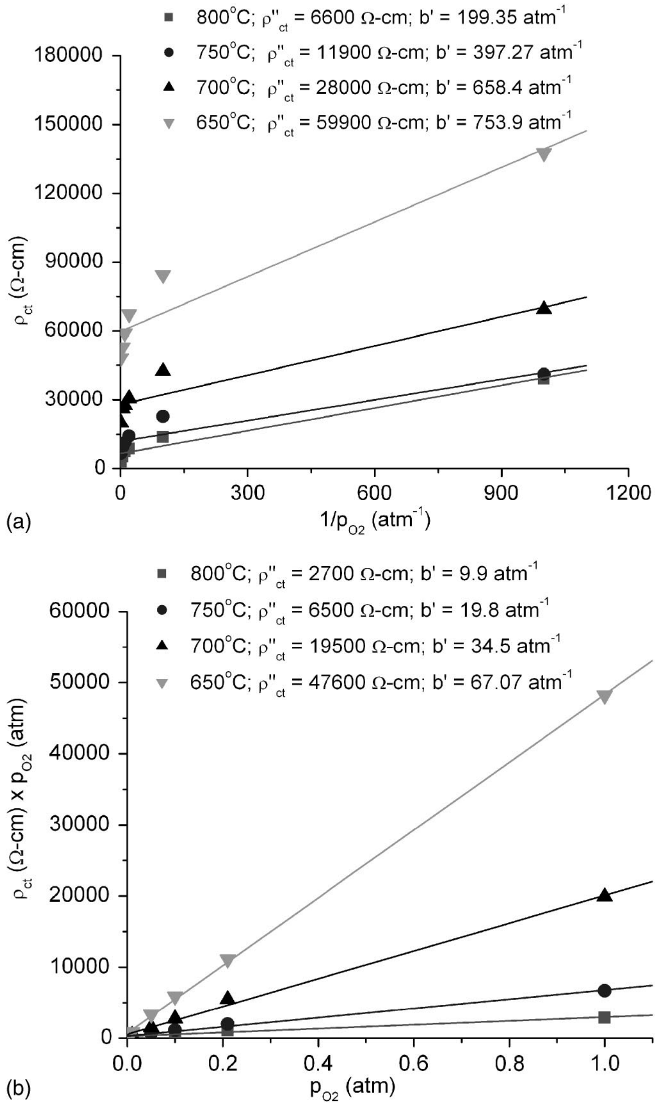

Figure 9. Plots of (a, top) ρ_{ct} *vs.* $1/p_{O_2}$ and (b, bottom) $\rho_{ct}p_{O_2}$ *vs.* p_{O_2} at various temperatures (associative adsorption model).

to dissociative adsorption are in better agreement. This suggests that the adsorption mechanism is most likely dissociative, and not associative, but while using the associative adsorption model it is not necessary to assume that adsorption of nitrogen is negligible, although in that case it is impossible to estimate b' or ρ''_{ct}. The estimated values of both b' and b^* were found to decrease with increasing temperature. The temperature dependence of adsorption coefficient can be given by $b(T) = b_0 \exp(-E_{ads}/k_BT)$, (in which b represents b' or b^*) where E_{ads} is negative. The magnitude of E_{ads} calculated from the slope of the Arrhenius plots of the estimated value of b^* is given in Fig. 11 and is between ~1.16 and ~1.3 eV.

For LSM electrodes of Ref. 17 also, the measured R_{ct} was found to increase with decrease in p_{O_2} and the p_{O_2} dependence of R_{ct} was also found to be in better agreement with the dissociative adsorption model. But in that case b^* did not vary much with temperature, indicating that the magnitude of E_{ads} is rather small in the case of LSM cathode on YSZ.

Dependence of R_{ct} and ρ_{ct} on temperature.—It was found that R_{ct} and ρ_{ct} increase exponentially with decreasing temperature. All samples with different TPB exhibited the same dependence of R_{ct} on

Table I. Values of $\rho_{ct}(\Omega$ cm) estimated from $1/R_{ct}$ *vs.* l_{TPB} plots at various temperatures and oxygen partial pressures.

	p_{O_2}					
Temperature (°C)	1 atm	0.21 atm	0.1 atm	0.05 atm	0.01 atm	0.001 atm
800	2900	5200	7300	8700	13700	39200
750	6700	9500	11400	14100	22700	41100
700	19900	26100	27600	30600	42400	69400
650	48200	52900	59000	67300	84400	137500

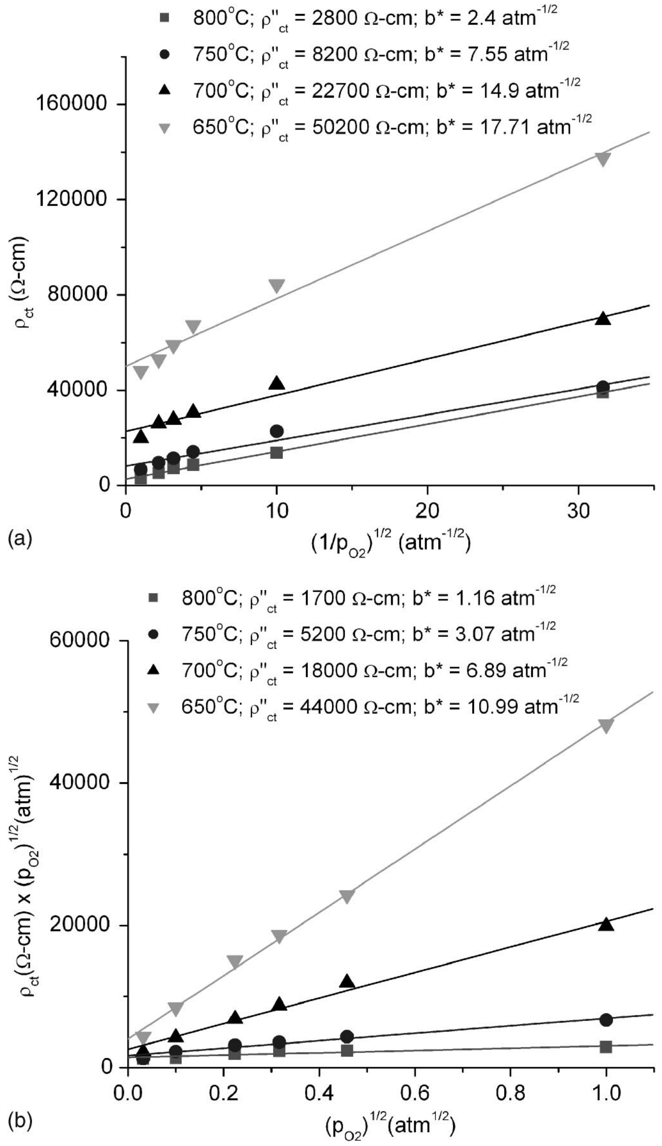

Figure 10. Plots of (a, top) ρ_{ct} *vs.* $1/\sqrt{p_{O_2}}$ and (b, bottom) $\rho_{ct}\sqrt{p_{O_2}}$ *vs.* $\sqrt{p_{O_2}}$ at various temperatures (dissociative adsorption model).

Table III. Estimated values ρ''_{ct} (Ω cm) from Fig. 9 and 10.

	Estimated from	800°C	750°C	700°C	650°C
Associative	Figure 9a	6600	11900	28000	59900
	Figure 9b	2700	6500	19500	47600
Dissociative	Figure 10a	2800	8200	22700	50200
	Figure 10b	1700	5200	18000	44400

temperature. In Fig. 12a, $\ln(\rho_{ct})$ is plotted *vs.* the inverse of absolute temperature for various p_{O_2}. From the slopes of the plots, the activation energy (E_a) for the overall charge-transfer process was estimated. It was observed that the activation energy varied over the p_{O_2} range investigated and was found to increase with increasing p_{O_2}, ranging between 0.75 eV at 0.001 atm and 1.63 at 1 atm. It was further noted that the activation energy for ρ''_{ct} (the charge-transfer resistance at a surface coverage equal to 1) from the dissociative adsorption model estimated from the Arrhenius plot in Fig. 12b is between ~1.65 and ~1.88 eV.

Table II. Estimated values of adsorption coefficients from Fig. 9 and 10.

	Estimated from	800°C	750°C	700°C	650°C
Associative b'	Figure 9a	199.35	397.27	658.4	753.9
	Figure 9b	9.9	19.8	34.5	67.07
Dissociative b^*	Figure 10a	2.4	7.55	14.9	17.71
	Figure 10b	1.16	3.07	6.89	10.99

Also for LSM electrodes, it was found that R_{ct} and ρ_{ct} increase exponentially with decrease in temperature.[17] The E_a for the overall charge-transfer process in the case of LSM on YSZ was ~1.5 eV and was more or less the same for the entire p_{O_2} range studied.

Implications of the temperature and p_{O_2} dependence of ρ_{ct}.—Equation 26 gives a relationship between ρ_{ct}, ρ''_{ct} and p_{O_2} for the dissociative adsorption model, and can be rewritten as follows

$$\rho_{ct} = \rho''_{ct}\left(\frac{1 + b^*\sqrt{p_{O_2}}}{b^*\sqrt{p_{O_2}}}\right) \tag{28}$$

in which ρ''_{ct} and b^* are not functions of p_{O_2}. At high values of p_{O_2}, that is, for $b^*\sqrt{p_{O_2}} \gg 1$, Eq. 28 can be approximated by

$$\rho_{ct} \approx \rho''_{ct} \tag{29}$$

and the temperature dependencies of ρ_{ct} and ρ''_{ct} are essentially the same. The temperature dependence of ρ''_{ct} may be given as

$$\rho''_{ct} \approx \rho''_{ct(0)} \exp\left[\frac{E_a}{k_B T}\right] \tag{30}$$

where $E_a > 0$. Note that as the temperature increases, ρ''_{ct} decreases. At low values of p_{O_2}, $b^*\sqrt{p_{O_2}} \ll 1$, and Eq. 28 can be approximated by

$$\rho_{ct} \approx \frac{\rho''_{ct}}{b^*\sqrt{p_{O_2}}} \tag{31}$$

The temperature dependence of b^* may be given by

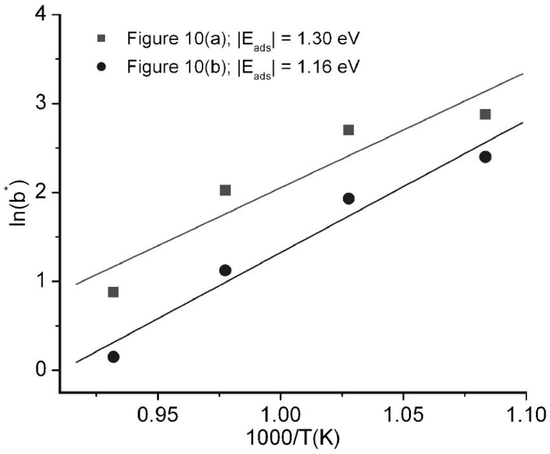

Figure 11. Arrhenius plots of b^* (dissociative adsorption model).

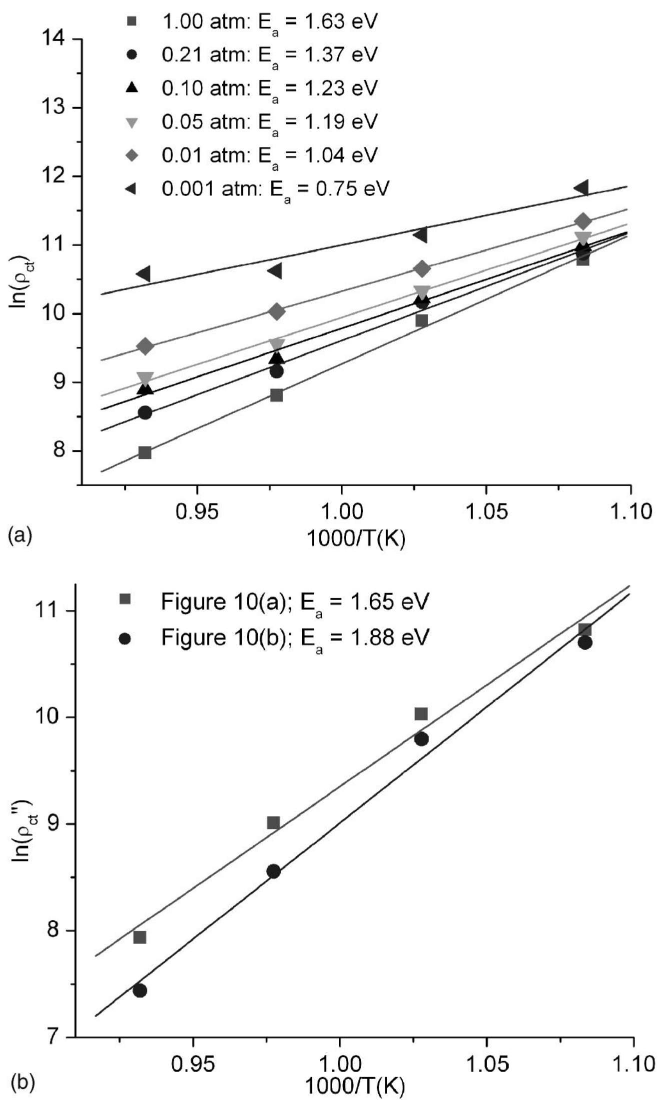

Figure 12. Arrhenius plots of (a, top) ρ_{ct} at various oxygen partial pressures and (b, bottom) ρ''_{ct} estimated from the dissociative adsorption model.

$$b^* = b_0^* \exp\left[-\frac{E_{ads}}{k_B T}\right] \qquad [32]$$

where $E_{ads} < 0$. Note that as the temperature increases, b^* decreases. Thus, the temperature dependence of ρ_{ct} may be given by

$$\rho_{ct} \approx \frac{\rho''_{ct(0)}}{b_0^*\sqrt{p_{O_2}}}\exp\left[\frac{(E_a + E_{ads})}{k_B T}\right] \qquad [33]$$

where note that $E_a > E_a + E_{ads}$. Thus, we expect effective higher activation energy at higher p_{O_2}. That is, as the temperature decreases, both ρ''_{ct} and b^* increase such that the temperature dependence of ρ_{ct} in that case should be weaker. As seen in Fig. 12a, the activation energy is higher at higher values of p_{O_2}. As stated earlier, in the case of LSM on YSZ,[17] the activation energy was essentially independent of p_{O_2} over the range investigated, which suggests a weaker adsorption of oxygen on LSM as compared to that on platinum.

Conclusions

Electrochemical reaction of oxygen reduction was investigated at platinum/YSZ electrodes using patterned electrodes deposited by photomicrolithography. A linear relation between $1/R_{ct}$, where R_{ct} is the area-specific charge-transfer resistance, and l_{TPB}, where l_{TPB} is the TPB line length (cm^{-1}) consistent with the occurrence of charge transfer at TPB, was observed over the range of temperatures and oxygen partial pressures, p_{O_2}, examined. Similar results were previously observed on a LSM/YSZ system.[17] In addition, the plots essentially went through the origin, indicating that the charge-transfer reaction almost exclusively occurred at the TPB, with negligible transport through platinum. By contrast, in the case of LSM/YSZ at high temperatures (800°C), small contribution due to transport through LSM was noted.[17] The slope of the plot of $1/R_{ct}$ *vs.* l_{TPB}, gives the charge-transfer resistivity, ρ_{ct}. The estimated value of ρ_{ct} is nearly 20 times lower for platinum on YSZ than that for LSM on YSZ, indicating a higher catalytic activity of platinum than LSM for the oxygen reduction reaction. R_{ct} and ρ_{ct} decrease with increase in p_{O_2} and increase in temperature. Assuming the adsorption of nitrogen is negligible, the variation of measured R_{ct} with p_{O_2} agrees better with the dissociative adsorption model rather than associative adsorption model. The adsorption coefficients were found to vary exponentially with temperature with the magnitude of the adsorption energy between ~1.16 and ~1.3 eV. The estimated activation energy for the charge-transfer resistivity, ρ_{ct}, varied from 0.75 eV for p_{O_2} of 0.001 atm and 1.65 eV for $p_{O_2} \sim 1$atm. The activation energy for charge-transfer resistivity corresponding to an oxygen surface coverage of 1, namely, ρ''_{ct}, was estimated to be between ~1.65 and ~1.88 eV.

Acknowledgments

This work was supported by the United States Department of Energy (DOE) under contract no. DE-FC26-02NT41602 at the University of Utah and through its High Temperature Electrochemistry Center (HiTEC) at the Pacific Northwest National Laboratory (PNNL). A part of the research described in this paper was performed in the Environmental Molecular Sciences Laboratory (EMSL), a national scientific user facility sponsored by the Department of Energy's Office of Biological and Environmental Research and located at the Pacific Northwest National Laboratory (PNNL).

The University of Utah assisted in meeting the publication costs of this article.

References

1. D. Y. Wang and A. S. Nowick, *J. Electrochem. Soc.*, **126**, 1155 (1979).
2. D. Y. Wang and A. S. Nowick, *J. Electrochem. Soc.*, **126**, 1166 (1979).
3. E. Ivers' Tiffee and A. V. Virkar, in *High Temperature Solid Oxide Fuel Cells: Fundamentals, Design and Applications*, S. C. Singhal and K. Kendall, Editors, Elsevier, Ltd., New York (2003).
4. J. Fleig, *Annu. Rev. Mater. Res.*, **33**, 361 (2003).
5. N. L. Robertson and J. N. Michaels, *J. Electrochem. Soc.*, **137**, 129 (1990).
6. H. Fukunaga, M. Ihara, K. Sakaki, and K. Yamada, *Solid State Ionics*, **86-88**, 1179 (1996).
7. J. Fleig, *J. Power Sources*, **105**, 228 (2002).
8. F. H van Heuveln, H. J. M. Bouwmeester, and F. P. F. van Berkel, *J. Electrochem. Soc.*, **144**, 126 (1997).
9. F. Zhao, Y. Jiang, G. Y. Lin, and A. V. Virkar, in *Solid Oxide Fuel Cells*, H. Yokokawa and S. C. Singhal, Editors, PV 2001-16, p. 501, The Electrochemical Society Proceedings Series, Pennington, NJ (2001).
10. A. Mitterdorfer and L. J. Gauckler, *Solid State Ionics*, **111**, 185 (1998).
11. J. Mizusaki, H. Tagawa, K. Tsuneyoshi, and A. Sawata, *J. Electrochem. Soc.*, **138**, 1867 (1991).
12. J. Mizusaki, H. Tagawa, T. Saito, T. Yamamura, K. Kamitani, K. Hirano, S. Ehara, T. Takagi, T. Hikita, M. Ippommatsu, S. Nakagawa, and K. Hashimoto, *Solid State Ionics*, **70/71**, 52 (1994).
13. A. Bieberle, L. P. Meier, and L. J Gauckler, *J. Electrochem. Soc.*, **148**, A646 (2001).
14. T. Horita, K. Yamaji, N. Sakai, H. Yokokawa, T. Kawada, and T. Kato, *Solid State Ionics*, **127**, 55 (2000).
15. T. Horita, K. Yamaji, N. Sakai, and H. Yokokawa, *J. Electrochem. Soc.*, **148**, J25 (2001).
16. V. Brichzin, J. Fleig, H.-U. Habermeier, and J. Maier, *Electrochem. Solid-State Lett.*, **3**, 403 (2000).
17. R. Radhakrishnan, A. V. Virkar, and S. C. Singhal, *J. Electrochem. Soc.*, **152**, A210 (2005).
18. T. H. Estell and S. N. Flengas, *J. Electrochem. Soc.*, **118**, 1890 (1971).
19. C. S. Tedmon, Jr., H. S. Spacil, and S. P. Mitoff, *J. Electrochem. Soc.*, **116**, 1170 (1969).
20. S. Pancharatnam, R. A. Huggins, and D. E. Mason, *J. Electrochem. Soc.*, **122**, 869

(1975).
21. R. J. Brook, W. L. Pelzmann, and F. A. Kroger, *J. Electrochem. Soc.*, **118**, 185 (1971).
22. R. E. W. Casselton, *J. Appl. Electrochem.*, **4**, 25 (1974).
23. J. E. Bauerle, *J. Phys. Chem. Solids*, **30**, 2657 (1969).
24. S. Pizzini, M. Bianchi, P. Colombo, and S. Torshio, *J. Appl. Electrochem.*, **3**, 153 (1973).
25. T. M. Gur, I. D. Raistrick, and R. A. Huggins, *J. Electrochem. Soc.*, **127**, 2620 (1980).
26. J. Mizusaki, K. Amano, S. Yamuchi, and K. Fueki, *Solid State Ionics*, **22**, 313 (1987).
27. J. Mizusaki, K. Amano, S. Yamuchi, and K. Fueki, *Solid State Ionics*, **22**, 323 (1987).
28. C. W. Tanner, K-Z. Fung, and A. V. Virkar, *J. Electrochem. Soc.*, **144**, 21 (1997).
29. E. Underwood, *Quantitative Stereology*, Addison Wesley Publishing Company, Inc., Reading, MA (1970).
30. A. W. Adamson and A. P. Gast, *Physical Chemistry of Surfaces*, 6th ed., Wiley, New York (1997).

INVESTIGATION OF ELECTROLYTE STABILITY USING AMPEROMETRIC SENSORS: IMPLICATIONS CONCERNING ELECTRODE POLARIZATION MEASUREMENTS

Anil V. Virkar[1] and Yi Jiang
Department of Materials Science and Engineering, University of Utah
122 S. Central Campus Drive, Salt Lake City, Utah 84112

ABSTRACT

Amperometric sensors with yttria-stabilized zirconia (YSZ) discs and YSZ cylinders were made with platinum electrodes applied on the YSZ disc, which served as working (inside) and counter (outside) electrodes, and a platinum wire electrode positioned along the circumference of the disc. Two sets of platinum electrodes were applied on the YSZ cylinder, one inside and the other outside. The YSZ cylinder was attached to the YSZ disc using a sealing glass. A YSZ disc with a tiny diffusion hole was glass-sealed on the other end of the YSZ cylinder. The amperometric sensor was tested at 800^{o}C in air over an applied DC voltage range from zero to 2.5 V. The measured current over a voltage range from ~0.4 to ~1.6 V exhibited a plateau. For applied voltage ≥ 1.7 V, the measured current increased, with a rapid increase for applied voltage ≥ 1.9 V. This rapid rise is consistent with the development of nonstoichiometry or the occurrence of YSZ electrolyte decomposition. The voltage between the reference and the working electrodes was measured. Based on this information, the cathodic activity of the platinum working electrode was estimated. Implications concerning the use of the three electrode system for the study of electrode polarization are discussed.

1. INTRODUCTION

The three electrode system comprising an electrolyte disc upon which working, counter and reference electrodes are applied in an axisymmetric arrangement, is routinely used for the investigation of electrode kinetics. The typical approach is to apply a DC voltage between the working and the counter electrodes, measure the current flowing, measure the voltage between the reference and the working electrodes, and determine the ohmic loss between the working and the reference electrodes by current interruption. It is generally recognized that the applied voltage must be low enough to avoid decomposition of the electrolyte. In many cases, however, the magnitude of the applied voltage above which decomposition of the electrolyte (or the development of oxygen deficiency) occurs

---

[1] To whom correspondence should be addressed.

cannot be readily determined, since it depends on transport properties of the electrolyte as well as of the electrode/electrolyte interfacial regions. In addition, one also often does not have sufficient information on concentration polarization at the working electrode for lack information on its porosity, tortuosity and thickness. In the extreme case if the working electrode is too thick, or not porous enough, or both, the net current due to the electrode reaction under investigation may become concentration polarization limited. Yet, with increasing applied voltage, the current may continue to increase due either to the occurrence of oxygen deficiency or electrolyte decomposition. Thus, the net measured current will have two contributions: (a) Current due to the actual electrode reaction, which is the object of the investigation. For example, the cathodic current could be for the reaction $1/2O_2 + 2e' \rightarrow O^{-2}$ under investigation. (b) Current due to decomposition or development of oxygen deficiency (nonstoichiometry). However, the experimenter would have no way of separating the two currents, and the entire current is inadvertently attributed to the cathodic current. This can lead to an overestimation of the electrocatalytic activity of the electrode, thus leading to an incorrect result. The degree to which overestimation can occur will depend upon a number of factors, such as: (a) The transport properties of the material and interfacial regions, (b) The range of stoichiometry of the material in question, and (c) The magnitude of the applied voltage.

The principal objective of the present work was to determine the relative magnitudes of the two currents. This required that at least over some range, the net cathodic current should be precisely known. A possible way of achieving this is to deliberately introduce a concentration polarization limit, which can be independently calculated and verified. A convenient method of achieving this is to a construct an amperometric sensor around the three electrode system, wherein above a certain applied voltage, the net oxygen flux entering the sensor chamber is fixed by the geometry of the diffusion hole. This also automatically fixes the maximum possible cathodic current. Thus, any measured current beyond the limiting current can be unequivocally attributed to current due to decomposition/nonstoichiometry development. Implications of the present work concerning the often used three-electrode system, at a minimum, is that it may be necessary to thoroughly characterize the working electrode microstructure (porosity, pore size, etc.) and thickness, so that a possible concentration polarization limit can be a-priori calculated, which will set upper limit to the current, that should not be exceeded.

In the present work amperometric sensors were fabricated using YSZ electrolyte discs upon which platinum working and counter electrodes were applied. A platinum wire reference electrode was positioned along the circumference of the disc. Two sets of platinum electrodes were applied on the YSZ cylinder, one outside and the other inside. The sensors were tested at 800°C under an applied DC voltage, varied between zero and ~2.5 V. From these measurements, area specific ionic charge transfer resistance, $r_i^{'}$, for the working electrode was estimated as a function of oxygen partial pressure, p_{O_2}.

2. EXPERIMENTAL PROCEDURE

Cylinders of YSZ (8 mol.% Y_2O_3-stabilized zirconia) of approximate dimensions: ~2 cm outside diameter x 2.2 cm length x 0.2 cm thickness were fabricated by a conventional process comprising pressing of YSZ powder followed by sintering in air at 1450°C for 2 hours. Discs of YSZ of approximate dimensions, 2.5 cm diameter x 0.1 to 0.2 cm in thickness were fabricated. In few of the discs, a hole of ~250 μm diameter was drilled in the center. On the other YSZ discs, platinum electrodes of 2 cm^2 area were applied on both sides, and fired at 1000°C in air. A platinum wire reference electrode was positioned along the disc circumference. Two platinum leads were attached to the two electrodes. On the YSZ cylinder, two sets of platinum electrodes were applied near the two ends of the cylinder, one near the diffusion hole (4 mm from the disc with the diffusion hole), and the other near the YSZ disc with platinum electrodes (4 mm from the YSZ disc with electrodes). Platinum wires were attached to these electrodes also. These served as potentiometric sensors, S1 and S2. The distance between the two potentiometric sensors (S1 and S2) was 14 mm. The two discs were glass-bonded to the cylinder, making sure that the platinum leads were taken out through the glass seals, and the seals were hermetic. This completes amperometric sensor fabrication with two sets of potentiometric sensors on the YSZ cylinder. Figure 1 shows a schematic.

A typical sensor was heated in air to 800°C and a DC voltage was applied across the two platinum electrodes on the YSZ disc with positive lead connected to the outside electrode. The corresponding current was measured. Under the applied voltage, oxygen from the sensor chamber was pumped out, lowering the p_{O_2} in the chamber. The Nernst potentials across the two potentiometric sensors give magnitudes of the local p_{O_2}, one near the diffusion hole, $p_{O_2}^{S_1}$, and the other near the inner electrode (cathode) on the YSZ disc, $p_{O_2}^{S_2}$. Measurements were conducted over a voltage range from 0 to ~2.5 V, which covers the initial region, the plateau region, and the post-plateau region of rapidly rising current.

3. RESULTS

Figure 2 shows the measured current (logarithmic scale) as a function of time on one of the sensors tested. The voltage was increased in steps of 0.1 V, and each voltage was maintained for 300 sec. Note that at low voltages (~0.2 V), there is a hump in the current, which is the result of non-steady conditions. Beyond a voltage of 0.4 V, the current is independent of voltage up to ~1.6 V. The plateau current is ~3 mA, which is in good agreement with the amperometric sensor model [1]. Beyond ~1.6 V, the current sharply increases, due to decomposition or the development of nonstoichiometry. At a voltage of 2.5 V the maximum current is ~800 mA, while the cathodic current due to the reaction $^1/_2O_2 + 2e' \rightarrow O^{-2}$ occurring at electrode I is only ~3 mA. Thus, a very large part of the current is due to decomposition or development of nonstoichiometry. Beyond 2 V, the current continuously increases due to nonstoichiometry or decomposition zone spreading into the YSZ electrolyte disc.

Figure 3 shows the measured current (logarithmic scale) on another sensor as a function of the applied voltage, varied between zero and 2.4 V in increments of 0.1 V. The hump in current at 0.2 V of applied voltage is again due to non-steady conditions, similar to that in amperometric sensor 1, which existed during the initial stage, as the YSZ chamber had not been completely pumped out. Thereafter, the current was ~3.4 mA and was essentially independent of voltage for up to ~1.6 V. Beyond this voltage, the current rapidly increased with increasing voltage to ~400 mA at a voltage of 2.4 V. This means at a voltage of 2.4 V, (400 – 3.4) mA or ~397 mA of the current was due to decomposition/nonstoichiometry development, and very little of the current was due to the cathodic reaction. Beyond 1.9 V, the measured current was not steady, and continued to increase with hold time. Thus, beyond 1.9 V, the current is not a unique function of applied voltage.

Figure 4 shows the measured current (linear scale) and the measured Nernst voltages across potentiometric sensors S1 and S2 as a function of the applied voltage. Over the plateau, the Nernst voltages slightly decrease with increasing voltage. Thus, over this range, the p_{O_2} in the chamber is not constant either. From the Nernst potentials, $p_{O_2}^{S_1}$ and $p_{O_2}^{S_2}$ were estimated. Over the plateau (~0.4 to ~1.6 V), the $p_{O_2}^{S_1}$ varies between ~0.022 and ~0.005 atm, while $p_{O_2}^{S_2}$ varies between ~0.0125 and ~0.0016 atm. Table I lists values of $p_{O_2}^{S_1}$ and $p_{O_2}^{S_2}$ at various applied voltages. For an applied voltage ≥ 1.7 V, the magnitudes of Nernst voltages increase rapidly. At S2 (near the YSZ disc), the lowest Nernst voltage was ~ -520 mV (highest magnitude), and that at S1 (near diffusion hole) was ~ - 350 mV.

Figure 5 shows plots of the applied voltage, and the measured voltage between the cathode and the reference electrode (linear scale, on the y-axis), vs. the measured current (logarithmic scale, on the x-axis). Note that for the entire pre-plateau, plateau, and initial parts of the post-plateau regions, the applied voltage (between the cathode and the anode) is only slightly greater than that measured between the cathode and the reference electrode. However, once past the plateau, even with further increase in applied voltage, the measured voltage between the cathode and the reference electrode actually decreases. For the highest applied voltage of 2.5 V, the measured voltage between the cathode and the reference electrode is only ~0.25 V. This implies that cathode/electrolyte interface became electrocatalytically more active – which is known for black zirconia.

4. DISCUSSION

Figures 2 through 5 show that the current deviates from the plateau above a voltage of ~1.6 V, and rapidly rises above ~1.9 V. Figure 3, for example, shows that at a voltage of ~2.2 V, the total current is ~90 mA. Of this, only ~3.4 mA is due to the cathodic reaction ($^1/_2O_2$ +

2e’ → O^{-2}) at electrode I. The remaining ~86.6 mA is due to decomposition or development of nonstoichiometry in YSZ. This is consistent with a sharp increase in the magnitude of Nernst potential (Figure 4), indicating a rapid decrease in chamber p_{O_2}. The lowest chamber p_{O_2} was $\sim 5\times10^{-11}$ atm. This signifies that YSZ near electrode I has either undergone decomposition, or has developed a significant oxygen deficiency.

Figure 5 shows plots of the applied voltage between the counter and the working electrodes, and the measured voltage between the working and the reference electrode, both on the y-axis (linear scale), and the measured current on the x-axis (logarithmic scale). Figure 6 shows the geometry of the YSZ disc with the locations of working, counter and reference electrodes. The working electrode is exposed to oxygen partial pressure $p^I_{O_2}$, while the counter and reference electrodes are exposed to oxygen partial pressure $p^{II}_{O_2}$, which is ~0.21 atm. Reduced (negative) electrochemical potentials of electrons at the working, the reference and counter electrodes are, respectively, φ^I, $\varphi(X)$, and φ^{II} (where $\varphi = -\tilde{\mu}_e / e$ with $\tilde{\mu}_e$ as the electrochemical potential of electrons and e is the electronic charge). The electrochemical potentials of oxygen ions similarly are $\tilde{\mu}^I_{O^{-2}}$, $\tilde{\mu}_{O^{-2}(X)}$, and $\tilde{\mu}^{II}_{O^{-2}}$. Now, inside the YSZ disc, the flux of O^{-2} ions from I to II is essentially unidirectional. At position X from electrode I inside the YSZ disc, which is directly under the reference electrode, the various potentials are $\mu^X_{O_2}$, φ^X, and $\tilde{\mu}^X_{O^{-2}}$. Neither $\mu^X_{O_2}$ nor φ^X are known. However, assuming symmetry,

$$\tilde{\mu}^X_{O^{-2}} = \frac{1}{2}\mu^X_{O_2} - 2e\varphi^X \approx \tilde{\mu}_{O^{-2}(X)} = \frac{1}{2}\mu_{O_2(X)} - 2e\varphi(X) \qquad (1)$$

Also, note that $\mu_{O_2(X)} = \mu^{II}_{O_2}$, which is known (that corresponding to air in this case), and $\varphi(X)$ is also known (measured relative to electrode I). Now, the flux of O^{-2} ions occurs from I to II. This is proportional to the difference in electrochemical potentials of oxygen, that is, proportional to

$$\tilde{\mu}^I_{O^{-2}} - \tilde{\mu}^X_{O^{-2}} \approx \tilde{\mu}^I_{O^{-2}} - \tilde{\mu}_{O^{-2}(X)} = \frac{1}{2}\left(\mu^I_{O_2} - \mu^{II}_{O_2}\right) - 2e\varphi^I + 2e\varphi(X) \qquad (2)$$

or

$$\left(\varphi(X) - \varphi^I\right) = \frac{\left(\tilde{\mu}^I_{O^{-2}} - \tilde{\mu}_{O^{-2}(X)}\right)}{2e} + \frac{\left(\mu^{II}_{O_2} - \mu^I_{O_2}\right)}{4e} = \frac{\left(\tilde{\mu}^I_{O^{-2}} - \tilde{\mu}_{O^{-2}(X)}\right)}{2e} + \frac{k_B T}{4e}\ln\left(\frac{p^{II}_{O_2}}{p^I_{O_2}}\right) \qquad (3)$$

Equation (3) is applicable only over the plateau (and pre-plateau), since it only accounts for the current attributable to the net cathodic reaction. Now, $\left(\varphi(X) - \varphi^I\right)$ is the voltage measured between the reference electrode and electrode I (cathode). The $p_{O_2}^I$ can be approximately estimated by extrapolating the line joining $p_{O_2}^{S_1}, x_1$ and $p_{O_2}^{S_2}, x_2$ to electrode I/YSZ interface. It is assumed here that electrode I is thin and highly porous. The first term in equation (3) is related to the net ionic current density flowing through the YSZ disc. It is easily seen that

$$|I_i| = \frac{\left(\tilde{\mu}_{O^{-2}}^{I} - \tilde{\mu}_{O^{-2}}^{X}\right)}{2e\left(X\rho_i + r_i^{'}\right)} \approx \frac{\left(\tilde{\mu}_{O^{-2}}^{I} - \tilde{\mu}_{O^{-2}(X)}\right)}{2e\left(X\rho_i + r_i^{'}\right)} \tag{4}$$

where I_i is the ionic current density, $r_i^{'}$ is the ionic area specific charge transfer resistance at electrode I and ρ_i is the electrolyte ionic resistivity. Thus, equation (3) can be rearranged as

$$r_i^{'} \approx \frac{\left(\varphi(X) - \varphi^I\right) - \frac{k_B T}{4e} \ln\left(\frac{p_{O_2}^{II}}{p_{O_2}^{I}}\right)}{|I_i|} - X\rho_i \tag{5}$$

With YSZ as the electrolyte, which has negligible electronic conductivity, the ionic current is essentially the same as the measured current. All parameters are known in equation (6), and thus one can estimate the ionic charge transfer resistance at electrode I/electrolyte interface, $r_i^{'}$. The ρ_i of YSZ at 800°C is ~30 Ωcm. The X was ~1 mm. Thus, $X\rho_i \approx 3$ Ωcm^2. The net current over the plateau was 3.4 mA, and the corresponding $I_i \approx 1.7 \times 10^{-3}$ A/cm^2. As sensor S2 was quite close to electrode I, it is assumed that $p_{O_2}^I \sim p_{O_2}^{S_2}$. Table I lists the applied voltage, the measured voltage between the cathode and reference electrodes, $\left(\varphi(X) - \varphi^I\right)$, $p_{O_2}^{S_1}$, $p_{O_2}^{S_2}$, and the estimated $r_i^{'}$ using equation (5).

Table I shows that the estimated $r_i^{'}$ at electrode I ranges between ~157 Ωcm^2 for $p_{O_2}^I$ ~0.0125 atm and ~893 Ωcm^2 for $p_{O_2}^I$~0.00158 atm. The $r_i^{'}$ is expected to be a function of oxygen surface coverage, which in turn is expected to follow one of the adsorption isotherms. If a dissociative adsorption is assumed, it is expected that a plot of $r_i^{'}$ vs. $1/\sqrt{p_{O_2}^{S_2}}$ should be a straight line. Figure 7 shows a plot of $r_i^{'}$ vs. $1/\sqrt{p_{O_2}^{S_2}}$. The agreement is reasonable. An important conclusion is that $r_i^{'}$ is a function of p_{O_2}, and over the range investigated, the $r_i^{'}$ is much greater than the ohmic contribution. Figure 7 shows that the last data point, corresponding to an applied voltage of 1.7 V deviates from the plot which implies that the effects of nonstoichiometry development/decomposition are already present. For higher applied voltages, however, the $\varphi(X)-\varphi^I$ decreases, even when the applied voltage was increased. This indicates improved electrocatalysis at electrode I. However, the current measured now contains two contributions; the cathodic current and that due to the occurrence of nonstoichiometry or decomposition.

The Three-Electrode System under an Applied DC Voltage: Returning to the three-electrode system under an applied voltage, a technique often used for the investigation of electrode kinetics, e.g. evaluation of a prospective cathode for a fuel cell, the present results have significant implications. Depending upon the nature of electrode (I), that is porosity, tortuosity, and thickness, the net current may become diffusion-limited (concentration polarization limited) – even in the absence of a diffusion hole and without the experimenter being aware of it. In such cases, the diffusion limit may occur due to low porosity and/or large thickness of the porous electrode. Suppose a three-electrode system is used for the investigation of electrode kinetics of a prospective cathode. Let us assume for simplicity that the counter electrode is highly porous and has a small thickness, so that concentration polarization at the counter electrode (II) can be ignored. The testing is conducted in air wherein the oxygen partial pressure is $p_{O_2}^{II}$. Under the action of externally applied voltage, E_A, a net current is established. A flux of molecular oxygen is established through the porous cathode such that at the interface between the cathode (electrode I) and the electrolyte, the local oxygen partial pressure is $p_{O_2}^{I}$. Figure 8 shows a schematic variation of μ_{O_2} through the electrode and the membrane. The figure only shows a schematic variation, and the actual variation need not be linear.

The preceding shows that, depending on the charge transfer characteristics, the porosity and the thickness of the electrode, and the magnitude of the applied DC voltage, a significant portion of the measured current may be due to electrolyte decomposition and/or the development of nonstoichiometry, and not attributable to the cathodic reaction. A significant contribution to the total current may also arise due to the development of nonstoichiometry at applied voltages significantly lower than the decomposition potential. As such, there will be situations in which the three-electrode system will lead to an overestimation of the electrode activity. For this reason, the only conditions under which the three-electrode system can be used without ambiguity, is under no applied DC bias. That is, the three-electrode system for solid-state electrochemical studies is ideally suited only for the determination of the exchange current density under no applied DC bias – and its application for the generation of the entire current – overpotential relationship may not be reliable. The greater the degree of nonstoichiometry that can develop, the greater will be the error. In this context, the use of the three-electrode system under an applied DC bias may be particularly problematic with ceria as the electrolyte.

5. SUMMARY

Amperometric oxygen sensors were fabricated with a reference electrode wound on the circumference of the YSZ disc. Platinum working and counter electrodes were applied on the YSZ disc, and platinum potentiometric sensors were applied on the YSZ cylinder of the chamber. The sensors were tested at 800^{o}C under an applied DC voltage ranging between zero and 2.5 V. Over the applied voltage range from ~0.4 V to ~1.6 V, the current exhibited a plateau, consistent with the expectations of an amperometric sensor. Beyond a voltage of ~1.6 V, the current rapidly increased, indicating either decomposition of the electrolyte or the occurrence of nonstoichiometry. Based on the measured current over the plateau region and the voltage measured between the reference and the working electrodes, the ionic charge transfer resistance, $r_i^{'}$, at the cathode was estimated. Measurements made using the potentiometric sensors showed that over the plateau region, the p_{O_2} in the chamber varied by a factor of eight. From these measurements, it was noted that the $r_i^{'}$ varied by a factor ~5.6 over the same range, such that the $r_i^{'}$ increased with decreasing p_{O_2}. Past the plateau, the measured current increased sharply. Since the maximum possible cathodic current was limited by the diffusion hole (to ~3 mA), all excess current could be unequivocally attributed to nonstoichiometry/decomposition. In a typical three-electrode system, if the electrode is too thick or too dense (low porosity), it is possible that the actual cathodic current may become concentration polarization limited. Yet, under the application of a DC bias, the measured current may continue to increase with increasing voltage. However, in such a case, a large part of the current may be due to the occurrence of decomposition or the development of nonstoichiometry. In many situations, the experimenter may be unaware of the existence of two currents, with the entire current being attributed to the electrode reaction, and thus leading to an overestimation of the electrode activity.

REFERENCES

1) W. Gopel, T. A. Jones, M. Kleitz, J. Lundstrom and T. Seiyama, '*Sensors*', Volume 2, VCH publication, Weinheim, Germany (1991).

ACKNOWLEDGEMENTS

This work is supported by the U.S. Department of Energy, under contract No: DE-FC26-02NT41602

Table I: Partial pressures of oxygen at the two potentiometric sensors, namely $p_{O_2}^{S_1}$ and $p_{O_2}^{S_2}$, and the measured voltage across the reference electrode and electrode I (cathode), namely, $\left(\varphi(X) - \varphi^I\right)$, as a function of applied voltage.

Applied Voltage (V)	$p_{O_2}^{S_1}$ (atm)	$p_{O_2}^{S_2}$ (atm)	$\left(\varphi(X) - \varphi^I\right)$ (V)	$1/\sqrt{p_{O_2}^{S_2}}$	$r_i^{'}$ (Ωcm^2)
0.4	0.02216	0.0125	0.3368	8.944	156.8
0.6	0.01159	0.00586	0.5394	13.063	265.6
0.8	0.00852	0.00414	0.741	15.542	379.5
1.0	0.00701	0.0032	0.942	17.678	494.2
1.2	0.00605	0.0025	1.148	20.00	612.1
1.4	0.00573	0.0022	1.34	21.32	723.2
1.6	0.00573	0.00196	1.537	22.588	837.6
1.7	0.00543	0.00158	1.636	25.158	892.9

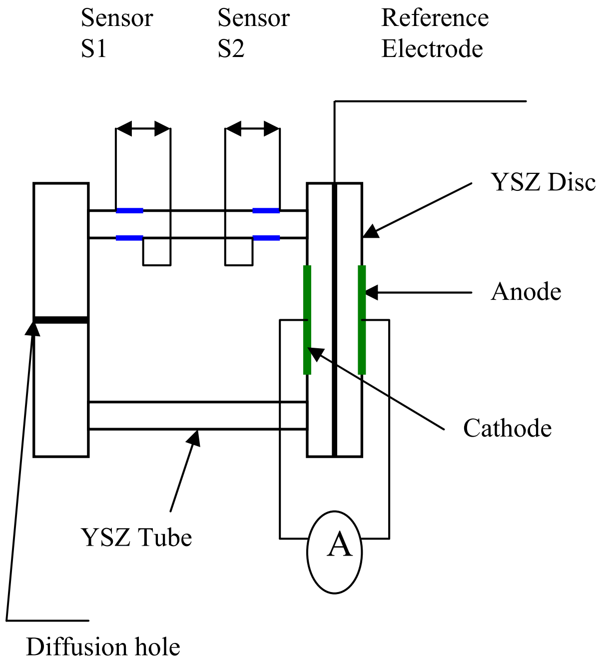

Figure 1: A schematic of the amperometric sensor fabricated and tested. S1 and S2 are potentiometric sensors used for the measurement of p_{O_2} in the sensor chamber.

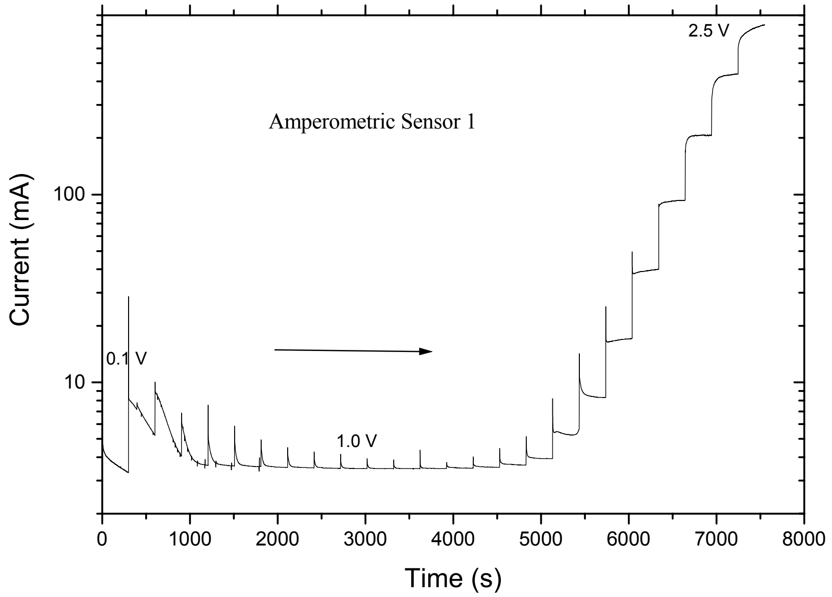

Figure 2: Measured current as a function of time. The voltage was increased in steps of 0.1 V, and maintained at a given voltage for 300 sec. At small applied voltages (~0.2 V), there is a hump in the current, which is due to non-steady state conditions. At intermediate voltage, note the existence of a plateau in current (~3 mA). Beyond a voltage of ~1.6 V, the current increases. The maximum current at 2.5 V is ~800 mA. Of this, only ~3 mA is due to the cathodic reaction. The rest is due to decomposition/nonstoichiometry development.

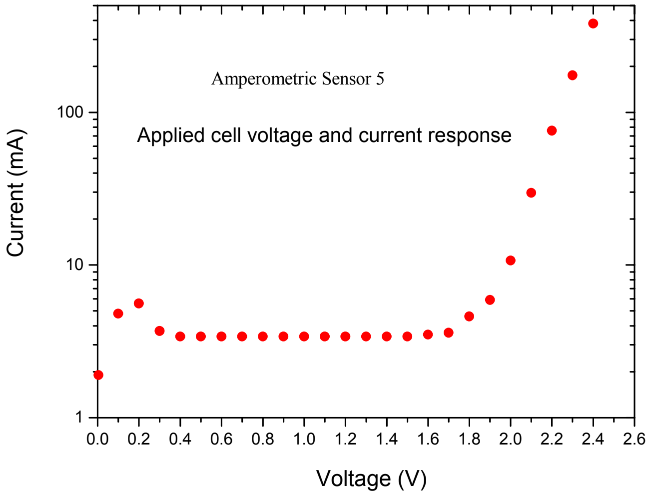

Figure 3: Measured current (mA) as a function of applied voltage. Higher current than the plateau at low applied voltages is due to non-steady state conditions. The plateau current is ~3.4 mA. Note the increasing current with increasing voltage past the plateau region.

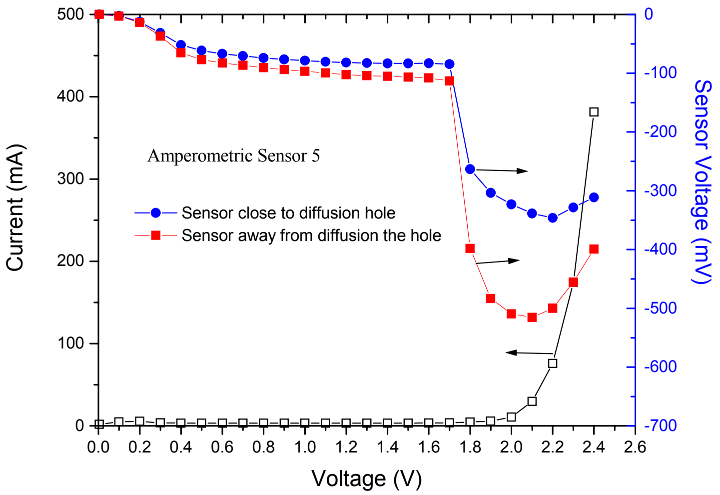

Figure 4: The measured Nernst voltages on sensors S_1 (close to the diffusion hole) and S_2 (close to the YSZ disc with electrodes – away from the diffusion hole) as a function of applied voltage.

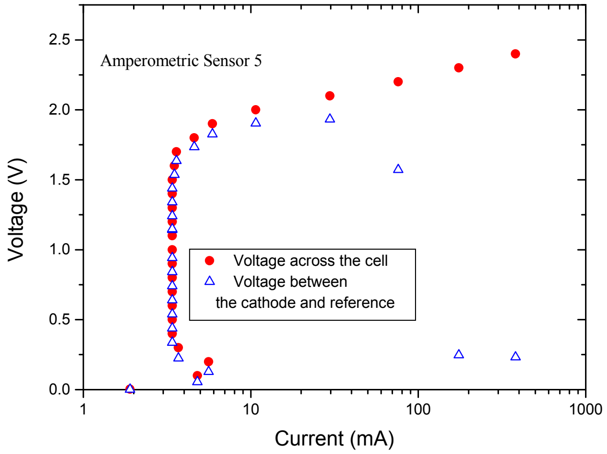

Figure 5: A plot of the applied voltage, and the measured voltage across the cathode and the reference electrode, vs. the current.

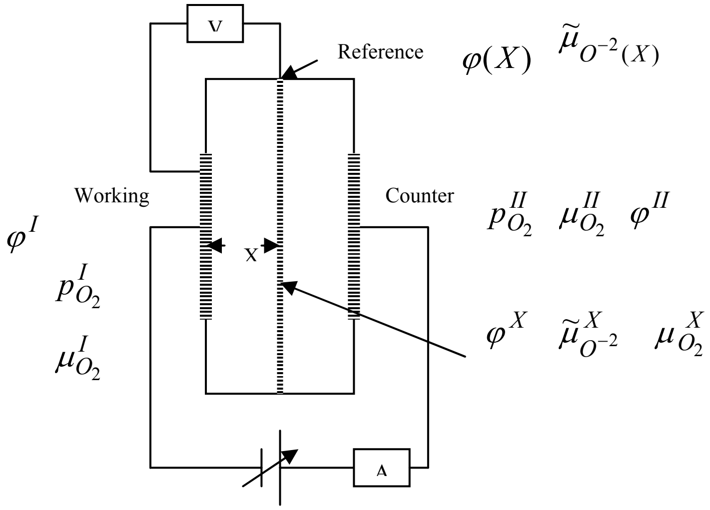

Figure 6: A schematic of the test set-up and the position of the reference electrode.

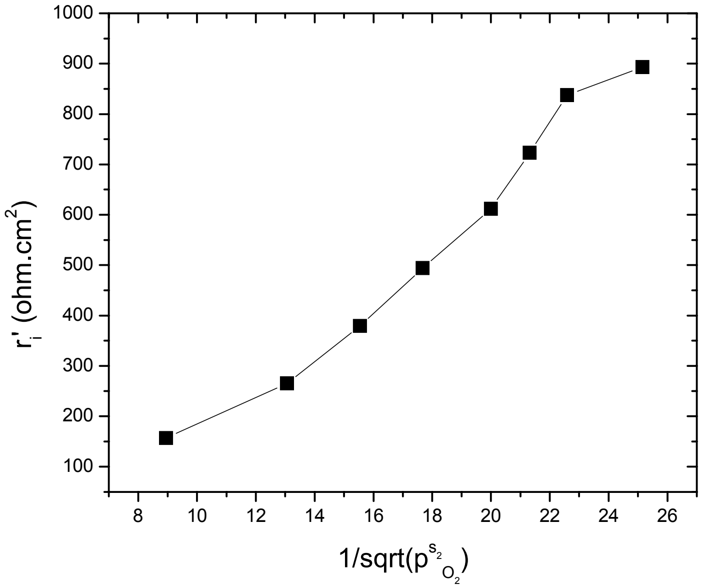

Figure 7: A plot of the $r_i^{'}$ vs. $1/\sqrt{p_{O_2}^{S2}}$.

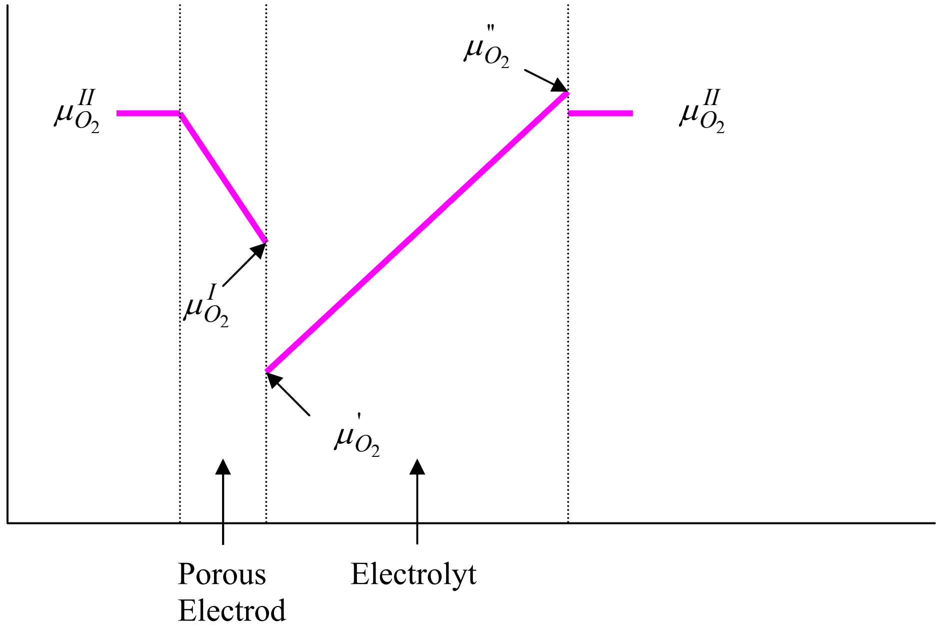

Figure 8: A schematic variation of μ_{O_2} through the electrode (cathode) and the electrolyte of a three-electrode system often used for the study of electrode kinetics. If $\mu_{O_2}^{'}$ is low enough, either a nonstoichiometry will be developed or electrolyte decomposition may occur. In either case, this will be reflected as additional current, not attributable to the cathodic reaction. This effectively leads to an overestimation of electrocatalytic activity.

MEASUREMENT OF TRANSPORT PROPERTIES OF PEROVSKITE CATHODES

R. Ganeshananthan and Anil V. Virkar
Department of Materials Science & Engineering, University of Utah
122. S. Central Campus Drive, Salt Lake City, Utah 84112

ABSTRACT

Conductivity relaxation experiments were conducted on porous $La_{0.5}Sr_{0.5}CoO_{(3-\delta)}$ (LSC50) samples over a temperature range from 350 to 750°C, and over an oxygen partial pressure, p_{O_2}, switch between 0.04 and 0.06 atm in order to determine the surface exchange coefficient, k_{chem}. The normalized conductivity data could be fitted to a first order kinetic equation. The time constant decreased with decreasing temperature between ~750 and ~450°C, but sharply increased with decreasing temperature between 450 and 350°C. The corresponding k_{chem} was estimated using three models: (a) A porous body model wherein it is assumed that the kinetics of surface exchange is the slowest. (b) Solution to the diffusion equation assuming the particles can be approximated as spheres. (c) Solution to the diffusion equation assuming the particles can be approximated as cylinders. The values of k_{chem} obtained from the three models were in good agreement. In all cases, it was observed that k_{chem} increases with decreasing temperature between 750 and 450°C, but below 450°C, it sharply decreases with further decrease in temperature.

1. INTRODUCTION

Mixed Ionic and Electronic Conducting (MIEC) materials are often used as oxygen separation membranes, in gas sensors and as cathodes in solid oxide fuel cells. The description of transport in MIECs requires the knowledge of two parameters, the chemical diffusion coefficient, $\tilde{D}$, and the chemical surface exchange coefficient, k_{chem} [1]. The former describes transport through bulk, while the latter describes transport across gas phase/solid phase interfaces. The parameters $\tilde{D}$ and k_{chem} are functions of composition, microstructure, temperature and atmosphere. Conventional methods for determining $\tilde{D}$ and k_{chem} include radio isotope, O^{18}, exchange (analyzed using secondary ion mass spectroscopy - SIMS), oxygen permeation experiments [2-4] and conductivity relaxation. The conductivity relaxation technique has been widely used because of simplicity of procedure, which involves measurement of conductivity as a function of time upon an abrupt change in p_{O_2}. When exposed to a p_{O_2} change, the sample under test re-equilibrates to the new p_{O_2} with a concomitant change in conductivity. This change can be an increase or decrease, depending on the new atmosphere and upon the defect chemistry. An analysis of the change of conductivity with time can be used to estimate $\tilde{D}$ and k_{chem}.

The ratio of $\tilde{D}$ to k_{chem} has units of length and is defined as the critical thickness, l_{cr} [5]. For sample thickness $>> l_{cr}$, the kinetics of oxygen exchange is governed by $\tilde{D}$. For sample thickness $<< l_{cr}$, the kinetics of oxygen exchange is governed by k_{chem}. Typically conductivity relaxation is conducted on dense bar-shaped samples of thickness $\geq l_{cr}$. On many materials, experimental work on dense samples over a temperature range between ~600 and 900°C has shown that both $\tilde{D}$ and k_{chem} increase with increasing temperature, and follow an Arrhenius behavior [6-8]. The use of a porous sample with average particle size $<< l_{cr}$ to determine k_{chem} has been demonstrated by this group in previous work [9-11]. The experimental approach is identical to that used on dense bodies but the kinetics of equilibration was shown to depend only on k_{chem} without any influence from $\tilde{D}$. The equilibration times for porous MIEC samples of composition $La_{0.6}Sr_{0.4}CoO_{3-\delta}$ (LSC40) and $La_{0.8}Sr_{0.2}FeO_{3-\delta}$ (LSF20) increased with decreasing temperature over a temperature range from 600 to 800°C, especially at lower p_{O_2}'s [9-11]. That is, the relaxation time was smaller at lower temperatures and the corresponding calculated k_{chem} increased with decreasing temperature over the temperature range investigated. That is, the temperature dependence of k_{chem} obtained using dense samples reported in the literature and porous samples are opposite. Clearly, the temperature dependence of k_{chem} obtained from porous samples cannot be described by a thermally activated process. Increasing k_{chem} with decreasing temperature appears to be consistent with its possible dependence on oxygen surface coverage, in turn governed by an adsorption isotherm such as Langmuir.

This paper presents further conductivity relaxation work on $La_{0.5}Sr_{0.5}CoO_{3-\delta}$ (LSC50) using porous samples of a very fine particle size in an attempt to investigate surface exchange kinetics over a wider temperature range, down to 350°C. LSC50 was chosen as the MIEC material of choice because of its excellent ionic conductivity even at low temperatures. The critical thickness, l_{cr}, is expected to decrease with decreasing temperature. For this reason, samples of a very fine particle size were made so that the average particle size would be below l_{cr} to as low a temperature as possible. It is expected that surface kinetics will be rate limiting down to some temperature below which diffusion becomes sluggish – and a transition from surface exchange control to diffusion control is expected at lower temperatures.

The analysis of data is done using the porous sample model developed previously [9-11], and also by approximating the particle shape in the porous sample to spherical and cylindrical geometries and using the mathematical solutions of diffusion equations given by Crank [12]. The mathematical solutions to diffusion equations for flux across a surface and into the bulk involve both diffusion and surface exchange terms. However, for a particle size well below l_{cr} at a given temperature, the solutions are sensitive to surface exchange kinetics only. The spherical and cylindrical models are then used to obtain values of k_{chem} down to a temperature where transition from surface exchange control to diffusion control occurs.

2. THEORETICAL BACKGROUND

When a porous MIEC sample placed in a chamber is subjected to an abrupt p_{O_2} change, four processes occur, each having a different time constant or a characteristic time. The four processes are: (a) Change of atmosphere in the chamber. (b) Transport of the gaseous atmosphere into the porous interstices of the porous sample. (c) Surface exchange on the interior surfaces of the porous body. (d) Chemical diffusion of oxygen into the particles of the sample. In order to determine k_{chem} by this technique, step (c) must be the slowest; that is, having a time constant or a characteristic time greater than for the other three processes. Figure 1 shows a schematic of the 4 processes that occur.

By selecting a small chamber size, and by using a high gas flushing rate, the time constant/characteristic time for process (a) can be made quite small. In reality the assumed ‘step change’ in p_{O_2} is not instantaneous and there is a finite gas exchange time. Gas exchange times of more than a few seconds can adversely affect the accuracy, especially at short time periods [13]. The time constant, τ_{ch}, to flush the chamber with the new atmosphere, as defined by den Otter et al. [14], is given by

$$\tau_{ch} = \frac{V_\mathrm{r}}{\Phi_\mathrm{v.tot}} . \frac{T_\mathrm{STP}}{T_\mathrm{r}} \tag{1}$$

where V_r and T_r are the reactor volume and temperature, respectively, $\Phi_\mathrm{v.tot}$ is the flow rate of the gas and T_STP refers to room temperature. Equation (1) assumes that the chamber can be treated as a continuously stirred tank reactor (CSTR), which requires perfect mixing (extreme limit of turbulent mixing) [15]. The experiments were conducted in a specially designed and built quartz tube. The effective volume of the sample chamber, i.e. chamber volume minus volume of sample and insulated current leads, was ~6.3±0.5 cm^3. At a gas flow rate of 600 ml/min, the time constant for switching the atmosphere in the chamber at 800˚C was approximately 0.17 sec. This calculation assumes a continuously stirred tank reactor (CSTR), which requires complete mixing, typical of extreme limit of turbulent behavior. Calculations using the effective tube diameter and volume flow rate, however, yield a Reynolds number of ~45 to 40 between 600 and 800$^\mathrm{o}$C, which corresponds to laminar flow and well below that for a turbulent flow. For a laminar flow, the change of atmosphere in the chamber cannot be described by a first order kinetic equation (implied in equation (1) as a time constant). Rather, the change of atmosphere essentially occurs as a step function (plug flow reactor (PFR)) [15]. Based on flow rates, chamber geometry, and sample dimensions, the estimated time for this step change across the sample was <0.09 second. That is, the time required for a complete change of atmosphere across the length of the sample in the chamber from the initial to final is <0.09 second. Thus, the assumption of CSTR overestimates the time required for chamber equilibration, and in reality the chamber flush time was closer to the plug flow behavior. Even with the assumption of CSTR, however, the time constant is rather small. This gas exchange process is illustrated schematically by Figure 1-(a).

The application of conductivity relaxation technique to porous bodies assumes gas transport in the porous interstices to be much faster than kinetics of surface exchange. By ensuring that the sample is sufficiently porous and relatively thin, the time constant/characteristic time for process (b) can similarly be made very small. An estimate of the time required for gas diffusion to occur into the pores of such samples was made. This calculation was based on binary diffusion into the porous body. The effective diffusion coefficient, D_{eff}, of oxygen-nitrogen through porous bodies is given by [16]:

$$D_{eff} = \frac{D_{O_2-N_2} V_v}{\varepsilon} \tag{2}$$

where $D_{O_2-N_2}$ is the binary diffusion coefficient of oxygen-nitrogen, which can be calculated using the Chapman-Enskog model [17], V_v is the porosity, and ε is the tortuosity factor. A one dimensional diffusion equation was solved numerically using D_{eff} and the time required for the p_{O_2} in the center of the sample to reach 99% of the p_{O_2} after the switch was calculated. For an assumed tortuosity factor of 5, the estimated time was between 0.055 and 0.14 sec over the temperature range investigated. This gas transport into the pores, process (b), is illustrated in Figure 1-(b).

Process (a) is not affected by the microstructure. Process (b), in general, is only weakly dependent on the microstructure of the porous sample[1]. However, processes (c) and (d) are clearly dependent on the sample microstructure. The time constant for process (c), τ_r, governed by k_{chem} can be defined approximately by:

$$\tau_r \propto \frac{1}{S_V k_{chem}} \approx \frac{d}{k_{chem}} \tag{3}$$

where S_V is the specific surface area of the body and d is the average particle size of the porous body. Similarly the time constant/characteristic time for process (d), τ_D, which is governed by $\widetilde{D}$, can be described by:

$$\tau_D \propto \frac{d^2}{\widetilde{D}} \tag{4}$$

Clearly process (d) is more influenced by the average particle size due to the d^2 dependence and τ_D decreases more rapidly with decreasing particle size than τ_r. A critical particle size, d_{cr}, can be defined at which τ_r and τ_D are equal. For $d < d_{cr}$, $\tau_r > \tau_D$, and for $d > d_{cr}$, $\tau_r < \tau_D$. By ensuring that $d << d_{cr}$, one can ensure that

---

[1] Assuming porosity is high enough and pore size is sufficiently large (so that Knudsen diffusion is ignored).

$\tau_D << \tau_r$. Under such conditions, process (c), illustrated by Figure 1-(c), is the slowest and a porous body can be used to measure k_{chem} by conductivity relaxation. The use of a porous sample instead of a dense sample also closely resembles actual SOFC cathodes, which are porous and of a fine microstructure. The objective of this work was to investigate this regime of kinetic behavior.

In porous samples of very fine microstructure, diffusion in very small particles is assumed fast, so that the concentration is essentially uniform within the solid at any time during equilibration (for $\tau_D << \tau_r$). If the specific surface area of the porous body of volume fraction porosity V_v is given by S_V (in cm^2/cm^3 or cm^{-1}), the average concentration at time t is $C(t)$ and the final equilibrated concentration is C_o, the mass balance of oxygen incorporation (or expulsion) is given by

$$S_V k_{chem}\left(C_o - C(t)\right)dt = \left(1 - V_v\right)dC(t) \tag{5}$$

the integration of which gives

$$\frac{C_o - C(t)}{C_o - C(0)} = \exp\left[-\frac{t}{\left(\dfrac{1-V_v}{S_V k_{chem}}\right)}\right] = \exp\left[-\frac{t}{\tau_r}\right] \tag{6}$$

which represents first order kinetics with time constant given by

$$\tau_r = \frac{\left(1 - V_v\right)}{S_V k_{chem}} \tag{7}$$

Note that the time constant τ_r is defined in terms of the specific surface area of the porous body, S_V, rather than the average particle size, *d*. This also means that if the above conditions are satisfied, the only relevant parameters are S_V and V_v, and the kinetics of equilibration is independent of other microstructural features, such as particle shape. In terms of the normalized conductivity, $g(t)$, the above may also be written as

$$g(t) = \frac{\sigma(t) - \sigma(0)}{\sigma_\infty - \sigma(0)} = 1 - \exp\left[-\frac{t}{\tau_r}\right] \tag{8}$$

where $\sigma(0)$ is the conductivity of the sample before the switch in p_{O_2}, $\sigma(t)$ is the conductivity at time t after the switch and σ_∞ is the conductivity after the sample is equilibrated to the new p_{O_2}. The experimental procedure consists of measuring the time dependence of conductivity after an abrupt change in atmosphere, fitting a first order kinetic equation to the normalized conductivity, $g(t)$ vs. t plot, and determining the time constant, τ_r, which is related to k_{chem}, V_v, and S_V by equation (7). The S_V can be determined using quantitative stereology [18]. Volume fraction porosity, V_v, can be measured by the fluid immersion method as well as by systematic point count using quantitative stereology [18]. From these measurements, k_{chem}, can be determined using porous samples, given in terms of measured parameters using equation (7).

Transport kinetics in porous samples can also be analyzed assuming that the particle geometry is approximately spherical or cylindrical. For spherical geometry, data can be analyzed using the diffusion equation:

$$\frac{\partial C}{\partial t} = \tilde{D}\left(\frac{\partial^2 C}{\partial r^2} + \frac{2}{r}\frac{\partial C}{\partial r}\right) \qquad 0 \le r \le a \qquad (9)$$

where a is the particle radius, with the initial condition

$$C(r, 0) = C(0) \qquad 0 \le r \le a$$

and boundary conditions

$$C(a, t) = C_o \qquad t > 0$$

and

$$-\tilde{D}\left.\frac{\partial C(r,t)}{\partial r}\right|_{r=a} = k_{chem}(C_o - C_s(t)) \qquad t > 0 \qquad (10)$$

where C_o is the concentration of oxygen in the particle after equilibration to a new p_{O_2}, $C(0)$ is the initial concentration of oxygen in the particle corresponding to the initial p_{O_2}, and $C_s(t)$ is the concentration of oxygen just inside the particle surface at time t. Using the solution to the diffusion equation given by Crank [12], the normalized conductivity, $g(t)$, for porous body containing spheres of radius a, assuming a linear relation between conductivity and concentration, can be described by[2]:

$$g(t) = \frac{\sigma(t) - \sigma(0)}{\sigma_\infty - \sigma(0)} = \frac{C(t) - C(0)}{C_o - C(0)} = \frac{M(t)}{M_\infty} = 1 - \sum_{n=1}^{\infty} \frac{6L^2 \exp(-\beta_n^2 \tilde{D} t / a^2)}{\beta_n^2 \left\{\beta_n^2 + L(L-1)\right\}} \qquad (11)$$

where $\sigma(0)$ is the initial conductivity, σ_∞ is the conductivity after the sample is equilibrated to the new p_{O_2} (that corresponding to C_o), and $\sigma(t)$ is the conductivity after time t, which corresponds to $C(t)$, the average concentration at time t, defined as:

$$C(t) = \frac{3}{a^3}\int_0^a C(r,t) r^2 dr \qquad (12)$$

---

[2] For the spherical geometry, this is only an approximation, and not valid rigorously.

$M(t)$ is the net amount of oxygen that entered (left) in time t after the change in p_{O_2} and M_∞ is the net amount of oxygen that entered (left) after an infinite time following the change in p_{O_2}. The β_n's are the positive roots of the transcendental equation

$$\beta_n \cot \beta_n + L - 1 = 0 \tag{13}$$

where

$$L = \frac{a k_{chem}}{\widetilde{D}} = \frac{a}{l_{cr}} \tag{14}$$

For a cylindrical geometry transport is analyzed in a long circular cylinder (length $>> r$) using the diffusion equation:

$$\frac{\partial C}{\partial t} = \frac{1}{r}\frac{\partial}{\partial r}\left(r\widetilde{D}\frac{\partial C}{\partial r}\right) \quad 0 \le r \le a \tag{15}$$

The same initial condition and boundary conditions given for the spherical geometry are applicable here. The normalized conductivity is given by [12][3]:

$$g(t) = \frac{\sigma(t) - \sigma(0)}{\sigma_\infty - \sigma(0)} = \frac{C(t) - C(0)}{C_o - C(0)} = \frac{M(t)}{M_\infty} = 1 - \sum_{n=1}^{\infty} \frac{4L^2 \exp(-\beta_n^2 \widetilde{D} t / a^2)}{\beta_n^2 \left\{ \beta_n^2 + L^2 \right\}} \tag{16}$$

The β_n's are now given by the positive roots of the transcendental equation [12]

$$\beta_n J_1(\beta_n) - L J_0(\beta_n) = 0 \tag{17}$$

where J_0 is the Bessel function of the first kind and of zeroth order, J_1 is the Bessel function of the first kind and of first order and L is defined in equation (14). The corresponding average concentration $C(t)$ at time t is given by:

$$C(t) = \frac{2}{a^2} \int_0^a C(r,t) r dr \tag{18}$$

Frequently a 'sum-of-least-squares' fitting program is used to fit experimental data to these models, where a numerical procedure is necessary to obtain solutions to equations (13) and (17). Values of β_n can be easily obtained using a numerical procedure given by den Otter et al. [14] or root finding operations built into commercially available mathematical softwares. However, as noted previously, in the limit of $a << l_{cr}$ the solutions to the diffusion equations are sensitive only to the kinetics of surface exchange. Thus, although the 'least-squares' procedure gives values for both $\widetilde{D}$ and k_{chem}, only the

---

[3] This also assumes a linear relationship between $\sigma(t)$ and $C(t)$, which is strictly valid only for cylinders aligned in one direction – the direction conductivity is measured.

surface exchange term is meaningful as large variations in $\widetilde{D}$ have little or no effect on the best fit. The objective of this paper is to present the results of a study on LSC50 from 350 to 800°C and compare values of k_{chem} obtained using the porous body analysis as well as using both spherical and cylindrical solutions for the diffusion equation particles in the porous body.

3. EXPERIMENTAL

LSC50 powder (Praxair Specialty Ceramics) was mixed with 25 wt.% carbon (HTW – Germany, 10-20 μm spherical particles) and attrition-milled in ethanol for 4 hrs. The dried powder was mixed with 3 wt.% ethylene glycol (as binder) and bars were die pressed uniaxially, and then isostatically pressed at 32,000 psi. The bars were heated at 1ºC/min in air to 500ºC to burn off carbon and create porosity, and sintered in air at 1000ºC to fabricate porous bars fine particle size and large specific surface area. A few bar samples were also impregnated with epoxy and polished to a level finish for stereological analysis on a scanning electron microscope (SEM).

Silver mesh and paste were used to attach silver leads in a four-probe configuration. The sample was placed in a quartz chamber and inserted into a tube furnace for conductivity relaxation measurements. A thermocouple was placed inside the sample chamber to measure possible temperature fluctuations during measurements. Experiments were carried out between 350 and 800˚C in 50 degree intervals for the p_{O_2} switch from 0.06 to 0.04 atm and 0.04 to 0.06 atm. Measurements were also made at the larger p_{O_2} step changes of 0.21 to 0.10 atm. Voltage and current were measured using a Solartron 1287 Electrochemical Interface and recorded using 'CorrWare' software from Scribner Associates.

4. RESULTS AND DISCUSSION

Figure 2 is a plot of the normalized conductivity, $g(t)$ vs. time for the LSC50 porous sample sintered at 1000°C. The plots are given for the p_{O_2} step change from 0.06 to 0.04 atm at 750, 600, and 450°C (with data for 350^{o}C given as an inset due to relatively long relaxation time). Data at other temperatures are not shown for the sake of clarity. The sample equilibration times decreased monotonically from 750°C (~55 sec) down to a minimum at ~500°C (~26 sec) to 450°C (~28 sec). Below this threshold the sample equilibration times increased quite sharply; 400°C (~45 sec) and 350°C (~150 sec) with decreasing temperature.

The k_{chem} is related to τ_r, S_V, and V_v, by equation (7) for the porous model. The pore surface area per unit volume, S_V, of the randomly oriented surfaces of a porous body can be obtained from the equation from quantitative stereology given by [18]

$$S_V = 2P_L \text{ cm}^{-1} \qquad (19)$$

From the measurements of P_L, the S_V for the porous LSC50 sample sintered at 1000°C was estimated to be ~29,000 cm^{-1}. The V_v was measured to be ~0.71. The k_{chem} obtained between 750ºC and 350ºC from the measured τ_r, S_V and V_v for the porous sample model are plotted in Figure 3 vs. 1000/T for a p_{O_2} step change from 0.06 to 0.04 atm. This figure clearly shows a monotonic increase in k_{chem} with decreasing temperature, from 1.35 x 10^{-6} cm/s at 750°C to 2.1 x 10^{-6} cm/s around 450°C. Below 450°C the k_{chem} appears to be thermally activated and decreases rapidly with decreasing temperature, to ~1 x10^{-7} cm/s at 350°C.

The normalized conductivity data from the above sample were also fitted to the solutions for the spherical and cylindrical models, equations (11) and (16). SEM micrographs of the sample revealed a uniform microstructure with average particle size ~0.5 microns. Hence, the radius a was chosen as 0.25 micron. Figure 3 also shows plots of k_{chem} vs. 1000/T obtained from the spherical and cylindrical models for the LSC50 sample sintered at 1000°C. The results from the spherical and cylindrical geometry solutions show similar trends, with k_{chem} increasing with decreasing temperature between ~750 and ~500^{o}C, and thereafter sharply decreasing with further decrease in temperature from ~500 to 350^{o}C. The agreement between the results from the spherical and cylindrical geometry solutions and the porous sample model is very good. The value of k_{chem} obtained from the porous sample model, in which it is a-priori assumed that $\tau_r >> \tau_D$, lies between the values obtained from the spherical and cylindrical models.

5. CONCLUSIONS

The present work has shown that the chemical surface exchange coefficient, k_{chem}, can be determined using porous MIEC materials such that over a temperature range, the slowest process is that of surface exchange. Such a condition is realized when the particle size, d, in the porous body is much smaller than the critical length, l_{cr}. Under such conditions, the time response of normalized conductivity to an abrupt p_{O_2} change can be described by a simple first order kinetics and the time constant can be uniquely related to k_{chem}. In the present work, three models were used for the estimation of k_{chem}; (a) Porous body model which depends only on S_v and V_v as the microstructural parameters, (b) A solution to the diffusion equation assuming the particles in the porous body to be spherical, and (c) A solution to the diffusion equation assuming the particles in the porous body to be cylindrical. For LSC50, the k_{chem} was determined for a p_{O_2} step change between 0.04 and 0.06 atm. over a range of temperatures between 350 and 750^{o}C. It was observed that the k_{chem} increased with decreasing temperature between 750 and ~450^{o}C. This is in contrast to results on dense samples, which show that the k_{chem} decreases with decreasing temperature over the same range. Increasing k_{chem} with decreasing temperature determined using porous samples may indicate a role for surface adsorption by a model such as Langmuir. For temperatures in the range from 450 to 350°C, the k_{chem} determined using porous bodies sharply decreased with decreasing temperature, consistent with a thermally activated process over this range.

ACKNOWLEDGEMENTS: This work was supported by the U.S. Department of Energy under Contract No. DE-FC26-02NT41602.

REFERENCES

1. H. J. M. Bouwmeester, H. Kruidhof and A. J. Burggraaf, *Solid State Ionics*, **72**, 185-194 (1994).
2. S. Carter, A. Selcuk, R. J. Chater, J. Kajda, J. A. Kilner and B. C. H. Steele, *Solid State Ionics*, **53-56**, 597-605 (1992).
3. I. Yasuda, K. Ogasawara, M. Hishinuma, T. Kawada and M. Dokiya, *Solid State Ionics*, **86-88**, 1197-1201 (1996).
4. R. H. E. van Doorn, I. C. Fullarton, R. A. de Souza, J. A. Kilner, H. J. M. Bouwmeester and A. J. Burggraaf, *Solid State Ionics*, **96**, 1-7 (1997).
5. B. C. H. Steele, *Solid State Ionics*, **75**, 157 (1995).
6. J. E. ten Elshof, M. H. R. Lankhorst and H. J. M. Bouwmeester, *J. Electrochem. Soc.*, **144**, No. 3 (1997).
7. L. M. van der Haar, M. W. den Otter, M. Morskate, H. J. M. Bouwmeester and H. Verweij, J. Electrochem. Soc., 149 (3), J41-J46 (2002).
8. S. Wang, A. Verma, Y. L. Yang, A. J. Jacobson and Ben Abeles, Solid State Ionics, 140, 124-133 (2001).
9. Ramanan Ganeshananthan and Anil V. Virkar, "Electrical Conductivity Relaxation on Dense and Porous La0.6Sr0.4CoO3-δ", in High Temperature Materials Chemistry Symposium in Honor of Professor C. B. Alcock – Q1, 204th ECS Meeting, October 12-16, 2003, Orlando FL.
10. Ramanan Ganeshananthan and Anil V. Virkar, submitted for publication to the *J. Electrochem. Soc.*, April 19th 2004.
11. Ramanan Ganeshananthan and Anil V. Virkar, "Surface Exchange Coefficient Measurements on Porous $La_{0.8}Sr_{0.2}FeO_{3-\delta}$ by Conductivity Relaxation", in Fifth International Symposium on Mixed Conducting Ceramics – S1, 206th ECS Meeting, October 3-8, 2004, Honolulu, HI.
12. J. Crank, *Mathematics of Diffusion*, 2nd Edition, p. 60, Oxford University Press, Oxford, UK (1995).
13. W. Preis, E. Bucher and W. Sitte, *J. Power Sources*, **106**, n. 1-2, 116 (2002).
14. M.W. den Otter, H.J.M. Bouwmeester, B. A. Boukamp and H. Verweij, *J. Electrochem. Soc.*, **148** (2), J1 (2001).
15. R. B. Bird, W. E. Stewart, and E. N. Lightfoot, *Transport Phenomena*, p. 736-737, John Wiley, New York (2002).
16. E.L. Cussler, *Diffusion – Mass Transfer in Fluid Systems*, Cambridge University Press, Cambridge, UK (1995).
17. S. Chapman and T. Cowling, *Mathematical Theory of Non-uniform Gases*, 3rd Edition, Cambridge University Press, Cambridge, UK (1970).
18. Erwin E. Underwood, *Quantitative Stereology*, p. 23, Addison-Wesley Publishing Co., Reading, MA (1970).

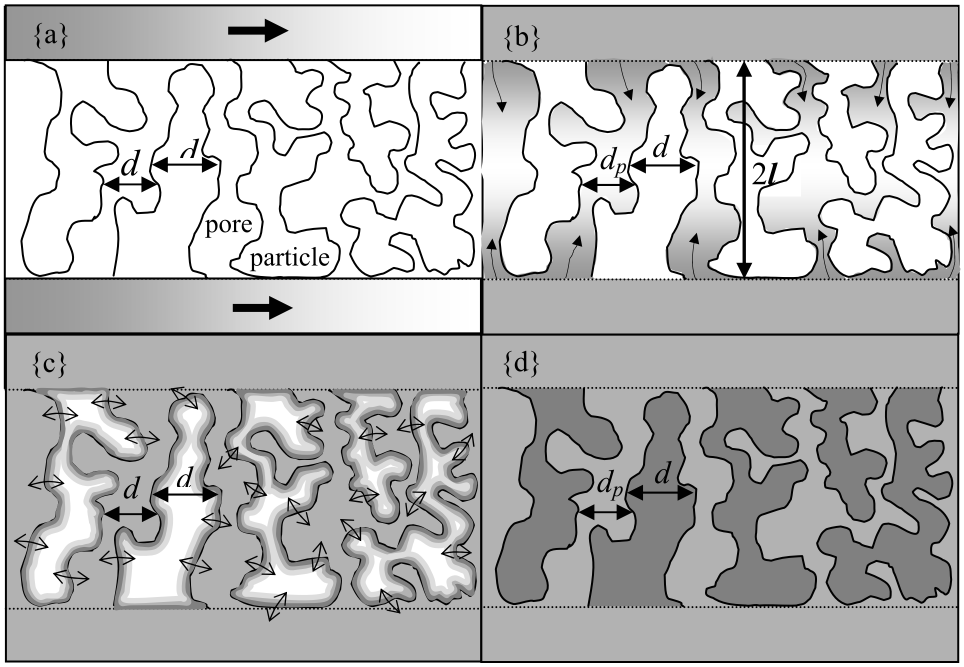

Figure 1. A schematic of the 4 processes that occur when an abrupt change in p_{O_2} is made: (a) change of atmosphere in the chamber; (b) gas transport into the porous interstices; (c) surface exchange on the interior surfaces; (d) chemical diffusion of oxygen into the particles.

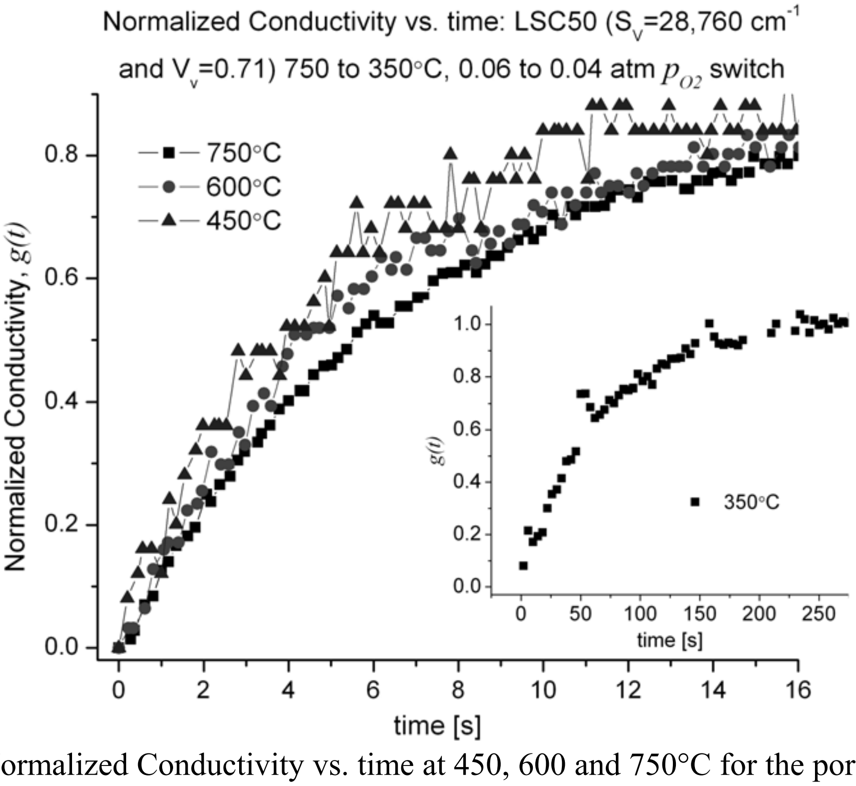
Normalized Conductivity vs. time: LSC50 (S_V=28,760 cm^{-1} and V_v=0.71) 750 to 350°C, 0.06 to 0.04 atm p_{O2} switch

Figure 2. Normalized Conductivity vs. time at 450, 600 and 750°C for the porous LSC50 sample sintered at 1000°C: p_{O_2} change from 0.06 to 0.04 atm. The inset shows data for 350°C.

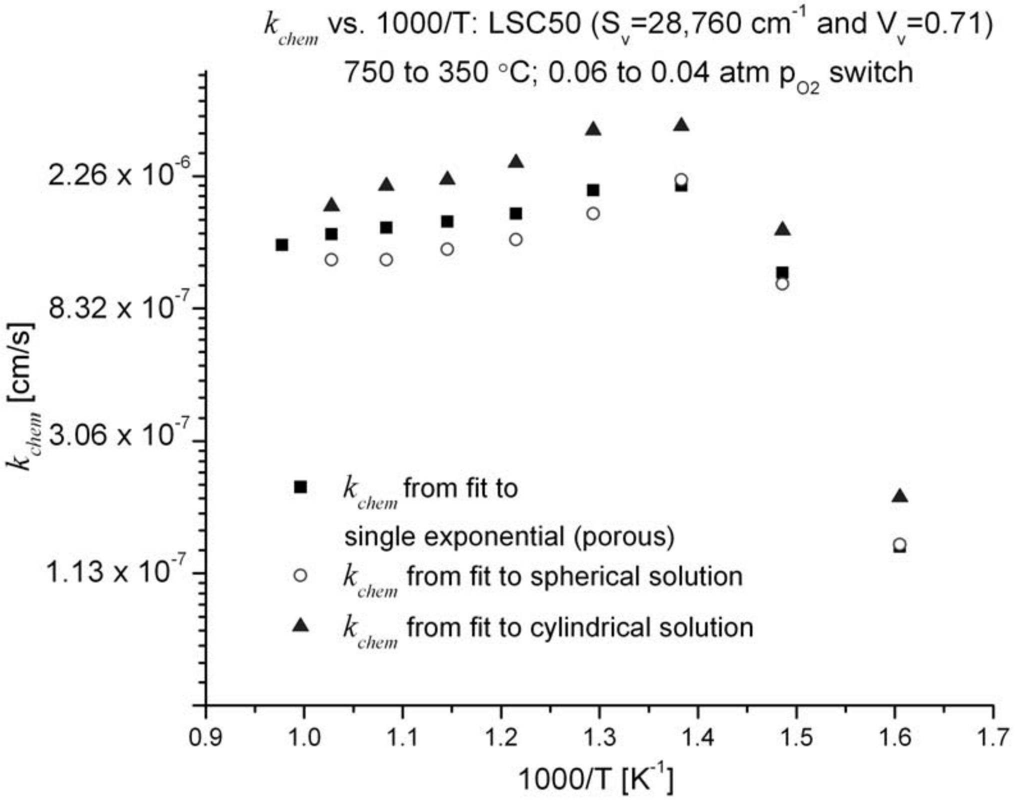

Figure 3. k_{chem} vs. 1000/T for the porous sample, spherical and cylindrical geometry models: 350 to 700°C for the porous LSC50 sample sintered at 1000°C; p_{O_2} change from 0.06 to 0.04 atm.

EFFECT OF MICROSTRUCTURE AND SPACE CHARGE ON CATHODIC POLARIZATION

Feng Zhao and Anil V. Virkar[1]
Department of Materials Science and Engineering, University of Utah
122 S. Central Campus Drive, Salt Lake City, Utah 84112

ABSTRACT

Bar-shaped samples of porous samaria-doped ceria (SDC) with large neck sizes were fabricated using a three-step method. In the first step, two phase samples containing NiO + SDC were fabricated by sintering powder compacts. In the second step, NiO was reduced to Ni at 800°C in a hydrogen-containing atmosphere. In the third step, Ni was removed by acid leaching, leading to the formation of porous SDC samples with wide inter-particle necks. The conductivity of bar samples was measured using a DC 4-probe technique between 650 and 800°C. The samples were then annealed at 1200 and 1400°C. The conductivity of the samples was again measured between 650 and 800°C. It was observed that the lower the annealing temperature, the lower was the conductivity. Anode-supported cells were fabricated with cathode made of Sr-doped $LaCoO_3$ (LSC) and SDC, wherein the SDC layer was formed by the three-step method. Cell performance was measured at 800°C with the cells subjected to thermal treatments at 1200 and 1400°C prior to infiltration of LSC using aqueous salt solutions. It was observed that the lower the annealing temperature, the lower was the cell performance. The observed behavior is attributed in part to space charge effects. Thermal treatments, however, may also lead to precipitation of insulating phases at grain boundaries thereby increasing resistance and lowering cell performance.

1. INTRODUCTION

Recent work has shown that cathodic polarization can be substantially reduced provided the porous cathode is a mixed conductor [1-4]. For this reason, the cathode must either be made of a single-phase mixed ionic/electronic conductor (MIEC), or a composite mixture of an oxygen ion conductor (e.g. yttria-stabilized zirconia, YSZ), and an electrocatalyst (e.g. LSM) which is an electronic conductor. In terms of the intrinsic charge transfer resistance (area specific charge transfer resistance, R_{ct} in Ωcm^2), the oxygen ion conductivity of the cathode, σ_{ic}, the grain size of the cathode, d, and the porosity of the cathode, V_v, the polarization resistance can be given by [2]

---

[1] To whom correspondence should be addressed.

$$R_p \approx \sqrt{\frac{dR_{ct}}{\sigma_{ic}(1-V_v)}} \tag{1}$$

For a given cathode material, equation (1) shows that the larger the σ_{ic}, the lower is the R_p, and thus the better is the cathode. It is known that the apparent conductivity of porous ceramics is a function of porosity and morphology, such as grain size, inter-particle neck size, etc. The smaller the grain size, generally the lower is the conductivity) (the higher is the resistivity). According to the analytical model on the role of connectivity on electrical conductivity of porous bodies including effects of grain boundaries and space charge, small neck size has a profoundly adverse effect on the effective conductivity [5]. Also, the space charge layer at grain boundaries and free surfaces in porous media can have a significant effect on the effective conductivity.

It has been reported that the grain-boundary resistivity is strongly influenced by thermal history [6-8]. After quenching from high temperatures, the grain-boundary resistivity is generally quite small. However, after annealing at lower temperatures, the resistivity increases significantly. The effect of heat treatment on zirconia electrolytes has been extensively studied and is closely related to the type of dopant and the dopant concentration [9-11]. Heat treatment leads to the segregation of a dopant-rich layer near grain boundaries and triple points and also the formation of a layer of space charge region, which has been attributed to the decrease in the conductivity of YSZ [12, 13]. However, very little information is available on the effect of high temperature heat treatment on conductivity of ceria-based materials, and especially for porous bodies.

In this study, the conductivity of porous SDC samples was measured using a four-probe DC technique. In order to study the effect of heat treatment on conductivity of porous bodies, porous SDC samples sintered at a high temperature were heat treated at lower temperatures. The porous SDC samples used in this study were made by the three step method involving a leaching step. Then the conductivity of the samples was measured again using a four-probe DC technique at various temperatures. The measurement temperature was always much lower than the thermal treatment temperature such that no microstructural changes were expected during the measurements.

The role of effective conductivity of porous ionic conductors on electrode polarization was examined. The effects of space charge and morphology were included in the model. A leaching process was used to fabricate porous SDC layers on anode-supported cells. Then, the cells with the porous layers were heat treated at lower temperatures. Subsequently, an infiltration process was used to fabricate composite cathodes. This involved the introduction of an aqueous solution of salts of La, Sr, and Co, followed by a low temperature (less than 1100^{o}C) firing to form LSC in-situ. Electrochemical testing of the as-fabricated cells was conducted to determine the possible effect of space charge.

2. EXPERIMENTAL

2.1 Fabrication of Porous Samaria Doped Ceria (SDC) Samples with Large Neck Sizes:
Powder mixtures of commercial NiO and SDC (combustion method) in various NiO:SDC weight ratios corresponding to 20:80, 30:70 and 40:60 were wet-milled, dried, and then screened. Bar-shaped powder compacts were formed by die-pressing and iso-static pressing. Bar samples were sintered in air at 1600°C for 2 hours. The samples were then reduced in 10% hydrogen + 90% nitrogen for 2 hours at 800°C, followed by 2 hours at 800°C in 100% hydrogen. Finally the reduced bar samples were leached in dilute nitric acid for 3 hours. This led to the removal of Ni as $Ni(NO_3)_2$, and created additional porosity. The resulting samples were single-phase, porous SDC. Four probe DC conductivity measurements were performed on as-processed porous samples.

2.2 Heat Treatment of Porous SDC Samples:
Some of the porous samples, of varying porosity levels and fabricated using the leaching process were heat treated at 1200°C for 20 hours and then air-quenched to room temperature at a quenching rate of ~6500°C/min. Total conductivity was measured using a four probe DC technique on samples with varying porosity levels over a range of temperatures between 650 and 800°C.

2.3 Microstructure Characterization:
After conductivity measurements, fractured pieces of each sample were impregnated with an epoxy. After curing and hardening the epoxy, the samples were mounted in a plastic mount, and subsequently polished to a 1 micron finish. The samples were then examined under a scanning electron microscope (SEM). The microstructures of porous samples were characterized by quantitative stereology to estimate the porosity.

2.4 Fabrication of Composite Cathodes by Infiltration & Electrochemical Testing of Single Cells:
Anode-supported cells with a Ni/YSZ anode support, a Ni/YSZ anode interlayer, and a thin film YSZ electrolyte/SDC barrier layer were green-formed by slurry coating pressed anode support discs. Subsequently, a layer of NiO + SDC powder mixture was applied on the SDC barrier layer. The resulting cells were sintered at 1600°C. Some of the cells were later annealed at 1400°C for 6 h and some at 1200°C for 20 h, followed by quenching to room temperature. The NiO + SDC layer was subjected to 10% hydrogen + 90% nitrogen for 4 hours at 800°C to reduce NiO to Ni. Nickel was leached out using dilute nitric acid for 2 hours, resulting in a highly porous framework of SDC with wide necks. An aqueous solution of $La(NO_3)_3$, $Sr(NO_3)_2$ and $Co(NO_3)_2$ in requisite proportions was infiltrated into the porous SDC and fired at 1100°C for 1 h to form a composite cathode containing LSC. Finally, the performance of the cells was tested at 800°C with hydrogen as fuel and air as oxidant. The ohmic contribution was measured by current interruption. After testing the microstructure was examined under SEM.

3. RESULTS & DISCUSSION

3.1 Microstructure of Porous SDC: Conductivity of Porous SDC Samples Before Heat Treatment:

Figure 1shows an SEM micrograph of a typical porous SDC bar fabricated. Bars of porosity ranging between 29% and 59% were fabricated. All samples exhibited good connectivity between grains. For samples fabricated using the leaching process, the porosity was mainly dictated by the selected weight ratio of NiO/SDC. During sintering of the samples, NiO and SDC grains grow simultaneously and fill up the space by forming regular polyhedra (tetrakaidecahedra). The NiO skeleton in the composite keeps the SDC skeleton from collapsing and vice-a-versa. Using this process, samples of density greater than 95% of the theoretical density were made. The NiO and SDC phases in the composite form two contiguous skeletons with large neck sizes (which are grain facets). After reducing NiO to Ni and leaching it away, samples with the desired microstructures of high porosity & large neck sizes were obtained.

Table I shows porosity and conductivity of porous samples made using NiO-SDC powders, wherein the porosity was created by leaching away Ni. The total conductivity of samples with varying porosity levels was measured over a range of temperatures by a four probe DC method. It is seen that with increasing porosity from 30% to 59%, the conductivity decreases from 0.053 to 0.027 S/cm at 800^{o}C. Figure 2 shows a plot of the relative conductivity vs. relative density. It is known that at relatively high volume fractions of insulating phases, the net conductivity can be far below that of the conductive phase corrected for porosity through a simple linear relationship, provided the inter particle contact is poor. That is, the conductivity is dependent not only on porosity, but also on other microstructural parameters, such as grain size and neck size, etc. When the neck size is large, the effective conductivity can be calculated using a simple phenomenological equation, namely

$$\sigma_{porous} \approx \sigma_o (1 - V_V) \tag{2}$$

3.2 Effect of Heat Treatment on Conductivity of Porous SDC Samples:

The results on conductivity measurements before and after heat treatment at 1200^{o}C for 20 h are listed in Table I. After heat treatment, the conductivity of the porous bodies decreased. At 650^{o}C, the conductivity decreased to half that of samples prior to the heat treatment. At a temperature of 800^{o}C, the conductivity decreased to ~75% of that without heat treatment. The effect of heat treatment on the conductivity can in part be attributed to space charge, because no change in the microstructures (based on SEM micrographs) of the porous bodies was observed. However, the possibility of formation of secondary insulating phases along grain boundaries cannot be ruled out. A careful microstructural analysis using transmission electron microscopy (TEM) will be required to determine the possible existence of secondary grain boundary phases. The following discussion is based on the assumption of the existence of a space charge layer.

By Schottky approximation and solving Possion's equation, the maximum space charge potential for the case of no externally applied voltage can be calculated and is given by [14-19]:

$$\Delta\phi(0) = \frac{Q_{GB}^2}{2e\varepsilon_0\varepsilon_r[A^{'}]_b} \tag{3}$$

where ε_r is the static dielectric constant of the material, ε_0 is the permittivity of free space, Q_{GB} is the charge in the grain boundary core, and $[A^{'}]_b$ is the dopant concentration in the bulk.

Space charge layer thickness can be given by [16, 17]

$$\lambda = \frac{Q_{GB}}{e[A^{'}]} \approx \sqrt{\frac{\varepsilon_0\varepsilon_r\Delta\phi(0)}{e[A^{'}]}} \tag{4}$$

From equation (3), it is apparent that the temperature dependence of $\Delta\phi(0)$ may be due to the temperature dependence of: (a) the effective charge in grain boundary core, Q_{GB}, (b) the relative static dielectric constant ε_r, and (c) the effective bulk acceptor concentration $[A^{'}]_b$. The effective bulk acceptor concentration $[A^{'}]_b$ and relative static dielectric constant ε_r, however, are nearly independent of temperature. Thus, the temperature-dependent behavior of grain boundary barrier height, $\Delta\phi(0)$, must be caused by the temperature dependence of Q_{GB}.

During the process of heat treatment, the dopant is expected to segregate along the grain boundary and free surfaces, i.e., annealing at intermediate temperatures should favor the creation of positively charged interfaces by enhancing dopant segregation. After quenching from the annealing temperature, the dopant segregation at the grain boundaries is almost frozen. Thus, in the annealed and quenched samples, it is expected that the grain boundary structure at the annealing temperature can be preserved at lower temperatures, e.g. with a more inhomogeneous point-defect distribution. Thus, the grain boundary barrier height should be higher in samples annealed at lower temperatures. This means, the variation in the grain boundary blocking effect can be related to the different levels of dopant segregation achieved by changing the thermal history. Higher segregation should result in both a large space charge thickness and greater depletion of oxygen vacancies leading to greater grain boundary resistivity.

3.3 Application of Space Charge Model to Composite Cathode:

Using model developed earlier [5], equation (1) and values of various parameters from the literature [20-22], the electrode polarization resistance can be calculated. Figure 3 shows the calculated polarization resistance as a function of grain size and neck size at 800^{o}C for an electrode using YSZ as the ionic conductor in the composite cathode, and the following parameters: ρ_g (YSZ grain resistivity) = 14 Ω.cm, ρ_{sc} (resistivity of the space charge layer) = 2,250 Ω.cm, ρ_{gb} (grain boundary core resistivity) = 10 Ω.cm, λ (space charge layer thickness) = 2 nm, δ_{gb} (grain boundary core thickness) = 0.4 nm, and R_{ct} = 2 Ω.cm^2· Figure 4 shows the calculated polarization resistance as a function of grain size and neck size at 650°C using the following parameters: ρ_g = 76 Ω.cm, ρ_{sc} = 14,520 Ω.cm, ρ_{gb} = 50 Ω.cm, λ = 2 nm, δ_{gb}= 0.4 nm, and R_{ct}= 4.15 Ω.cm^2. It is seen that the polarization resistance rises sharply for small necks and large grains. Over the range of particle sizes and neck sizes (angle) that the calculations were performed, the polarization resistance varies between ~0.15 and ~0.8 Ωcm^2 at 800°C, and between ~0.5 and ~2.8 Ωcm^2 at 650°C. This result has significant implications concerning the role of grain boundaries and grain size on the polarization resistance of composite and single phase MIEC cathodes. The results show that a low polarization resistance is realized if the particle size is small and the neck size is large.

3.4 The Possible Effect of Space Charge on Cell Performance:

Figure 5 shows voltage and power density vs. current density plots at 800°C for cells with cathode fabricated by the infiltration method. In each case, cell with the SDC ionic conductor skeleton in the composite cathode was annealed and then quenched to room temperature prior to cathode precursor infiltration. The as-fabricated cell without heat treatment exhibits the highest performance. By contrast, the cell annealed at 1200°C for 20 hours exhibits the lowest performance. A possible explanation is that the lower the annealing temperature, the greater is the space charge width, the higher is the ionic resistivity in the cathode interlayer, and thus the higher is the activation polarization (Equation (1)). Since the anode interlayer was subjected to the same thermal treatment, it is expected that a similar effect likely exists in the anode interlayer (higher ionic resistivity in YSZ annealed at a lower temperature). Figure 6 shows the ohmic overpotential determined by current interruption as a function of current density for cells with various thermal histories. It is seen that the cell annealed at 1200°C has a slightly higher ohmic resistance. This is also consistent with expectations since the ionic resistivity of the YSZ/SDC bi-layer electrolyte is expected to increase by annealing at a lower temperature (1200°C) due to the space charge effect. The observation, that the effect is small is also consistent with the fact that the overall ohmic contribution is generally small in cells with a thin film electrolyte. Figure 7 shows electrode polarization, which was obtained by subtracting the ohmic contribution, as a function of current density for cells with various thermal histories. Figure 7 shows that the variation in total electrode polarization with annealing temperature is substantial, with the cell annealed at 1200°C exhibiting the highest polarization and the as-fabricated cell exhibiting the lowest polarization. Higher polarization in the cell annealed at 1200°C is again consistent with a larger space charge effect. While the results are consistent with space charge effect, the possibility of secondary, insulating phases precipitating along grain boundaries in samples annealed at a lower temperature, thus raising the net resistivity cannot be ruled out. A careful characterization of grain boundary regions will be required to answer this question.

4. SUMMARY

The present work shows that samples fabricated using the leaching method exhibits the desired microstructure comprising a wide neck size and high effective conductivity in porous SDC. The present results also show that annealing at lower temperatures increases the resistivity, consistent with the existence of a space charge effect which leads to a high resistivity region near grain boundaries due to the depletion of oxygen vacancy concentration. Measurements on anode-supported cells show that cells annealed at a lower temperature (prior to the introduction of cathode precursor by infiltration) exhibit lower performance, which can be attributed to greater electrode polarization. This higher polarization can be attributed to the expected greater space charge effect in samples annealed at a lower temperature. However, even though the results are consistent with the possible existence of a space charge effect, the formation of insulating phases along grain boundaries in annealed samples as a possible reason for higher resistivity and higher polarization resistance in annealed cells cannot be ruled out. This will require careful characterization of grain boundary regions.

REFERENCES

1. T. Kenjo, S. Osawa, and K. Fujikawa, *J. Electrochem. Soc*., 138, **349** (1991).
2. C. W. Tanner, K-Z. Fung, and A. V. Virkar, *J. Electrochem. S*oc., 144, **21-30** (1997).
3. H. Deng, M. Zhao, and B. Abeles, *Solid State Ionics*, 74 75 (1994).
4. I. V. Murygin, *Elektrokhimiya*, 23[6]740 (1987).
5. Feng Zhao and A. V. Virkar, *Proceedings - Electrochemical Society* (2004), Hawaii.
6. M. J. Verkerk, B. J. Middelhuis and A. J. Burggraaf, *Solid State Ionics* 6 (1982) 159.
7. M. V. Inozemtsev, M.V. Perfil'ev and A.S. Lipilin, *Elektrokhimiya* 10(1974) 1471.
8. A.N. Vlasov, M.V. Perfilier, *Solid State Ionics* 76 (1995) 155.
9. S.P.S. Badwal, *Solid State Ionics* 52 (1992) 23.
10. F.K. Moghadam, D.A. Stevenson, *J. Am. Ceram. Soc*. 65(1982) 213.
11. E.P. Butler, R.K. Slotwinski, N. Bonanos, J. Drennan, B.C.H. Steele, in: N. Claussen, M. Ruhle, A.H. Heuer (Eds.), *Science and Technology of Zirconia II*, Vol 12, American Ceramic Society, Columbus, OH, 1984, p. 572.
12. F.K. Moghadam, T. Yamashita, D.A. Stevenson, in: A.H. Heuer, L.W. Hobbs (Eds.), *Science and Technology of Zirconia*, Vol. 3, American Ceramic Society, Columbus, OH, 1981, p. 364.
13. J. Kondoh, S. Kikuchi, Y. Tomii, Y. Ito, *Physica.* B 262(1999)177.
14. Harbeke G., Springer Series in Solid State Science, Vol. 57. *Springer-Verlag, Berlin*, 1985.
15. Blatter, G. and Greuter, F., *Phys. Rev*., 1985, B33(6), 3952.
16. Greuter, F. and Blatter, G., *Semicond. Sci. Technol*., 1990, 5, 111.
17. Vollmann, M. and Waser, R., *J. Am. Ceram. Soc*., 1994, 77(1), 235.
18. W. Schottky, *Z. Phys*., 113, 367(1939)
19. R. Waser and R. Hagenbeck, *Acta mater.* 48(2000) 797-825.
20. X. Guo and J. Maier, *J. Electrochem. Soc*., **148**, E121 (2001).

21. D. Y. Wang, D. S. Park, J. Griffith and A. S. Nowick, *Solid State Ionics*, **2,** 95(1981).
22. W. D. Kingery, J. Am. Ceram. Soc., 57 (1974) 1.

ACKNOWLEDGEMENTS

This work is supported by the U.S. Department of Energy, under contract No: DE-FC26-02NT41602.

Table I: Conductivity of porous SDC before and after thermal treatments.

T(^{o}C)		650	700	750	800
Conductivity (S/cm) Before heat treatment	30%	0.018	0.028	0.035	0.053
	38%	0.011	0.019	0.029	0.044
	59%	0.008	0.012	0.019	0.027
Conductivity (S/cm) After heat treatment	30%	0.007	0.012	0.022	0.042
	38%	0.0055	0.011	0.018	0.038
	59%	0.005	0.009	0.014	0.024

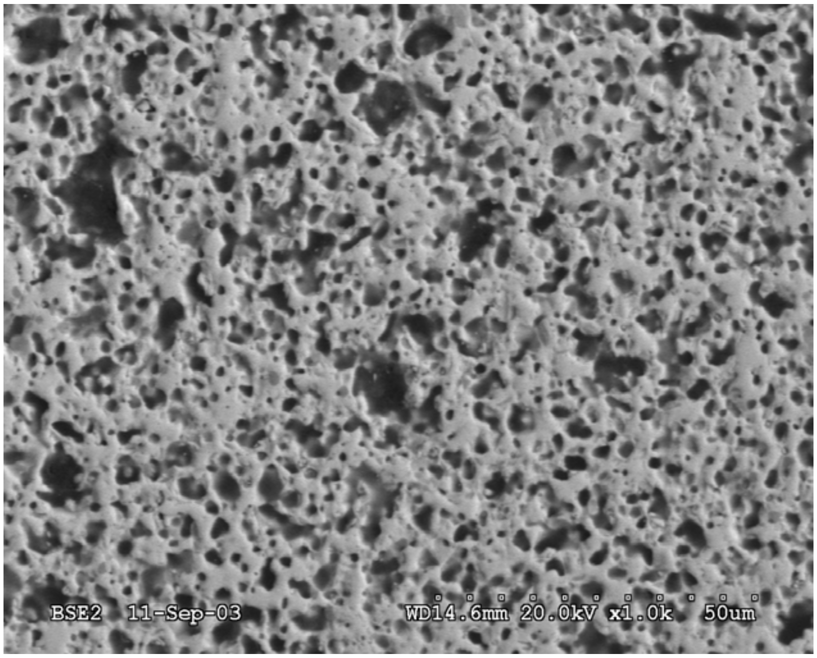

Figure 1: An SEM micrograph of a SDC bar (porosity = 30%) sintered at 1600^{o}C/2 hours (method comprising the fabrication of SDC + NiO composite, reduction of NiO to Ni, and removal of Ni by leaching). Conductivity data are given in Table I.

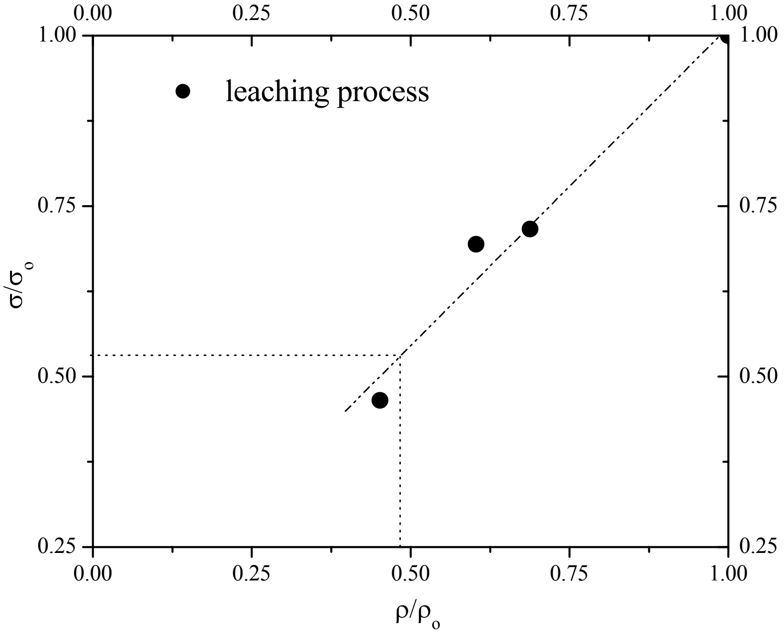

Figure 2: Relative conductivity vs. relative density. The relative conductivity is defined as the ratio of the conductivity of a sample with a given porosity to that of the fully sintered (negligible porosity) sample. Similarly, the relative density is the ratio of density of a sample with a given porosity to that of a fully dense sample.

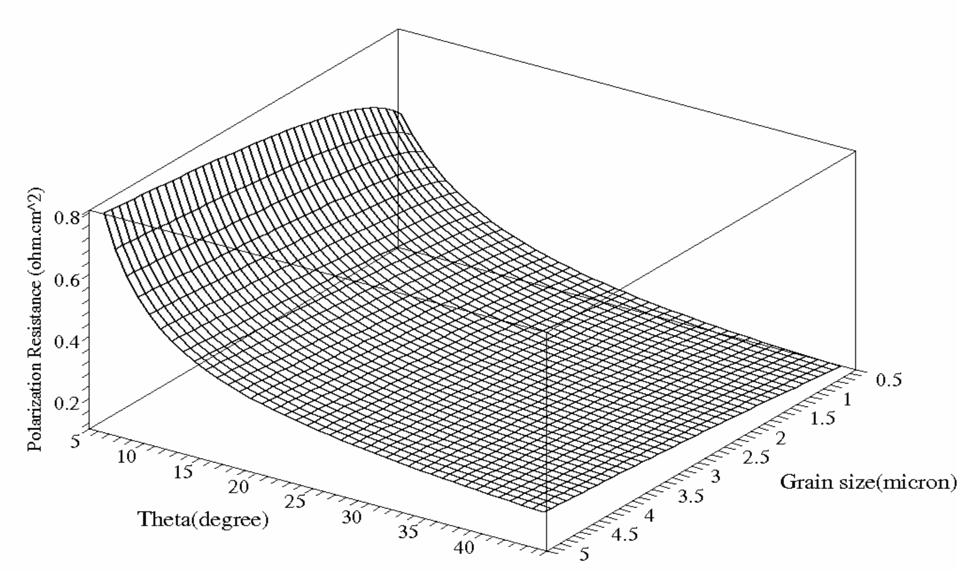

Figure 3: Calculated area specific electrode polarization resistance, using YSZ as the ionic conductor in a composite cathode, as a function of angle (relative neck size) and grain size at 800°C. Note that the polarization resistance rises sharply at small angles (narrow necks).

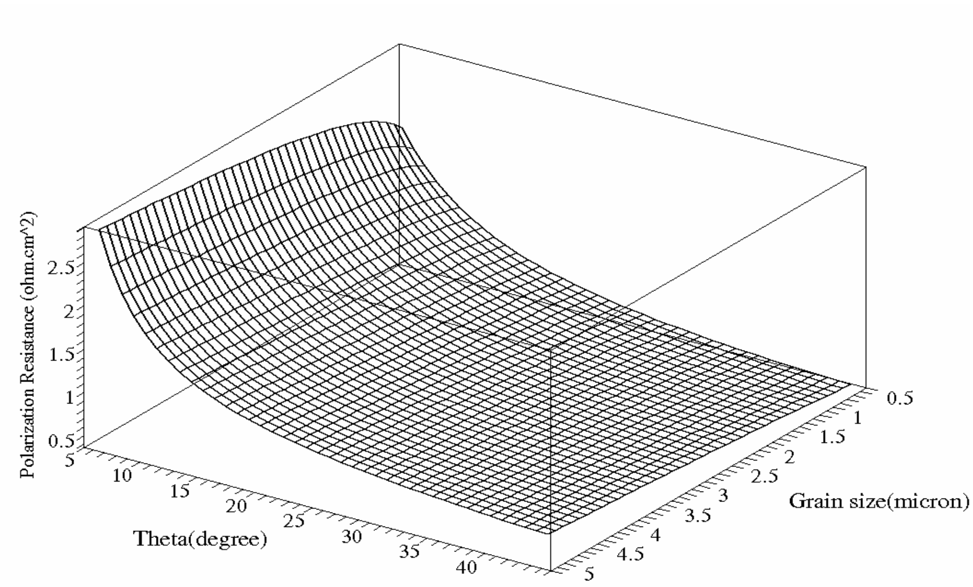

Figure 4: Calculated area specific electrode polarization resistance, using YSZ as the ionic conductor in a composite cathode, as a function of angle (relative neck size) and grain size at 650°C. Note that the polarization resistance rises sharply at small angles (narrow necks).

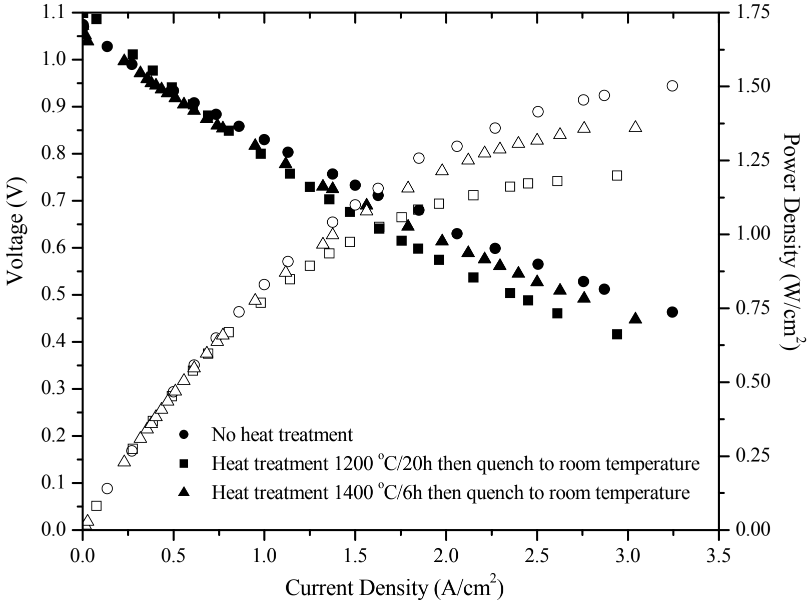

Figure 5: Voltage and power density vs. current density plots at 800°C for cells with cathode fabricated using the infiltration method, wherein the cell with the ionic conductor skeleton in the composite cathode was annealed and then quenched to room temperature prior to cathode infiltration.

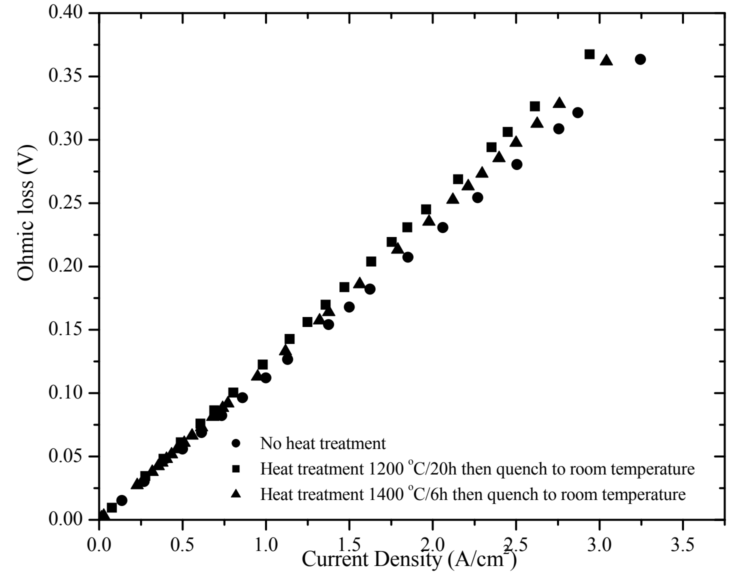

Figure 6: Ohmic overpotential (by current interruption) as a function of current density for cells with various thermal histories.

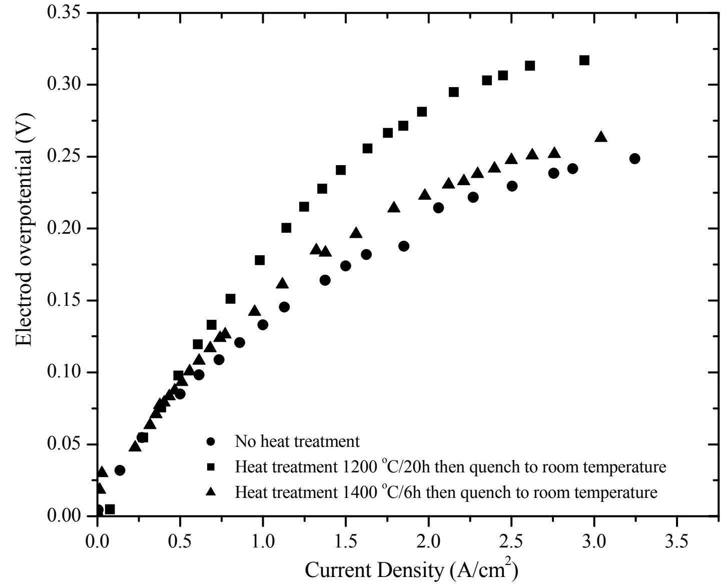

Figure 7: Electrode polarization as a function of current density for cells with various thermal histories.

EFFECT OF MORPHOLOGY AND SPACE CHARGE ON CONDUCTION THROUGH POROUS OXIDE CERAMICS

Feng Zhao and Anil V. Virkar[1]
Department of Materials Science and Engineering, University of Utah
122 S. Central Campus Drive, Salt Lake City, Utah 84112

ABSTRACT

An analytical model on the role of connectivity on electrical conductivity of porous bodies, including the roles of grain boundaries and space charge, was developed. Porous samaria-doped ceria (SDC) samples were fabricated using two methods: (1) conventional sintering of powder compacts and (2) a method comprising the fabrication of sintered NiO + SDC two phase samples, followed by reduction of NiO to Ni, and the removal of Ni by acid leaching. The latter method can fabricate porous sample with preferred high porosity and larger inter-particle neck. Electrical conductivities of as-fabricated bar samples were measured using DC 4-probe technique. The electrical conductivity of some of porous SDC samples fabricated using leaching process, as a function of temperature and oxygen partial pressure, is measured with DC 4-probe method. It was observed that the neck size has significant effect on the effective conductivity of porous body. The increase of electrical conductivity with reducing oxygen partial pressure can be explained well by the space charge model. Finally the model was applied to composite electrode. The effect of morphology of porous ionic conductor framework in composite cathode on electrode polarization was discussed.

INTRODUCTION

Recently porous ionic and mixed ionic/electronic conductors have become of interest for applications such as electrode materials in solid oxide fuel cells [1] and ceramic gas sensors [2, 3]. The apparent conductivity of porous ceramics is a function of porosity [4-5], grain size, inter-particle neck size etc. The smaller the grain size, generally the higher is the net resistivity. It was frequently reported that the grain boundary resistivity is

---

[1] To whom correspondence should be addressed.

several orders magnitude higher than that of bulk [6-10] This effect has often been attributed to an intergranular siliceous phase [11-13]. However, for materials of high-purity, the specific grain-boundary conductivity was measured to be still several orders magnitude lower than that of the bulk [14]. This low conductivity can not be attributed to the intergranular siliceous phase. Part of this resistance, however, is attributable to space charge effects, which tend to lower the charge carriers concentration near grain boundaries. Frenkel [15] is the first to propose the existence of space charge. Its mathematical analysis and implications concerning conductivity were presented by Lehovec [16], Kliewer & Koehler [17]. Subsequently, many researchers have examined the existence of space charge, but with essentially the same formalism as given by Kliewer & Koehler. Recent work by Guo [18-19] has shown that in YSZ, the grain boundary resistivity can be attributed to a space charge region (depletion of oxygen vacancies), which appears near grain boundaries. Some researchers also reported that the space charge effect on the conductivity mechanism of cerium oxide in the nanometer and micrometer size range. Kim et al. [20] discussed the conductivity mechanism of nanocrystalline ceria and concludes the space charge potential is weakly dependent on temperatures and oxygen partial pressure and leads to the much higher grain boundary resistivity. Tschoepe [21-22] discussed the rather different nature of the electrical transport properties in the nano and microcrystalline ceria by varying temperature and oxygen partial pressure and concluded that the electronic conductivity of nanocrystalline increase with decreasing grain size. Guo et al. [24] studied the properties of blocking grain boundaries in Yttria-doped and undoped ceria. The author conclude that the blocking effect in grain boundary for ceria of high purity can be attributed to the positive space charge potential leading to the depletion of oxygen vacancy. Some models were also developed to take into account of the space charge effects in nanocrystalline ceramics and polycrystalline. Tiku and Kroger [24] computed the potential difference between grain boundary and bulk and the concentrations of native and foreign point defects in the bulk, grain boundary and space charge region as a function of grain size for polycrystalline Al_2O_3 system and concluded that the contribution of space charge region to conductivity may be neglected. Tschope et al. [25] calculated the electrical conductivity of mesoscopic cubic cerium oxide crystals with space charge layers as a function of grain size. They found that the characteristic grain-size-dependent increase of electronic and decrease of ionic conductivity by assuming positive space charge. Lubomirsky et al. [26] modeled the distribution of mobile charge carriers in the space charge region of grain boundaries. They found the depletion effects are more pronounced at edges and corners just due to geometry. So far all of the studies of space charge studies have been reported on dense body. In the space-charge model, a grain boundary consists of a grain-boundary core (crystallographic mismatch region) and two adjacent space-charge layers. Depending upon the dopant type and amount, it may in principle be possible to actually enhance the oxygen vacancy concentration near grain boundaries. If the space charge region suppresses ionic conduction, measures should be taken to minimize the grain boundary effect through compositional and microstructural modifications. Despite of careful processing of fabricating the porous samples, the defect density in surface cores is much higher than in the bulk. The defects may include surface adatom, surface vacancies, adsorbed species from surrounding atmosphere etc. In addition, since with porosity, the subsurface space charge layers occupy a noticeable part of the skeleton volume of porous sample and they may narrow the path of charge carrier, consequently transport properties of porous oxide ceramics are significantly affected by the subsurface space charge region than that of dense bodies. The other factor involves the nature of inter-particle necks (or throat diameter). If the contact between particles is poor, the overall resistance can be large.

Yttria doped zirconia (YSZ) and doped cerium oxide are at present the two most widely used electrolyte materials for solid state electrochemical devices, for example, solid oxide fuel cells, oxygen separation membrane, steam electrolyzes and sensors. YSZ is a pure ionic conductor over a wide temperature range and oxygen partial pressure range. However doped ceria is an electron and oxygen ion mixed conductor with temperature and P_{O_2}. At high temperatures and at low P_{O_2}, it exhibits much n-type conductivity. At high P_{O_2} and low temperatures, ionic conductivity is dominant.

In this study, a simple, one dimensional model of the role of connectivity on electrical conductivity of porous bodies, including the roles of grain boundaries and space charge, was developed. The model developed accounts for transport through three regions: the bulk of the grain, the space charge region, and the structural part of the grain boundary. Doped ceria is chosen as a model material. The model also incorporates the effect of P_{O_2} on the carrier concentrations in the space charge layer and in the bulk and its associated effect on the bulk resistivity and that of the space charge layer. The effective resistivity of doped ceria was calculated as functions of grain size and neck size for a given P_{O_2} & a given temperature. Finally the effect of effective conductivity of porous ionic conductors on the electrode polarization was evaluated. The effect of space charge and morphology was included in the composite electrode model.

To investigate the connectivity effect, porous bar samples of samaria doped ceria (SDC) with widely varying neck sizes were fabricated, and the conductivities were measured using a four-probe DC technique. The electrical conductivity of some of porous SDC samples fabricated using leaching process, as a function of temperature and oxygen partial pressure, is measured with DC 4-probe method. In order to study the effect of space charge on cell performance, anode-supported cells were fabricated with cathode made of Sr-doped $LaCoO_3$ (LSC) and SDC, wherein the SDC layer was formed by the leaching process. Cell performance was measured at 800^{o}C with the cells subjected to thermal treatments at 1200 and 1400^{o}C, prior to infiltration of LSC using aqueous salt solutions.

MODEL

<u>Effective Resistivity of a Porous Body: No Space Charge Effect:</u> Figure 1(a) shows two grains with a grain boundary in between. Figure 1(b) shows a half of the grain of radius R and neck size r_0 with half of the grain boundary associated with it. This is the geometry used in the calculations.

After analysis (see Appendix A), the effective resistivity as a function of the relative neck size α is given by

$$\rho_{eff} \approx \frac{\rho_g}{2\sqrt{1-\alpha^2}} \ln\left[\frac{1+\sqrt{1-\alpha^2}}{1-\sqrt{1-\alpha^2}}\right] + \frac{\rho_{gb}\delta_{gb}}{2r\alpha^2\sqrt{1-\alpha^2}} \tag{1}$$

where

R: the radius of the particle, which is assumed to be a grain.

r_0: the radius of the inter-particle neck.

α: relative neck size, given by $\alpha = r_o/R$.

ρ_g: grain resistivity without the space charge effect (Ωcm).

$\rho_{gb}\delta_{gb}$: grain boundary area specific resistance(Ωcm^2).

Effective Resistivity of Porous Body: Space Charge Effect Included: A porous body is modeled as a one dimensional array of cut spheres with contact area corresponding to the neck size. The geometry of the particle used for calculations is shown in Figure 23. It consists of a half of the grain with half of the grain boundary associated with it. The net resistance is divided into three regions: (1) Region I correspond to the net resistance for the range between $x = x_0+\lambda$ to $x = R$. The corresponding resistance is R_I. (2) Region II corresponds to the net resistance for the range $x = x_0$ to $x = x_0+\lambda$. The corresponding resistance is R_{II}. (3) Region III corresponds to the transport across grain boundary core. The effective resistance, which includes the effects of space charge, grain boundary and of the neck morphology, is given by (see Appendix B)

$$R_{eff} = R_I + R_{II} + R_{III} \tag{2}$$

where

$$R_I = \int_{\cos^{-1}\left(\frac{R-x_0-\lambda}{R}\right)}^{\frac{\pi}{2}} \frac{\rho_g \rho_{sc} R \sin^3\theta d\theta}{\pi(2R\lambda\sin^2\theta - \lambda^2)\rho_g + \pi(R^2\sin^4\theta - 2R\lambda\sin^2\theta + \lambda^2)\rho_s} \tag{3}$$

$$R_{II} = \int_{\cos^{-1}\left(\frac{R-x_0}{R}\right)}^{\cos^{-1}\left(\frac{R-x_0-\lambda}{R}\right)} \frac{\rho_{sc} d\theta}{\pi R\sin\theta} \tag{4}$$

$$R_{III} = R_{gb} = \frac{\rho_{gb}\delta_{gb}}{2\pi r_0^2} = \frac{\rho_{gb}\delta_{gb}}{2\pi(R\sin\theta)^2} \tag{5}$$

with

R: the radius of the particle, which is assumed to be a grain.

r_0: the radius of the inter-particle neck.

θ: angle describing neck region given by half the angle of the cone formed by the neck joined to the center of the grain

$$\theta = \cos^{-1}\left(\frac{R - r_0}{R}\right) \tag{6}$$

λ: width of the space charge region. For simplicity, it is assumed here that in this region, the conductivity is uniform.

ρ_g: grain resistivity without the space charge effect (Ωcm).

ρ_{sc}: resistivity in the space charge region (Ωcm). This may be higher or lower than the grain resistivity.

$\rho_{gb}\delta_{gb}$: grain boundary area specific resistance(Ωcm^2). This is only that part associated with the structural disorder of a grain boundary. In general, the grain boundary resistivity is not amenable to a separate, unequivocal determination, and neither is the thickness. Hence, this is given as a product $\rho_{gb}\delta_{gb}$, which is the common practice.

In general, the particle size, R, is in the micron range, the grain boundary thickness is in angstroms, and the space charge width, λ is assumed to be in several to hundreds of nanometers. Thus, we expect that $R>\lambda>\delta_{gb}$ and typically $R>\lambda>>\delta_{gb}$).

R_{eff}: the net resistance of half a grain with half the grain boundary associated with it.

Based on the assumption that the grains(or particles) are arranged on a square lattice, the effective DC resistivity of such a material can be computed by the following equation:

$$\rho_{eff} = \frac{4R_{eff}R^2}{R - x_0} = \frac{4R_{eff}R}{\cos\theta} \tag{7}$$

Curvature may have some effect on local energies and stoichiometry, in this study the curvature effect was neglect and the equipotential lines was assumed straight.

Resistivity in Bulk and Space Charge Layer for Doped Ceria: In the following discussion, all of the defects are assumed in thermodynamic equilibrium. Doped ceria is chosen here as a model materials. Doped ceria is known [27-30] to be mixed conductors of oxygen ions and electrons. Oxygen vacancies were created by introducing acceptor dopants by

$$A_2O_3 \rightarrow 2A^{'} + V_O^{\bullet\bullet} + 3O_O^{\times} \tag{8}$$

At elevated temperatures and reduced oxygen partial pressures, electrons and oxygen vacancy can be generated by

$$O_O^{\times} \rightarrow 2e^{'} + V_O^{\bullet\bullet} + \frac{1}{2}O_2 \tag{9}$$

The corresponding law of mass action equation can be expressed as

$$n^2[V_O^{\bullet\bullet}] = k\exp(-\frac{\Delta H^0}{k_B T})(P_{O_2}/P^0)^{-0.5} \tag{10}$$

where n is electron concentration, $\left[V_O^{\bullet\bullet}\right]$ is oxygen concentration, k is a constant, H_R is the enthalpy of reaction (9) and k_B the Boltzmann constant, P_{O_2} is the oxygen partial pressure in ambient atmosphere.

According to the condition for local charge neutrality, the concentrations of $V_O^{\bullet\bullet}$ for the bulk can be expressed as:

$$[V_O^{\bullet\bullet}]_b = \frac{[A^{'}]_b + n}{2} \tag{11}$$

The dopant concentration in bulk, $[A^{'}]_b$, P_{O_2} and temperature T were given by the experimental conditions. For cerium oxide, $k = 1.2\times10^{74}$ and ΔH^0 =4.67 eV [31]. From equation (10) and (11) the defect concentration (oxygen vacancies and electrons) in the bulk can be calculated at various temperatures and oxygen partial pressures.

It is generally accepted that the total electrical conductivity for doped ceria is the sum of ionic conductivity and electronic conductivity.

$$\sigma = 2e[V_O^{\bullet\bullet}]\mu_{V_O^{\bullet\bullet}} + en\mu_e \tag{12}$$

Then the total conductivity in the bulk can be expressed as

$$\sigma_{bulk} = \sigma_{i(bulk)} + \sigma_{e(bulk)} = 2e[V_O^{\bullet\bullet}]_b\,\mu_{V_O^{\bullet\bullet}} + en_b\mu_e \tag{13}$$

where $[V_O^{\bullet\bullet}]_b$ & n_b are concentrations in the bulk in cm^2/volt.sec. $\mu_{V_O^{\bullet\bullet}}$ and μ_e are mobilities of oxygen vacancy and electron, respectively.

Then the resistivity in the bulk can be written as

$$\rho_b = \frac{1}{\sigma_b} = \frac{1}{2e[V_O^{\bullet\bullet}]_b\,\mu_{V_O^{\bullet\bullet}} + en_b\mu_e} \tag{14}$$

For ceria, the electron mobility was given by [31]

$$\mu_e(T) = \frac{3.9\times10^2}{T}\exp(-\frac{4.63\times10^3}{T}) \tag{15}$$

and the effective mobility of oxygen vacancies was given by [32]

$$\mu_{V_O^{\bullet\bullet}}(T) = \frac{2.92\times10^2}{T}\exp(-\frac{7.84\times10^3}{T}) \tag{16}$$

In the above analysis, constancy of the mobilities of oxygen vacancy and electrons was assumed. The assumption is based on an ideal-solid-solution model that was utilized by Wang et al. [29] on the nonstoichiometry of doped ceria.

According to the constancy of the electrochemical potential for mobile defects, the concentration $n_j(x)$ of any dilute defect j with charge z in the space charge layer is given as

$$\frac{n_j(x)}{n_j(bulk)} = \exp[-z\frac{e\Delta\phi(x)}{kT}] \tag{17}$$

x is the distance from the interface between the grain boundary core and the space charge layer, at the interface x=0; $\Delta\phi(x)$ is the electrostatic potential referenced to the bulk, i.e., so called space charge potential. By solving Poisson's equation, it is related to the dopant concentration and space charge layer thickness by (for $x < \lambda^*$) [33]

$$\Delta\phi(x) = \frac{e[A^{'}]_b}{\varepsilon_0 \varepsilon_r}\left(x - \lambda^*\right)^2 \tag{18}$$

where $[A^{'}]_b$ is the dopant concentration in the bulk in #/cm^3, ε_0 is permittivity of free space, space charge layer thickness λ^*, and Debye length λ can be given respectively as

$$\lambda^* = \lambda\sqrt{\frac{4e}{kT}\Delta\phi(0)} \text{ and } \lambda = \sqrt{\frac{kT\varepsilon_0\varepsilon_r}{4e^2[A^{'}]_b}} \tag{19}$$

where $\Delta\phi(0)$ is space charge potential at grain boundary. ε_r is the dielectric constant of material. For ceria ε_r = 26 [34] Then the electron and oxygen vacancy concentration in space charge layer can be expressed respectively as

$$n_{(x)} = n_b \exp(\frac{q\Delta\phi(x)}{kT}) \tag{20}$$

$$[V_O^{\bullet\bullet}]_{(x)} = [V_O^{\bullet\bullet}]_b \exp(-\frac{2q\Delta\phi(x)}{kT}) \tag{21}$$

Then the specific conductivity in the space charge layer at a distance of x from grain boundary core is given as

$$\sigma_{sc(x)} = 2e[V_O^{\bullet\bullet}]_{(x)}\mu_{V_O^{\bullet\bullet}} + en_{(x)}\mu_e \tag{22}$$

The average electronic conductivity in the space charge layer can be given as

$$\sigma_{e(sc)} = \frac{1}{\frac{1}{\lambda^*}\int_0^{\lambda^*}\frac{1}{\sigma_e(x)}dx} \tag{23}$$

Inserting equation (18), (19) and (20) into equation (22) and rearranging

$$\sigma_{e(sc)} = \frac{e\mu_e n_b \lambda^*}{\int_0^{\lambda^*}\frac{1}{\exp[\frac{e^2[A^{'}]_b}{\varepsilon_0\varepsilon_r kT}\left(x-\lambda^*\right)^2]}dx} = \sigma_{e(bulk)}\frac{\lambda^*}{\int_0^{\lambda^*}\frac{1}{\exp[\frac{e^2[A^{'}]_b}{\varepsilon_0\varepsilon_r kT}\left(x-\lambda^*\right)^2]}dx} \tag{24}$$

In the same way, the average ionic conductivity in the space charge layer can be given as

$$\sigma_{i(sc)} = \frac{1}{\frac{1}{\lambda^*}\int_0^{\lambda^*} \frac{1}{\sigma_i(x)} dx} \tag{25}$$

Inserting equation (18), (19) and (21) into equation (25) and rearranging

$$\sigma_{i(sc)} = \frac{z_i e \mu_{V_O^{\bullet\bullet}} [V_O^{\bullet\bullet}]_b \lambda^*}{\int_0^{\lambda^*} \frac{1}{\exp[-\frac{z_i e^2 [A']_b}{\varepsilon_0 \varepsilon_r kT}\left(x-\lambda^*\right)^2]} dx} = \sigma_{i(bulk)} \frac{\lambda^*}{\int_0^{\lambda^*} \frac{1}{\exp[-\frac{z_i e^2 [A']_b}{\varepsilon_0 \varepsilon_r kT}\left(x-\lambda^*\right)^2]} dx} \tag{26}$$

Thus the average resistivity in space charge region can be given

$$\rho_{sc} = \frac{1}{\sigma_{sc}} = \frac{1}{\sigma_{e(sc)} + \sigma_{i(sc)}} \tag{27}$$

EXPERIMENTAL

Fabrication and Conductivity Measurement of Porous Samaria Doped Ceria (SDC) Samples with Widely Varying Neck Sizes: Two different methods were used to make samples of various porosities. In the first method, powder compacts were formed by die-pressing and iso-static pressing. Then the samples were sintered in air over a range of temperatures (ranging between 1200°C and 1600°C) to achieve varying porosity levels.

The process for making the second group of samples is as follows: Powder mixtures of commercial NiO and SDC (combustion method) in various NiO:SDC weight ratios corresponding to 20:80, 30:70 and 40:60 were wet-milled, dried, and then screened. Powder compacts were formed by die-pressing and iso-static pressing. Bar samples were sintered in air at 1600°C for 2 hours. The bar samples were then reduced in 10% hydrogen for 2 hours at 800°C, followed by a treatment in 100% hydrogen for 2 hours. Finally the reduced bar samples were leached in dilute nitric acid solution for 3 hours. This led to the removal of Ni as $Ni(NO_3)_2$, and created additional porosity. The resulting samples were single-phase, porous SDC.

Total conductivity of the two groups of samples of varying porosity levels was measured over a range of temperatures by four probe DC method. Prior to the measurement of conductivity, the samples were thermally treated at 1200 ^{o}C for 4hour to ensure the same space charge length among the samples. After testing, fractured pieces of each sample were impregnated with an epoxy. Upon curing and hardening the epoxy, the samples were mounted in plastic mount, and subsequently polished to a 1 micron finish. The samples were then examined under a scanning electron microscope (SEM). The microstructures of porous samples were characterized by quantitative stereology to estimate the porosity.

Conductivity Measurement of Porous SDC Sample at Various P_{O_2} & at Various Temperatures: Total conductivity of porous SDC samples fabricated using leaching process, were measured using four-probe technique under various P_{O_2} and temperatures. The P_{O_2} was changed from 1 atm (pure oxygen) to lower values step by step and finally to a reducing atmosphere. Oxygen partial pressure was controlled by N_2/O_2 mixtures for P_{O_2} higher than 10^{-5} atm, or H_2/H_2O mixtures for reducing atmospheres. P_{O_2} was monitored using a oxygen sensor. After the measurement at 600 ^{o}C, the sample was heated to higher temperatures to take new measurements.

Fabrication of Composite Cathodes by Infiltration: The fabrication process of anode-supported cells with a Ni/YSZ anode support, a Ni/YSZ anode interlayer, and a thin film YSZ electrolyte/SDC barrier layer is described in the second chapter. At this stage coatings of NiO+SDC powder in requisite proportions were applied onto the sintered SDC barrier layers and fired at temperatures up to 1600 ^{o}C. Some of the cells were annealed at 1400 ^{o}C for 6 h and 1200^{o}C for 20 h and then quenched to room temperature. The NiO + SDC layer was subjected to 10% hydrogen for 4 hours at 800 ^{o}C to reduce NiO to Ni. Nickel was leached out with dilute nitric acid for 2 hours, resulting in a highly porous framework of SDC with wide necks. A solution of $La(NO_3)_3$, $Sr(NO_3)_2$ and $Co(NO_3)_2$ in requisite proportion was impregnated into the porous SDC and fired at 1100^{o}C for 1 h to form a composite cathode containing LSC. Finally, the performance of the cells was tested at 800 °C. The ohmic contribution was measured by current interruption. After testing the microstructure was investigated under SEM.

RESULTS AND DISCUSSION

Effect of Neck Size on Effective Resistivity of Porous Body: Equation 1 shows that the effective conductivity of a porous conductor depends on the grain resistivity, ρ_g, the grain boundary resistivity parameter, namely $\rho_{gb}\delta_{gb}$, and the relative neck size α, given by $\alpha = r_o/R$. Of particular interest is to determine the relative contributions of the two terms as a function of α for small values of α. Note that as $\alpha\rightarrow 0$, both of the terms go to infinity (become singular). Our interest is in determining which of the terms goes to infinity faster as $\alpha\rightarrow 0$. It is readily shown that as $\alpha\rightarrow 0$, the above equation can be approximately given by

$$\rho_{eff} = \rho_g \ln\left(\frac{2}{\alpha}\right) + \frac{\rho_{gb}\delta_{gb}}{2R\alpha^2} \tag{28}$$

As seen from equation (28), as $\alpha\rightarrow 0$, both terms become infinite. One can use 'Hospital's' rule to show that the second term goes to infinity faster. The ratio of the derivative of the second term to the first varies as $1/\alpha^2$. This result has significant implications concerning the resistivity of porous bodies, the role of grain boundaries, and the cathodic polarization resistance of composite cathode. That is, a poorly sintered cathode (with narrow necks) will exhibit high effective resistivity and thus high polarization resistance. The role of grain boundaries on ρ_{eff} is actually disproportionately high on ρ_{eff}, due mainly to small neck sizes.

Morphology and Space Charge Effect on Effective Resistivity in Porous Doped Ceria: For the case of T = 600°C, P_{O_2} = 0.21 atm, doping level =10% (corresponding to $[A']_b$ = $2.686\times10^{21}/\text{cm}^3$, $n_b = 1.86\times10^{14}/\text{cm}^3$ and $\left[V_O^{\bullet\bullet}\right]_b = 1.34\times10^{21}/\text{cm}^3$), space charge potential $\Delta\phi(0)$ = 0.4V [23]. Using equation (19), the Debye length and space charge layer thickness can be calculated as 0.1 nm and 0.4 nm. Using equation (24), (26) and (27), the average conductivity in the space charge layer can be given as

$$\rho_{sc} = \frac{1}{\sigma_{i(sc)} + \sigma_{e(sc)}} = \frac{1}{0.005\sigma_{i(bulk)} + 2.268\sigma_{e(bulk)}} \tag{29}$$

The ionic conductivity in bulk, $\sigma_{i(bulk)}$ and electronic conductivity in bulk, $\sigma_{e(bulk)}$ can be calculated using equation (13). Thus the average resistivity in space charge layer can be calculated using equation (29).

In the similar way the average resistivity in space charge layer at higher temperatures and at various oxygen partial pressures can be calculated as well. Using the calculated bulk conductivity and average space charge conductivity at various temperature and at various P_{O_2}, as well as equation (3 – 5) and (7), the effective conductivity of porous doped ceria at specific neck size and specific grain size can be calculated.

Figure 2(a) shows the calculated resistivity (on a linear scale) of half of a grain with half of the grain boundary for porous doped ceria as a function of grain size and neck size at 600°C and P_{O_2} = 0.21 atm using the following parameters: ρ_g = 52 Ωcm, ρ_{sc} = 1.06×10^4 Ωcm, ρ_{gb} = 50 Ωcm*, λ^* = 0.4 nm, and δ_{gb} = 0.4 nm [35]. Figure 2(b) shows the calculated resistivity (on a log scale) of half of a grain with half of the grain boundary for porous doped ceria as a function of grain size and neck size under the same condition. On the basis of these figures it is seen that the effective resistivity rapidly rises for small narrow necks. The effective resistivities of porous samples with 0.5 micron grain size in the case of 5° angle and 45° angle are 3.25×10^3 Ωcm and 1.77×10^2 Ωcm, respectively. The effective resistivities of porous samples with 5 micron grain size in the case of 5°

---

* As the grain boundary core has a strong disordered structure, it is usually accepted that the activation enthalpy and entropy of migration should be much lower than those of bulk and space charge layers [18]. Furthermore, the charge carrier concentration in the core area is higher [36]. Thus the resistivity in the grain boundary core should be lower than those of bulk and space charge layer. In the following analysis, a value of lower resistivity was assumed and used for the calculation of effective resistivity.

angle and 45° angle are 6.46×10^2 Ωcm and 1.09×10^2 Ωcm respectively. It is seen that the effective resistivity for 0.5 micron grain size is over 18 times greater for the case of 5° angle as compared to 45° angle. Also the effective resistivity for 5 micron grain size is over 6 times greater for the case of 5° angle as compared to 45° angle. The rapid rise in the net resistance at small angles (narrow neck sizes) underscores the importance of good particle to particle contacts.

Figure 3(a) shows the calculated resistivity (on a log scale) of half of a grain with half of grain boundary for a porous doped ceria as a function of grain size and neck size at 800°C and P_{O_2} = 0.21 atm using the following parameters: ρ_g = 12 Ωcm, $\rho_{sc} = 2.41\times10^3$ Ωcm, ρ_{gb} = 10 Ωcm, λ^* = 0.4 nm, and δ_{gb} = 0.4 nm. Figure 3(b) shows the calculated resistivity (on a log scale) of half of a grain with half of grain boundary for a porous doped ceria as a function of grain size and neck size under the same condition. It was observed the similar trend that the effective resistivity rapidly rises for small narrow necks. It is also interesting to note that at 800°C, the effective resistivity for a grain size 0.5 micron in the case of 5 degrees is 7.39×10^2 Ωcm, which is just 0.22 times of that at 600 °C.

Table 1 shows porosity and conductivity as a function of sintering conditions for porous samples fabricated using a conventional method. Table 2 shows porosity and conductivity as a function of sintering conditions for porous samples made using NiO-SDC powders, wherein the porosity was created by leaching away Ni. From Tables 1 & 2, it is seen that for the samples fabricated using the conventional sintering method, at a high sintering temperature of 1600°C, a dense sample with 4.2% porosity can be obtained, as shown in Figure 4. With the decrease of the sintering temperature to 1400°C & 1200°C, the porosity increases to 33.5% & 51.2% respectively. These samples were not well sintered. Also it is seen that the inter-particle (inter-grain) neck sizes are small, as seen in Figures 5 & 6. In the second group of samples fabricated using the leaching process, the porosity was dictated by the weight ratio of NiO/SDC. During sintering of the samples, the NiO and SDC grains grow simultaneously and fill up space by forming regular polyhedra (tetrakaidecahedra). The NiO skeleton in the composite keeps the SDC skeleton from collapsing and vice-a-versa. Using this process, samples of greater than 95% theoretical density were made. The NiO and SDC skeletons in the composite form two continuous phases with a large neck size. After reducing NiO to Ni and leaching it away, samples with the preferred microstructures of high porosity & large neck sizes were obtained. From Figures 7 through 9, it is seen that with the increase of porosity from 31.2% to 54.8%, the samples exhibit good connectivity between grains compared to those sintered using the conventional method, shown in Figures 5 & 6.

The results of conductivity measurements listed in Table 1 & 2 show that the effects of microstructural on the apparent conductivity are rather large. It is seen that in the first group of samples fabricated using the conventional method, the conductivity of the dense sample is 0.071 S/cm at 800^{o}C, which is twice that of the sample with 33.5% porosity. The conductivity of the sample with 51.2 % porosity is 4.31x10^{-4} S/cm at 800^{o}C, which is much lower than can be rationalized on the basis of a simple phenomenological equation, namely

$$\sigma_{porous} = \sigma(1 - V_V) \tag{30}$$

In the porous samples fabricated using the reducing-leaching method, with the porosity increase from 31.2% to 54.8%, corresponding to a conductivity decrease from 0.05 to 0.0328 S/cm. The decrease of conductivity is not as large as in the samples fabricated using the conventional method. This shows that the conductivity is dependent, not only on porosity, but also to other microstructural parameters, such as grain size, neck size etc. Usually when the grain size is in the nanometer range, the grain boundary dominates conductivity. For samples with grain sizes on the order of microns, the grain boundary effect is generally significant, but not dominant. Therefore, the large difference in conductivity of the two groups of samples must be attributed to the differences in the neck sizes, i.e., the connectivity (inter-particle neck size) plays an important role in determining the conductivity of porous ionic conductors. Comparison of Figure 6 and Figure 9 shows that while these two samples exhibit similar porosity levels, their conductivity values are two orders of magnitude apart as shown in Figure 10 which shows a plot of the relative conductivity vs. relative density. It is known that at relatively high volume fractions of insulating phases, the net conductivity can be far below that of the conductive phase corrected for porosity through a simple linear relationship, provided the inter particle contact is poor. The results show that the conductivity is dependent not only on porosity, but also on other microstructural parameters, such as grain size and neck size, etc. When the neck size is large, the effective conductivity can be calculated on the basis of a simple phenomenological equation (30) .The most probable reason for the large difference of conductivities is the connectivity. That is, the samples sintered by the conventional method exhibit relatively small neck sizes compared to those fabricated by the reducing-leaching method.

Oxygen Partial Pressure Effect on Effective Resistivity of Bulk and Space Charge Layer: Figure 11 shows the calculated defect concentration (on a log scale) in a space charge layer as a function of distance from grain boundary core using the following parameters: T= 600 ^{o}C, space charge potential=0.4V [23], doping level =10%(corresponding to n_b= $1.86\times10^{14}/cm^3$ and $\left[V_O^{\bullet\bullet}\right]_b$ =$1.34\times10^{21}/cm^3$). Note that in the space charge layer the oxygen vacancy concentration decreases and the electron concentration increases with the decreasing of the distance from grain boundary core. At grain boundary core area, the oxygen vacancy concentration is still higher than that of electrons. For the case of T = 800^{o}C, space charge potential=0.4V, doping level =10% as shown in Figure 12, Note that the lines of oxygen vacancy concentration and electron concentration cross at ζ (distance from grain boundary core) = 0.1 nm. When $\zeta < 0.1$ nm the so called “inversion layer” is formed. If the inversion layer is dominant in the space charge layer, the phenomenon of the space charge layer conductivity being higher than that of the bulk will be observed.

Figure 13 shows the calculated ionic, electronic and total conductivity (ionic plus electronic) in the bulk and the space charge layer as a function of various oxygen partial pressures using the following parameters: T = 600 ^{o}C, space charge potential=0.4V, doping level = 10 mol%. Note that in the bulk and in the space charge layer, the electronic conductivity increases about 3-4 orders magnitude when the P_{O_2} decreases from 1 atm to 10^{-15} atm. However the ionic conductivity for all cases remains independent of P_{O_2}. Also the ionic conductivity dominates the total conductivity over the whole P_{O_2} range.

Figure 14 shows the calculated ionic, electronic and total conductivity (ionic plus electronic) in the bulk and the space charge layer as a function of various oxygen partial pressures using the following parameters: T = 800 ^{o}C, space charge potential = 0.4V, doping level = 10 mol%. It is seen that the average electronic conductivity in the space charge layer dominates the average total conductivity when $P_{O_2} < 10^{-7.6}$ range, which is in good agreement with expectation. At a higher temperature, the electron concentration can be larger at low P_{O_2}, thus the space charge layer exhibits lower resistivity than the bulk.

Figure 15 shows the calculated effective conductivity of porous doped ceria as a function of oxygen partial pressure at various temperatures for the case of grain size = 2.5 μm, theta = 18^{o} (an indicator of relative neck size) and porosity = 30%. It is seen that at 600^{o}C the conductivity remains constant with P_{O_2}. This can be attributed the dominant ionic conductivity which is nearly constant with various P_{O_2}. However the effective conductivity increases from 0.02 S/cm to 0.033 S/cm with the decrease of P_{O_2} from 1atm to 10^{-15} atm, which shows the effect of P_{O_2} on the effective conductivity. Figure 16 shows the measured effective conductivity of porous doped ceria as a function of oxygen partial pressure at various temperatures. The result shows similar trend with the previous simulation results. Thus the increase of electrical conductivity with reducing oxygen partial pressure can be explained very well by the space charge model.

Application of Space Charge Model in Composite Cathode: Recent work has shown that cathodic polarization can be substantially reduced provided the porous cathode is mixed conducting [37-40]. For this reason, the cathode must either be made of a single-phase MIEC material, or a composite mixture of an oxygen ion conductor (e.g. YSZ) and an electrocatalyst (e.g. LSM), which is an electronic conductor. In terms of the intrinsic charge transfer parameter (area specific charge transfer resistance, R_{ct} in Ωcm^2), the oxygen ion conductivity of the cathode, σ_{ic}, the grain size of the cathode, d, and the porosity of the cathode, V_v, the polarization resistance of the cathode is given as[38]

$$R_p \approx \sqrt{\frac{dR_{ct}}{\sigma_{ic}(1-V_v)}} \tag{31}$$

For a given cathode material, equation shows that the larger the σ_{ic}, the lower is the R_p, and thus the better is the cathode.

Using equation (31) and parameter value from literature [33], the electrode polarization resistance can be calculated. Figure 17 shows the calculated polarization resistance as a function of grain size and neck size at 800°C for an electrode using YSZ as the ionic conductor in the composite cathode, and the following parameters: ρ_g (YSZ grain resistivity) = 14 Ω.cm, ρ_{sc} (resistivity of the space charge layer) = 2,250 Ω.cm, ρ_{gb} (grain boundary core resistivity) = 10 Ω.cm, λ (space charge layer thickness) = 2 nm, δ_{gb} (grain boundary core thickness) = 0.4 nm, R_{ct} = 2 $\Omega.cm^2$· Figure 18 shows the calculated polarization resistance as a function of grain size and neck size at 650°C using the following parameters: ρ_g = 76 Ω.cm, ρ_{sc} = 14,520 Ω.cm, ρ_{gb} = 50 Ω.cm, λ = 2 nm, δ_{gb}= 0.4 nm, R_{ct}= 4.15 $\Omega.cm^2$. It is seen that the polarization resistance rises sharply for small necks and large grains. Over the range of particle sizes and neck sizes (angle) that the calculations were performed, at 800°C the polarization resistance varies between ~0.15 and ~0.8 Ωcm^2 at 800°C, and between ~0.5 and ~2.8 Ωcm^2. This result has significant implications concerning the role of grain boundaries and grain size on the cathodic polarization resistance of composite and single phase MIEC cathodes. The results show that a low polarization resistance is realized if the particle size is small and the neck size is large.

<u>Space Charge Effect on Cathodic Polarization:</u> Figure 19 shows voltage and power density vs. current density plots at 800°C for cells with cathode fabricated by the

infiltration method. In each case, cell with the SDC ionic conductor skeleton in the composite cathode was annealed and then quenched to room temperature prior to cathode infiltration. The as-fabricated cell without heat treatment exhibits the highest performance. By contrast, the cell annealed at 1200°C for 20 hours exhibits the lowest performance.

During the process of heat treatment, the dopant is expected to segregate along the grain boundary and free surfaces, i.e., annealing at intermediate temperatures should favor the creation of positively charged interfaces by enhancing dopant segregation. After quenching from the annealing temperature, the dopant segregation at the grain boundaries is almost frozen. Thus, in the annealed and quenched samples, it is expected that the grain boundary structure at the annealing temperature can be preserved at lower temperatures, e.g. with a more inhomogeneous point-defect distribution. Thus, the grain boundary barrier height should be higher in samples annealed at lower temperatures. This means, the variation in the grain boundary blocking effect can be related to the different levels of dopant segregation achieved by changing the thermal history. The higher segregation should result in both a wide space charge thickness and a large depletion of oxygen vacancies leading to greater grain boundary resistivity. Thus the lower the annealing temperature, the greater is the space charge width, and the higher is the ionic resistivity in the cathode interlayer, and thus the higher is the activation polarization (Equation (31)). Since the anode interlayer was subjected to the same thermal treatment, it is expected that the same effect likely exists in the anode interlayer (higher ionic resistivity in YSZ annealed at a lower temperature). Figure 20 shows the ohmic overpotential determined by current interruption as a function of current density for cells with various thermal histories. It is seen that there is a small difference in the ohmic resistance between these cells. It is seen that the cell annealed at 1200°C has a slightly higher ohmic resistance. This is also consistent with expectations since the ionic resistivity of the YSZ/SDC bi-layer electrolyte is expected to increase by annealing at a lower temperature (1200°C) due to the space charge effect. The observation, that the effect is small is also consistent with the fact that the overall ohmic contribution is generally small in cells with a thin film electrolyte. Figure 21 shows electrode polarization as a function of current density for cells with various thermal histories, which was obtained by subtracting the ohmic contribution. Figure 21 shows that the variation in total electrode polarization with annealing temperature is considerably greater, with the cell annealed at 1200°C exhibiting the highest polarization and the as-fabricated cell exhibiting the lowest polarization. Higher polarization in the cell annealed at 1200°C is again consistent with greater space charge effect. While the results are consistent with space charge effect, the possibility of secondary, insulating phases precipitating along grain boundaries in samples annealed at a lower temperature, thus raising the net resistivity cannot be ruled out. A careful characterization of grain boundary regions will be required to answer this question.

SUMMARY

An analytical equation to describe the conductivity of porous bodies, which incorporates the effects of the structural part of the grain boundary, the effect of space charge, and the relative neck size between contacting particles, was derived. Using calculated values of parameters, the effect of grain size and neck size on transport properties of porous ionic conductors was evaluated. The results show that a small neck size has a profoundly adverse effect on conductivity. The space charge layer in the grain boundary regions and free surfaces in porous bodies also has a significant effect on the effective conductivity. Oxygen partial pressure effect on effective resistivity of bulk and space charge layer was evaluated. By the comparison of calculated and measured effective conductivity of porous doped ceria as a function of oxygen partial pressure at various temperatures, it was concluded that the increase of electrical conductivity with reducing oxygen partial pressure can be explained very well by the space charge model. The simulation results also show that the ionic conductivity will influence the electrode polarization of composite electrode.

The present work shows that samples fabricated using the leaching method exhibits the desired microstructure comprising wide neck size and high effective conductivity in porous SDC. Samples with essentially the same porosity levels can exhibit conductivity values that differ by two orders of magnitude, the difference being primarily attributable to the relative neck size, which is a measure of particle to particle connectivity.

Measurements on anode-supported cells show that cells annealed at a lower temperature (prior to the introduction of cathode by infiltration) exhibit lower performance, which can be attributed to greater electrode polarization. This higher polarization can be attributed to the expected greater space charge effect in samples annealed at a lower temperature. However, even though the results are consistent with the possible existence of a space charge effect, the formation of insulating phases along grain boundaries in annealed samples as a possible reason for higher resistivity and higher polarization resistance in annealed cells cannot be ruled out. This will require careful characterization of grain boundary regions

APPENDIX A

Figure 22 shows the geometry of the particle used for calculation.

For region I, corresponding to the net resistance for the range between *x= x₀* to *x= R*,

$$R_I = \int dR = \frac{\rho}{\pi}\int_0^R \frac{dx}{x(2R' - x)} = \frac{\rho}{\pi}\int_{x_0}^R \frac{dx}{x(R - x)} \qquad \text{(A-1)}$$

$$R_I = \left[-\frac{\rho}{2\pi R}\ln(\frac{R - x}{x})\right]_{x=x_0}^{x=R} = -\frac{\rho}{2\pi R}\ln(\frac{R - x_0}{x_0}) \qquad \text{(A-2)}$$

Where α $\alpha = \frac{y_0}{R}$ and $x_0 = R - R(1 - \alpha^2)^{\frac{1}{2}}$ (A-3)

Thus $$R_I = \frac{\rho}{2\pi R}\ln\left[\frac{1 + \sqrt{1 - \alpha^2}}{1 - \sqrt{1 - \alpha^2}}\right] \qquad \text{(A-4)}$$

At region II corresponding to the transport across the grain boundary core, R_{II} can be given as

$$R_{II} = R_{gb} = \frac{\rho_{gb}\delta_{gb}}{2\pi r_0^2} \qquad \text{(A-5)}$$

$$R_{eff} = R_I + R_{II} \qquad \text{(A-6)}$$

Thus the effective resistivity can be given as

$$\rho_{eff} \approx \frac{\rho_g}{2\sqrt{1-\alpha^2}} \ln\left[\frac{1+\sqrt{1-\alpha^2}}{1-\sqrt{1-\alpha^2}}\right] + \frac{\rho_{gb}\delta_{gb}}{2r\alpha^2\sqrt{1-\alpha^2}} \tag{A-7}$$

APPENDIX B

Figure 23 shows the geometry of the particle used for calculation.

For region I, corresponding to the net resistance for the range between $x = x_0+\lambda$ to $x = R$,

$$y = \sqrt{2Rx - x^2} = R\sin\theta \tag{B-1}$$

$$x = R - R\cos\theta \text{ and } dx = R\sin\theta d\theta \tag{B-2}$$

Also it is easy to see that

$$\Delta y = \frac{\lambda}{\sin\theta} \qquad \text{and} \qquad \sin\theta = \frac{y}{R} = \frac{\sqrt{2Rx - x^2}}{R} \tag{B-3}$$

Then one can arrive at

$$y_g = y - \Delta y = R\sin\theta - \frac{\lambda}{\sin\theta} \tag{B-4}$$

Thus

$$\pi(y^2 - y_g^2) = \pi(y^2 - (y - \Delta y)^2) = \pi(2R\lambda - \frac{\lambda^2}{\sin^2\theta}) \tag{B-5}$$

In the bulk and space charge parallel region

$$\frac{1}{dR_I} = \frac{1}{\frac{\rho_g dx}{\pi y_g^2}} + \frac{1}{\frac{\rho_s dx}{\pi(y^2 - y_g^2)}} \tag{B-6}$$

Then

$$dR_I = \frac{\rho_g \rho_s R\sin^3\theta d\theta}{\pi(2R\lambda\sin^2\theta - \lambda^2)\rho_g + \pi(R^2\sin^4\theta - 2R\lambda\sin^2\theta + \lambda^2)\rho_s} \tag{B-8}$$

The integral of the above equation from $x = x_0+\lambda$ to $x = R$, i.e., integrate from $\theta = \cos^{-1}(\frac{R - x_0 - \lambda}{R})$ to $\theta = \pi/2$, can be given as

$$R_I = \int_{\cos^{-1}(\frac{R-x_0-\lambda}{R})}^{\frac{\pi}{2}} \frac{\rho_g \rho_{sc} R \sin^3 \theta d\theta}{\pi(2R\lambda \sin^2 \theta - \lambda^2)\rho_g + \pi(R^2 \sin^4 \theta - 2R\lambda \sin^2 \theta + \lambda^2)\rho_s} \qquad \text{(B-9)}$$

At region II, corresponding to the net resistance for the range $x = x_0$ to $x = x_0+\lambda$

$$dR_I = \frac{\rho_s dx}{\pi y^2} = \frac{\rho_s R \sin\theta d\theta}{\pi(R\sin\theta)^2} = \frac{\rho_s d\theta}{\pi R \sin\theta} \qquad \text{(B-10)}$$

The integral of the above equation between $x = x_0$ to $x = x_0+\lambda$, i.e., from $\theta = \cos^{-1}(\frac{R-x_0}{R})$ to $\theta = \cos^{-1}(\frac{R-x_0-\lambda}{R})$, can be given as

$$R_{II} = \int_{\cos^{-1}(\frac{R-x_0}{R})}^{\cos^{-1}(\frac{R-x_0-\lambda}{R})} \frac{\rho_{sc} d\theta}{\pi R \sin\theta} \qquad \text{(B-11)}$$

At region III corresponding to the transport across the grain boundary core, R_{III} can be given as

$$R_{III} = R_{gb} = \frac{\rho_{gb}\delta_{gb}}{2\pi r_0^2} = \frac{\rho_{gb}\delta_{gb}}{2\pi(R\sin\theta)^2} \qquad \text{(B-12)}$$

From Equations (A-9), (A-11) and (A-12), it is apparent that if x_0 and λ are known, $\cos^{-1}(\frac{R-x_0}{R})$ and $\cos^{-1}(\frac{R-x_0-\lambda}{R})$ can be calculated. Thus R_I , R_{II} and R_{III} can be calculated. Thus the effective resistance can be given as

R_{eff}= R_I (after integration) + R_{II} (after integration) + R_{III} (B -13)

REFERENCES

1. J. W. Kim, A. V. Virkar, K.-Z. Fung, K. Metha, and S. C. Singhal, *J. Electrochem. Soc.*, 146, 69 (1999).
2. P. jasinski, T. Suzuki, H. U. Anderson, *Sensors and Actuators* B 95(2003) 73-77.
3. H. J. Beie, A. Gnorich, *Sensors and Actuators* B 4(1991) 393-399.
4. A. D. Brailsford, D. K. Hohnke, *Solid state Ionics*, 11 (1983) 133.

5. M. Kleitz, L. Dessemond, M.C. Steil, *Solid State Ionics*, 75 (1995) 107.
6. C. Tian and S.-W. Chan, *Solid State Ionics*, 134, 89-102 (2000).
7. J.-H. Hwang, D. S. McLachlan. And T. O. Mason, *J. Electroceram.*, 3, 7-16 (1999).
8. Y.-M. Chiang, E. B. Lavik, and D. A. Blom, *Nanostruct. Mater.*, 9, 633 (1997).
9. K. El Adham and A. Hammou, *Solid state Ionics*, 9&10, 905-12(1983).
10. J. Hong, K. Mehta, and A. V. Virkar, *J. Electrochem. Soc.*, 145, 638 (1998).
11. R. Gerhardt and A. S. Nowick, *J. Am. Ceram. Soc.*, 69 641-46 (1986).
12. R. Gerhardt, A. S. Norwick, M. E. Mochel, and I. Dumler, *J. Am. Ceram. Soc.*, **69**, 647-51(1986).
13. J. Tanaka, J.-F. Baumard, and P. Abelard, *J. Am. Ceram. Soc.*, 70, 637-43(1987).
14. G. M. Christie and F. P. F. van Berkel, *Solid State Ionics*, 83 17-27(1996).
15. J. Frenkel, p. 37 in ‘Kinetic Theory of Liquids’, Dover, NY (1946).
16. K. Lehovec, J. Chem. Phys., 21 [7] 1123-1128 (1953).
17. K. L. Kliewer and J. S. Koehler, Phys. Rev., 140 [4A], A1226-A1240 (1965).
18. X. Guo, *Solid State Ionics*, 81 235-242(1995).
19. X. Guo, *Solid State Ionics*, 99 137-142(1997).
20. S. Kim and J. Maier, *J. Electrochem. Soc.*, 149, 10 (2002).
21. A. Tschöpe, E. Sommer and R. Barringer, *Solid State Ionics* **139**, 255(2001)
22. A. Tschöpe, *Solid State Ionics* **139**, 267(2001)
23. X. Guo, W. Sigle and J. Maier, *J. Am. Ceram. Soc.*, **86**, 77-87(1987).
24. S. K. Tiku and F. A. Kroger, *J. Am. Ceram. Soc.*, **63**, 183(1987).
25. A. Tschöpe, C. Bäuerle and R. Birringer, *J. App. Phys.*, 95, **1204**(2004).
26. I. Lubomirsky, J. Fleig and J. Maier, *J. App. Phys.*, 92, **6819**(2002).
27. H. L. Tuller and A. S. Nowick, *J. Electrochem. Soc.*, 126, **209** (1979).
28. D. Scheider, M. Gödickemeier, and L. J. Gauckler, *J. Electroceram.*, 1, **165**(1997).
29. D. Y. Wang and A. S. Nowick, *J. Solid State Chem.*, 35, **325**(1980).
30. R. Gerhardt and A. S. Nowick, *J. Am. Ceram. Soc.*, 69, **641**(1986).
31. H.L. Tuller, in Nonstoichiometric Oxides, edited by T. O. Sørensen (Academic Press, New York, 1981), P. 271.
32. S. Wang, T. Kobayashi, M. Dokiya and T. Hashimoto, *J. Electrochem. Soc.*, **147 (10)**, 3906-09 (2000).
33. X. Guo and J. Maier, *J. Electrochem. Soc.*, **148**, E121 (2001).
34. D. Y. Wang, D. S. Park, J. Griffith and A. S. Nowick, *Solid State Ionics*, **2,** 95(1981).
35. S. P. S. Badwal and J. Drennan, *J. Mater. Sci.*, 22, 3231 (1987).
36. W. D. Kingery, J. Am. Ceram. Soc., 57 (1974) 1.
37. T. Kenjo, S. Osawa, and K. Fujikawa, *J. Electrochem. Soc.*, 138, **349** (1991).
38. C. W. Tanner, K-Z. Fung, and A. V. Virkar, *J. Electrochem. Soc.*, 144, **21-30** (1997).
39. H. Deng, M. Zhao, and B. Abeles, *Solid State Ionics*, 74 75 (1994).
40. I. V. Murygin, Elektrokhimiya, 23[6]740 (1987).

Table I: Porosity and conductivity as a function of sintering conditions. (Samples fabricated by the conventional method)

SDC (Ce/Sm = 80/20)		Sintered at 1600°C 4 hours	Sintered at 1400°C 4 hours	Sintered at 1200°C 4 hours
Porosity		4.2%	33.5%	51.2 %
Conductivity (S/cm)	650(°C)	0.0272	0.0115	$5.18\text{x}10^{-5}$
	700(°C)	0.0373	0.0166	$1.19\text{x}10^{-4}$
	750(°C)	0.0563	0.0252	$2.52\text{x}10^{-4}$
	800(°C)	0.0706	0.032	$4.31\text{x}10^{-4}$

Table II: Porosity and conductivity as a function of sintering conditions (Samples fabricated by the reducing-leaching method).

SDC (Ce/Sm = 80/20)		Sintered at 1600°C 2hours	Sintered at 1600°C 2hours	Sintered at 1600°C 2hours
Porosity		31.2%	39.7%	54.8%
Conductivity (S/cm)	650(°C)	0.016	0.0152	0.0103
	700(°C)	0.0248	0.024	0.0156
	750(°C)	0.0361	0.035	0.023
	800(°C)	0.0506	0.049	0.0328

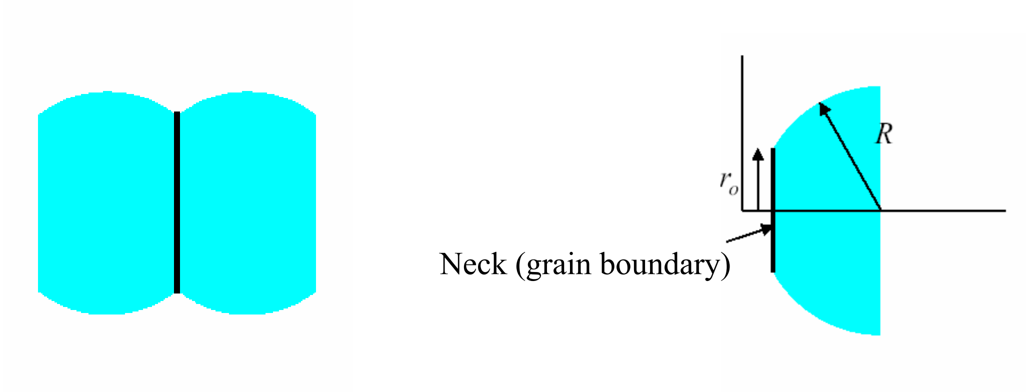

Figure 1(a): A schematic of two grains in the pillar, with a grain boundary in between. Figure 1(b): A schematic of a half of the grain with half of the grain boundary associated with it. This is the geometry used in the calculations.

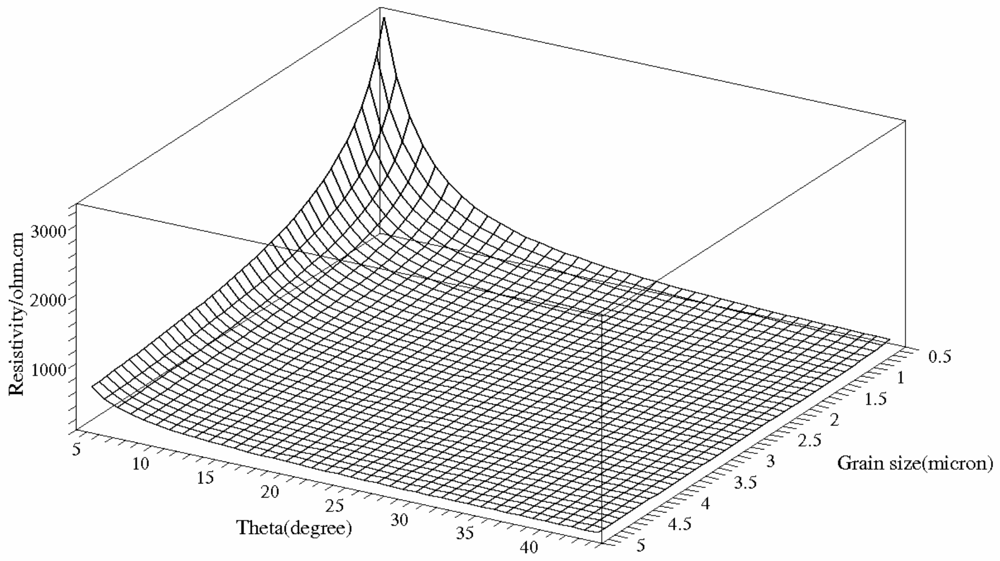

Figure 2(a): Effective resistivity (linear scale) of half a grain (with half a grain boundary) as a function of angle (relative neck size) and grain size at 600 °C $PO_2 = 0.21$ atm.

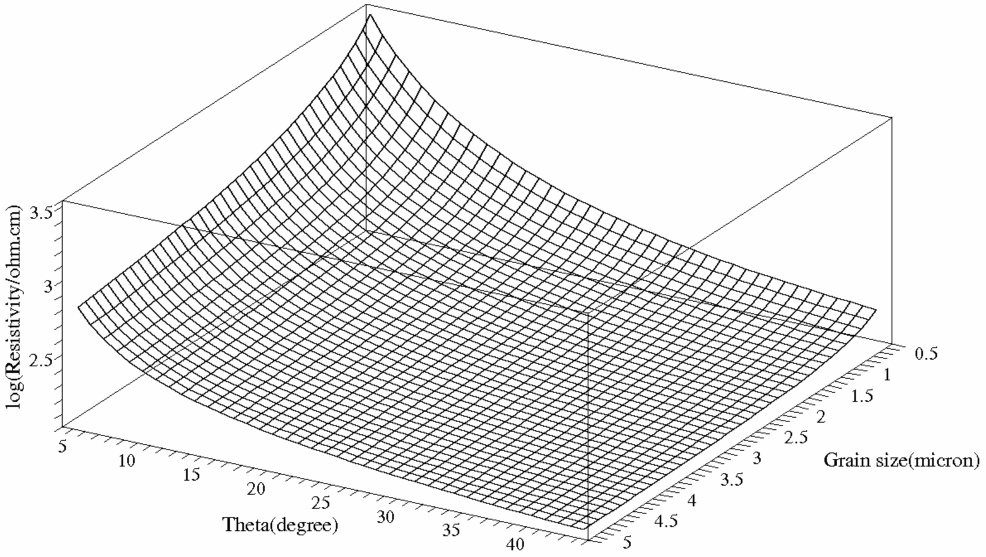

Figure 2(b): Effective resistivity (log scale) of half a grain (with half a grain boundary) as a function of angle (relative neck size) and grain size at 600 °C $PO_2 = 0.21$ atm.

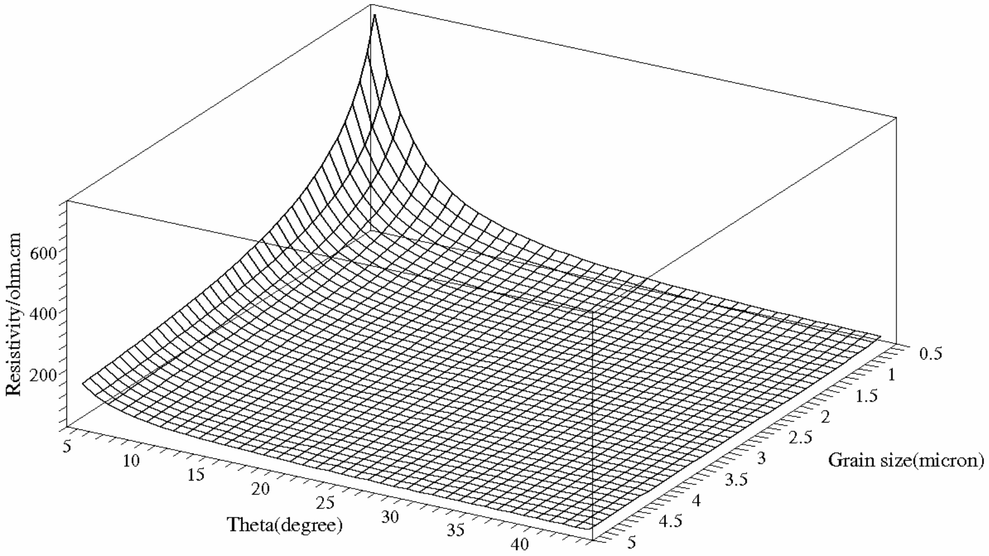

Figure 3(a): Effective resistivity (linear scale) of half a grain (with half a grain boundary) as a function of angle (relative neck size) and grain size at 800 °C $PO_2 = 0.21$ atm.

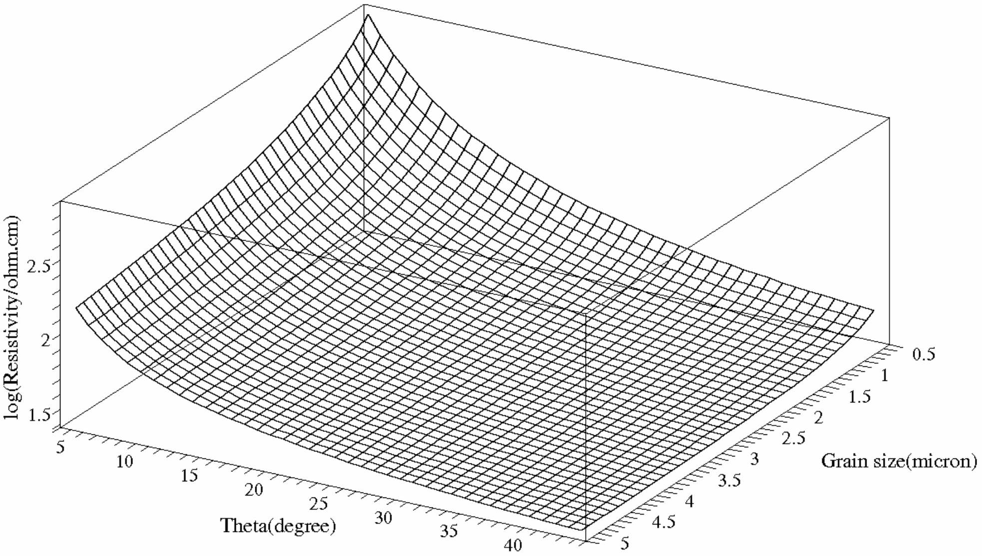

Figure 3(a): Effective resistivity (log scale) of half a grain (with half a grain boundary) as a function of angle (relative neck size) and grain size at 800 °C $PO_2 = 0.21$ atm.

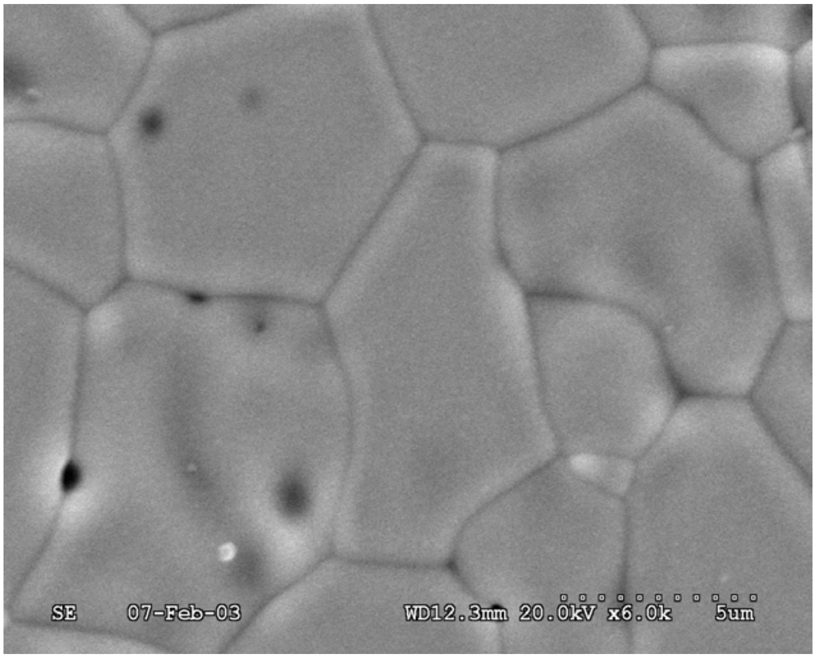

Figure 4: An SEM micrograph of Sm_2O_3-doped ceria (SDC) bar (porosity = 4.2%) sintered at 1600^oC /4 hours. Note the relatively coarse grain size. Conductivity and grain size data are given in Table I.

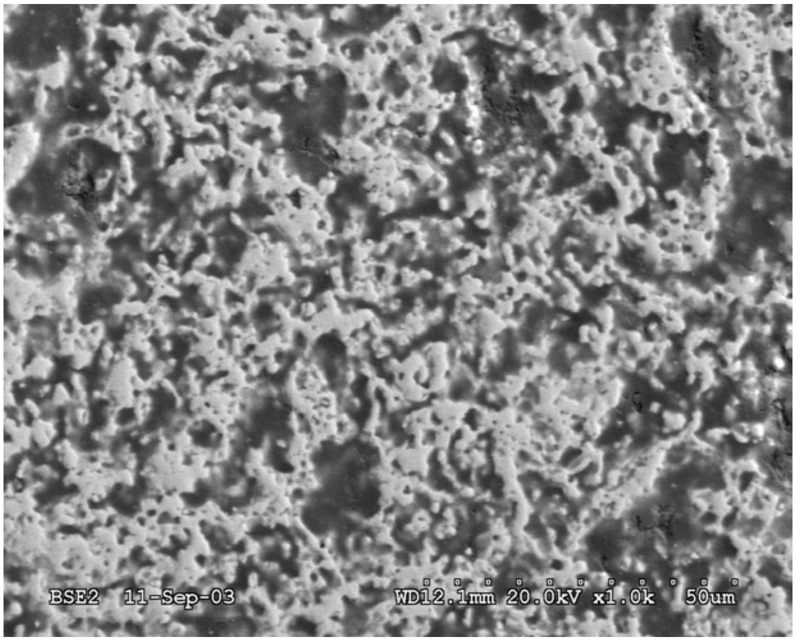

Figure 5: An SEM micrograph of a Sm_2O_3-doped ceria (SDC) bar (porosity = 33.5%) sintered at 1400^oC /4 hours (conventional method). Conductivity and grain size data are given in Table I.

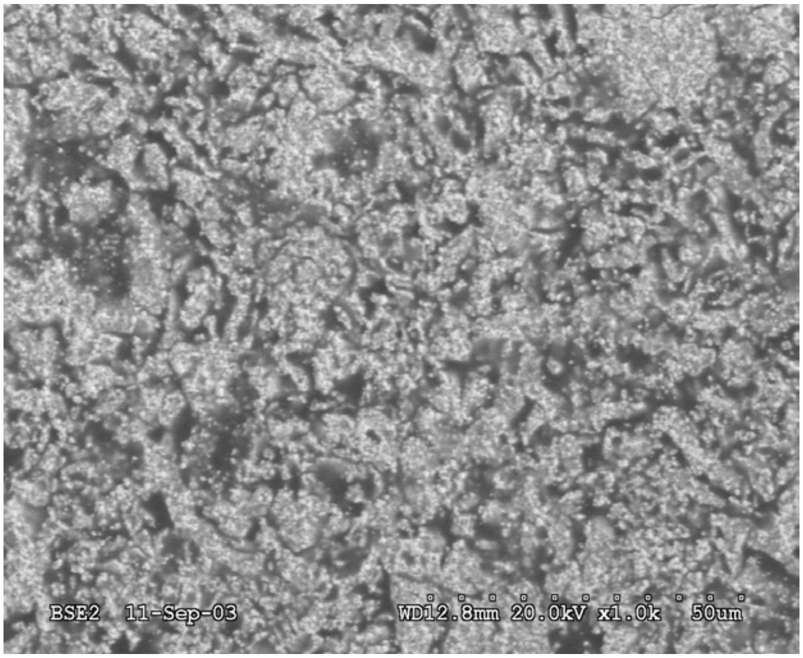

Figure 6: An SEM micrograph of a Sm_2O_3-doped ceria (SDC) bar (porosity = 51.2%) sintered at 1200°C /4 hours (conventional method). Conductivity and grain size data are given in Table I.

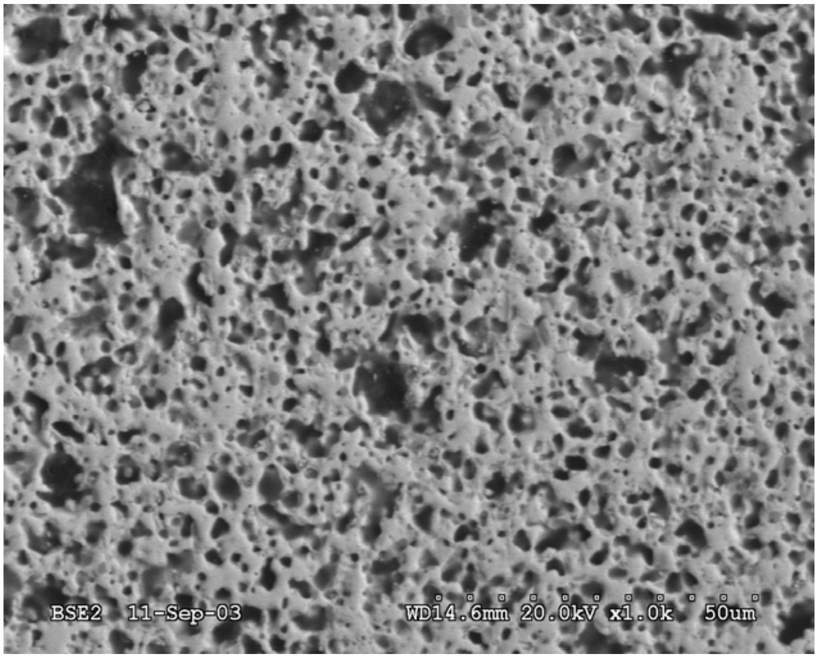

Figure 7: An SEM micrograph of a Sm_2O_3-doped ceria (SDC) bar (porosity = 31.2%) sintered at 1600°C /2 hours (method comprising the fabrication of SDC + NiO composite, reduction of NiO to Ni, and its removal by leaching). Conductivity and grain size data are given in Table II.

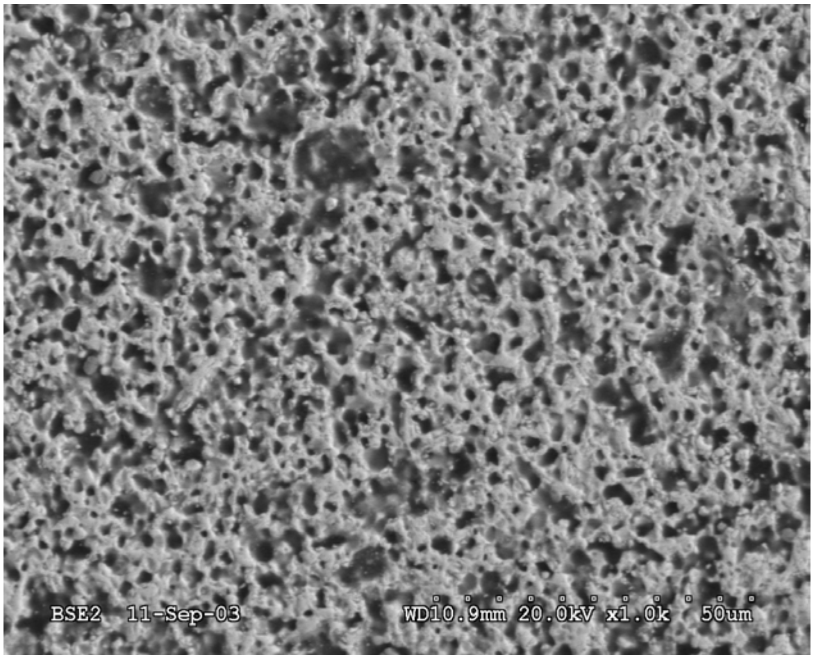

Figure 8: An SEM micrograph of a Sm_2O_3-doped ceria bar (porosity = 39.7%) sintered at 1600°C /2 hours (method comprising the fabrication of SDC + NiO composite, reduction of NiO to Ni, and its removal by leaching). Conductivity and grain size data are given in Table II.

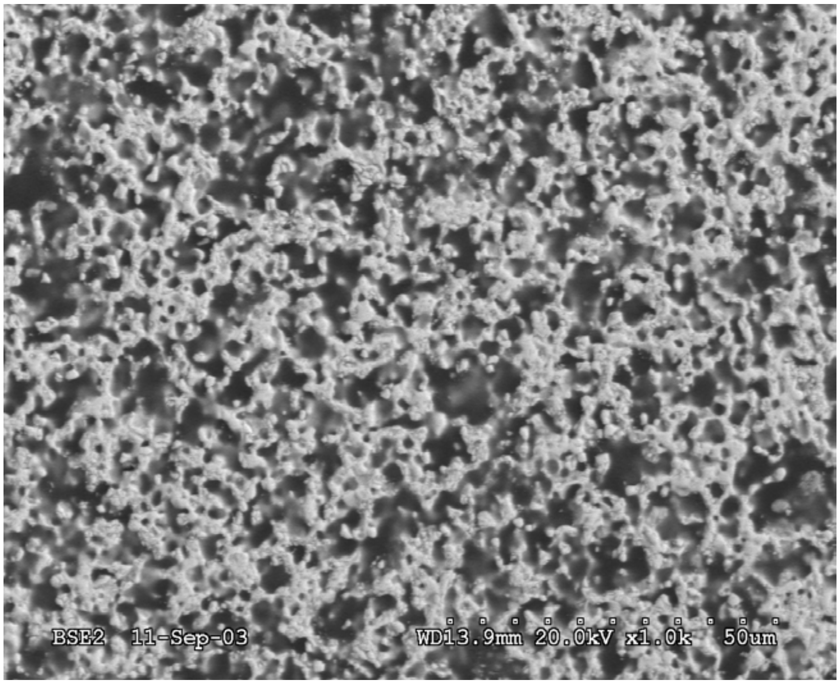

Figure 9: An SEM micrograph of a Sm_2O_3-doped ceria bar (porosity = 54.8%) sintered at 1600°C /2 hours (method comprising the fabrication of SDC + NiO composite, reduction of NiO to Ni, and its removal by leaching). Conductivity and grain size date are given in Table II.

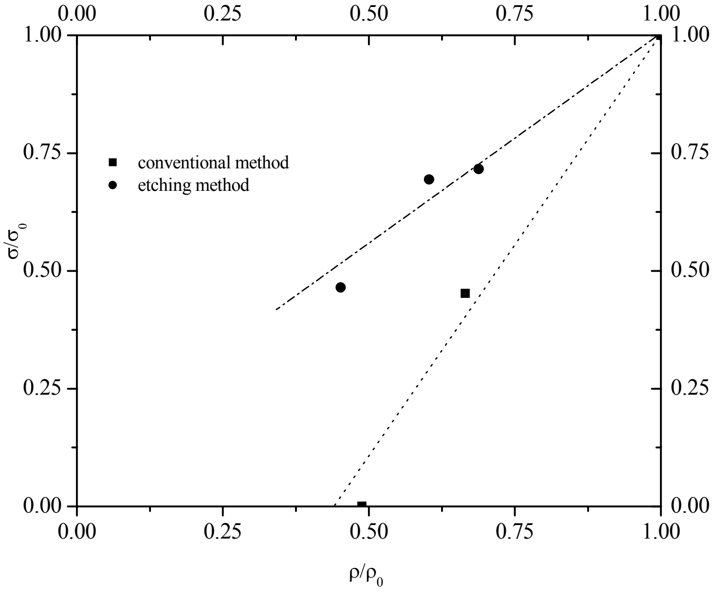

Figure 10: Relative conductivity vs. relative density. The relative conductivity is defined as the ratio of the conductivity of a sample with a given porosity to that of the fully sintered (negligible porosity) sample. Similarly, the relative density is the ratio of density of a sample with a given porosity to that of a fully dense sample.

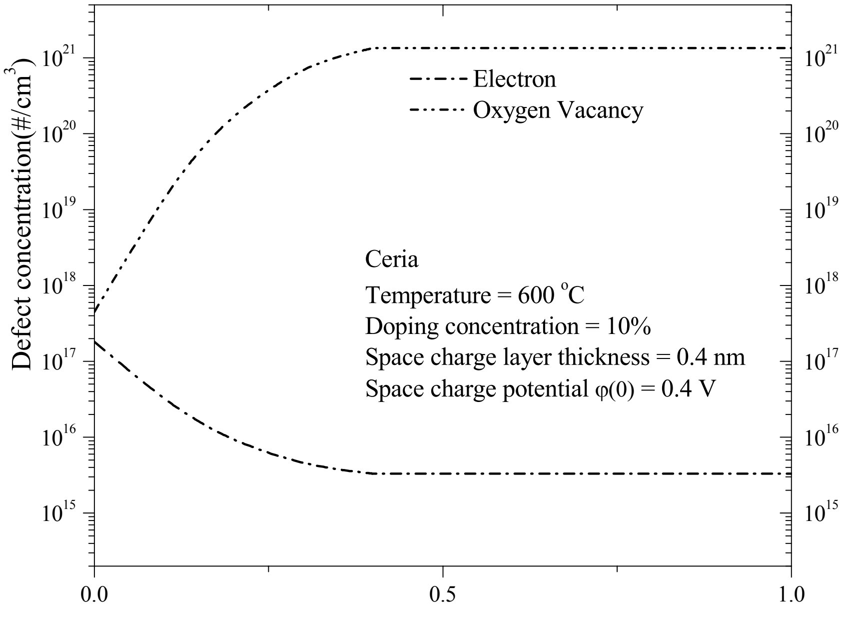

Figure 11 Calculated defect concentrations (on a log scale) in a space charge layer as a function of distance from grain boundary core at 600 °C.

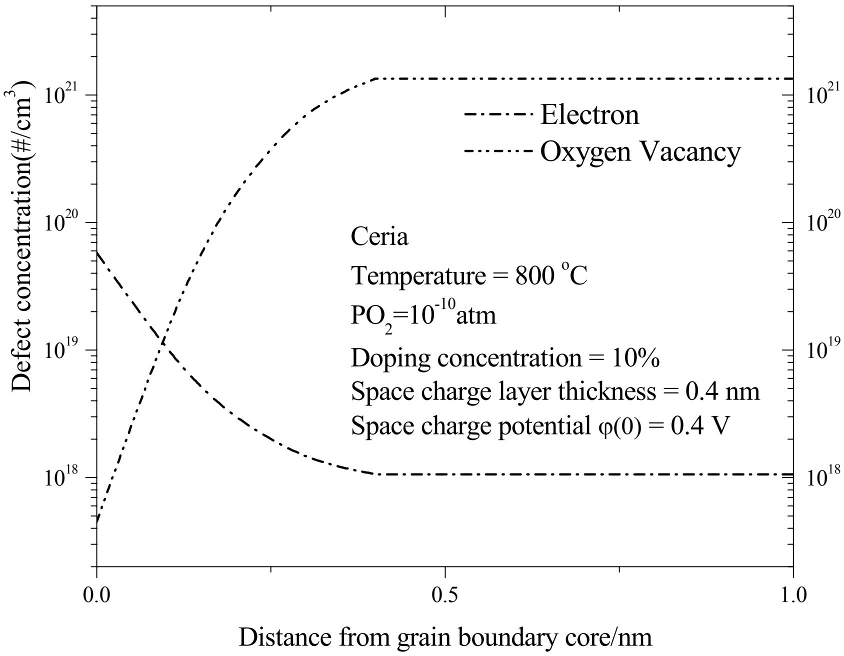

Figure 12 Calculated defect concentrations (on a log scale) in a space charge layer as a function of distance from grain boundary core at 800 °C.

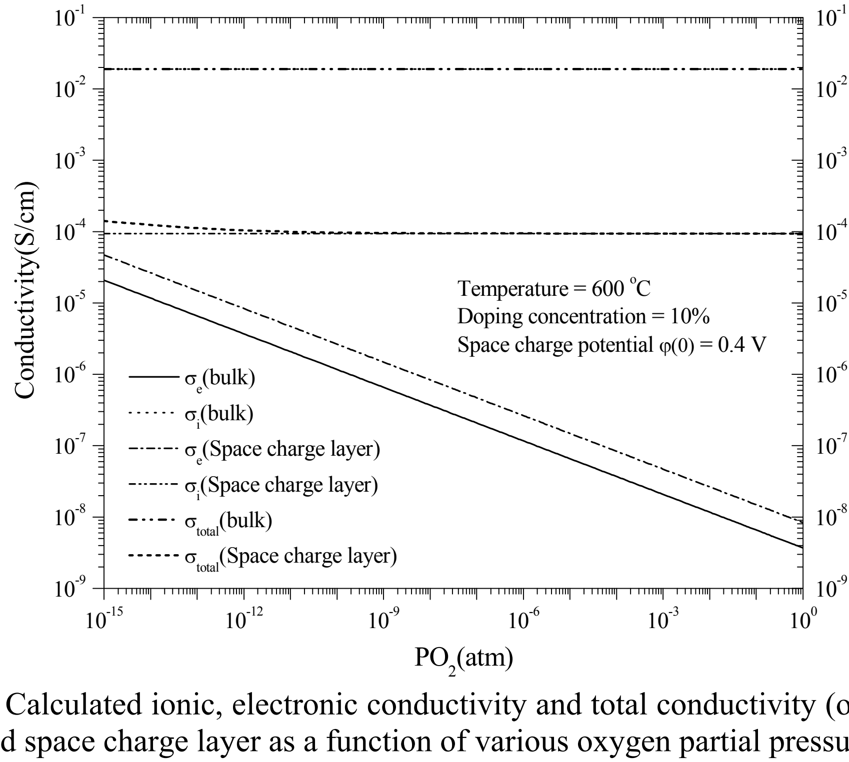

Figure 13 Calculated ionic, electronic conductivity and total conductivity (on a log scale) in bulk and space charge layer as a function of various oxygen partial pressures

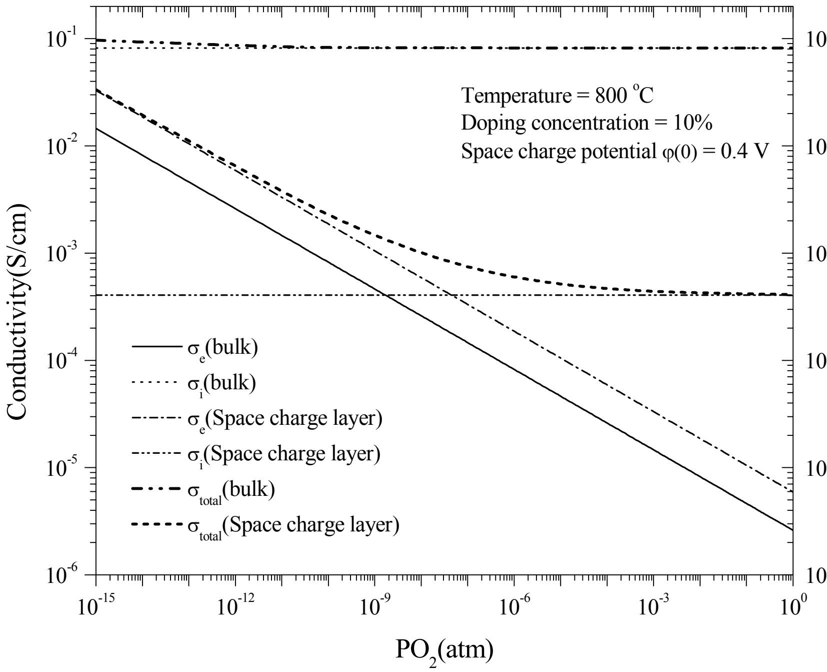

Figure 14 Calculated ionic, electronic conductivity and total conductivity (on a log scale) in bulk and space charge layer as a function of various oxygen partial pressures

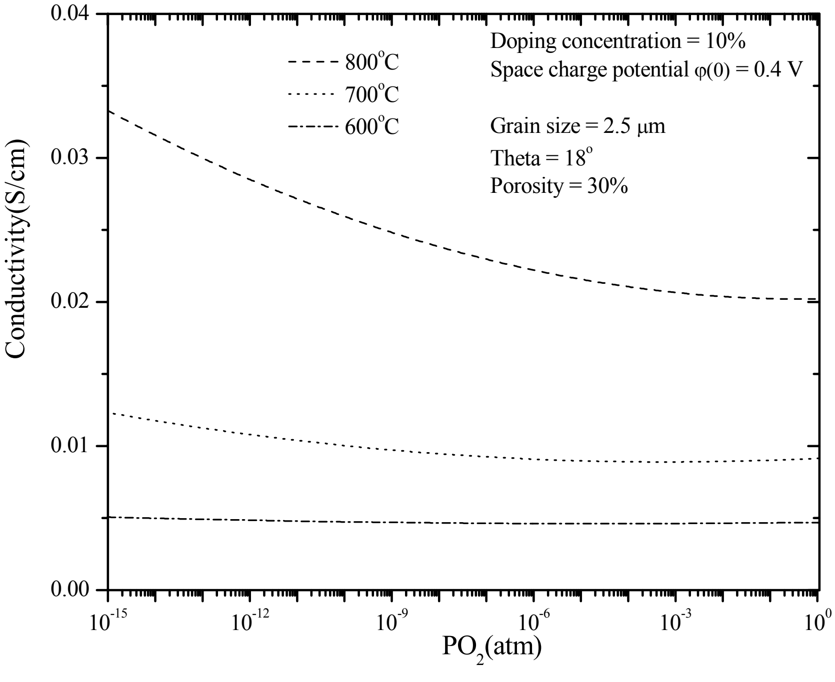

Figure 15 Calculated ionic and electronic conductivity (on a log scale) as a function of various oxygen partial pressures.

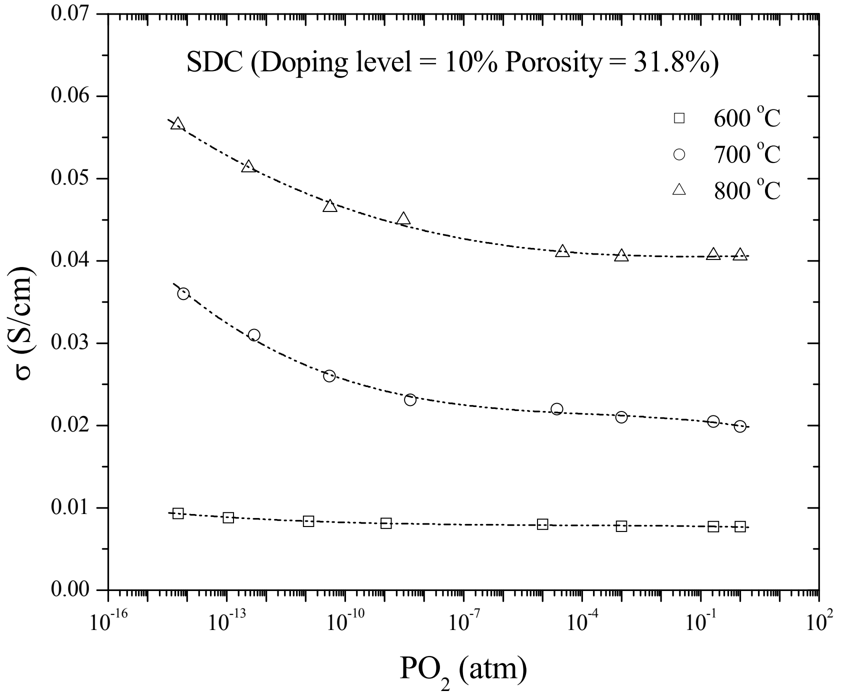

Figure 16 Measure electrical conductivity (on a log scale) by 4-probe technique as a function of various oxygen partial pressures.

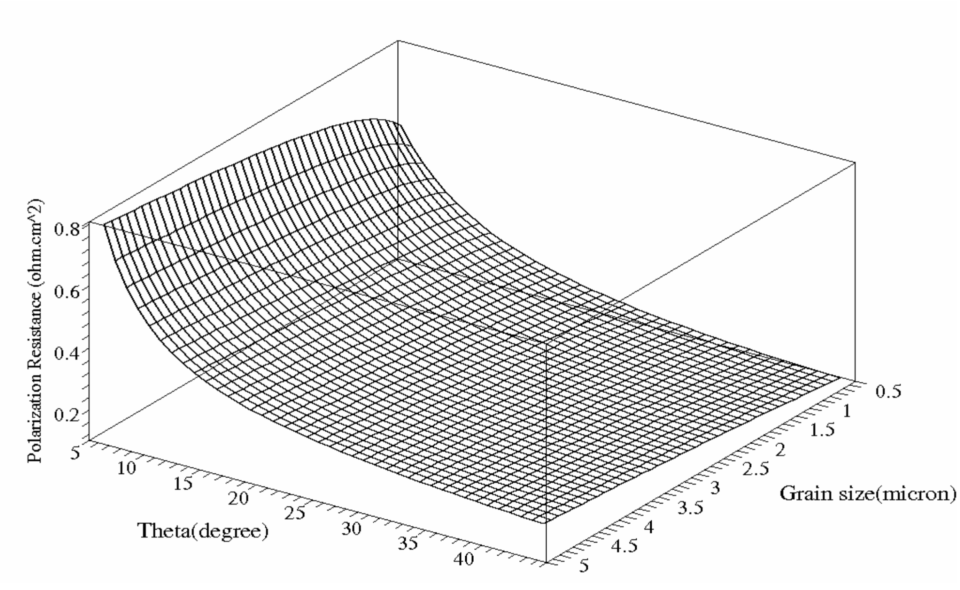

Figure 17: Calculated electrode polarization resistance, using YSZ as the ionic conductor in a composite cathode, as a function of angle (relative neck size) and grain size at 800^{o}C. Note that the polarization resistance rises sharply at small angles (narrow necks).

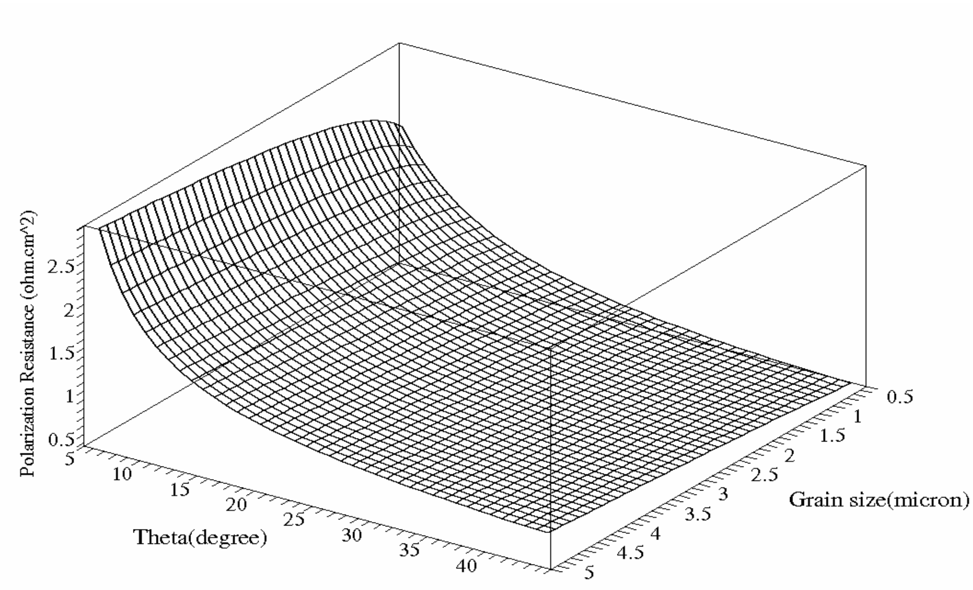

Figure 18: Calculated electrode polarization resistance, using YSZ as the ionic conductor in a composite cathode, as a function of angle (relative neck size) and grain size at 650°C. Note that the polarization resistance rises sharply at small angles (narrow necks).

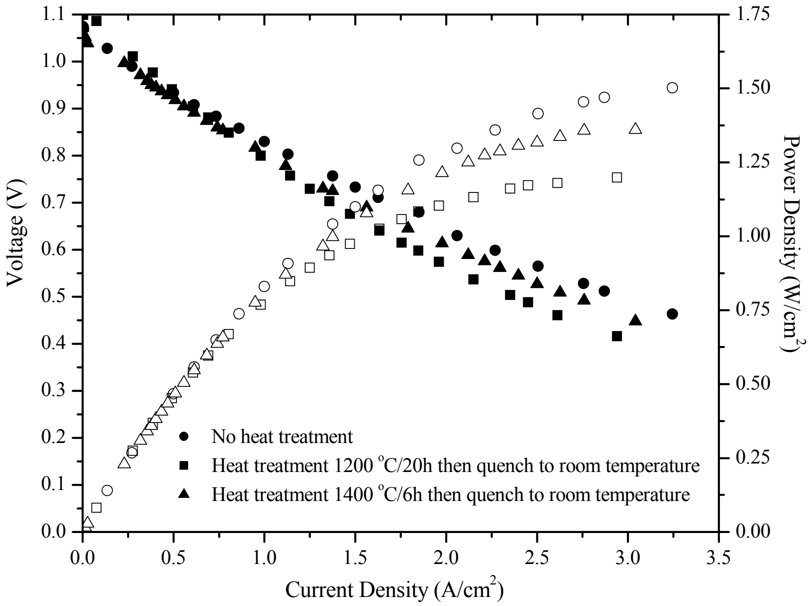

Figure 19: Voltage and power density vs. current density plots at 800°C for cells with cathode fabricated using the infiltration method, wherein the cell with the ionic conductor skeleton in the composite cathode was annealed and then quenched to room temperature prior to cathode infiltration.

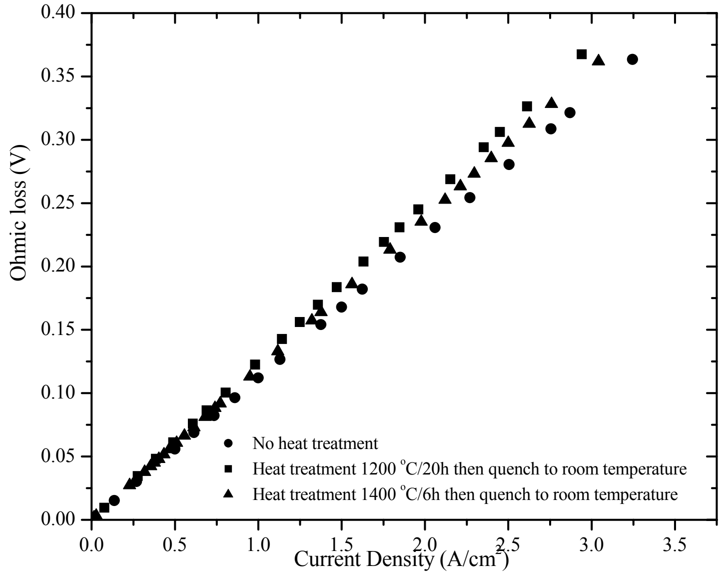

Figure 20: Ohmic overpotential (by current interruption) as a function of current density for cells with various thermal histories.

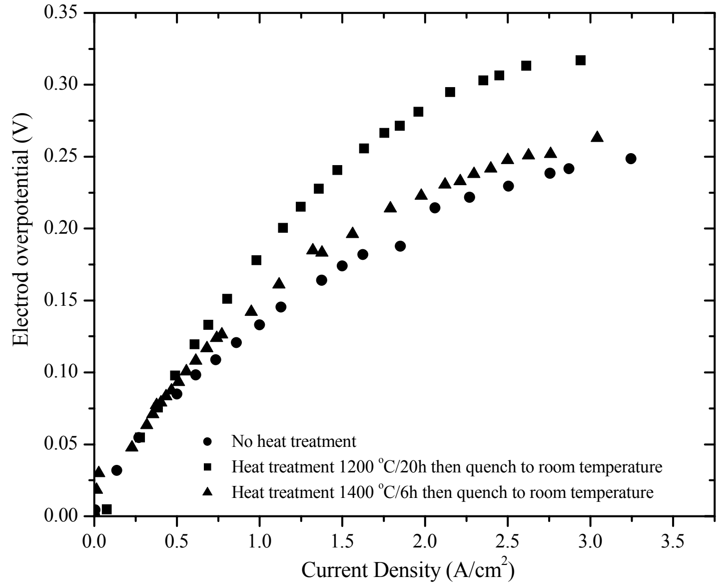

Figure 21: Electrode polarization as a function of current density for cells with various thermal histories.

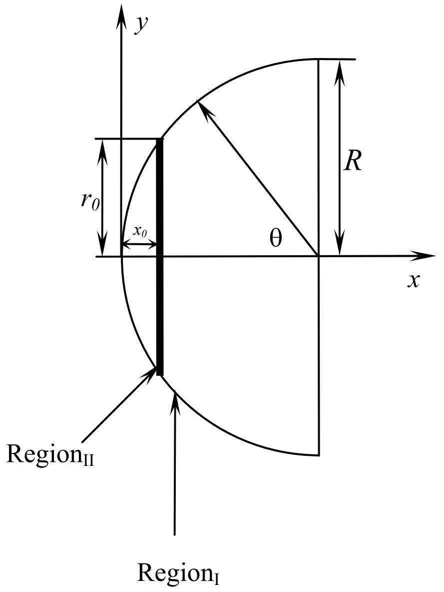

Figure 22: Geometry of the particle used for calculation (no space charge effect included).

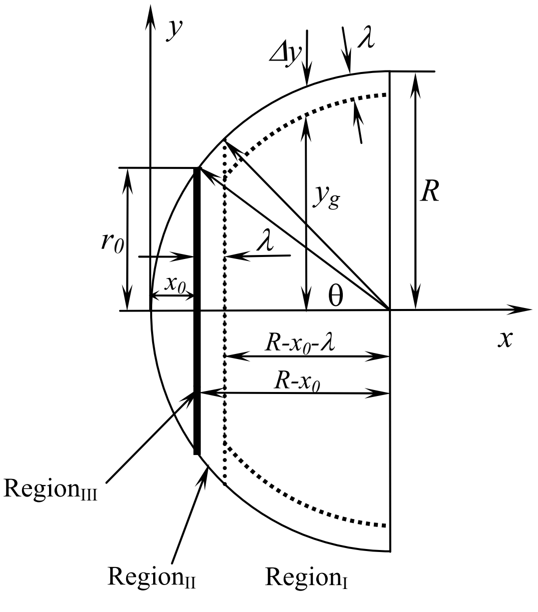

Figure 23: Geometry of the particle for calculation (space charge effect included).